HAL
open science

High Intensity Laser-Plasma Grating Interaction: surface wave excitation and particle acceleration

Bigongiari Alessandra

To cite this version:

Bigongiari Alessandra. High Intensity Laser-Plasma Grating Interaction: surface wave excitation and particle acceleration. Plasmas. Ecole Polytechnique X, 2012. English. NNT : . pastel-00758355

HAL Id: pastel-00758355

https://pastel.hal.science/pastel-00758355v1

Submitted on 28 Nov 2012

HAL is a multi-disciplinary open access archive for the deposit and dissemination of scientific research documents, whether they are published or not. The documents may come from teaching and research institutions in France or abroad, or from public or private research centers.

L'archive ouverte pluridisciplinaire **HAL**, est destinée au dépôt et à la diffusion de documents scientifiques de niveau recherche, publiés ou non, émanant des établissements d'enseignement et de recherche français ou étrangers, des laboratoires publics ou privés.

THESE DE DOCTORAT

presentée par

Alessandra BIGONGIARI

pour obtenir le grade de

DOCTEUR DE L'ECOLE POLYTECHNIQUE

Spécialité: physique

High Intensity Laser-Plasma Grating Interaction: Surface Wave Excitation and Particle Acceleration

soutenue publiquement le 19 Septembre 2012 devant le jury composeé de:

Emmanuel D'HUMIERES	Université Bordeaux 1	Rapporteur
Erick LEFEBVRE	CEA/DAM	Examinateur
Jean-Pierre MATTE	Université du Québec	Rapporteur
Patrick MORA	Ecole Polytecnique	Prèsident du jury
Denis PESME	Ecole Polytecnique	Invité
Michèle RAYNAUD	CEA/DSM	Directeur de thèse
Caterina RICONDA	Université Paris VI	Directeur de thèse

Abstract

Surface waves in solids were first observed by Wood in 1902 as an anomaly in the diffraction of a continuous light source from a metal grating: the diffracted spectrum presented dark lines corresponding to certain wavelengths, which were later explained (Fano, 1941) in terms of the excitation of a surface wave sustained by the grating. Similarly to the metal grating case, a surface plasma wave (SPW) can be resonantly excited by a laser pulse at the surface of a laser-produced overdense plasma, if the correct matching conditions are respected. SPWs propagate along the plasma-vacuum interface and are characterized by a localized, high frequency, resonant electric field. In the present work we describe numerically the dynamics of the plasma and the field distribution associated with SPW excitation, using two-dimensional particle-in-cell (PIC) simulations, where the plasma surface is initially pre-formed so that the SPW excitation conditions are fulfilled. We examine the surface wave excitation for a large range of laser intensities ($I\lambda_0^2 = 10^{15} - 10^{20}$W cm$^{-2}\mu m^2$) in order to study the transition from the non-relativistic to the relativistic regime. The simulations where the wave is resonantly excited are compared to cases where the resonant conditions are not provided and the coupling of the laser pulse with the target is analyzed. We have considered the following aspects of the laser-plasma interaction, for different laser and target parameters: i) the laser absorption and the electric field at the surface ii) the generation of a quasi-static magnetic field iii) the electron heating and iiii) the acceleration of ions. The possibility to excite a surface plasma wave on a structured target for a large range of laser energies has been demonstrated. In the cases where the surface wave is excited the electric field component normal to the target is amplified at the surface by a factor ranging from 3.2 to 7.2 with respect to the laser field. The absorption is also increased, for example it raises from 27% when the SPW is not excited up to 73% for $I\lambda_0^2 = 10^{19}$W cm$^{-2}\mu m^2$. We have defined the optimal conditions for efficient coupling, which correspond to the relativistic laser intensities ($I\lambda_0^2 > 10^{18}$W cm$^{-2}\mu m^2$). In this regime the main absorption mechanism is vacuum heating, associated to particles oscillating in the field perpendicular to the target, which is enhanced by the stronger, localized field of the SPW. The generation of a quasi-static magnetic field has been studied analytically and compared to the result of PIC simulations. The field structure, which is different in presence of a SPW compared to a flat target, suggests that the enhanced field strength has caused partial confinement of particles at the target surface when SPW is present. The effects of the surface wave are more pronounced in thin laminar targets, where electrons recirculate into the target and therefore interact several times with the wave. Efficient electron heating increases the energy of the ions

that are accelerated at both the irradiated and non-irradiated target surface by the hot electrons space-charge field. For the thinnest target investigated (3.5μm) the high energy cut-off of ions is about 14MeV, approximately twice the value obtained when the SPW is not excited.

Acknowledgements

I first would like to thank my supervisors Michèle Raynaud of CEA/DSM and Caterina Riconda of Université Paris VI for their constant support and encouragement and for giving me the chance to work in an always friendly and stimulating environment.

I owe my deepest gratitude to Anne Heron of CPHT for her invaluable support in the use and modification of the simulation code that I have used to perform the numerical study of laser-plasma grating interaction.

I wish to thank Jean-Claude Adam and Denis Pesme of CPHT and all the collegues of LULI and LSI who constantly helped me whith their suggestion and remarks.

I would also like to thank all the researchers from the CPU of Prague, the LULI of Ecole Polytechnique, the IRAMIS/SPAM of CEA Saclay and the CNR/INO of Pisa who have partecipated to the LASERLAB project, the experimental campaign based on the analytical and numerical work presented in this thesis.

Finally I would like to thank my family and friends, in particular Lorenzo, Alberto, Jerome, Anna, Marc, Gauthier, David, Blaise, Xue, Helene and the association X'Doc.

Contents

Introduction **1**

1 Relevant physics issues **5**
1.1 Electro-magnetic (EM) waves inside a plasma . . . 5
1.1.1 Plasma with a constant density gradient . . . 7
1.2 Relativistic effects . . . 8
1.3 Ponderomotive force . . . 10
1.4 Laser absorption in over-dense plasmas . . . 12
1.4.1 Resonant absorption . . . 13
1.4.2 Vacuum heating . . . 15
1.4.3 J×B heating . . . 17
1.4.4 Experimental results on laser absorption . . . 17
1.5 Plasma expansion and ion acceleration . . . 18
1.5.1 Target Normal Sheath Acceleration . . . 18
1.5.2 Shocks . . . 20
1.6 Surface waves: analytical model . . . 23
1.6.1 First order fields . . . 24
1.6.2 Surface waves at the plasma-vacuum interface . . . 25
1.6.3 Electrostatic and Electromagnetic limits . . . 27
1.6.4 Effects of electron temperature . . . 28

2 Resonant excitation of a SPW **35**
2.1 Laser-plasma coupling via SPW . . . 38
2.1.1 Local field amplification . . . 38
2.1.2 Enhanced absorption via SPW . . . 40
2.2 Effect of density variation . . . 44
2.3 Incidence angles out of resonance . . . 45
2.4 Effects of the modulation depth . . . 48
2.5 Effects of the target thickness . . . 53
2.6 Conclusion . . . 54

3 Magnetic field generation **57**
3.1 Analytical model for magnetic field generation . . . 57
3.2 Quasi-static magnetic field in PIC simulations . . . 64
3.2.1 Magnetic field when the SPW is excited . . . 65

3.2.2 Magnetic field for the flat target . . . 69
3.3 Conclusion . . . 71

4 Electron heating **73**
4.1 Electron energy . . . 75
4.1.1 Non-resonant angles . . . 78
4.1.2 Modulation depth . . . 80
4.2 Electron emission angles . . . 83
4.2.1 Non-resonant angle of incidences . . . 92
4.2.2 Effects of the modulation depth . . . 96
4.3 Laminar targets . . . 99
4.3.1 Electron heating . . . 100
4.3.2 Non-resonant incidence and reduced modulation depth . . . 105
4.4 Conclusion . . . 107

5 Ion acceleration **111**
5.1 Characteristics of ion emission . . . 112
5.2 The shock front . . . 118
5.3 Non-resonant angles . . . 121
5.4 Reduced modulation depth . . . 125
5.5 The laminar target . . . 130
5.5.1 Non-resonant angles and reduced modulation depth . . . 135
5.6 Ion energy at the end of the interaction . . . 140
5.7 Conclusion . . . 141

6 The case of a Gaussian laser pulse **145**
6.1 SPW excitation . . . 146
6.2 Electron heating . . . 148
6.3 Ion acceleration . . . 152
6.4 The magnetic field . . . 155
6.5 Conclusion . . . 156

Conclusions **159**

Appendices **165**
.1 Particle In Cell codes . . . 167
.1.1 The principle of PIC technique . . . 167
.1.2 Technical aspects . . . 169
.2 Modifications, diagnostics and tests . . . 172
.3 Angle-energy relation . . . 173
.4 Laserlab project (June 2012) . . . 175

Introduction

The recent development of Ti-Sapphire lasers providing ultra-short ($\tau \leqslant 100$fs) intense ($I\lambda_0^2 \geqslant 10^{17}$W cm$^{-2}\mu m^2$) IR laser pulses [1] and the plasma mirror technique [2] which permits high pulse contrast ($> 10^{11}$), allow the creation of a sharp-edged overdense plasma before any eventual smoothing of the density gradient by hydrodynamic expansion in thick plasmas ($L_x \gg c/\omega_{pe}$, where L_x indicates the plasma thickness, ω_{pe} is the plasma frequency and c/ω_{pe} is the skin depth). In such sharp-edged overdense plasmas the electromagnetic energy is weakly absorbed in an optical skin depth by collisional processes and through collisionless mechanisms [5] such as sheath inverse bremsstrahlung [16], $\mathbf{J} \times \mathbf{B}$ heating [17], vacuum heating [18] and anomalous skin-layer heating [39]. Owing to the ultra-short laser pulse duration and the steep density profile of the plasma, the laser reflection is very high, and can easily exceed 80% [42] thus limiting the production of high energy particles. This is a drastic limitation in all applications related to particle acceleration and for the fast ignitor scheme in the context of inertial confinement fusion [45, 46].

To overcome these difficulties, new mechanisms have been investigated in order to improve laser absorption and electron acceleration by considering structured targets: for example in [35] it was observed experimentally that the total number of fast electrons ejected from the irradiated surface of a sub-wavelength grating target was two times higher than that of a planar target while in [47] an enhancement in hard-x-ray emission from short-lived solid density plasmas was obtained by modulation of the interacting surface with nanostructures. The interaction of a laser pulse with structured targets has also been studied theoretically and numerically for the generation of harmonics [56], to enhance laser absorption [57] and to increase the efficiency of laser energy conversion into accelerated ions and their maximum energy [58].

More specifically, structured targets allow the excitation of surface plasma waves (SPWs) [73, 76, 77]. These waves are supported by a stepwise profile, overdense ($\omega_{pe} > \omega_0$, where ω_0 is the laser frequency) plasma when the conditions for resonant excitation are satisfied. SPWs propagate along the plasma-vacuum interface and are characterized by a localized, high frequency, resonant electric field.

In a previous work limited to a weakly relativistic laser intensity ($I\lambda_0^2 = 10^{18}$W cm$^{-2}\mu m^2$, where I is the intensity and λ_0 is the wavelength of the laser) [77], the possibility of resonant excitation of a SPW by ultrashort (60fs) high intensity laser pulse incident on an overdense ($n_e = 25n_c$, where $n_c \equiv \omega_0^2 m_e/4\pi e^2$ is the cut-off density at which $\omega_{pe} = \omega_0$), pre-structured plasma was demonstrated. A dramatic increase of both the laser absorption (up to 70%) and the electron energy (several MeV) was observed. A

highly amplified local electric field was also observed at the surface, associated with the SPW, which has important consequences on electron heating.

It is worth noticing that a high contrast and an ultrashort duration of the laser pulse are essential prerequisites for SPW absorption to work at very high intensities. The interaction time should be short enough to prevent the grating structure from being washed out by the plasma expansion, while too strong a pre-pulse would destroy the grating even before the short pulse interaction. This latter effect, which has probably been the main limiting factor for experimental investigations of SPW absorption in the past, can now be prevented by the above mentioned plasma mirror techniques for pulse cleaning. This motivates further theoretical and numerical works.

In this work we present two-dimensional particle-in-cell (PIC) simulations where the plasma surface is initially pre-formed so that the SPW excitation conditions are fulfilled. The effects of different parameters on laser-plasma coupling will be investigated, such as the laser intensity, plasma density and target geometry.The aim is to determine the range of parameters which optimize the effects of SPW excitation on laser absorption and particle acceleration.

In chapter 1, we present a review of laser-plasma physics concepts which are relevant for the understanding of the interaction regime that will be investigated in this work.

In chapter 2 we have studied the laser absorption and the characteristics of the electric field at the target surface when a SPW is excited and compared to cases which do not match the conditions for resonant excitation, *i.e.* where the laser pulse impinges the grating with a non-resonant angle of incidenceor a flat target. The dependence of laser-target coupling has been examined for different target parameters such as the plasma density, the depth of the surface grating and the target thickness.

In chapter 3 we have examined the generation of a quasi-static magnetic field near the plasma surface, possibly leading to higher field values compared to other known mechanisms [67] when the SPW is excited. These include: nonparallel electron density gradient and temperature [60], the radiation pressure associated with the laser pulse itself [45] and/or the current of fast electrons generated during the interaction [61]. The growth of intense magnetic fields localized in the vicinity of the interaction layer can play an important role: for instance it was found to determine the divergence of the beam of energetic particles entering the plasma [79, 66] and the number of particle in the beam [68].

In chapter 4 the electron heating is analyzed in presence of a SPW and the electron energies observed are compared to the non-resonant cases. The angular distribution of energetic electrons ('hot') and the electron currents are examined and the role of the target geometry is investigated. The optimal conditions for electron heating are determined as a function of the laser intensity, the target thickness and the depth of the surface grating.

The enhanced electron heating via SPW's has important consequences on ion acceleration which is investigated in chapter 5. The angular distribution of the accelerated ions is examined for different laser angles of incidence and target characteristics. Two acceleration mechanisms are observed: the target normal sheath acceleration, which is driven by the 'hot' electron space charge field and acceleration in the shock wave which is ponderomotively launched at the irradiated surface.

In chapters 2-5 we considered a laser pulse profile such that the intensity of the laser was uniform on the target surface, in order to simplify the study of the laser-plasma grating interaction. This does not reproduce the real envelope of a laser pulse, which has a given transversal size. In chapter 6 we have examined the effect of the finite transverse size of the pulse envelope, approximating his profile in the direction perpendicular to the laser propagation with a Gaussian function. The characteristics of SPW excitation and particle acceleration are analyzed and compared to the case where the pulse intensity was uniform in the transverse direction.

Finally, in the Conclusion, the different aspects of laser plasma coupling via the excitation of a SPW will be summarized, and the efficiency of this scheme and its possible applications will be discussed.

Chapter 1

Relevant physics issues in laser-overdense plasma interaction

In this chapter a review of laser-plasma physics concepts is presented which are relevant for the understanding of the interaction regime that will be investigated. In fact the excitation of a surface plasma wave (SPW) occurs at the interface of the vacuum with an over-dense plasma which can be created during the interaction of an intense laser-pulse with a solid target. We will initially derive (section 1.1) some basic equations which describe the interaction of electro-magnetic waves with plasma, then we will introduce relativistic effects which are important for intense laser pluses (section 1.2) and the ponderomotive force (section 1.3) and, in section 1.4, we will review the laser absorption mechanisms which are efficient in the interaction regime which we will study in the following chapters. In section 1.5 we will review the theory and literature which describes the plasma expansion occurring after the interaction with the laser and the acceleration of ions by different mechanisms. The latter will be useful in the following chapters where the acceleration of particles in presence of a surface wave is studied. Finally (section 1.6) we will introduce surface waves using an analytical model and the motivations which are at the basis of this work.

1.1 Electro-magnetic (EM) waves inside a plasma

We will recover here some useful notions concerning the propagation of a purely EM wave, having only transverse fields with respect to the propagation direction, inside a plasma. In a plasma, the presence of charged particles, ions and electrons, which are free to move under the effect of the wave's fields, modifies the evolution of EM waves compared to the vacuum. In absence of external charge and current sources the set of Maxwell's equations can be expressed as

$$\nabla \times \mathbf{B} = \epsilon \frac{1}{c}\frac{\partial}{\partial t}\mathbf{E} \tag{1.1}$$
$$\nabla \times \mathbf{E} = -\frac{1}{c}\frac{\partial}{\partial t}\mathbf{B} \tag{1.2}$$
$$\nabla \cdot (\epsilon \mathbf{E}) = 0 \tag{1.3}$$
$$\nabla \cdot (\mathbf{B}) = 0 \tag{1.4}$$
$$\tag{1.5}$$

The dielectric function ϵ and the conductivity of the plasma may be determined using Maxwell's equations in the presence of a density and velocity perturbation of the plasma particles. We can assume that only electrons move, as the period of the wave will be typically much shorter than the time required for ions to be accelerated by the electromagnetic field to a significant velocity ($\sim 1/\omega_{pi} = (4\pi e^2 n_i/m_i)^{-1/2}$, where m_i and n_i are the ion mass and density respectively). Thus, in addition to Maxwell's equations, the following linearized ($v = v_0 + v_1$, $v_1 \ll c$) momentum equation for the electron fluid will be used

$$\frac{\partial \mathbf{v_1}}{\partial t} = -\frac{e\mathbf{E}}{m_e} \tag{1.6}$$

where v_1 is the velocity perturbation of the electron fluid (the unperturbed velocity is $v_0 = 0$).
Defining the electron density as $n_e = n_0 + n_1$, where n_1 is the perturbation and n_0 is the unperturbed density ($n_1 \ll n_0$), equations (1.1) and (1.3) may be rewritten as

$$\nabla \times \mathbf{B} = \frac{4\pi}{c}\mathbf{J} + \frac{1}{c}\partial_t \mathbf{E} \tag{1.7}$$
$$\nabla \cdot (\mathbf{E}) = -e4\pi(n_e - n_0) = -e4\pi n_1 \tag{1.8}$$

where we assumed $n_i = n_0$ for the ion density and $Z = 1$ for the ion charge. The electron current coming from the perturbation is $J = -e(n_0 + n_1)v_1$, thus linearizing we get $J = J_1 = -en_0 v_1$. Therefore, using equations (1.1) and (1.7) we obtain

$$-\nabla^2 \mathbf{E} = -\frac{1}{c^2}\left[\left(4\pi \frac{\partial \mathbf{J}}{\partial t}\right) + \frac{\partial^2 \mathbf{E}}{\partial t^2}\right] \tag{1.9}$$
$$-\nabla^2 \mathbf{E} = -\frac{1}{c^2}\left[\left(-e4\pi n_0 \frac{\partial \mathbf{v_1}}{\partial t}\right) + \frac{\partial^2 \mathbf{E}}{\partial t^2}\right] \tag{1.10}$$

Then using (1.6) and imposing fields of the type $\tilde{E}e^{i\mathbf{kr}-iwt}$ (where $\mathbf{k}$ is the wave vector, ω is the frequency and $\mathbf{r}$ is a generic space variable), we get the dispersion relation for a EM wave inside a plasma

$$k^2 = \frac{\omega^2}{c^2} - \frac{\omega_p^2}{c^2} = \epsilon_p \frac{\omega^2}{c^2} \tag{1.11}$$
$$or \qquad k^2 c^2 = \omega^2 - \omega_p^2$$

and the expression for the dielectric function of the plasma

$$\epsilon_p = 1 - \frac{\omega_p^2}{\omega^2} \tag{1.12}$$

where we have used the definition of *plasma frequency* $\omega_p = (4\pi e^2 n_e/m)^{1/2}$. Note that ω_p is the minimum frequency for the propagation of a light wave in a plasma *i.e.*, k becomes imaginary for $\omega < \omega_p$: since the characteristic response time for electrons is ω_p^{-1}, the electrons shield out the field of a light wave when $\omega < \omega_p$. The condition $\omega = \omega_p$ defines the maximum plasma density at which a light wave can penetrate, called *critical density* $n_c = \omega_p^2 m/4\pi e^2 = (1.1 \times 10^{21}/\lambda^2[\mu\mathrm{m}^2])cm^{-3}$.

1.1.1 Plasma with a constant density gradient

We will now consider a plane electromagnetic wave normally incident onto a plasma slab whose density is not homogeneous. The expressions of the fields inside a density gradient will be derived, which will be useful in section 1.4.1, where we describe the *resonance absorption* of EM radiation. In fact resonant absorption occurs when a density gradient is present which is parallel to the incoming wave electric field, so that a resonant field is driven.

In the following we will use a Cartesian coordinate system where the plasma fills the $x > 0$ semi-plane and we will assume variations only in the x direction. The wave equation for the electric field $\mathbf{E} = E(x)\hat{y}$ is

$$\frac{d^2E}{dx^2} + \frac{\omega^2}{c^2}\epsilon(\omega, x)E = 0 \tag{1.13}$$

Assuming that the plasma density is a linear function of the position of the form $n_e = n_c x/L$, we find

$$\frac{d^2E}{dx^2} + \frac{\omega^2}{c^2}(1 - x/L)E = 0 \tag{1.14}$$

which, after a change of variable $x \to \chi = (\omega^2/c^2L)^{1/3}(x - L)$, becomes

$$\frac{d^2E}{d\chi^2} - \chi E = 0 \tag{1.15}$$

This differential equation has two linearly independent solutions: the well-known Airy functions A_i and B_i [3]. The general solution of (1.15) can be written as

$$E(\chi) = c_1 A_i(\chi) + c_2 B_i(\chi) \tag{1.16}$$

where the two constants c_1 and c_2 are determined by the boundary conditions. The asymptotic behavior of the Airy functions for $\chi \to \infty$ is given by the following asymptotic formulae:

$$A_i(\chi) = \frac{e^{-2/3\chi^{2/3}}}{2\sqrt{\pi}\chi^{1/4}} \tag{1.17}$$

$$B_i(\chi) = \frac{e^{2/3\chi^{2/3}}}{2\sqrt{\pi}\chi^{1/4}} \tag{1.18}$$

As we expect E to be a standing wave outside the plasma ($\chi < 0$) and to decay as ($\chi \to \infty$), we will chose $c_2 = 0$ as the Airy function $B_i \to \infty$ for $\chi \to \infty$. In order to determine c_1 we have to match the total field at the surface $x = 0$ (i. e. for $\chi = -(L\omega/c)^{2/3}$) with the field of the incident light wave. If we assume $L\omega/c \gg 1$, *i.e.* the gradient scale length is much greater then the field wavelength, than we can use the asymptotic representation of $A_i(-\chi)$

$$A_i(-\chi) = \frac{\cos\left(2/3\chi^{2/3} - \pi/4\right)}{\sqrt{\pi}\chi^{1/4}} \tag{1.19}$$

Writing $\phi = 2/3\chi^{2/3} - \pi/4$, we can write the field $E(x = 0)$ as follows:

$$E(x = 0) = c_1 \frac{e^{i\phi} + e^{-i\phi}}{2\sqrt{\pi}(L\omega/c)^{1/6}} \tag{1.20}$$

then choosing $c_1 = E_L 2\sqrt{\pi}(L\omega/c)^{1/6}e^{-i\phi}$ the field at the plasma surface can be seen as the sum of the incident field E_L and a reflected wave with the same amplitude but shifted in phase [8]:

$$E(x = 0) = E_L(1 + e^{-i2\phi}) \tag{1.21}$$

Finally the general form of the field is

$$E(\chi) = E_L 2\sqrt{\pi}(L\omega/c)^{1/6}e^{i\phi}A_i(\chi) \tag{1.22}$$

The related magnetic field, directed along $\hat{z}$, is obtained from (1.2)

$$B(\chi) = -iE_L 2\sqrt{\pi}(c/\omega L)^{1/6}e^{i\phi}\frac{\partial A_i(\chi)}{\partial \chi} \tag{1.23}$$

were we used $\partial\chi/\partial x = (\omega^2/c^2L)^{1/3}$.

1.2 Relativistic effects

The interaction of a laser pulse with a plasma can be modified as a consequence of the relativistic effects associated with the quiver motion of electrons. We enter the relativistic regime when the momentum p_q associated with the oscillatory motion of

the electron in the electromagnetic field approaches $m_e c$. This is usually expressed in terms of the adimensional parameter a_0 as follows

$$a_0 = \frac{p_q}{m_e c} == \frac{eA_0}{m_e c} = \frac{eE_0}{m_e c\omega} > 1. \tag{1.24}$$

where E_0 and A_0 are the electric field and vector potential amplitudes respectively, and ω is the frequency. We will consider the case of the motion of an electron in the field of a plane wave, propagating along x and described by the vector potential

$$\mathbf{A}(x,t) \equiv \mathrm{Re}\left[\mathbf{e}\tilde{A}(x,t)e^{-i\omega t}\right] \tag{1.25}$$

where $|\tilde{\mathbf{A}}|$ corresponds to A_0 used in (1.24) and $\mathbf{e}$ is the polarization vector given by the relations

$$\mathbf{e} = \begin{cases} \mathbf{e}_y & \text{for the linear polarization,} \\ \frac{1}{\sqrt{2}}(\mathbf{e}_y + i\mathbf{e}_z) & \text{for the circular polarization.} \end{cases} \tag{1.26}$$

The plane wave is invariant for translation along the plane perpendicular to the x axis, thus we have the conservation of the canonical moment

$$\mathbf{\Pi} \equiv \left(\mathbf{p}_\perp - \frac{e}{c}\mathbf{A}\right). \tag{1.27}$$

where $\mathbf{p}_\perp$ is the momentum of the particle perpendicular to the direction of propagation of the wave. In the reference frame where the electron has no drift motion along x, *i.e.* $\langle p_x \rangle = 0$ and assuming $\mathbf{\Pi} = 0$, we will define the value of the relativistic factor γ averaged over the period as:

$$\langle \gamma \rangle = \sqrt{1 + \langle \mathbf{a}_L^2 \rangle}, \tag{1.28}$$

where $\mathbf{a}_L = e\mathbf{A}/m_e c$ (which means $a_0 = \frac{e|\tilde{\mathbf{A}}|}{m_e c}$).

Particularly for the circular polarization we note that $\mathbf{a}_L^2$ is constant. This means that the amplitude of the field does not depend on time (in fact the field vector has a uniform circular motion in the plane perpendicular to the propagation direction) and the relativistic factor is constant in time, *i.e.* $\langle \gamma \rangle = \gamma$. This allows the derivation of the equation for the *relativistic dielectric constant*. In fact the relation

$$\mathbf{J} = -en_e\mathbf{v} = -en_e\frac{\mathbf{p}}{m_e\gamma}, \tag{1.29}$$

shows that for circular polarization the current $\mathbf{J}$ has the same frequency as $\mathbf{p}$, that is the same as the laser pulse. Thus the only difference that we find with the non-relativistic case is that the electron mass is multiplied by the constant factor $\gamma = \sqrt{1 + \mathbf{a}_L^2}$ and the non-relativistic result can be generalized in the relativistic regime as

$$\epsilon = 1 - \frac{\omega_p^2}{\omega^2\gamma}. \tag{1.30}$$

Contrastingly, for the linear polarization, γ is not constant and the spectrum of $\mathbf{J}$ has all the harmonics of the principal frequency ω. However it is still possible to define a refraction index, by replacing γ in (1.30) with its averaged value

$$\epsilon = 1 - \frac{\omega_p^2}{\omega^2 \langle\gamma\rangle} \tag{1.31}$$

where the average value of the relativistic factor over a laser period is $\langle\gamma\rangle = \sqrt{1 + \mathbf{a}_0^2/2}$, for linear polarization. Thus we found that the refraction index η depends on the polarization. However we have to remember that this result was derived for a plane wave in the steady regime: in the case of a laser pulse having an envelope which is limited in time and space it is not possible to define a reference frame where $\langle p_x \rangle = 0$ and the dependence of the phase/group velocity on the field amplitude may cause dispersion and self-modulation [4].

1.3 Ponderomotive force

The ponderomotive force is a time-averaged force exerted by an electromagnetic wave impinging on a plasma. It is a non-linear effect, arising from the spatial gradients in the intensity of the electromagnetic wave and it is related to the more general concept of light pressure. In order to introduce the ponderomotive force associated with a laser pulse interacting with a plasma, we will initially consider the motion $\mathbf{x} = \mathbf{x}(t)$ of a charged particle in an EM field, described by the relations :

$$\frac{d\mathbf{p}}{dt} = -e\left[\mathbf{E}(\mathbf{x},t) + \frac{1}{c}\mathbf{v}\times\mathbf{B}(\mathbf{x},t)\right] \tag{1.32}$$

$$\mathbf{p} = \gamma m\mathbf{v}, \qquad \frac{d\mathbf{x}}{dt} = \mathbf{v}. \tag{1.33}$$

where p is the momentum of the particle and $\gamma = \sqrt{1 + p^2/m^2c^2}$. Assuming that the electromagnetic field of the laser oscillates at a main frequency ω, characterized by an amplitude having a "slow" temporal variation compared to the oscillation period $T = 2\pi/\omega$ and a "smooth" spatial variation compared to $\lambda = cT$, it can be described by the general equation

$$\mathbf{E}(\mathbf{x},t) \equiv \mathrm{Re}\left[\tilde{\mathbf{E}}(\mathbf{x},t)e^{-i\omega t}\right] = \frac{1}{2}\tilde{\mathbf{E}}(\mathbf{x},t)e^{-i\omega t} + \mathrm{c.c}, \tag{1.34}$$

where Re stands for 'the real part of' and the whole spatial dependence is included in the complex amplitude $\tilde{\mathbf{E}}(\mathbf{x},t)$, which is slowly varying in time. (In the following we will mark the complex amplitude of a variable which includes only the spatial dependence, as shown in eq.(1.34) with $\tilde{}$). The particle motion can be decomposed in a slowly varying part $\mathbf{x}_s(t)$ and an oscillating one $\mathbf{x}_q(t)$ as follows:

$$\mathbf{x}(t) = \mathbf{x}_s(t) + \mathbf{x}_q(t), \qquad \mathbf{x}_q(t) = \mathrm{Re}\left[\tilde{\mathbf{x}}_q(\mathbf{x},t)e^{-i\omega t}\right] \tag{1.35}$$

so that $\mathbf{x}_s(t)$ describes the slowly varying motion of the particle in the EM field, that corresponds to the motion of its center of oscillation, while $\mathbf{x}_q(t)$ will describe the quiver

motion about the center of oscillation. When this decomposition is possible, the motion of the center of oscillation can be described defining a slowly varying effective force, called the *ponderomotive force*. In order to give a simple idea of this force we will use a non-relativistic perturbative derivation, which will be valid for non-relativistic field intensities, *i.e.* for small amplitude fields. In this limit, assuming that at the lower perturbation order $\mathbf{x}_s(t)$ is constant over an oscillation period, we can write

$$m\frac{d\mathbf{v}_q}{dt} \simeq -e\mathbf{E}(\mathbf{x}_s,t), \qquad \frac{d\mathbf{x}_q}{dt} = \mathbf{v}_q, \tag{1.36}$$

which, using the complex representation, rapidly gives the amplitudes

$$\tilde{\mathbf{v}}_q = \frac{iq}{m\omega}\tilde{\mathbf{E}}_s, \qquad \tilde{\mathbf{x}}_q = -\frac{q}{m\omega^2}\tilde{\mathbf{E}}_s, \tag{1.37}$$

where $\tilde{\mathbf{E}}_s \equiv \tilde{\mathbf{E}}(\mathbf{x}_s,t)$. In order to obtain the equation of motion $\mathbf{x}_s(t)$ we will now derive the second order terms and keep only the terms having non-zero average over a period. Taking the expansion of the electric field about the center of oscillation

$$\mathbf{E}(\mathbf{x},t) = \mathbf{E}(\mathbf{x}_s+\mathbf{x}_q,t) \simeq \mathbf{E}(\mathbf{x}_s,t) + \mathbf{x}_q\cdot\boldsymbol{\nabla}\mathbf{E}(\mathbf{x}_s,t), \tag{1.38}$$

and the magnetic term of the Lorentz force in equation (1.33), which gives a second order term, we obtain

$$m\frac{d\mathbf{v}_s}{dt} \simeq q\left\langle \mathbf{x}_q(t)\cdot\boldsymbol{\nabla}\mathbf{E}(\mathbf{x}_s,t) + \frac{\mathbf{v}_q(t)}{c}\times\mathbf{B}(\mathbf{x}_s,t)\right\rangle \tag{1.39}$$

$$= q\frac{1}{2}\mathrm{Re}\left[\tilde{\mathbf{x}}_q\cdot\boldsymbol{\nabla}\tilde{\mathbf{E}}_s^* + \frac{\tilde{\mathbf{v}}_q}{c}\times\tilde{\mathbf{B}}_s^*\right]. \tag{1.40}$$

where we assumed that the form of the magnetic field $\mathbf{B}(\mathbf{x}_s,t)$ is similar to that of the electric field in (1.34) and $\tilde{\mathbf{B}}_s \equiv \tilde{\mathbf{B}}(\mathbf{x}_s,t)$. Applying equation $c\boldsymbol{\nabla}\times\mathbf{E} = -\partial_t\mathbf{B}$ to the field $\mathbf{B}(\mathbf{x}_s,t)$ and substituting with the equation for $\tilde{\mathbf{v}}_q$ and $\tilde{\mathbf{x}}_q$ obtained at the first order we can rewrite equation (1.39) as

$$m\frac{d\mathbf{v}_s}{dt} = -\frac{q^2}{2m\omega^2}\mathrm{Re}\left[\tilde{\mathbf{E}}_s\cdot\boldsymbol{\nabla}\tilde{\mathbf{E}}_s^* + \tilde{\mathbf{E}}_s\times\boldsymbol{\nabla}\times\tilde{\mathbf{E}}_s^*\right]. \tag{1.41}$$

If we expand the vector products, the term in square brackets becomes

$$\tilde{\mathbf{E}}_s\cdot\boldsymbol{\nabla}\tilde{\mathbf{E}}_s^* + \tilde{\mathbf{E}}_s\times\boldsymbol{\nabla}\times\tilde{\mathbf{E}}_s^* = \frac{1}{2}\boldsymbol{\nabla}\tilde{\mathbf{E}}_s\cdot\tilde{\mathbf{E}}_s^* = \frac{1}{2}\boldsymbol{\nabla}|\tilde{\mathbf{E}}_s|^2. \tag{1.42}$$

Thus we finally obtain the non relativistic expression of the ponderomotive force F_p:

$$m\frac{d\mathbf{v}_s}{dt} = -\frac{q^2}{4m\omega^2}\boldsymbol{\nabla}|\tilde{\mathbf{E}}_s|^2 \equiv \mathbf{F}_p. \tag{1.43}$$

We recall that in this derivation we used the complex form for the oscillating fields, therefore the average over the oscillation period reads

$$\langle AB \rangle = \frac{1}{2}\mathrm{Re}(\tilde{A}\tilde{B}^*), \tag{1.44}$$

then the quadratic amplitude of the real field $\mathbf{E} = \mathbf{E}(\mathbf{x}, t)$ is $\langle \mathbf{E}^2 \rangle = |\tilde{\mathbf{E}}_s|^2/2$ and we can rewrite (1.43) as

$$\mathbf{F}_p = -\frac{q^2}{2m\omega^2}\boldsymbol{\nabla}\left\langle \mathbf{E}^2 \right\rangle. \tag{1.45}$$

This result is valid in the non-relativistic limit. The relativistically correct calculation [15] shows that the cycle-averaged energy of a point charge in the oscillation center system ($\langle p_x \rangle = 0$) is

$$U_p = -mc^2\left[\left(1 + \frac{q^2}{\alpha m^2 c^2}|\tilde{\mathbf{A}}|^2\right)^{1/2} - 1\right] \tag{1.46}$$

where $\tilde{\mathbf{A}} = \tilde{\mathbf{A}}(\mathbf{x}, t)$ is the slowly varying amplitude of the vector potential $\mathbf{A}(\mathbf{x}, t) = \mathrm{Re}(\tilde{\mathbf{A}}(\mathbf{x}, t)e^{-i\omega t} + \text{c.c.}$, and $\alpha = 1$ or 2 for circular and linear polarization respectively. U_p is commonly referred as the *ponderomotive potential*. Thus the relativistic ponderomotive force equation (which reduces to (1.45) in the non-relativistic limit) for an EM wave in the vacuum is

$$\mathbf{f}_p = -\boldsymbol{\nabla}U_p = -mc^2\boldsymbol{\nabla}\left(1 + \frac{q^2}{\alpha m^2 c^2}|\tilde{\mathbf{A}}|^2\right)^{1/2} \tag{1.47}$$

Note that the term in bracket is the effective mass $m_{eff} = m\langle\gamma\rangle = m\left(1 + \frac{q^2}{\alpha m^2 c^2}|\tilde{\mathbf{A}}|^2\right)^{1/2}$ of the center of oscillation, and that in the relativistic regime it contains a factor expressing the inertia associated with the high frequency motion. In fact, in the relativistic regime the equation of motion becomes

$$\frac{d(m_{eff}\mathbf{v}_s)}{dt} = -c^2\boldsymbol{\nabla}m_{eff}. \tag{1.48}$$

The expression of $\langle\gamma\rangle$ defined above corresponds to (1.28) if we consider $m = m_e$, $q = e$ and $a_0 = \frac{e|\tilde{\mathbf{A}}|}{m_e c}$ as in (1.24).

The ponderomotive force definition is very useful in the description of laser-plasma interaction. However it has to be noticed that the derivation above is valid only if the temporal variation of the laser envelope is slow compared to the laser period, to allow the definition of an oscillation center.

1.4 Laser absorption in over-dense plasmas: non collisional mechanisms

As the preservation of the surface profile is a critical issue for the surface wave excitation, the laser pulse has to be ultra-short ($< 100fs$) in order to limit plasma expansion. In

such a plasma the thermal velocity of electrons is of the order of some hundreds of eV and collisional processes are not assumed to play an important role on the short time-scales ($< 1ps$) which are typical of the interaction. For these reasons we will present only the non-collisional absorption mechanisms which are present in over-dense plasmas.

1.4.1 Resonant absorption

Resonant absorption is a non-collisional absorption mechanism which takes place at the critical surface (defined as the surface where $n_e = n_c = \omega^2 m_e/4\pi e^2$, where ω is the frequency of the incident radiation) of a plasma having a density gradient. In order to have resonant absorption it is necessary to have a laser pulse with an electric field component parallel to the plasma gradient, that is $\mathbf{E} \cdot \nabla n_e \neq 0$. In fact this component induces electron oscillations along the direction of the density gradient, generating fluctuations in the plasma density. The oscillations can be amplified if a resonance is present in such a way to transfer an important part of the laser electro-magnetic energy into an electro-static oscillation, that is an electron plasma wave. We can describe this process with a simplified $2D$ model, following [8]: a plane plasma target, having a density gradient described by the function $n_e = n_c x/L$ fills the $x > 0$ half-plane. The wave vector of the laser field has to be in the plane of incidence in order to have a component parallel to the gradient, thus $\mathbf{E} = E_x\hat{x} + E_y\hat{y}$. Electrons oscillating between regions of different density create a density fluctuation δn such that:

$$\delta n = n_e(\mathbf{r} + \mathbf{r}_{osc}) - n_e(\mathbf{r}) \simeq \mathbf{r}_{osc} \cdot \nabla n_e \tag{1.49}$$

Where $\mathbf{r}_{osc} = e\mathbf{E}/m_e\omega^2$ is the amplitude of the oscillation of the electron in the electric field. Using Poisson's equation $\nabla \cdot (\epsilon_p \mathbf{E}) = 0$, where $\epsilon_p(x) = 1 - \frac{\omega_p^2}{\omega^2} = 1 - n_e(x)/n_c$ is the dielectric function of the plasma which varies along the gradient, we find

$$\nabla \cdot \mathbf{E} = -\frac{1}{\epsilon_p}\frac{\partial \epsilon_p}{\partial x} E_x \tag{1.50}$$

Thus we will have a resonance for $\epsilon_p(x) = 0$, that is at the critical density, where $\omega = \omega_p$. From eq.1.49 we see that the resonant frequency is also the frequency of the density fluctuation that is amplified.

For obliquely incident light, with an angle of incidence θ with respect to the target surface normal, the plasma dielectric function is [8]

$$\epsilon_p(x) = 1 - \frac{\omega_p^2}{\omega^2} - \sin\theta^2. \tag{1.51}$$

Thus the wave is reflected at a density $n_c \cos\theta^2$, that is less than the critical density, but its field can still tunnel into the critical density region, exciting the resonance.

We will now try to estimate the electric field driving the resonance at the critical surface. From Ampere's law we find that the relation between the electric field component E_x and the magnetic field parallel to the plasma surface B_z is

$$k_y B_z = -i\frac{\omega}{c}\epsilon_p(x)E_x \tag{1.52}$$

which, using the conservation of $k_y = \omega/c \sin\theta$, becomes

$$E_x = \sin\theta B_z/\epsilon_p(x) \tag{1.53}$$

Then we express B_z at the resonance point, $x = L$, as its value at the turning point $x = L\cos\theta^2$ multiplied by an exponential decay from the turning point to the resonance point. The decay constant will be estimated by integrating the evanescent wave vector $|k| = \sqrt{\epsilon_p(x)}\omega/c$ between the turning point and the resonance point. Using the expression (1.51) we obtain

$$|k| = \frac{1}{c}\int_{L\cos\theta^2}^{L}\sqrt{\omega_p^2 - \omega^2\cos\theta^2} = \frac{2\omega L}{3c}\sin^3\theta \tag{1.54}$$

Airy functions allow the estimation of B_z at the turning point for the linear density profile: $B_z \approx 0.9(c/\omega L)^{1/6}E_L$, where E_L is the amplitude of $\mathbf{E}$ in the free space. Then, using eq.(1.54) we obtain the form of the driven field as a function of the angle of incidence, density gradient scale length, laser field and frequency:

$$B_z = 0.9(c/\omega L)^{1/6}E_L \exp\left(-\frac{2\omega L}{3c}\sin^3\theta\right) \tag{1.55}$$

$$E_x = 0.9(c/\omega L)^{1/6}\frac{\sin\theta}{\epsilon_p(x)}E_L \exp\left(-\frac{2\omega L}{3c}\sin^3\theta\right) \tag{1.56}$$

where we used eq.(1.53). We observe that the driven field vanishes for vanishing $\sin\theta$ as there is no component of the incident wave field parallel to the density gradient any more. At the same time the field becomes very small for long L, *i.e.* for density gradients having a big scale length, as the field has to tunnel for a very long distance before reaching the critical density surface.

The solution found with this simple model is close to the one found numerically in [14], where the wave equation was solved. It is possible to calculate the wave absorption, assuming a generic wave damping mechanism (which could be collisions, linear and nonlinear wave particle interaction or propagation of the wave out of the resonant region) having characteristic frequency $\nu \ll \omega$. Then the dielectric function becomes $\epsilon_p(x) = 1 - \frac{\omega_p^2}{\omega(\omega+i\nu)}$ (see [8]) and we can estimate the absorbed energy as

$$I_{abs} = \int_0^\infty \nu\frac{E_x^2}{2\pi}dx = 0.81(c/\omega L)^{1/3}\sin^2\theta E_L^2 \exp\left(-\frac{4\omega L}{3c}\sin^3\theta\right)\int_0^\infty \nu\frac{1}{\epsilon_p(x)^2}dx \tag{1.57}$$

For $\nu \ll \omega$, considering the gradient expression, we can approximate the dielectric function contribution as$|\epsilon_p|^2 = (1-x/L)+(\omega/\nu)^2(x/L)^2$, which gives the integral value $\int_0^\infty \nu((1-x/L)+(\omega/\nu)^2(z/L)^2)dx = \pi\omega/\nu$. Finally the estimated intensity absorbed by resonant absorption is given by

$$I_{abs} = 0.81(\pi c/\nu L)^{1/3}\sin^2\theta E_L^2 \exp\left(-\frac{4\omega L}{3c}\sin^3\theta\right) \tag{1.58}$$

We observe that the resonant absorption depends linearly on the laser intensity by the factor E_L^2. However, it has to be noted that for relativistic laser intensities the ponderomotive force defined in section 1.3 may steepen the density gradient in such a way that electron oscillations in the density gradient are no possible any more.

1.4.2 Vacuum heating

In the case of a laser pulse incident on a plasma with a very steep density gradient, resonance absorption may not be possible. In fact, if the density gradient scale length is much less than the wavelength of light, a proper oscillation in the resonant field cannot be sustained. An alternative collisionless absorption mechanism, where the laser non-resonantly couples with the plasma can take place in these conditions, which has been proposed by Brunel [18]. This mechanism is known as Brunel heating, vacuum heating or not-so-resonant resonant absorption. In Brunel heating the electrons at the target or critical density surface are pulled into the vacuum and pushed back into the target by the component of the laser electric field perpendicular to the surface, in a half laser cycle. The electrons re-enter the target with a velocity of the order of their quiver velocity, associated with the laser field in the vacuum. As the laser can penetrate into the target only up to the skin depth, the electrons do not feel any restoring force in the second half of the laser cycle and are irreversibly accelerated into the target. As the driving force is the component of the laser electric field normal to the target, oblique incidence with p-polarization is required for Brunel heating to occur. Moreover as the electrons are accelerated at each laser cycle, in Brunel heating packets of electrons are injected into the target with a frequency equal to the the laser frequency. In order to understand this process we will present here a simple capacitor model, following [5]. Consider a plane wave $\mathbf{E}(\mathbf{x},\mathbf{t}) = \mathbf{E_0}\sin(\omega_\mathbf{0}\mathbf{t} - \mathbf{k_0}\mathbf{x})$, incident on a plasma having a steep density profile. At the surface of the target the incident and reflected waves will be present at the same time, thus, approximating the reflected wave as having the same amplitude of the incident one, the driving field (perpendicular to the target) at the surface is $E_d = 2E_0\sin\theta$, where θ is the angle of incidence, defined with respect to the target normal. Assuming that the electrons are dragged out in the vacuum over a distance Δx, the Poisson equation at the surface gives

$$\Delta E = -4\pi e\int_{-\Delta x}^{x=0} n dx = 4\pi e n\Delta x \tag{1.59}$$

where the electron density in the Δx band is $N/A\Delta x$ for a target surface area A. Setting $\Delta E = E_d$ we have the number of electrons pulled out per unit area.

$$\frac{N}{A} = \frac{2E_0 \sin\theta}{4\pi e} \tag{1.60}$$

The energy absorbed by the wave is simply $u_{abs} = N/2m_e v_d^2$, where $v_d = eE_d/m_e\omega$ and we assume that we are not in the relativistic regime. The power absorbed per unit area can be approximated as

$$I_{abs} = \frac{1}{A}\frac{du_{abs}}{dt} \approx \frac{N}{2A}\omega m_e v_d^2 = \frac{E_0 \sin\theta}{8\pi e} m_e \omega \frac{e^2 E_d^2}{m_e^2 \omega^2} = \frac{e8E_0^3 \sin\theta^3}{8\pi m_e \omega} \tag{1.61}$$

We can now calculate the fraction of power that is absorbed from the wave $f_{abs} = I_{abs}/I_0$, where $I_0 = cE_0^2/8\pi$ is the power of the incident wave per unit area:

$$f_{abs} = \frac{8eE_0 \sin\theta^3}{m_e \omega c} = 8\frac{v_{osc} \sin\theta^3}{c} \tag{1.62}$$

where $v_{osc} = eE_0/m_e\omega$. We notice that the absorption scales linearly with v_{osc}/c and it increases for increasing angles.This simple model includes the relevant physics and gives the correct scaling with laser parameters. However with a more detailed treatment Brunel [18] found the following equation for the fraction of laser energy absorbed via vacuum heating:

$$f_{abs} = \frac{\alpha}{2\pi}\frac{v_{osc}^3}{c v_L^2 \cos\theta} \tag{1.63}$$

where $v_L = eE_L/m_e\omega$ and α is a coefficient that gives an estimate of the amount of oscillatory motion lost in heating the plasma. Kato *et al.* [10] found that this coefficient depends on the density of the plasma target as follows

$$\alpha \approx \frac{\alpha_\phi}{1 - \frac{\omega_0^2}{\omega_p^2}} \tag{1.64}$$

where $\alpha_\phi = O(1)$ depends on the initial phase ϕ of the driving field. Thus, in the regime of very strongly overdense plasmas, where $\omega_0^2/\omega_p^2 \ll 1$, the α coefficient depends weakly on density.

Vacuum heating has been studied in literature by numerical simulations. For example Gibbon and Bell [52] studied vacuum heating by 1D PIC simulation (they mimic a laser with oblique incidence using a Lorentz frame transformation) for ultra-short ($\tau_L < 100fs$) laser pulse in the intensity range $I\lambda_0^2 = 10^{15-18}$W cm$^{-2}\mu m^2$: they found that absorption varied from 10% to 80% depending on the intensity and scale length of the plasma. *The scale length of the plasma, which is not treated in the model presented here, is studied in detail in [53, 19, 20] where it is found that vacuum heating becomes less efficient when the gradient scale length is too small.* This appears to be a consequence of the reduced penetration depth of the driving field in the plasma so that fewer electrons can be involved in the mechanism.

1.4.3 J×B heating

At high laser intensity ($a_0 > 1$) the longitudinal motion of the electrons in the laser field, due to the $\mathbf{v} \times \mathbf{B}$ component of the Lorentz force, becomes comparable to the transverse motion associated with the electric field. An absorption mechanism similar to the one described by Brunel can take place where the electrons are driven across the the vacuum plasma interface by the magnetic field rather than by the electric field [5]. In this case the absorption can take place even for normal laser incidence and electron packets will be accelerated with a frequency which is double the laser frequency. If the magnitude of the force is large enough, a fraction of electrons can be adiabatically accelerated from the surface into the overdense plasma. If we assume a step-like density profile, as for the vacuum heating, starting at $x = 0$ and a normally incident wave, we can write the vector potential inside the plasma as

$$\mathbf{A}(x,t) = A_0 e^{-q_p x} \hat{y} \cos(\omega t) \tag{1.65}$$

where $q_p = \frac{1}{c}(\omega_p^2 - \omega^2)^{1/2}$ is the inverse of the penetration depth of the wave into the plasma, defined by the dispersion relation (1.12). Using $\mathbf{B} = \nabla \times \mathbf{A}$ and $\mathbf{p}_\perp = m\mathbf{v}_\perp = \frac{e}{c}\mathbf{A}$(from (1.27)) we obtain the following relation for the force, in the non-relativistic regime:

$$\mathbf{F}_L = -\frac{e^2}{mc^2}\left[\mathbf{A} \times \boldsymbol{\nabla} \times \mathbf{A}\right] = A_0^2 e^{-2q_p x} \frac{e^2}{4q_p mc^2}(1 + \cos(2\omega t)) \tag{1.66}$$

where we used the trigonometric identity $\cos(2\omega t) = \cos^2(\omega t) - 1$. The mean energy that electrons absorb from the laser scales as the ponderomotive energy defined in (1.46) which in the present case takes the form:

$$\mathbf{F}_p =< \mathbf{F}_L >= A_0^2 e^{-2q_p x} \frac{e^2}{4q_p mc^2} \tag{1.67}$$

Notice that the magnitude of the force goes down for increasing electron density (corresponding to large values of q_p) as fewer and fewer electrons can be adiabatically accelerated into the plasma, decreasing the absorption efficiency. It is interesting to note that, if one integrates (1.67) from the boundary $x = 0$ to infinity and multiplies by the plasma density n_e, the result is twice the laser energy density, that is the total radiation pressure on the target surface, as was expected.

1.4.4 Experimental results on laser absorption

Several experiments with multi-terawatt lasers have been performed in which the dominant mechanism is believed to be a mixture of vacuum heating, resonance absorption and $J \times B$ absorption. We will briefly mention here only some experimental results to give an idea of the typical absorption percentage in the regime of high intensity,

short laser pulses which is the regime that we will investigate in the present work. For example in the measurements carried out at Rutherford Labs [31] in the UK, it was found that the fraction of energy absorbed was about 40% at $I\lambda_0^2 = 10^{19}$W cm$^{-2}\mu m^2$ for a 45° angle of incidenceand a pulse duration of $\tau_L = 400fs$. In a similar experiment performed at LLNL in the USA [33], where the angle of incidence was 22°, it was found that the absorbed energy was lower, *i.e.* $\simeq 30\%$. However for ultra-short pulses ($< 100fs$) the absorption mechanisms cited in this section are less efficient and laser reflection is higher, reaching 80% [22].

1.5 Plasma expansion and ion acceleration

In this section we will present the mechanisms of ion acceleration which are relevant for the case of a super-intense laser pulse interacting with a dense (solid) target.

Initially the plasma expansion will be treated analytically using a self-similar model, in order to introduce the first acceleration mechanism, *target normal sheath acceleration* (TNSA). This mechanism, which is efficient both at the irradiated and rear side of the target, is particularly important for ion acceleration occurring at the rear, *i.e.* the side that is not irradiated, where it is driven by the electrons generated at the front (irradiated) side which travels through the target.

The second mechanism is shock acceleration, which is ponderomotively driven by the intense pulse at the irradiated side. While TNSA accelerates ions outside the target (both at the front and the rear), shock acceleration accelerates ions inside the target.

1.5.1 Target Normal Sheath Acceleration

According to this model ions are accelerated normally to the target surface by the electric field associated with an electron plasma sheath. The electron sheath is set by the hot electrons accelerated by the laser pulse at the front surface and which have propagated through the target. After this initial phase the acceleration proceeds as a plasma expansion into a vacuum. The expansion is driven by the electric field due to space-charge separation at the plasma front: electrons transfer their energy to the ions via the electric field, which progressively decreases until the acceleration ceases. We will first calculate the electric field of the sheath assuming ions are not moving during the sheath formation and fill the half space $x < 0$. Electrons are assumed to be at equilibrium with a temperature T_e, such that the electron density is given by

$$n_e = n_0 \exp(e\phi/k_B T_e) \tag{1.68}$$

where ϕ is the electrostatic potential. Substituting (1.68) into the Poisson equation we get

$$\frac{\partial^2 \phi}{\partial x^2} = -4\pi e(Zn_i - n_e) = 4\pi e[n_o \exp(e\phi/k_B T_e) - Zn_i] \tag{1.69}$$

This equation can be integrated analytically [40] to obtain the electrostatic potential

$$\phi = -\frac{k_B T_e}{e}\left[2\ln\left(1+\frac{x}{\sqrt{2e_N}\lambda_D}\right)+1\right] \tag{1.70}$$

where $e_N \approx 2.71828...$ is the basis of the natural logarithm. Thus we may calculate the field at the target vacuum interface, which initially drives the ion acceleration

$$E = \frac{\partial\phi}{\partial x}|_{x=0} = \sqrt{2/e_N}\frac{k_B T_e}{\lambda_D e} = \sqrt{8\pi n_0 k_B T_e/e_N} \tag{1.71}$$

At later time the ion motion has to be taken into account and plasma expansion can be described by a self similar solution. We will consider a plasma such that $p_e = n_e k_B T_e$, *i.e.* electrons are isothermal, while the ion temperature can be neglected ($T_i \ll T_e$). The electric field driving the expansion can be obtained from the electron fluid momentum by neglecting the electron inertia:

$$E = -\frac{1}{n_e e}\frac{\partial p_e}{\partial x} \tag{1.72}$$

Using (1.72) and assuming charge neutrality $n_e \simeq Zn_i$ the equation of motion for the ions becomes

$$\left(\frac{\partial v_i}{\partial t} + v_i\frac{\partial v_i}{\partial x}\right) = \frac{ZeE}{m_i} = -c_s^2\frac{1}{n_i}\frac{\partial n_i}{\partial x} \tag{1.73}$$

where $c_s = (Zk_B T_e/m_i)^{1/2}$ is the ion sound velocity. The equation of continuity for the ions closes the system describing plasma expansion

$$\frac{\partial n_i}{\partial t} + \frac{\partial(n_i v_i)}{\partial x} = 0 \tag{1.74}$$

A self similar solution of this set of equations exists [41], such that

$$v_i = c_s + x_i/t \tag{1.75}$$

Using (1.75) into (1.73) and integrating from $x = 0$ to $x = c_s t$ we obtain the ion density

$$n_i = n_{i0}\exp(-1 - x/c_s t) \tag{1.76}$$

where n_{i0} is the unperturbed ion density. From 1.72 we find the accelerating field

$$E_{SS} = \frac{k_B T_e}{e c_s t} = \frac{k_B T_e}{e L_p} \tag{1.77}$$

where we defined the plasma scale length $L_p = c_s t$. Note that the self similar solution is valid if $L_p > \lambda_D$, that means it is not valid at the beginning of the expansion. We can consider that at very early times the solution is still given by (1.71). An estimate of the ion front position can be obtained by observing that at the ion front the validity of the self similar solution model breaks, as the local Debye length $\lambda_D = (T_e/4\pi n_e(x)e^2)^{1/2}$ becomes equal to the plasma scale length $c_s t$. Imposing $\lambda_D = c_s t$ we find the front position as a function of time $x = 2c_s t \ln(ec_s t/k_B T_e) - c_s t$; then substituting into (1.76), we have the velocity of the ions at the front

$$v_{i,front} = 2c_s \ln(ec_s t/k_B T_e) \tag{1.78}$$

Using (1.73) we find that the electric field at the front is twice the field we calculated in (1.77), *i.e.* $E_{front} = 2E_{SS}$. A precise expression for the field E_{front} was found by Mora [41], using a Lagrangian code solving equations (1.68-1.69) and (1.73-1.74):

$$E_{front} = \frac{2k_B T_e}{e(2e_N \lambda_D^2 + c_s^2 t^2)^{1/2}}. \tag{1.79}$$

This expression reduces to (1.71) for $t = 0$ and to (1.77) for later times, where $c_s t/\lambda_D >> 1$.

We observe that the electron temperature T_e and density of the electrons which are accelerated through the target is a crucial parameter for ion acceleration. Thus electron acceleration is directly related to ion acceleration and an enhancement of the production of hot electrons would result in a stronger driving field, which would accelerate ions to higher energies.

1.5.2 Shocks

A shock wave can be defined as a finite amplitude jump in the macroscopic parameters (density, temperature, etc.) of a medium. It has been identified as a possible acceleration mechanism by Silva [36] in 1D and 2D PIC simulations. According to this model ions are accelerated by a collisionless electrostatic shock, which is ponderomotively launched by the laser pulse at the front target surface and then propagates almost unperturbed through the target. The shock velocity, v_{shock}, can be estimated from the momentum conservation:

$$v_{shock} = \sqrt{\frac{(1 + \alpha_{ref})I}{m_i n_i c}} \tag{1.80}$$

where I is the intensity of the laser pulse and α_{ref} is the fraction of reflected light. In the simplest picture of the acceleration by a collisionless electrostatic shock, ions

are accelerated inside the target by 'collisions' with the potential barrier at the shock front, as from a moving wall. The maximum ion velocity, v_{imax}, is determined by the momentum conservation: $v_{imax} = 2v_{shock}$.

In order to give a picture of the formation of a shock and ion reflection, we will use a 1D fluid model, where electrons are assumed to be isothermal, in equilibrium at the temperature T_e, and the Sagdeev approach [9]. The Poisson equation, describing the perturbation in the direction of propagation of the shock is

$$\frac{\partial^2 \phi}{\partial x^2} = -4\pi e(n_i - n_e) = 4\pi e[n_o \exp(e\phi/k_B T_e) - n_i] \tag{1.81}$$

where we used the usual expression $n_e = n_0 \exp(e\phi/k_B T_e)$ for the electron density. Ions are assumed to be cold, therefore the equation of continuity for the ion fluids reads:

$$\frac{\partial n_i}{\partial t} + \frac{\partial n_i v_i}{\partial x} = 0. \tag{1.82}$$

and the equation for the ion fluid momentum is:

$$\frac{\partial v_i}{\partial t} + v_i \frac{\partial v_i}{\partial x} = -\frac{e}{m_i}\frac{\partial \phi}{\partial x}. \tag{1.83}$$

Then we use the Sagdeev approach, *i.e.* we look for a solution of the form $n_i(x-Vt)$, $v_i(x-Vt)$ and $\phi(x-Vt)$ which describes a disturbance of constant shape propagating with velocity V. In the reference frame of the disturbance, position and velocity become

$$x' = x - Vt \qquad v' = v_i - V \tag{1.84}$$

thus the space and time partial derivatives become

$$\frac{\partial}{\partial x} = \frac{\partial}{\partial x'} \qquad \frac{\partial}{\partial t} = -V\frac{\partial}{\partial x'} \tag{1.85}$$

Substituting (1.84) and (1.85) into the continuity and moment equations (1.82) and (1.83) we find the equations in the disturbance reference frame:

$$\frac{\partial n_i' v_i'}{\partial x'} = 0 \tag{1.86}$$

$$v_i' \frac{\partial v_i'}{\partial x'} = -\frac{e}{m_i}\frac{\partial \phi}{\partial x'}. \tag{1.87}$$

Integrating these equations we obtain

$$n_i v_i' = c_1 \tag{1.88}$$

$$m_i \frac{v_i'^2}{2} + e\phi = c_2. \tag{1.89}$$

where c_1 and c_2 are constant which will be chosen after the physical interpretation of the results. While in the laboratory frame the disturbance is traveling with velocity V and the plasma is at rest, in the frame of the disturbance the plasma is impinging with a velocity $-V$ on it. Then (1.88) represents the conservation of the flux of the impinging plasma which is outside the disturbance, thus $c_1 = -n_0 V$. Similarly equation (1.89) represents the conservation of the energy of the ions impinging on the disturbance, thus $c_2 = m_i V^2/2$. Using (1.88) and (1.89) with this choice of c_1 and c_2 we obtain the ion density n_i

$$n_i = n_0 \left(1 - \frac{2e\phi}{m_i V^2}\right)^{-1/2}. \tag{1.90}$$

Following [9], the Poisson equation can be seen as the analogue of the momentum equation of a particle moving under the action of a conservative force F by setting the correspondences $\phi \to r$, $x' \to t$ and

$$F/m = 4\pi e \left[n_o \exp(e\phi/k_B T_e) - \left(1 - \frac{2e\phi}{m_i V^2}\right)^{-1/2} \right] \tag{1.91}$$

Then, using the identity $\frac{\partial^2 \phi}{\partial x'^2} = \frac{\partial \phi}{\partial x'} \frac{\partial}{\partial \phi} \left(\frac{\partial \phi}{\partial x'}\right)$, we will integrate (1.81) to obtain the analogue of the energy conservation law:

$$\frac{1}{2}\left(\frac{\partial \phi}{\partial x'}\right)^2 + U(\phi) = \xi \tag{1.92}$$

where we have defined a pseudo-potential such that $F = -dU(\phi)/d\phi$ and ξ is the integration constant representing the pseudo-energy of the particle. $U(\phi)$ is obtained from the integration of F from a generic point ϕ to $\phi = 0$ (we look for a solution such that $\phi \to 0$ for $x' \to \infty$ which corresponds to the unperturbed region):

$$\begin{aligned} U(\phi) &= -4\pi n_0 \left[k_B T_e \exp(e\phi/k_B T_e) - m_i V^2 \left(1 - \frac{2e\phi}{m_i V^2}\right)^{1/2} \right] \\ &+ 4\pi n_0 \left[k_B T_e + m_i V^2 \right] \end{aligned} \tag{1.93}$$

The latter can be re-written as a function of the Mach number $M = V/c_s$

$$\frac{U(\phi)}{4\pi n_0 k_B T_e} = -\left[\exp(e\phi/k_B T_e) - M^2 \left(1 - \frac{2}{M^2}\frac{e\phi}{k_B T_e}\right)^{1/2} \right] + 1 + M^2 \tag{1.94}$$

where $c_s = (k_B T_e/m_i)^{1/2}$ is the ion sound speed. In order to obtain shock wave solutions the pseudo-potential $U(\phi)$ has to fulfill some conditions. If we impose that far from the

disturbance, where $\phi \to 0$, $\frac{\partial \phi}{\partial x'}|_{\phi=0} = 0$, we have $\xi = 0$ in (1.92). Thus $U(\phi)|_{\phi=0} = 0$ while for $\phi > 0$ it has to be negative in order to trap a particle as a potential well. This can be imposed expanding $U(\phi \approx 0)$ in a power series up to the second order:

$$\frac{U(\phi \approx 0)}{4\pi n_0 k_B T_e} \approx \frac{1}{2}\left(\frac{1}{M^2} - 1\right)\left(\frac{e\phi}{k_B T_e}\right)^2 < 0 \tag{1.95}$$

gives the lower limit for the shock propagation velocity: $M > 1$, *i.e.* the velocity of the shock has to be higher than the sound speed. A second condition is that there must be a reflection at some point ϕ_m, that means a point where $U(\phi_m) = 0$. The reflection has to occur in the interval $0 < \phi_m < \phi_{crit}$, where $\phi_{crit} = \frac{k_B T_e}{e}\frac{M^2}{2}$ is the value above which the argument of the square root in (1.94) becomes negative and $U(\phi)$ is not defined anymore. In other words $U(\phi_{crit}) \geq 0$ so that

$$\frac{U(\phi_{crit})}{4\pi n_0 k_B T_e} = -\exp(M^2/2) + 1 + M^2 \geq 0 \tag{1.96}$$

which gives the upper limit for the shock propagation velocity: $M \leq 1.6$. If no dissipation is included in the model, the pseudo particles will start from $\phi = 0$ (corresponding to $x' = \infty$), then they will be reflected at $\phi = \phi_m$ (corresponding to $x' = 0$, *i.e.* the shock front position), and move back to $\phi = 0$ (corresponding to $x' = -\infty$), performing a single oscillation (in space). In this case the shock consists of a localized perturbation, whose maximum amplitude is ϕ_m, which is known as an *ion-acoustic soliton* [38]. If on the contrary some dissipation is included, which would decrease the pseudo-energy $\frac{1}{2}\left(\frac{\partial \phi}{\partial x'}\right)^2$, the pseudo-particles will be trapped in the potential well which means that the electrostatic potential ϕ will oscillate in space about some positive value ϕ_0. This corresponds to the case of a *collisionless shock*. Actually dissipation is not needed for the pseudo particle to be trapped in the pseudo-potential well as we will explain in the following. In fact, if we assume that the ions have a small thermal spread in energy about $e\phi_m$ so that the electrostatic potential barrier $e\phi$ of the wave front is large enough to reflect some of the ions, while the rest goes over the shock wave (in the region $x' < 0$), the reflected ions cause an increase in the ion density in the upstream region, so that $\frac{1}{2}\left(\frac{\partial \phi}{\partial x'}\right)^2$ is reduced as

$$\frac{\partial \phi}{\partial x'} = \frac{1}{n_0}\int_0^{x'} (n_e - n_i)dx'. \tag{1.97}$$

Thus the virtual particle loses progressively its energy and falls inside the potential well performing a damped oscillation. The shock that is formed is characterized by different states of the plasma in the upstream and downstream region and by an *oscillatory front*.

1.6 Surface waves: analytical model

As discussed in section 1.4.4, the absorption mechanisms which take place in the case of the interaction of a laser pulse with a target having solid density and sharp

interface, causes only a limited absorption of the incident radiation. This point is crucial in order to have the generation of hot electrons which will eventually accelerate ions, as discussed in section 1.5.1. For this reason we are interested in exploring new laser-plasma coupling mechanisms, such as the excitation of a surface wave at the vacuum-plasma interface, which would be an intermediate step in the energy transfer from the pulse to the particles. In order to understand the potential advantages of such coupling, we will study in this section the basic characteristics of these waves.

In the following, the surface wave field is calculated by a simple non-relativistic hydrodynamic model. We assume that this model is valid in order to describe the surface wave that is excited at the beginning of the interaction of a laser pulse with a cold plasma, where kinetic effects are not important yet. Thus the cold plasma limit is considered initially (section 1.6.1), then, in section 1.6.4, the effects of electron temperature are taken into account.

1.6.1 First order fields

In this section we will study the propagation of a wave at the interface of two semi-infinite non magnetic media, having frequency dependent dielectric functions ϵ_1 and ϵ_2. The two media are separated by a planar interface at $x = 0$, such that the medium 1 fills the half-space $x < 0$ and the medium 2 fills the half-space at $x > 0$. In general, Maxwell equations for an EM wave obliquely incident on a plasma, have solutions that may be classified [12] into i) s-polarized modes, when the magnetic field $\mathbf{B}$ is in the plane defined by the wave vector and the normal to the interface and ii) p-polarized modes when the electric field $\mathbf{E}$ is in the plane defined by the wave vector and the normal to the interface (while $\mathbf{B}$ is perpendicular to that plane). In non-magnetic media surface waves can be considered to be p-polarized modes [72]. Thus, choosing the y axis as propagation direction for the wave, we seek the conditions under which a traveling wave with its magnetic field along z may propagate along the interface $x = 0$. Moreover, the fields have to decay away from the interface, in the $x > 0$ and $x < 0$ direction. The magnetic and electric fields in the two regions can be written as

$$\mathbf{B}_i = \hat{z} B_{iz} e^{-q_i|x|} e^{iky - i\omega t} \tag{1.98}$$

$$\mathbf{E}_i = \hat{x} E_{ix} e^{-q_i|x|} e^{iky - i\omega t} + \hat{y} E_{iy} e^{-q_i|x|} e^{iky - i\omega t} \tag{1.99}$$

where k is the wave vector parallel to the interface and q_i $(i = 1, 2)$ are the evanescence lengths in the two media. The evanescence lengths are obtained using (1.1) and (1.2) as follows:

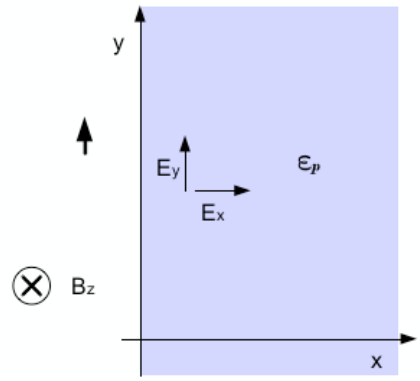

Figure 1.1: Vacuum-plasma interface: The half-space $x > 0$ is filled with a plasma of dielectric constant $\epsilon_p(\omega) = 1 - \omega_p^2/\omega^2$.

$$
\begin{aligned}
\nabla \times \nabla \times \mathbf{E_i} &= -\frac{1}{c}\frac{\partial}{\partial t}\left(\epsilon_i \frac{1}{c}\frac{\partial}{\partial t}\mathbf{E_i}\right) \\
-\nabla^2 E_i &= -\frac{\epsilon_i}{c^2}\frac{\partial^2 E_i}{\partial t^2} \\
k^2 - q_i^2 &= \epsilon_i \frac{\omega^2}{c^2} \\
q_i &= \sqrt{k^2 - \epsilon_i \frac{\omega^2}{c^2}} \qquad (1.100)
\end{aligned}
$$

1.6.2 Surface waves at the plasma-vacuum interface

Now we will analyze the case in which the medium 1 is the vacuum and the medium 2 is a plasma of dielectric function $\epsilon_p(\omega)$, given by equation (1.12). In the vacuum, where $\omega_p = 0$, the dielectric constant is $\epsilon_v = 1$.

The magnetic field $\mathbf{B}$ is in the $\mathbf{z}$ direction and is continuous at the interface $x = 0$:

$$
\begin{aligned}
\mathbf{B} &= \hat{z} B_z e^{-q_p x} e^{iky - i\omega t}\theta(x) \\
&\quad + \hat{z} B_z e^{q_v x} e^{iky - i\omega t}\theta(-x)
\end{aligned}
$$

where

$$
\begin{aligned}
q_v &= \sqrt{k^2 - \frac{\omega^2}{c^2}} \qquad (1.101) \\
q_p &= \sqrt{k^2 - \frac{\omega^2}{c^2}\epsilon_p} = \sqrt{k^2 - \frac{\omega^2}{c^2}(1 - \omega_p^2/\omega^2)} \qquad (1.102)
\end{aligned}
$$

are the inverse evanescence lengths in the vacuum and plasma regions respectively.

To obtain the components of the electric field we will use the equation

$$\nabla \times \mathbf{B} = \frac{4\pi}{c}\mathbf{J} + \frac{1}{c}\partial_t \mathbf{E} = \frac{-i\omega\epsilon\mathbf{E}}{c^2} \tag{1.103}$$

where $\epsilon = \epsilon_p$ inside the plasma region and $\epsilon = 1$ in the vacuum. From (1.103) we get

$$\begin{aligned} E_x &= E_{px}\hat{x}e^{-q_p x}e^{iky-i\omega t}\theta(x) \\ &\quad E_{vx}\hat{x}e^{q_v x}e^{iky-i\omega t}\theta(-x) \end{aligned} \tag{1.104}$$

where

$$E_{px} = -\frac{kc}{\omega\epsilon_p}B_z \tag{1.105}$$

$$E_{vx} = -\frac{kc}{\omega}B_z \tag{1.106}$$

and

$$\begin{aligned} E_y &= E_{py}\hat{y}e^{-q_p x}e^{iky-i\omega t}\theta(x) \\ &\quad E_{vy}\hat{y}e^{q_v x}e^{iky-i\omega t}\theta(-x) \end{aligned} \tag{1.107}$$

where

$$E_{py} = -\frac{cq_p}{i\omega\epsilon_p}B_z \tag{1.108}$$

$$E_{vy} = \frac{cq_v}{i\omega}B_z \tag{1.109}$$

Imposing the continuity at $x = 0$ of the electric field E_y (parallel to the interface), we have

$$E_{py} = E_{vy} = E_y \tag{1.110}$$

and we obtain the condition on the evanescence lengths

$$\frac{q_p}{q_v} = -\epsilon_p \tag{1.111}$$

Thus from equations 1.101 and 1.102 we may get the dispersion relation for the surface wave

$$\begin{aligned} \sqrt{k^2 - \frac{\omega^2}{c^2}\epsilon_p} &= -\epsilon_p\sqrt{k^2 - \frac{\omega^2}{c^2}} \\ \frac{k^2c^2}{\omega^2} &= \frac{\omega^2 - \omega_p^2}{2\omega^2 - \omega_p^2} \end{aligned} \tag{1.112}$$

We notice that these results are also valid for the case of a Drude metal having dielectric constant $\epsilon_p = 1 - \omega_p^2/\omega^2$.

1.6.3 Electrostatic and Electromagnetic limits

From the fields equations we notice that the surface waves have both transverse and longitudinal fields. We will investigate now the two limits: $\omega \simeq \omega_p/\sqrt{2}$ and $\omega << \omega_p$. We will see that they correspond to the limit in which only the electric field parallel to the propagation direction is important (electrostatic limit) and the limit in which only the transversal fields are dominant (EM limit).

In the limit in which $\omega << \omega_p$ the dispersion relation (1.112) may be expanded in terms of ω/ω_p :

$$\frac{k^2c^2}{\omega^2} = \left(\frac{1-\omega_p^2/\omega^2}{2-\omega_p^2/\omega^2}\right) \approx 1 + \frac{\omega^2}{\omega_p^2} + 2\frac{\omega^4}{\omega_p^4} + ... \tag{1.113}$$

$$\frac{kc}{\omega} \approx 1 + \frac{1}{2}\frac{\omega^2}{\omega_p^2} + \frac{7}{8}\frac{\omega^4}{\omega_p^4} + .. \tag{1.114}$$

We can use this relation to compare the magnitude of the fields near the surface, *i.e.* B_z, E_y, E_{vx} and E_{px}. Taking as reference value B_z and using equation (1.108) (equation (1.109) would be the same), where we approximate $k^2\omega^2/c^2$ by the expansion (1.113), up to the second order, we obtain

$$|E_y| = \sqrt{\frac{k^2c^2}{\omega^2} - 1}\; B_z \approx \omega/\omega_p B_z \tag{1.115}$$

that means $E_y << B_z$. Similarly, from equations (1.105) and (1.106) we obtain

$$|E_{vx}| \approx \left(1 + \frac{\omega^2}{\omega_p^2}\right) B_z \approx B_z \tag{1.116}$$

$$|E_{px}| \approx \frac{\left(1 + \frac{\omega^2}{\omega_p^2}\right)}{\left(1 - \frac{\omega_p^2}{\omega^2}\right)} B_z \approx \frac{\omega^2}{\omega_p^2} B_z \tag{1.117}$$

$$\tag{1.118}$$

Thus in the limit in which $\omega << \omega_p$, we have an electromagnetic wave whose electric field component that is parallel to the interface is negligible in the vacuum. The electric field perpendicular to the surface, which is discontinuous at $x = 0$, is comparable with the magnetic field outside the plasma while it is negligible inside the plasma.

In the limit in which $\omega \simeq \omega_p/\sqrt{2}$, we will express the frequency as $\omega = \omega_p/\sqrt{2} - \delta\omega$, where $\delta\omega/\omega_p << 1$. Therefore the dispersion relation (1.112) may be expanded in terms of $\delta\omega/\omega_p$:

$$\begin{aligned} \frac{k^2c^2}{\omega^2} &= \frac{\omega_p^2/2 - \sqrt{2}\omega_p\delta\omega - \omega_p^2}{2(\omega_p^2/2 - \sqrt{2}\omega_p\delta\omega) - \omega_p^2} \approx \frac{-\omega_p^2/2 - \sqrt{2}\omega_p\delta\omega}{-2\sqrt{2}\omega_p\delta\omega} \\ &= \frac{\omega_p}{4\sqrt{2}\delta\omega} >> 1 \end{aligned} \tag{1.119}$$

and the dielectric constant expansion is

$$\epsilon_p \approx \frac{1}{2} - \sqrt{2}\delta\omega \tag{1.120}$$

So, from (1.108), using (1.119) and (1.120) we get

$$|E_y| = \sqrt{\frac{k^2c^2}{\omega^2} - 1}B_z \approx \sqrt{\frac{\omega_p}{4\sqrt{2}\delta\omega} - 1}B_z \approx \frac{1}{2}\sqrt{\frac{\omega_p}{\sqrt{2}\delta\omega}}B_z \tag{1.121}$$

that means $E_y >> B_z$.
Then from (1.105) and (1.106) we obtain

$$|E_{vx}| \approx \frac{1}{2}\sqrt{\frac{\omega_p}{\sqrt{2}\delta\omega}}B_z \tag{1.122}$$

$$|E_{px}| \approx \frac{\frac{1}{2}\sqrt{\frac{\omega_p}{\sqrt{2}\delta\omega}}}{\frac{1}{2} - \sqrt{2}\delta\omega}B_z \approx \sqrt{\frac{\omega_p}{\sqrt{2}\delta\omega}}B_z \tag{1.123}$$

that means again $E_{ix} >> B_z$. *Thus, in the limit in which $\omega \simeq \omega_p/\sqrt{2}$, we have an electrostatic wave whose electric field components E_x and E_y have the same magnitude order while the magnetic field is negligible.*

1.6.4 Effects of electron temperature

When the effects of the electrons thermal speed are considered, the linearized momentum equation 1.6 is replaced by the new linearized momentum equation

$$\frac{\partial \mathbf{v_1}}{\partial t} = -\frac{e\mathbf{E}}{m_e} - \frac{1}{n_0 m_e}\nabla P_e \tag{1.124}$$

where P_e is the electron pressure. If we assume that time variations are so fast that no significant heat exchange can take place, then the process can be considered as adiabatic, so that the pressure-density relationships are

$$\begin{aligned} P_e &= Cn_e^\gamma \\ P_e &= n_e k_B T_e \end{aligned} \tag{1.125}$$

where T_e is the electron temperature while ions, being much heavier, are taken as 'frozen'. The electron density is $n_e = n_0 + n_1$, where n_1 is the perturbation and n_0 the equilibrium electron density. C is a constant while $\gamma = (f+2)/f$, where f denotes the number of degrees of freedom of the physical problem. Contrastingly, when temporal variations are so slow that the plasma has sufficient time to redistribute energy, we have the isothermal case, and the pressure-density relationships are

$$T_e = C \tag{1.126}$$
$$P_e = n_e k_B T_e$$

where C is a constant. Using both relations in 1.125 we see that

$$\nabla P_e = \gamma C n_e^{\gamma-1} \nabla n_e = \gamma k_B T_e \nabla n_e \tag{1.127}$$

If no assumption is made on the plasma evolution timescales, the index γ can be regarded as a *polytropic index*, describing not only the adiabatic case, but also the isobaric $\gamma = 0$, the isothermal $\gamma = 1$ and the isometric $\gamma = \infty$, cases. The electron temperature can be expanded as $T_e = T_0 + T_1$, thus the linearized (first order) moment equation 1.124 can be written as

$$\frac{\partial \mathbf{v_1}}{\partial t} = -\frac{e\mathbf{E}}{m_e} - \frac{\gamma k_B T_e}{n_0 m_e} \nabla n_1 = -\frac{e\mathbf{E}}{m_e} - \frac{\beta^2}{n_0} \nabla n_1 \tag{1.128}$$

where $\beta^2 = \frac{\gamma k_B T_0}{m_e}$ is a parameter proportional (the proportionality constant depends on the model used to describe the process) to the square of the thermal speed of the electrons. In the following we will use the linearized continuity equation (first order approximation)

$$\frac{\partial n_1}{\partial t} + n_0 \nabla \cdot \mathbf{v_1} = 0 \tag{1.129}$$

Combining the time derivative of (1.129) and the divergence of equation (1.128) we obtain a relation for the electron density

$$\frac{\partial^2 n_1}{\partial t^2} - \frac{e}{m} \nabla \cdot \mathbf{E} - \frac{\gamma k_B T_e}{m_e} \nabla^2 n_1 = 0 \tag{1.130}$$

which, using (1.3) becomes

$$\frac{\partial^2 n_1}{\partial t^2} + \omega_p^2 n_1 - \beta^2 \nabla^2 n_1 = 0 \tag{1.131}$$

Supposing that the density perturbation has the form $n_1 = g(x) e^{iky - i\omega t}$, we have

$$\frac{\partial^2 g(x)}{\partial x^2} = g(x) \left(k^2 + \frac{\omega_p^2 - \omega^2}{\beta^2} \right) \tag{1.132}$$

and choosing a vanishing solution, we obtain the electron density perturbation (for $x > 0$)

$$n_1 = A e^{-q_t x} e^{iky - i\omega t} \tag{1.133}$$

where A is a constant and $q_t = \left(k^2 + \frac{\omega_p^2 - \omega^2}{\beta^2}\right)^{1/2}$.
Substituting (1.128) in (1.10), and using (1.3) we obtain

$$\begin{aligned}\nabla(\nabla \cdot E) - \nabla^2 E = \quad & -\frac{1}{c^2}\left[-e4\pi n_0\left(-\frac{eE}{m_e} - \frac{\gamma k_B T_e}{n_0 m_e}\frac{\nabla(\nabla \cdot E)}{-e4\pi}\right)\right] \\ & -\frac{1}{c^2}\frac{\partial^2 E}{\partial t^2}\end{aligned} \tag{1.134}$$

From (1.133) we get

$$\nabla(\nabla \cdot E) = -e4\pi(-q_t\hat{x} + ik\hat{y})Ae^{-q_t x}e^{iky - i\omega t} \tag{1.135}$$

Substituting (1.135) into (1.134) we find

$$\nabla^2 E = \frac{\omega_p^2}{c^2}E - e4\pi(-q_t\hat{x} + ik\hat{y})Ae^{-q_t x}e^{iky - i\omega t}(1 - \beta^2/c^2) - \frac{\omega^2}{c^2}E$$

If we express the electric field as $E = h(x)e^{iky - i\omega t}$, then we obtain

$$\frac{\partial^2 h(x)}{\partial x^2} = h(x)\left(k^2 + \frac{\omega_p^2 - \omega^2}{c^2}\right) - e4\pi(-q_t\hat{x} + ik\hat{y})Ae^{-q_t x}(1 - \beta^2/c^2) \tag{1.136}$$

which gives the solution

$$h(x) = E_0 e^{-q_p x} - e4\pi\frac{1 - \beta^2/c^2}{q_t^2 - q_p^2}(-q_t\hat{x} + ik\hat{y})Ae^{-q_t x} \tag{1.137}$$

where $\mathbf{E_0} = E_{0x}\hat{x} + E_{0y}\hat{y}$ and $E_{0x,y}$ are constants. So finally the electric field inside the plasma is given by

$$E_{px} = \left[E_{0x}e^{-q_p x} + e4\pi\frac{1 - \beta^2/c^2}{q_t^2 - q_p^2}q_t Ae^{-q_t x}\right]e^{iky - i\omega t} \tag{1.138}$$

$$E_{py} = \left[E_{0y}e^{-q_p x} - e4\pi\frac{1 - \beta^2/c^2}{q_t^2 - q_p^2}ikAe^{-q_t x}\right]e^{iky - i\omega t}. \tag{1.139}$$

This is the same expression as that obtained in [73]. Using (1.2) we can calculate the expression of the magnetic field B_z inside the plasma

$$\begin{aligned}B_{pz} &= \frac{c}{i\omega}\left[\left(-q_p E_{0y} - ikE_{0x}\right)e^{-q_p x} - e4\pi\frac{1 - \beta^2/c^2}{q_t^2 - q_p^2}(-q_t ik + ikq_t)Ae^{-q_t x}\right]e^{iky - i\omega t} \\ &= \frac{c}{i\omega}\left(-q_p E_{0y} - ikE_{0x}\right)e^{-q_p x}e^{iky - i\omega t}\end{aligned} \tag{1.140}$$

The relation linking E_{0y} and E_{0x} can be found using (1.8):

$$\nabla \cdot (\mathbf{E}) = -e4\pi A e^{-q_t x} e^{iky-i\omega t} \tag{1.141}$$

$$\left[(-q_p E_{0x} + ikE_{0y})e^{-q_p x} + (k^2 - q_t^2)e4\pi \frac{1-\beta^2/c^2}{q_t^2 - q_p^2} A e^{-q_t x}\right] e^{iky-i\omega t} \tag{1.142}$$

so that applying again the definition of $q_p = \sqrt{k^2 + \frac{\omega_p^2 - \omega^2}{c^2}}$ and $q_t = \sqrt{k^2 + \frac{\omega_p^2 - \omega^2}{\beta^2}}$, we get

$$(-q_p E_{0x} + ikE_{0y})e^{-q_p x} - e4\pi A e^{-q_t x} = -e4\pi A e^{-q_t x} \tag{1.143}$$

and finally we have

$$E_{0x} = \frac{ik}{q_p} E_{0y} \tag{1.144}$$

Using this expression we can rewrite (1.140) as

$$\mathbf{B}_{pz} = \frac{c}{i\omega q_p}(k^2 - q_p^2)E_{0y}e^{-q_p x} + cc \tag{1.145}$$

$$= -\frac{c}{k\omega}(k^2 - q_p^2)E_{0x}e^{-q_p x} + cc \tag{1.146}$$

We can now apply the continuity relationships of the fields $\mathbf{B}_z$ and $\mathbf{E}_y$ inside and outside the plasma, where the fields outside the plasma have the same expression seen in the previous section which we rewrite here

$$\mathbf{B}_v = B_z \hat{z} e^{q_v x} e^{iky-i\omega t} \tag{1.147}$$

$$\mathbf{E}_v = E_{vx}\hat{x} e^{q_v x} e^{iky-i\omega t} + E_{vy}\hat{y} e^{q_v x} e^{iky-i\omega t} \tag{1.148}$$

The magnetic field B_z has to be continuous at $x = 0$, then using (1.109) and (1.146) we get

$$\begin{aligned} E_{vy}(x=0) &= \frac{cq_v}{i\omega} B_v(x=0) = \frac{cq_v}{i\omega} B_{pz} \\ &= -\frac{c^2}{\omega^2}\frac{q_v}{q_p}\frac{\omega^2 - \omega_p^2}{c^2} E_{0y} e^{iky-i\omega t} \\ &= -\frac{\omega^2 - \omega_p^2}{\omega^2}\frac{q_v}{q_p} E_{0y} e^{iky-i\omega t} \end{aligned} \tag{1.149}$$

Using the continuity of E_y at $x = 0$ and combining relations (1.139) and (1.149) we obtain

$$E_{py}(x=0) = \left[E_{0y} - e4\pi\frac{1-\beta^2/c^2}{q_t^2-q_p^2}ikA\right]e^{iky-i\omega t} = E_{vy}(x=0)$$

$$\frac{E_{0y}}{ik}\left(1+\frac{\omega^2-\omega_p^2}{\omega^2}\frac{q_v}{q_p}\right) = \frac{\beta^2}{\omega_p^2-\omega^2}e4\pi A \tag{1.150}$$

Thus from (1.150) , (1.144) it is possible to express the fields inside the plasma as

$$E_{py} = E_{0y}\left[e^{-q_p x} - \left(1+\epsilon_p\frac{q_v}{q_p}\right)e^{-q_t x}\right]e^{iky-i\omega t} + cc. \tag{1.151}$$

$$E_{px} = E_{0y}\left[\frac{ik}{q_p}e^{-q_p x} + \left(1+\epsilon_p\frac{q_v}{q_p}\right)\frac{q_t}{ik}e^{-q_t x}\right]e^{iky-i\omega t} + cc. \tag{1.152}$$

and outside the plasma as

$$E_{vy} = -E_{0y}\left(1-\frac{\omega_p^2}{\omega^2}\right)\frac{q_v}{q_p}e^{q_v x}e^{iky-i\omega t} = -E_{0y}\epsilon_p\frac{q_v}{q_p}e^{q_v x}e^{iky-i\omega t} + cc. \tag{1.153}$$

$$E_{vx} = -E_{0y}\frac{ik}{q_v}\left(1-\frac{\omega_p^2}{\omega^2}\right)\frac{q_v}{q_p}e^{q_v x}e^{iky-i\omega t} = E_{0y}\frac{ik\epsilon_p}{q_p}e^{q_v x}e^{iky-i\omega t} + cc. \tag{1.154}$$

where we applied relationships (1.109) and (1.106). We can now derive a dispersion relation by adding a boundary condition. *We suppose that the electrons are reflected at the plasma vacuum interface as is found when a charge separation field is generated (Debye sheath) by the hot electrons accelerated toward the vacuum.*

The components of the velocity v_1 are obtained from (1.128) and (1.133):

$$v_{1x} = \frac{eE_{px}}{i\omega m_e} - \frac{q_t\beta^2}{i\omega n_0}Ae^{-q_t x}e^{iky-i\omega t} + cc \tag{1.155}$$

$$v_{1y} = \frac{eE_{py}}{i\omega m_e} + \frac{k\beta^2}{\omega n_0}Ae^{-q_t x}e^{iky-i\omega t} + cc \tag{1.156}$$

and the linearized current will be $j = -en_0v_1$. From (1.155) and *using the condition* $v_1 = 0$ *at* $x = 0$, we have

$$0 = \frac{eE_{px}(x=0)}{i\omega m_e} - \frac{q_t\beta^2}{i\omega n_0}A \tag{1.157}$$

In order to perform substitutions in the latter equation we will use the relation

$$E_{0y}\left(1+\frac{\omega^2-\omega_p^2}{\omega^2}\frac{q_v}{q_p}\right)\frac{\omega_p^2-\omega^2}{e4\pi ik} = \beta^2 A \tag{1.158}$$

obtained by manipulating equations (1.150), and (1.161) for the expression of E_{px} at $x = 0$. Thus substituting into (1.157) we obtain

$$
\begin{aligned}
0 &= \frac{e}{m_e} E_{0y} \left[\frac{ik}{q_p} + \left(1 + \epsilon_p \frac{q_v}{q_p}\right) \frac{q_t}{ik} \right] - E_{0y} \left(1 + \epsilon_p \frac{q_v}{q_p}\right) \frac{\omega_p^2 - \omega^2}{e4\pi ik} \frac{q_t}{n_0} \\
0 &= -\frac{k^2}{q_p} + \left(1 + \epsilon_p \frac{q_v}{q_p}\right) q_t - \left(1 + \epsilon_p \frac{q_v}{q_p}\right) \frac{\omega_p^2 - \omega^2}{\omega_p^2} q_t \\
0 &= -\frac{k^2}{q_p} + \left(1 + \epsilon_p \frac{q_v}{q_p}\right) q_t (1 - \frac{\omega_p^2 - \omega^2}{\omega_p^2}) \\
0 &= -k^2 \omega_p^2 + (q_p + \epsilon_p q_v) q_t \omega^2 \\
k^2 \omega_p^2 &= q_t q_p \omega^2 + (\omega^2 - \omega_p^2) q_v q_t
\end{aligned} \tag{1.159}
$$

This is the same dispersion relation as obtained in ref.[73] for a surface wave, with the same boundary conditions described above.

Using (1.159) and (1.144) we can reformulate the electric field and the electron density as follows

$$
E_{py} = E_{0x} \left[\frac{q_p}{ik} e^{-q_p x} + \frac{\omega_p^2}{\omega^2} \frac{ik}{q_t} e^{-q_t x} \right] e^{iky - i\omega t} + cc \tag{1.160}
$$

$$
E_{px} = E_{0x} \left[e^{-q_p x} - \frac{\omega_p^2}{\omega^2} e^{-q_t x} \right] e^{iky - i\omega t} + cc \tag{1.161}
$$

$$
n_1 = E_{0x} \frac{\omega_p^2}{\omega^2} \frac{k^2 - q_t^2}{e4\pi q_t} e^{-q_t x} e^{iky - i\omega t} + cc \tag{1.162}
$$

and substituting these relations into (1.155) the electron velocities become

$$
\begin{aligned}
v_{1x} &= \frac{eE_{px}}{i\omega m_e} - \frac{\beta^2}{i\omega n_0} E_{0x} \frac{\omega_p^2}{\omega^2} \frac{k^2 - q_t^2}{e4\pi} e^{-q_t x} e^{iky - i\omega t} + cc \\
&= \frac{eE_{px}}{i\omega m_e} - \frac{e}{i\omega m_e} E_{0x} (1 - \frac{\omega_p^2}{\omega^2}) e^{-q_t x} e^{iky - i\omega t} \\
&= \frac{e}{i\omega m_e} E_{0x} \left[e^{-q_p x} - e^{-q_t x} \right] e^{iky - i\omega t} + cc
\end{aligned} \tag{1.163}
$$

$$
\begin{aligned}
v_{1y} &= \frac{eE_{py}}{i\omega m_e} + \frac{k\beta^2}{\omega n_0} E_{0x} \frac{\omega_p^2}{\omega^2} \frac{k^2 - q_t^2}{e4\pi q_t} e^{-q_t x} e^{iky - i\omega t} + cc \\
&= \frac{eE_{py}}{i\omega m_e} + \frac{e}{i\omega m_e} E_{0x} ik (1 - \frac{\omega_p^2}{\omega^2}) e^{-q_t x} e^{iky - i\omega t} \\
&= \frac{e}{\omega m_e} E_{0x} \left[-\frac{q_p}{k} e^{-q_p x} + \frac{k}{q_t} e^{-q_t x} \right] e^{iky - i\omega t}
\end{aligned} \tag{1.164}
$$

We can verify that in the limit of low electron temperature which corresponds to $\beta \ll c$, we have $q_t \to \infty$ and we find the same results as from the cold plasma model. We observe that the electron density in this limit becomes a δ_D-like function (where D stands for Dirac) which is related to the discontinuity in the electric field component E_x.

The wave vector of the surface wave k given by (1.159) as a function of the electron thermal velocity is plotted in fig.1.2.

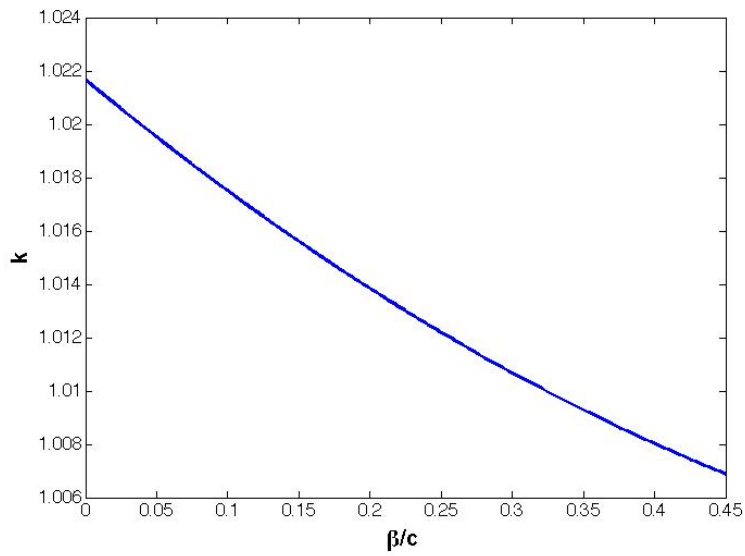

Figure 1.2: Plot of the wave vector of the surface wave as a function of the parameter $\beta = (k_B T_0/m_e)^{1/2}$ for $n_e = 25n_c$.

The wave vector decreases for increasing values of the electron thermal velocity, nevertheless we notice that the temperature causes little modification of the wave vector k in the range of non-relativistic thermal velocities, i.e. $\beta/c \ll 1$, which is also the limit of our model. Moreover, in the relativistic case other effects would come into play and eventually modify the dispersion relation: for example the dielectric constant ϵ_p of the plasma would be modified as discussed in section 1.2. However, if we consider the dispersion relation of equation (1.112) but using the relativistic dielectric factor from (1.30), then expanding k as done in (1.114) we find $\frac{kc}{\omega} \approx 1 + \gamma\frac{\omega^2}{\omega_p^2}$. Thus the relativistic correction would have the opposite effect with respect to the temperature correction, as k increases with the electron velocity, and the two effects may eventually balance.

Chapter 2

Resonant excitation of a Surface Plasma Wave (SPW)

Electron surface waves were first observed (Wood, 1902) experimentally as an anomaly in the diffraction of a continuous light source from a metal grating: in the diffracted spectrum dark lines corresponding to certain wavelengths appeared, which were later explained (Fano, 1941) in terms of the excitation of a surface wave sustained by the grating.

Similarly to the metal grating case, a surface plasma wave (SPW) can be resonantly excited by a laser pulse at the vacuum-plasma interface of an over-dense plasma, if the correct matching conditions are provided. In fact, in section 1.6.2, we have described analytically the properties of a surface wave propagating at the interface of an overdense ($\omega_p > \omega_{laser}$) plasma and observed that the same description can be applied to a Drude metal.

Considering the same geometry as used in sec.1.6.2, the phase matching conditions for a laser having frequency ω_0 and wave vector modulus k_0 are $\omega_0 = \omega$ and $k_0 \sin\theta = k$, where θ is the laser angle of incidence. The wave vector k and frequency ω of the SPW are related by the dispersion relation (1.159) which in the case of low electron temperature $v_{th}/c \ll 1$, as is our case at the beginning of the interaction, reduces to equation (1.112). As the phase velocity of the surface wave is lower than c, we have to consider a target having a periodic modulation at the surface such that $k = k_0(\sin\theta + n\lambda_0/a_m)$ in order to preserve momentum and obtain phase matching, where a_m is the periodicity of the modulation and n is an integer.

SPWs propagate along the plasma-vacuum interface and are characterized by a localized, high frequency, resonant electric field. The resonance condition can be obtained, in terms of plasma and laser parameters, combining the phase matching conditions with the surface wave dispersion. For the order $n = 1$ in the matching conditions, the resonance is given by the relation

$$\sin(\theta) + \lambda_0/a_m = \sqrt{(1 - n_e/n_c)/(2 - n_e/n_c)} \simeq 1 + \frac{1}{2}\frac{n_c}{n_e} \tag{2.1}$$

where $n_c = 1.1 \times 10^{21} cm^{-3} \lambda_0^{-2} \mu\mathrm{m}^2$. The last equality is valid for $n_e/n_c \gg 1$, which is the case for a highly overdense plasma, such as the plasma generated by a laser pulse

interacting with a solid target [43, 44]. The latter condition corresponds to the EM limit of the surface wave, in the analytical description of sec. 1.6.3.

In the following we present two-dimensional particle-in-cell (PIC) simulations where the plasma surface is initially pre-formed so that the SPW excitation conditions are fulfilled. *This work was performed using HPC resources from GENCI-CCRT (Grant 2011-t2012056851).* The PIC method is particularly suitable for the simulation of plasma dynamics when a kinetic description is necessary, as is the case for high intensity laser-plasma interaction. In this scheme the individual particles in a Lagrangian frame are tracked in continuous phase space, while moments of the distribution such as densities and currents are computed simultaneously on Eulerian (stationary) mesh points. The reduction to 2D permits correct description of the geometry of our specific case while limiting the computational cost. For a general description of PIC codes, see the appendix .1.

As seen in section 1.6, SPWs propagate along the plasma-vacuum interface and are characterized by a very localized electric field. In [77] it was found that the field of the surface wave is higher than the laser incident field and laser absorption increases dramatically (compared with a flat target) when a SPW is excited on a pre-structured plasma.

We wish here to investigate local field amplification and laser absorption via SPW excitation in the transition from the non-relativistic to the relativistic regime, observing the laser overdense plasma coupling via surface plasma waves over a wide range of pulse intensities (from $I\lambda_0^2 = 10^{15}$ to $I\lambda_0^2 = 10^{20}$W cm$^{-2}\mu m^2$). We will investigate the role of the electron density on the coupling efficiency by increasing the electron density from $25n_c$ to $100n_c$ and examine the effect of the modulation depth, by decreasing the amplitude (from the maximum to the minimum) of the surface modulation from $d = \lambda_0$ to $d = \lambda_0/5$. Finally we will study the effect of the target thickness, passing from a semi-infinite target to a laminar target.

The two-dimensional PIC simulations are performed by using the code EMI2D [88]. In figure 2.1 is shown a general scheme of our simulations.The incoming laser beam is p-polarized (the only possible polarization for surface plasma wave excitation [12, 72]) so that the laser electric field is in the (x, y) simulation plane. The latter is characterized by a temporal Gaussian shape of total length $400\omega_0^{-1}$ and full width at half maximum (FWHM) corresponding to $\simeq 56\,(\frac{\lambda_0}{\mu m})$ fs.

In the simulations the box size is $6\lambda_0$ along the y direction and $46\lambda_0/76\lambda_0$ along the x direction for the semi-infinite and laminar target respectively. The plasma is initially described by a Maxwellian distribution with electron temperature $T_e = 1$keV [1] (thermal velocity $v_{th} = 0.044c$) and ion temperature $T_i = T_e/10$ (here $m_i/m_e = 1836$, where m_i and m_e are the ion and electron mass). The charge of the ions was $Z = 1$. The laser enters the simulation box at the left side and there is a vacuum length of $38\lambda_0$ in front of the target which allows spatial expansion of particles, minimizing edge

[1] This value of the initial electron temperature is commonly used in PIC simulations [7, 79] of laser-plasma interaction for the range of laser intensities examined in this work. It can be considered as a good compromise between the temperature estimated experimentally (~ 0.5keV) [30] and the need to avoid very small values of λ_D in the code, which would entail heavier computational requirements (see also appendix .1).

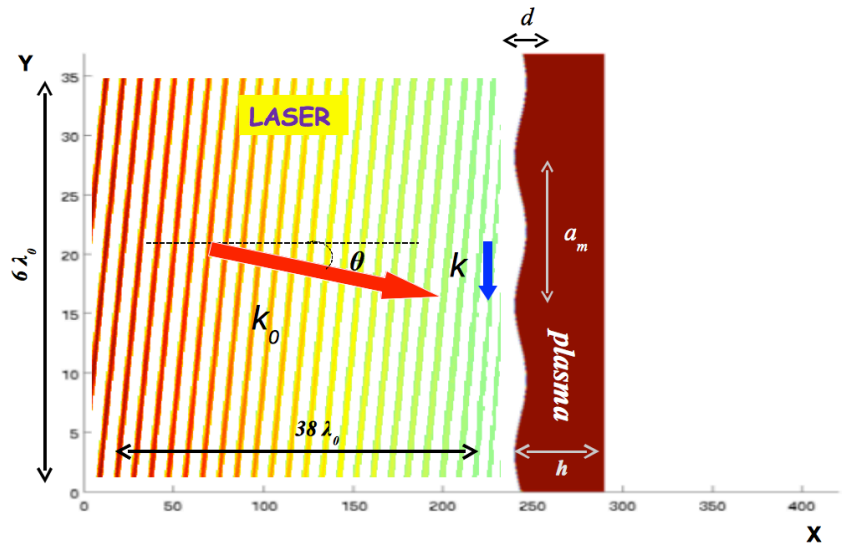

Figure 2.1: General scheme of the simulation set-up where θ is the laser angle of incidence, k indicates the SPW wave vector, k_0 is the laser wave vector, a_m is the grating periodicity and d is the grating depth. Lengths are expressed in units of k_0^{-1}.

effects. The particle boundary conditions are periodic in the y direction and the fast electrons reaching the right side of the box are cooled in a buffer or reflected for the semi-infinite and laminar targets respectively. The grid size[2] used was $\triangle x \approx 5\lambda_D$ and $\triangle y \approx 4\lambda_D$ (therefore it depends on the initial plasma density taken in the simulation), where $\lambda_D = v_{th}/\omega_p$ is the Debye length, in order to resolve correctly lengths below the plasma skin depth $\lambda_p = c/\omega_p$. The time interval used was $\triangle t \approx \triangle y/c$, and the number of particles[2] per cell was NP = 100.

In the simulations lengths and time are normalized respectively to the inverse of the laser wave vector k_0^{-1} and the inverse of the laser frequency ω_0^{-1}. The electric and magnetic fields are normalized to $E_0 = B_0 = m_e c\omega/e$. If $\lambda_0 = 1\mu m$, $E_0 = 3 \times 10^{10}$V cm^{-1} and $B_0 = 107$ MG.

In order to underline the computational requirements associated with these simulations, we have to consider that, for the typical size $6\lambda_0 \times 8\lambda_0$ of the plasma target which will be considered and the typical density $n_e = 25n_c$, we have a total of $\sim 10^6$ plasma points. This means that the total number of particles is $\sim 10^8$. The code was parallelized (see appendix .1) in order to treat such a large number of particles and grid points, and for most of the simulations 32 processors were used. The total CPU time necessary to complete a simulation, which has a typical duration of $1000\omega_0^{-1}$, is $\sim 600H$.

[2]The accuracy and stability of the code for this grid size and number of particles has been validated by test simulations as explained in appendix .2.

2.1 Laser-plasma coupling via SPW

In the present section we will consider the case of the *semi-infinite* target as the reference case for the SPW field and laser absorption. In the simulations electrons reaching the right end of the plasma are cooled and re-enter the plasma at thermal velocity (defined since the beginning of the simulation) as if there was an infinite plasma at thermodynamic equilibrium adjacent to the zone where hot electrons are generated and travel. This choice is motivated by the fact that, as we will see in section 4.3, in the laminar target we observe electron recirculation inside the target which has an important influence on absorption and field amplification and we want to separate this effect, which depends on target thickness, from the study of SPW excitation. The dependence of local field amplification and absorption on target thickness will be treated in section 2.5. We will initially take an angle of incidence of $\theta = 30^o$, a plasma density $n_e = 25n_c$ and a modulation periodicity $a_m = 2\lambda_0$ which fulfill the phase matching conditions for SPW excitation. We notice that we are considering a plasma which is strongly overdense but whose electron density is lower than the electron density obtained in the interaction of a laser pulse of intensity $I\lambda_0^2 > 10^{15}$W cm$^{-2}\mu m^2$ with solid targets. For example, in Al foils the maximum electron density can reach $600n_c$ when the target is fully ionised. Nevertheless, as we will show in section 2.2, the laser-plasma coupling shows a weak dependence on density for strongly overdense plasmas ($n_e \geq 25n_c$), thus we can extend our simulation results to the case of solid density targets and avoid high density simulations that would be computationally demanding. The plasma occupies the right half-space for an extension of about $8\lambda_0$ with the tips of the modulated surface located at $x = 240k_0^{-1}$ and the laser pulse peak impinges onto the modulated surface at $t_{peak} = 440\omega_0^{-1}$. The modulation depth (from the maximum to the minimum) was equal to λ_0. In order to compare the effects of the SPW excitation with a standard target most of the simulations were complemented with simulations having the same characteristics but a flat plasma-vacuum interface.

2.1.1 Local field amplification

For the physical parameters considered in the simulation, the surface wave excited via laser-grating coupling is such that the x-component of the electric field is larger, on the vacuum side, by roughly a factor of $(n_e/n_c)^{1/2}$ than the y-component, which corresponds to the analytical result found in section 1.6.3. Therefore we consider the x component of the electric field at the plasma surface as the reference field for the surface wave amplitude, and we will label it as E_{sw}.

In figure 2.2, E_{sw} is shown at $t_{Emax} = 460\omega_0^{-1}$, *i.e.* at the time when it reaches the maximum value in the PIC simulation having laser intensity $I\lambda_0^2 = 10^{16}$W cm$^{-2}\mu m^2$, and after half laser period. The SPW field structure is localized at the modulated surface and propagates along the $\hat{y}$ direction with the expected value for the k vector that is $k \simeq k_0 = 2k_0 \sin 30°$, as visible in the figure, and verified by considering the spatial Fourier transform of the field. The oscillation frequency is $\omega = \omega_0$, as we can observe comparing the two pictures which are taken with a time delay of half a laser period, in agreement with the resonant excitation conditions of the SPW. The same

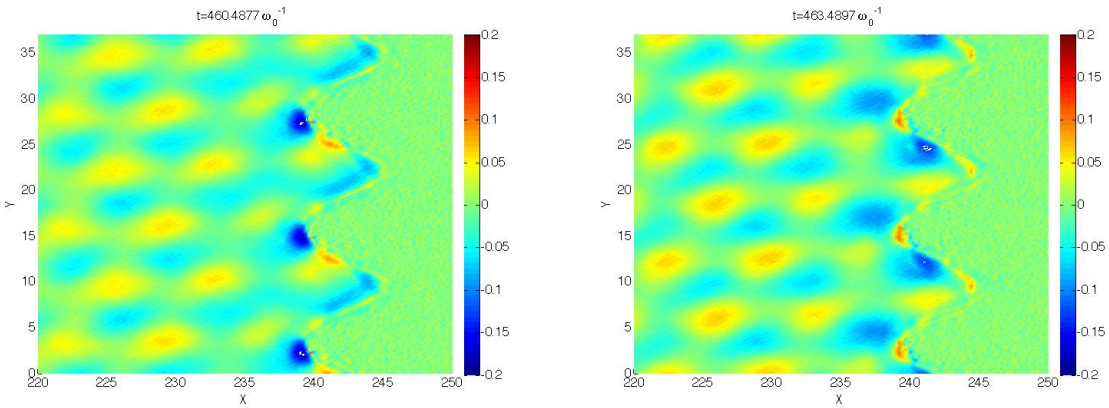

Figure 2.2: x component of the SPW field and the exciting laser field in the xy plane (in each figure, the vacuum is on the left and the plasma on the right, the modulated surface being at $x = 240k_0^{-1}$), at its maximum amplitude ($t_{Emax} = 460\omega_0^{-1}$) and after half period ($t = 463\omega_0^{-1}$). The SPW is excited at the plasma surface by a pulse of intensity $I\lambda_0^2 = 10^{16}$W cm$^{-2}\mu m^2$. The field is in units of E_0 and the lengths are in units of k_0^{-1}.

features of the field are observed on the plasma surface as we vary the laser intensity from $I\lambda_0^2 = 10^{15}$W cm$^{-2}\mu m^2$ to $I\lambda_0^2 = 10^{20}$W cm$^{-2}\mu m^2$; only the time for which a maximum of the field is observed, t_{Emax}, varies, ranging between $450 - 520\omega_0^{-1}$. The x component of the SPW field is found to be more intense than the corresponding component of the laser field $E_{Lx} = E_L \sin\theta$: we can express this field amplification defining an amplification factor $\eta = E_{sw}/E_{Lx}$. The value of the amplification factor depends on the laser pulse field, as shown in fig. 2.3, where η is plotted as a function of the laser parameter a_0. It ranges from a maximum value of 7.3 for $I\lambda_0^2 = 10^{15}$W cm$^{-2}\mu m^2$ to a minimum value of 3.2 for $I\lambda_0^2 = 10^{18}$W cm$^{-2}\mu m^2$. The parameter η then rises again for increasing intensity above the relativistic limit, reaching a saturation value of ~ 5 at $I\lambda_0^2 = 7 \times 10^{19}$W cm$^{-2}\mu m^2$.

In general the saturation value of η should depend on the rate at which the SPW transfers its energy to particles, via Landau damping or particle acceleration, or to fields, e.g. by re-emitting electromagnetic radiation. If the effective damping rate resulting from such processes is high enough, a steady state in which η remains constant is reached during the laser pulse. We can infer that at the transition from the non-relativistic to the relativistic limit ($a_0 \sim 1$ corresponding to $I\lambda_0^2 = 10^{18}$W cm$^{-2}\mu m^2$) the typical damping time becomes comparable to the SPW growth time as the surface wave shows a minimal amplification: the wave does not grow further as its energy is immediately transfered to particles or fields. This is consistent with the results for absorption presented in the following section (see fig.2.4), where laser absorption at the point $a_0 \sim 1$ increases significantly compared to the case at lower intensity. *In the lower intensity cases η is larger, presumably because the wave is damped more slowly by the electrons.* This hypothesis is confirmed by the fact that, in those simulations, the SPW and the related electron heating are observed to last much longer, after the laser is over, than for higher intensities, for which the SPW wave quickly vanishes after the laser pulse.

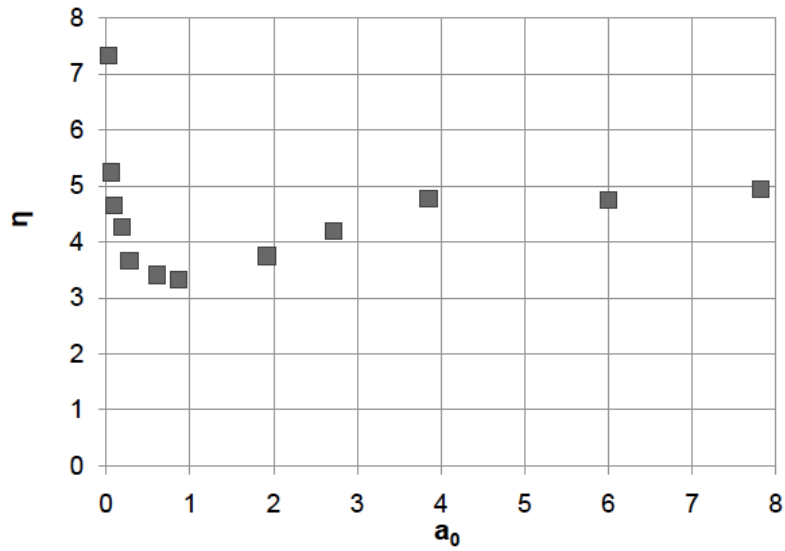

Figure 2.3: Plot of the amplification factor $\eta = E_{sw}/E_{Lx}$ as a function of the laser parameter a_0, where E_{sw} is the component of the SPW electric field along the x-direction and E_{Lx} is the laser one.

We have shown in this section that *SPWs can be excited in a large range of laser intensity ranging from* $I\lambda_0^2 = 10^{15}$ *to* $I\lambda_0^2 = 10^{20}\,W\ cm^{-2}\mu m^2$ *when the matching condition of the resonance excitation is fulfilled.* In the next section we will examine the laser absorption induced by the wave excitation for the same laser pulse intensity range.

2.1.2 Enhanced absorption via SPW

The laser absorption at the end of the simulation ($t_{end} = 1000\omega_0^{-1}$) is plotted in picture 2.4 as a function of the laser parameter $a_0 = E_L/E_0 = eE_L/m_e c\omega_0$. The latter is calculated considering the ratio between the reflected laser energy and the incoming one such that the absorption fraction is given by $1 - \frac{\mathcal{E}_{reflected}}{\mathcal{E}_{incident}}$. The case where the SPW is excited is in dark gray in contrast with the case where no SPW is present (case of a flat plasma surface) in light gray, for different laser intensities. In the simulations where the surface wave is present we observe an enhanced laser absorption, up to 77% for $I\lambda_0^2 > 10^{19}$W cm$^{-2}\mu m^2$ while it is only 40% for the case of a flat target. We observe that the absorption abruptly changes its slope at $I\lambda_0^2 > 10^{17}$W cm$^{-2}\mu m^2$, for both cases.

We first discuss briefly the results of the case of a flat surface. The drop of absorption with increasing the laser intensity from $a_0 \ll 1$ to $a_0 = 1$, observed in fig 2.4, can be associated with the fact that the ponderomotive pressure of the laser on the plasma locally steepens the electron density. The steepening may induce a decrease of the absorption related to mechanisms involving the presence of a density gradient, such as resonance absorption, discussed in section 1.4.1. This is also consistent with refs.[52, 54] where it was found that, for a given initial value of L_n/λ_0, where $L_n^{-1} = (1/n)dn/dx$

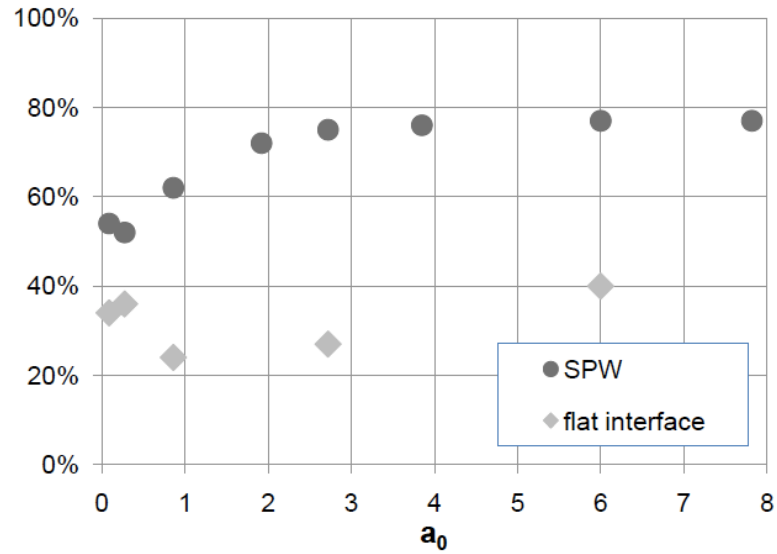

Figure 2.4: Plot of the laser absorption ratio as a function of the laser parameter $a_0 = eE_L/m_e c\omega = 0.86\sqrt{I\lambda_0^2/(10^{18}\text{W cm}^{-2}\mu m^2)}$: in dark gray filled circle the laser absorption ratio in the case where the surface plasma wave is excited, in light gray filled diamond the laser absorption ratio in the case of a flat interface.

is the typical scale of density variation, the absorption would increase with increasing laser intensity, and for a given intensity the absorption would decrease as L_n/λ_0 becomes smaller. At higher intensities, as a_0 increases from 1 to 6, the absorption increases and reaches 40%. This is not surprising since at high field intensity the dominant absorption mechanisms, vacuum heating and $\vec{J} \times \vec{B}$ heating, which do not require a large density gradient scale length (discussed in section 1.4.2 and 1.4.3), become more efficient.

Let us now look at the case where the SPW is excited. In this case an important parameter is the evanescence length of the SPW inside the plasma and at the vacuum side. The value of the evanescence length $L_{E,pl} = 1/q_p$ corresponding to the SPW field extension inside the plasma can be easily determined in the high density and low temperature limit in terms of basic parameters by using eq.(1.102). From the SPW dispersion relation up to the second order in ω_p/ω_0 in eq.(1.113), we obtain $L_{E,pl} \sim c/\sqrt{2}\omega_{pe}$. For the vacuum side we have $L_{E,v} = 1/q_v \sim \lambda_0$. Another important quantity is the excursion length of the electron in the field: we define here this excursion length as $\Lambda_{osc} \equiv v_{osc}/\omega_0$ where $v_{osc} = p_{osc}/m_e\gamma_{osc}$ is the electron oscillation velocity in the SPW field with $\gamma_{osc} = (1 + p_{osc}^2/m_e^2c^2)^{1/2}$ and the momentum is $p_{osc} = eE_{sw}/\omega_0$. $L_{E,pl}$ is the typical depth inside the plasma at which an electron can still feel the effect of the SPW field: if the electron excursion length perpendicular to the surface, Λ_{osc}, is larger, it does not feel the fields anymore and it is lost in the bulk, absorbing energy "non adiabatically" from the wave. In the opposite limit if $\Lambda_{osc} << L_{E,pl}$, the particle oscillates many times back and fort following the field oscillations before the average drift motion due to the ponderomotive force pushes the electrons inside the bulk. Since the surface wave is evanescent also at the vacuum side, the same reasoning can be

performed for the electrons accelerated by the localized surface wave field towards vacuum. However theese particles will feel the effect of the restoring force due to the charge imbalance generated by the ions that move on much longer time scales, so that eventually they will be pulled back into the plasma as well. *Thus SPW excitation can enhance laser absorption both by increasing the field intensity at the surface, which results in an higher Λ_{osc}, and providing localized fields which gives a ponderomotive contribution to electron acceleration.* The typical electric field envelope of the SPW, perpendicular to the surface, is schematically represented in fig.2.5 (red line) and it is compared with the case (blue line) where only the laser field is present (without SPW excitation).

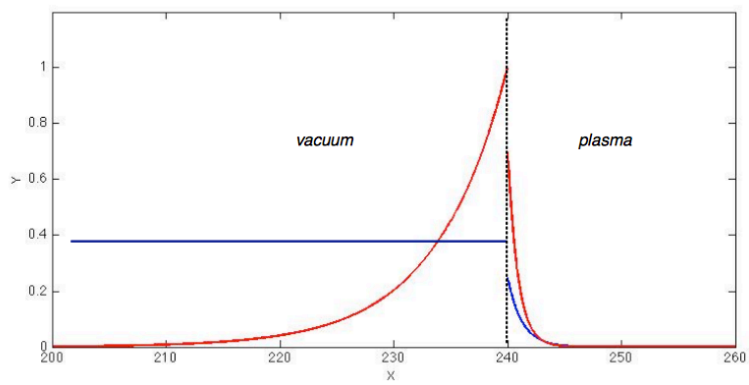

Figure 2.5: Plot of the SPW field envelope (red) and laser field when the SPW is not excited (blue). Note that for the laser field the evanescence length inside the plasma is c/ω_p.

.

For low laser intensity $I\lambda_0^2 \sim 10^{16}$W cm$^{-2}\mu m^2$ and $n_e/n_c = 25$ we have $\Lambda_{osc} =\lesssim L_{E,pl}$, thus fewer electrons will be adiabatically accelerated into the plasma by vacuum heating and/or the $J \times B$ mechanism but many electrons can still be accelerated outside and into the plasma via the ponderomotive force associated with the surface wave fields. However in this regime the radiation pressure is low and plasma expansion allows the creation of a density gradient at the target surface: in this case resonance absorption may become very important. Indeed we observe that the main absorption mechanism at the lowest intensities is resonant absorption even in the case of the modulated surface, where the surface wave is excited. As the intensity increases, this mechanism remains efficient until the ponderomotive pressure associated with the field at the surface steepens the density profile sufficiently.

To support our argument regarding the steepness of the density gradient for the two intensity regimes and its relation with the importance of resonant absorption at low laser intensities compared to the other mechanisms, we reproduce in figure 2.6 the density profile for two laser intensities, $I\lambda_0^2 = 10^{16}$W cm$^{-2}\mu m^2$ and $I\lambda_0^2 = 10^{19}$W cm$^{-2}\mu m^2$, representing the low intensity and relativistic regimes respectively. For the low intensity case the density gradient before reaching the critical density is about λ_0 and it is constant in time while for the high intensity one the gradient steepens during the

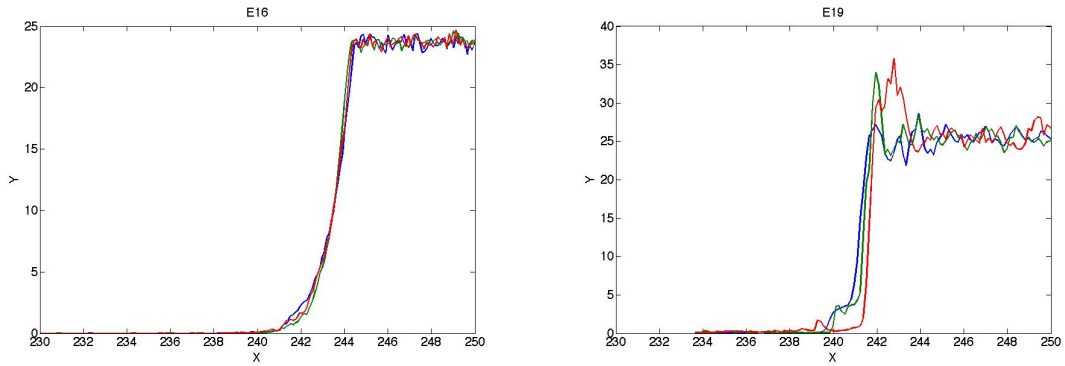

Figure 2.6: Plot of the density gradient in the direction of the surface normal at $y = 2\lambda_0$ for three different times $t = 400(blue), 460(green), 500(red)\omega_0^{-1}$, for $I\lambda_0^2 \sim 10^{16}$W cm$^{-2}\mu m^2$ (left) and $I\lambda_0^2 \sim 10^{19}$W cm$^{-2}\mu m^2$ (right).

laser-plasma interaction, and the scale length rapidly becomes lower than $0.2\lambda_0$. *This confirms what was said above, i.e. in the low intensity regimes electrons gain energy via resonance absorption in the density gradient while for relativistic pulse intensities the electron excursion length is such that resonance absorption in the gradient is not possible any more and electrons gain energy via vacuum or $J \times B$ heating.*

In fact, both in the flat surface case and in the case where we excite SPW, we observe in fig.2.4 that absorption initially decreases for increasing laser intensity, but then it starts growing at a given value of a_0 which corresponds to the point where vacuum heating becomes efficient replacing resonance absorption. Comparing the SPW and flat interface curve in fig.2.4 we observe however that the value of a_0 for which we have the transition between the two absorption mechanisms is not the same in the case of the flat surface ($a_0 = 0.86$) and in the case of modulated surface with SPW excitation ($a_0 = 0.272$): the value a_0 is smaller when the SPW is excited. This fact is consistent with the field amplification as the surface wave excited via laser-grating coupling has a perpendicular field component that can be quite larger than the corresponding component of the laser field, which gives an higher Λ_{osc}. However field amplification is not sufficient to explain the differences between the two curves since, for example, the flat surface case for $a_0 = 2.72$ has an absorption value which is much lower than the value at $a_0 = 0.86$ for the resonant case, where the amplification changes the effective field strength parameter into $a_0\prime = \eta 0.86 = 2.75$. In fact, the spatial form of the SPW field, which is very localized, also plays a role in the enhancement of absorption, providing a ponderomotive contribution to electron acceleration, as previously mentioned.

For relativistic values such that $I\lambda_0^2 \gtrsim 10^{18}$W cm$^{-2}\mu m^2$, Λ_{osc} increases up to its maximum value $\sim 0.16\lambda_0$ thus it becomes comparable to or larger than $L_{E,p}$ and a larger number of electrons are accelerated into the plasma. In this regime, vacuum heating enhanced by the presence of the field of the surface wave sets in, while resonance absorption in the density gradient is reduced.
We also observe (fig.2.4) that, increasing the laser intensity above $I\lambda_0^2 = 10^{19}$W cm$^{-2}\mu m^2$ ($a_0 = 2.72$) the absorption tends to saturate. This can be explained in terms of the gradient steepening which becomes pronounced for rising laser intensities, affecting

the absorption mechanisms. In fig.2.6 we observed a gradient scale-length lower than $\sim 0.2\lambda_0$ at $t = 500\omega_0^{-1}$ for $I\lambda_0^2 = 10^{19}$W cm$^{-2}\mu m^2$. In fact the vacuum heating has a dependence on the electron density gradient, as we discussed in section 1.4.2 (see also [19, 20]), because the latter determines the penetration of the laser field inside the plasma. Thus also the 'enhanced vacuum heating' via SPW could be affected by the profile steepening caused by laser pressure at the surface, as fewer and fewer electrons can be adiabatically accelerated into the plasma, so that the reduced scale-length of the density gradient and SPW field increase may balance and the absorption saturates. However other mechanisms that contribute to absorption are affected by the density value. Particularly, as described in section 1.4.3, at very high laser intensity there is a second order contribution to absorption due to $J \times B$ which may be non negligible. Also the absorption efficiency of $J \times B$ decreases for increasing electron density, which contributes to explain the saturation observed in fig.2.4 at high laser intensities.

Moreover we shall consider other effects which may be important at high laser intensities. One is the effect of the strong, quasi-static, magnetic field (along $-\hat{z}$) observed at the target surface, which will be examined in chapter 3: in fact the Larmor radius of the most energetic particles, calculated by the relativistic expression $R_L = \lambda_0\gamma/(B_z 2\pi)$ is of the same order as the scale length of the magnetic field, which would eventually confine particles at the surface. Another mechanism which may be considered for very large SPW amplitude, is wave breaking [78], which would add further electron heating in the direction of propagation of the SPW.

Finally the SPW excitation induces a large increase of the absorption. We can identify two regimes depending on the laser intensity: in the low intensity regime, resonant absorption take place while in the high intensity regime enhanced vacuum heating via SPW becomes dominant. In the next section we will investigate the dependence of SPW amplification and laser absorption on plasma density as it is a parameter which can give further indications about the dominant absorption mechanisms.

2.2 Effect of density variation

We will now investigate the effect of the density variation on SPW excitation and laser-plasma coupling. The target parameters considered will be the same as those used in section 2.1, particularly we recall that the target is *semi-infinite*. In the following the electron density is varied from 25 to $100n_c$ keeping the matching conditions for resonant excitation of the SPW. It should be noted that, as long as $n_e \gg n_c$, further increasing n_e does not change drastically the matching conditions which were defined in eq. (2.1). This is interesting from an experimental point of view as it is difficult to control the electron plasma density precisely in laser-solid interaction experiments.

In table 2.1 we report the laser absorption and η as functions of the laser intensity for two electron densities: 25 and $100n_c$. We also performed simulations for intermediate density values ($50n_c$ and $75n_c$) but we found that the density variation was not strong enough to cause significant modifications in the observed parameters, which are found to be weakly dependent on density in this range (strongly overdense plasmas).

We can note that increasing the electron density does not significantly change the

Table 2.1: Absorption and SPW field amplification factor, η, as a function of the laser intensity and the electron plasma density.

$I\lambda_0^2$ (W cm$^{-2}\mu m^2$)	n_e/n_c	η	Absorption
10^{16}	25	4.6	54%
10^{16}	100	4.9	44%
10^{18}	25	3.3	62%
10^{18}	100	3.5	59%
10^{19}	25	4.2	75%
10^{19}	100	4.8	64%

efficiency of the laser-SPW coupling and the value of η is slightly increased from $n_e = 25n_c$ to $n_e = 100n_c$. We observe that the increased field amplification corresponds to a reduced absorption, which confirms what was said in the previous section (2.1.2) about the damping of the SPW. However, it is important to underline that even if we have a decrease of the absorption at $100n_c$, the value is nevertheless higher than that obtained at lower density when no SPW is excited: *increasing the electron density only slightly affects the absorption enhancement.*

The decrease of the absorption is consistent with the dependence on electron density of the fraction of laser energy absorbed via vaccuum heating, mentionned in section 1.4.2. In fact, as discussed in reference [10], the efficiency of the vacuum heating mecanism is reduced when the plasma density is increased.

However especially at the highest intensities the laser absorption is still very large and this is consistent with the idea that, for $a_0 \gtrsim 1$, the effects of vacuum heating mechanism are enhanced by the SPW local field amplification, so that laser plasma coupling is dramatically improved compared to the case of a flat interface. Hence SPW excitation may sustain large values of absorption also in high density regimes where basic collisionless mechanisms become less efficient.

2.3 Incidence angles out of resonance

In order to separate the role of the target shape from the effective contribution due to the resonant excitation of a SPW, laser interaction with gratings out of resonance may be studied. This can be done either by varying the grating periodicity, keeping the laser incidence constant, or by varying the laser incidence keeping the grating periodicity constant. We have preferred this last choice as it is the one commonly encountered in experiments [35]. In this section we will examine the case of two different laser angle

of incidences: 20° and 10°. For these two values[3], keeping the same surface target as the one used previously to match the 30° incident pulse (grating periodicity $a_m = 2\lambda_0$ and modulation depth $d = \lambda_0$) the phase matching condition for SPW excitation is not fulfilled. We will again consider a *semi-infinite* target with electron density $n_e = 25n_c$.

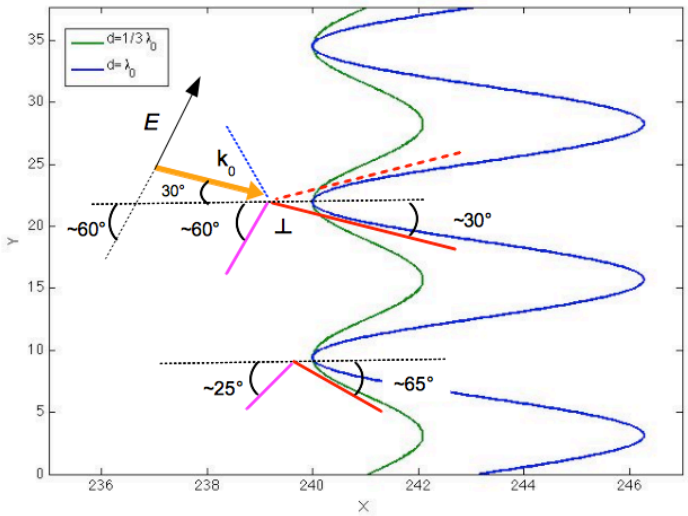

Figure 2.7: Scheme of the angular directions of the laser pulse vector k_0 (orange) and tangents to the modulation surface (red) for two modulation depth values, $d = \lambda_0$ (blue line) and $d = \lambda_0$ (green line) when the periodicity is $a_m = 2\lambda_0$. The purple lines are perpendicular to the red ones. Solid red/purple lines are associated with the lower part of the tip while dotted lines correspond to the upper part.

Let us first analyze the results obtained for $I\lambda_0^2 = 10^{16}$W cm$^{-2}\mu m^2$. We found an absorption of 60% and 68% for the case of 20° and 10° incidence respectively which is higher than the resonant case (54% at 30° incidence). Thus the absorption is increased when the pulse angle of incidenceis decreased, approaching the normal incidence, even if *the surface wave is not excited.* Fourier transforms of the field in the (x,y) space confirm, for both 10° and 20°, the absence of surface wave excitation.
This apparently contradictory result is related to the presence of resonant absorption in the density gradient. At this low intensity the laser pressure is weak, allowing some plasma expansion so that the excursion length Λ_{osc} is much smaller than the gradient scale length ($\Lambda_{osc} \approx 0.03\lambda_0$ for $I\lambda_0^2 = 10^{16}$W cm$^{-2}\mu m^2$ as discussed in section 2.1.2) and the gradient density length is about λ_0. As seen in section 1.4.1 the absorption in this case is proportional to $\sin^2\theta$ for a density gradient $\lesssim \lambda_0$, where θ is the laser angle of incidencefor a plane target. *In presence of a modulation, we have to consider the angle between the wave vector and the surface normal, which changes along the*

[3]In this study angles larger then 30° are not reported because in this case, owing to the modulation depth considered, the upper part of the modulation partially shades the lower one from the laser pulse and the coupling is not the same on the two sides of each modulation tips. This can be seen on fig.2.7 where the laser wave vector and the tangent to the modulation curve are shown with the respective angular values.

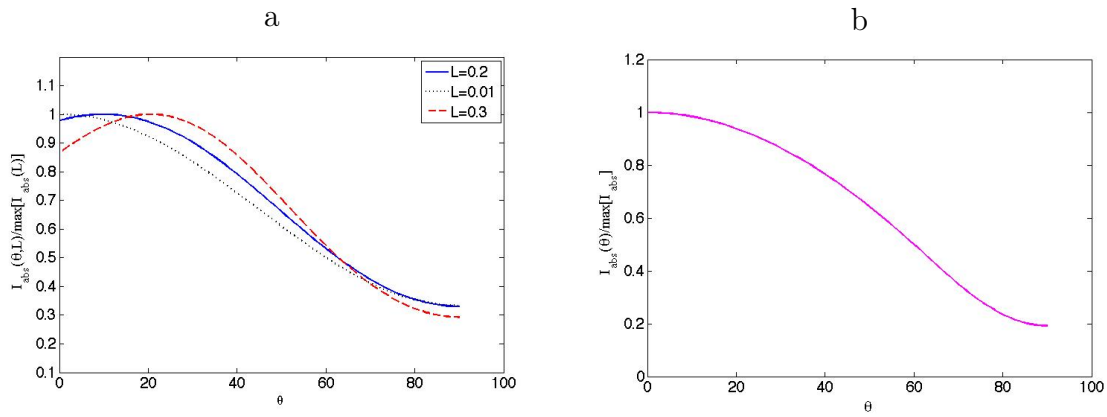

Figure 2.8: (a) Plot of the resonant absorption as a function of the laser angle of incidencefor different values of the gradient scale-length $L = 0.01, 0.2, 0.3$. We assumed the values $\pi c/\nu = 1$ in equation (1.58). b) Plot of the absorption due to vacuum heating as a function of the angle of incidence θ, from equation (1.62). In both cases we used $\theta' = \theta_T + \theta$ where $\theta_T = \pm 60°$ in the equations, summing the result for the positive and negative value of θ_T. Each curve is normalized to its maximum.

modulation. If we approximate the modulation as a saw having a slope corresponding to the curve tangent, as shown in figure 2.7 (red line), the angle to consider for the resonance absorption, that we will label θ', will be $\theta' = \theta_T + \theta$, where θ_T is the angle formed by the saw surface normal (purple line) with $\hat{x}$ and θ is the angle of incidence(the angle formed by the wave vector and $\hat{x}$). In our case (modulation depth $d = \lambda_0$ and periodicity $a_m = 2\lambda_0$) we have two values $\theta_T = \pm 60°$, the positive values corresponding to the upper sides of saw (dotted blue line), the negative ones to the lower sides (solid purple line). Thus the absorption of the periodic grating can be approximated (see eq.1.58), as proportional to the geometric factor $G_r \approx \sin^2(\theta + 60°) + \sin^2(\theta - 60°)$, which decreases from 1.5 to 1.25 for θ increasing from normal incidence to 30° .

In figure 2.8a a plot of laser energy absorption is shown, for resonant absorption mechanism, which is obtained as a function of the laser angle of incidence, using equation (1.58) for $\theta = \theta'$. We considered three values of the gradient scale length $L/\lambda_0 = 0.3$, 0.2 and 0.01. We observe that the plot confirms an increase of the absorption for laser angle of incidences decreasing from 30° to 10° for intermediate values of the gradient scale length.

A similar argument can be applied also to vacuum heating. In fact as seen in section 1.4.2 the absorption depends on $\sin^3\theta$ and, as discussed above, θ is the angle of incidencefor a plane target while we are observing a modulated surface, thus θ' has to replace θ in equation (1.62). Observing the absorption in the case of the vacuum heating mechanism in figure 2.8b, we find that the latter always increases for decreasing angle of incidence(for the present target shape). Thus, with these arguments we have a roughly qualitative agreement of the observed data with theory, keeping in mind that the models considered here for the description of the absorption mechanisms are very simplified.

At higher laser intensity, where the resonant absorption is lower, the main absorption

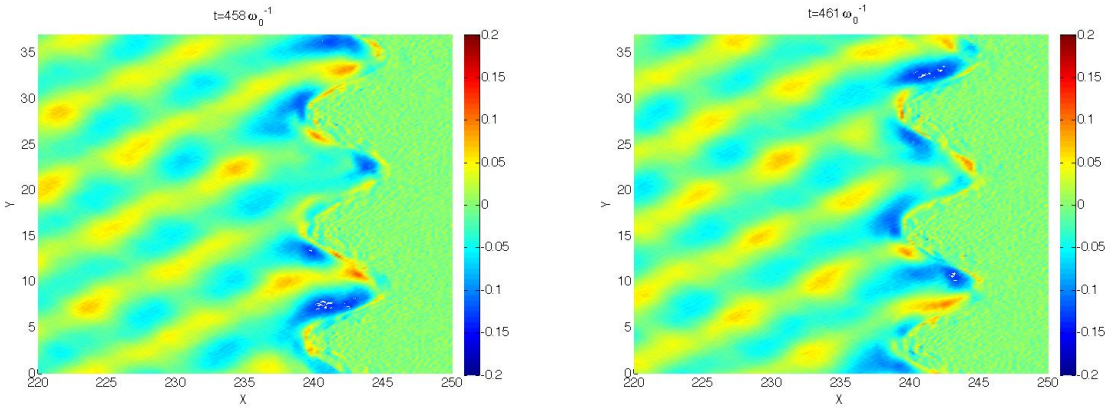

Figure 2.9: x component of the electric field in the xy plane for the non-resonant angle of incidence $\theta = 10°$ (in each figure, the vacuum is on the left and the plasma on the right, the modulated surface being at $x = 240k_0^{-1}$), at $t = 458\omega_0^{-1}$ and after half period ($t = 461\omega_0^{-1}$). The SPW is excited at the plasma surface by a pulse of intensity $I\lambda_0^2 = 10^{16}$W cm$^{-2}\mu m^2$. The field is in units of E_0 and the lengths are in units of k_0^{-1}.

mechanisms are $J \times B$ and vacuum heating. For $I\lambda_0^2 = 10^{19}$W cm$^{-2}\mu m^2$, we found an absorption of 75% for the resonant incidence ($\theta = 30°$) while it is 60% and 72% for the non-resonant incidence cases $\theta = 20°$ and $\theta = 10°$ respectively. We notice that, in this case the absorption initially decreases when the laser incidence moves from resonance condition to $\theta = 20°$. However for $\theta = 10°$ absorption rise again and attains a value which is close to the one observed at the resonance. This means that for angles approaching normal incidence the 'regular' vacuum heating, thanks to a very favourable geometry factor, may reach the same level of absorption as the 'enhanced' vacuum heating resulting from SPW field amplification.

This section raises the question of the interest of SPW excitation versus pure geometric effects as is observed that the grating alone may increase the absorption even if SPW is not excited. However as it will be shown also in section 4.2.1, even in the cases where laser absorption is quite similar (as for $I\lambda_0^2 = 10^{19}$W cm$^{-2}\mu m^2$), the electronic emission are very different when the SPW is excited from that observed for the non-resonant incidence. This is due to the form of the local field at the plasma-vacuum interface. In fact, as seen if one compares fig.2.2 with fig.2.9 , when the SPW is not excited the electric field is not spatially periodic along y any more and this causes a drastic change in the induced electron current.

There is another parameter that has to be taken into account when considering geometric effects: the depth of the modulation. This will be the subject of the next section.

2.4 Effects of the modulation depth

The effects of the grating depth have been extensively studied in metal targets [12], where this parameter is found to determine the laser absorption at resonance. Even

if though experimental results have been reproduced numerically, using the Rayleigh method and the extinction theorem (see [13] and references therein), a consistent physical interpretation is missing. *However in the cases mentioned above, the laser intensity is such that the target is not ionized and transformed into a plasma: the process of laser absorption and surface wave excitation is not affected by factors such as the density gradient or plasma expansion and the role of the modulation depth may be different.*

Grating depth variation effects on electric field amplification and laser absorption will be here analyzed for $I\lambda_0^2 = 10^{16}$W cm$^{-2}\mu m^2$ and $I\lambda_0^2 = 10^{19}$W cm$^{-2}\mu m^2$ representing respectively the low and high laser intensity regimes. As in the previous sections, the target has a periodicity $a_m = 2\lambda_0$, is *semi-infinite* and has an electron density $n_e = 25n_c$.

We chose to explore the range of the sub-lambda modulation depths in order to avoid the previously mentioned shadowing problems, which, given the periodicity of the target and the incident angle, would occur for depths $d > \lambda_0$ (from the maximum to the minimum) for the angle of incidence $\theta = 30°$.

It is to be noticed here that reducing the modulation depth also modifies the angle θ_T formed by the surface normal with $\hat{x}$ (the surface is approximated by a 'saw', as in the previous section), which will approach 0° (see fig.2.7). Thus θ', which is the angle to consider for resonance absorption and vacuum heating, will approach θ, *i.e.* the laser angle of incidence, and the effects of the geometry of the target will be substantially reduced. As a consequence the absorption due to the favourable geometry of the target should be less important and the SPW effects will be more evident even though this would result in a decrease of the total absorption.

We will initially consider the dependence of the resonant laser-grating coupling, corresponding to $\theta = 30°$, on the modulation depth and then compare with the non-resonant angle of incidence $\theta = 10°$, for which we have observed the larger absorption in section 2.3.

As shown in section 2.2, when the modulation depth is reduced from λ_0 to $\lambda_0/3$ and $\lambda_0/5$, keeping the laser angle of incidenceat 30°, we observe a decrease of the absorption in our PIC simulations, both in the low and high intensity regimes. As a consequence of the different absorption, the surface wave may undergo a different damping as discussed in section 2.3. For this reason we will examine in detail also the amplification factor η associated with each value of the modulation depth (in tab.2.3) that we have considered and compare with the absorption values.

In the *low intensity regime* we find that absorption goes from 54% to 36% when the modulation depth is reduced from $d = \lambda_0$ to $d = \lambda_0/3$ while the amplification factor slightly decreases, going from $\eta = 4.6$ to $\eta = 4.1$. Reducing further the modulation to $\lambda_0/5$ we obtain an absorption of 34% for $I\lambda_0^2 = 10^{16}$W cm$^{-2}\mu m^2$, the latter being the same value as the flat interface value for that laser intensity, and an amplification $\eta = 4$. Thus we notice that the amplification factor is reduced for decreasing d in this regime while in general we observe an increase of η for decreasing absorption as a consequence of SPW damping. This result is in accordance with the analysis done in section 2.1.2, according to which the resonant absorption is important in this regime: in fact this mechanism is not directly responsible of the SPW damping and the absorption is not related to the amplification factor. *We may also remark that the density gradient scale*

Table 2.2: Absorption as a function of the laser intensity and the depth of the modulation for $n_e = 25n_c$ and $\theta = 30°$.

d	$I\lambda_0^2 = 10^{16}$W cm$^{-2}\mu m^2$	$I\lambda_0^2 = 10^{19}$W cm$^{-2}\mu m^2$
λ_0	54%	75%
$\lambda_0/3$	36%	51%
$\lambda_0/5$	34%	35%
0	34%	27%

Table 2.3: Amplification η as a function of the laser intensity and the depth of the modulation for $n_e = 25n_c$ and $\theta = 30°$. (Notice that, $\eta = 2$ because of the superposition of the incident and reflected fields, for the flat target).

d	$\eta(I\lambda_0^2 = 10^{16}$W cm$^{-2}\mu m^2)$	$\eta(I\lambda_0^2 = 10^{19}$W cm$^{-2}\mu m^2)$
λ_0	4.6	4.2
$\lambda_0/3$	4.1	4.4
$\lambda_0/5$	4	4.6
0	2	2

length for the intensity $I\lambda_0^2 = 10^{16}\,W\ cm^{-2}\mu m^2$ is of the order of $\sim \lambda_0$ as shown in fig.2.6a, that is larger than the two values $d = \lambda_0/3$ and $d = \lambda_0/5$ considered here. Eventually this may affect the laser-grating coupling or decrease the relative importance of the wave compared to gradient-related absorption mechanisms.

Also in the *high intensity regime* ($I\lambda_0^2 = 10^{19}$W cm$^{-2}\mu m^2$) the absorption decreases for increasing d, and goes from 75% to 51% when the modulation depth is reduced from λ_0 to $\lambda_0/3$ while the amplification factor is slightly increased, from $\eta = 4.2$ to $\eta = 4.4$. For $d = \lambda_0/5$ the absorption is only 35%, but it remains larger than the flat surface value, 27%, and the amplification factor grows to $\eta = 4.6$. The results for the high intensity regime appear consistent with what was said in section 2.3 as the decrease of the absorption, associated with the enhanced vacuum heating, corresponds to an increase of the wave amplitude, *i.e.* of the factor η. Vacuum heating, which represents the main damping mechanism, is more important in this regime as electrons may have an excursion length large enough to escape the wave. We notice that in

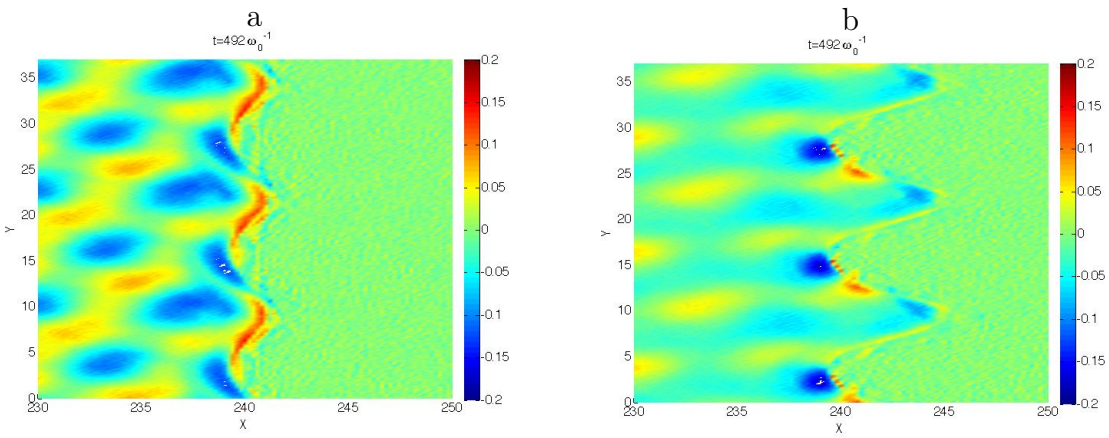

Figure 2.10: Electric field E_x for the semi-infinite target, at $t = 492\omega_0^{-1}$,$I\lambda_0^2 = 10^{16}$W cm$^{-2}\mu m^2$ ($a_0 = 0.086$), (a) for the modulation depth $d = \lambda_0/3$ and (b) for the modulation depth $d = \lambda_0$, $n_e = 25n_c$, when SPW is excited.

this case the scale length of the gradient at the surface is smaller than the modulation depths considered even if close to the smaller value, $\lambda_0/5$. *Thus for reduced modulation depth the laser-grating coupling is such that the SPW effects are dominant over the other mechanisms.*

We shall now examine the SPW field for two different modulation depths $d = \lambda_0/3$ and $d = \lambda_0$ in order to study qualitatively how its distribution is modified when we change the modulation depth.

Fig.2.10 contrasts the E_x field for $d = \lambda_0/3$ and $d = \lambda_0$ at $I\lambda_0^2 = 10^{16}$W cm$^{-2}\mu m^2$. We see the that the electric field distribution changes in the two cases: the field at the surface, which is evanescent towards the vacuum, appears more symmetric on the two sides of each tip when $d = \lambda_0/3$ while for $d = \lambda_0$ it is localized on the lower part of each tip. It is to be noticed that the time corresponding to the maximum amplification is different in the two modulation depths as it is reached at $t = 461\omega_0^{-1}$ when $d = \lambda_0$ and $t = 435\omega_0^{-1}$ when $d = \lambda_0/3$.

Fig.2.11 contrast the E_x field for $d = 1/3\lambda_0$ and $d = \lambda_0$ at $I\lambda_0^2 = 10^{19}$W cm$^{-2}\mu m^2$. In this case we observe that the electric field near the surface is concentrated inside the modulation dips for $d = \lambda_0$, while for the target having $d = \lambda_0/3$ the field is localized outside the dips, around $x = 238k_0^{-1}$. It is to be noticed that even for $I\lambda_0^2 = 10^{19}$W cm$^{-2}\mu m^2$ the time corresponding to the maximum amplification is different for the two modulation depths, occurring at $t = 486\omega_0^{-1}$ when $d = \lambda_0$ and $t = 457\omega_0^{-1}$ when $d = \lambda_0/3$. This means that in both cases the SPW reaches its maximum amplitude earlier when the modulation depth is reduced.

Finally we may compare the absorption obtained for the resonant case $\theta = 30°$ with $d = \lambda_0/3$, with those for the non-resonant case having the same target parameters but $\theta = 10°$. The aim is to confirm the fact that the high values of absorption found for non-resonant incidence when $d = \lambda_0$ are simply a consequence of the favourable target geometry and SPW effects are dominant when geometry effects are reduced. Particularly the effects of SPW should be more evident in the high intensity range, where

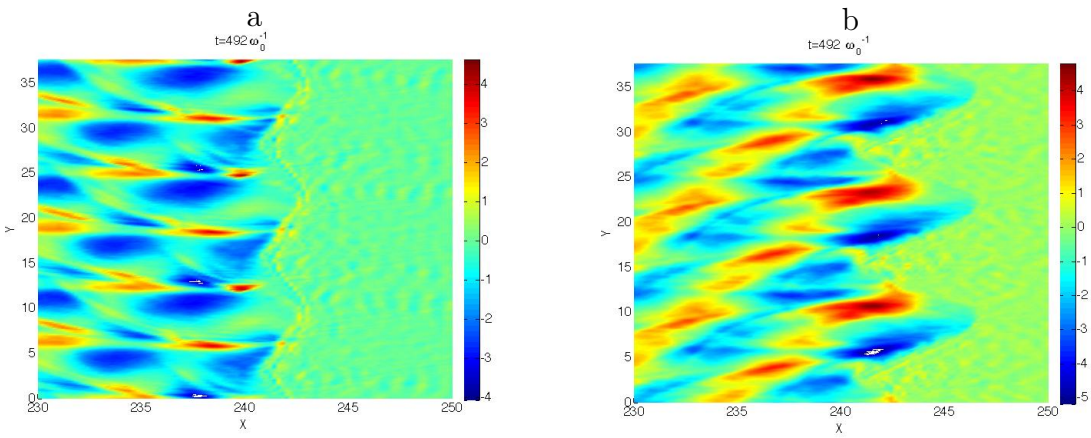

Figure 2.11: Electric field E_x for the semi-infinite target, at $t = 492\omega_0^{-1}$,$I\lambda_0^2 = 10^{19}$W cm$^{-2}\mu m^2$ ($a_0 = 2.72$), (a) for the modulation depth $d = \lambda_0/3$ and (b) for the modulation depth $d = \lambda_0$, $n_e = 25n_c$, when SPW is excited.

the vacuum heating mechanism is dominant. For low laser intensity the absorption at the non-resonant angle of incidence $\theta = 10°$ is 34% at $I\lambda_0^2 = 10^{16}$W cm$^{-2}\mu m^2$, that is the same value of absorption as found for the flat surface, at that laser intensity. However this value is only slightly lower than the resonant value 36%. At $I\lambda_0^2 = 10^{19}$W cm$^{-2}\mu m^2$ instead we found that the absorption at the non-resonant angle of incidence $\theta = 10°$ is 35%, which is much lower than the resonant value 51%. *Thus in this case ($d = lambda_0/3$) we observe that the absorption is lower for angle of incidences which do not match the resonance and the effects of the SPW excitation are clearer than the case with $d = \lambda_0$, where geometry effects and SPW excitation were mixed.*

We may conclude that by decreasing the modulation depth we reduce the importance of the target geometry and increase the importance of the resonant coupling. Decreasing the modulation depth, we will have a general decrease in the absorption but at the same time we will increase the difference between the case where SPW is excited and non-resonant incidence. However, the modulation depth cannot be excessively reduced, as we observe that for $d = \lambda_0/5$ the coupling is lost at low laser intensities or much reduced for higher intensities. In fact we have to consider also the plasma expansion, which produces a density gradient in front of the target of the order of λ_0 (see section 2.1.2) which can interfere with laser absorption via SPW excitation. This may be confirmed by three facts: i) the coupling is lost first for lower intensities where the density gradient is larger ii) in the literature [12], when SPWs are excited in metal for low laser intensities, so that there is essentially no density gradient at the target surface, the coupling is observed up to very small modulation depths ($d < \lambda_0/10$) iii) the saturation of the SPW amplitude occurs earlier when the modulation depth is reduced and it rapidly decays, which suggests that the absorption mechanism is modified.

For the reasons exposed above we may also conclude that $d = \lambda_0/3$ is a good compromise in order to both limit the geometry effects and preserve the coupling between the laser and the grating.

2.5 Effects of the target thickness

In the previous section we have studied the case of a semi-infinite target, which corresponds to a simulation where electrons reaching the right end of the plasma are cooled and re-enter the plasma at thermal velocity. We have shown that we can define the optimum SPW excitation conditions which optimize the laser absorption in the plasma. A large number of works where a laminar target was used [21, 27] have demonstrated the interest of laminar targets for particles acceleration in laser-overdense plasma interaction. Particularly it was observed that the emission of correlated bunches of ions at the rear surface which has been associated with hot electrons reaching the unirradiated surface. Namely, in the case of a laminar target energetic electrons entering the target reach the rear (unirradiated) side where a Debye sheath forms immediately as a consequence of charge separation. This sheath reflects electrons towards the front (irradiated side) of the target where they are reflected once more from the front sheath towards the rear and so on. The hot electron density at one side then corresponds to a superposition of laser accelerated electrons and electrons that are re-entering the target at intervals of twice the transit time. This mechanism is called *electron re-circulation* and will be discussed further in section 4.3, where electron heating is examined.
We chose to set the laser intensity value at $I\lambda_0^2 = 10^{19}$W cm$^{-2}\mu m^2$ as we have observed in the previous sections that in the low intensity regime the absorption is lower, which would make the effects of recirculation less visible and difficult to analyze.

Table 2.4: Absorption and SPW field amplification factor, η, as a function of target thickness for resonantly modulated and flat target for $I\lambda_0^2 = 10^{19}$W cm$^{-2}\mu m^2$, $d = \lambda_0$ (res=modulated target and resonant laser incidence, flat=flat target).

target type	thickness	η	absorption	d
res	$3.5\lambda_0$	3.5	85%	λ_0
res	$3.5\lambda_0$	4.3	52%	$\lambda_0/3$
nres 10°	$3.5\lambda_0$	-	39%	$\lambda_0/3$
flat	$3.5\lambda_0$	2	28%	0
res	$8\lambda_0$	4.1	74%	λ_0
flat	$8\lambda_0$	2	27%	0
res	s-inf	4.2	75%	λ_0
res	s-inf	4.4	51%	$\lambda_0/3$
nres 10°	s-inf	-	35%	$\lambda_0/3$
flat	s-inf	2	27%	0

The results are summarized in table 2.4, where the absorption and the amplification factor are given as a function of the target thickness, for both resonantly modulated and flat targets. We observe that the absorption is higher in the case of the thinner target,

of thickness $h = 3.5\lambda_0$, while for $h = 8\lambda_0$ it has already diminished to values close to the semi-infinite target. The amplification factor η is lowered when the thickness of the target decreases, as a consequence of the stronger absorption which damps the SPW. In fact electrons which are recirculating inside the target may interact with the SPW many times during the interaction, taking further energy from the wave. This mechanism is efficient if the interaction time and the target thickness are such that the hot electrons have the possibility to enter the SPW field with the correct phase in order to be efficiently accelerated [76]. This is confirmed by the fact that with increasing target thickness the absorption rapidly decreases to the level of the semi-infinite target where no recirculation occurs. The comparison of the resonantly modulated target with the flat ones shows that the energy and number of hot electrons is also determinant in order to increase the absorption via the recirculation mechanism. In fact we note that for the flat interface, where fewer hot electrons are excited, the absorption does not change when the thickness is reduced, staying close to the constant percentage 27% of the semi-infinite target.

Thus the use of a thin target having a modulated surface such as to resonantly excite a SPW may further enhance the effect of the wave on laser absorption as electrons recirculating in the target may interact many times with the wave before it is damped. This makes SPW excitation on thin laminar targets an attractive way to increase laser absorption at very high laser intensities, which has interesting consequence in particles acceleration as will be discussed in chapters 4 and 5.

2.6 Conclusion

We have defined the laser-grating matching conditions for the resonant excitation of a surface plasma wave and demonstrated that, when the latter are satisfied, the wave can be excited for a large range of laser intensities. Two aspects of the interaction have been considered: the amplification of the laser field via the resonant excitation of a surface wave and the absorption of the laser energy.

When the SPW is excited we observe a very localized electric field at the surface, directed along the target normal, whose amplitude is larger than the corresponding component of the laser field by a factor ranging from $\eta = 3.2$ to $\eta = 7.2$. The amplification varies with the laser intensity and its variation can be related to the rate at which the wave is damped by the transfer of its energy to the particles. The SPW transfers its energy to the particles via mechanisms such as vacuum heating, which is associated with particles oscillating in the field perpendicular to the target, or eventually wave-breaking which is efficient for very large field amplitude and its role becomes dominant in the high intensity regime ($I\lambda_0^2 > 10^{18}$W cm$^{-2}\mu m^2$). *Laser absorption is enhanced by SPW excitation because of its greater field intensity and localized distribution.* In fact the laser absorption is increased in presence of a surface wave, for example it increases from 27% when the SPW is not excited up to 75% at $I\lambda^2 = 10^{19}$W cm$^{-2}\mu m^2$. At the same time the wave is damped by electrons which are absorbing its energy and its maximum amplitude may be reduced, which explains the variation of the amplification factor with the laser intensity. These results have been published in [50].

At low intensities a density gradient is found at the target surface which has a scale length larger than the one found in the high intensity regime so that absorption mechanisms associated with the density gradient scale length are more important.

The coupling of the laser pulse with the grating has been investigated for different target parameters, such as the plasma density, the shape of the target surface and the target thickness.

We have considered different plasma densities (from 25 to 100 times the critical density) and found that the absorption is slightly reduced, even though it always remains higher than in the case of a flat target, where the SPW was not excited. This can be attributed to the fact that the penetration length of the field is reduced and fewer electrons are involved in the vacuum heating mechanism. Then we have studied the dependence of absorption and field amplification on the target geometry, considering a pulse impinging on a modulated target at different angle of incidences, which did not match the resonance conditions. *It has been observed that there is an important effect associated with the angle formed by the laser field and the normal to the modulation curve* which may induce large absorption even for non-resonant incidence. *Reducing the depth of the surface modulation to values smaller than the wavelength, this effect can be reduced and we notice a great difference in the absorption when the SPW is excited compared to the non-resonant incidence*, where laser absorption approaches the value obtained for a flat target. We also note that the modulation depth cannot be reduced too much as the coupling may be affected for values smaller than the gradient scale length at the target surface.

Finally we have examined the dependence of the absorption and field amplification on the target thickness, considering a semi-infinite target and two different laminar targets: we find that the *absorption is increased for decreasing target thickness, while the amplitude of the SPW field is reduced.* This can be attributed to electrons which are recirculating inside the target and interact several times with the wave field, absorbing more energy. Namely, in the case of a laminar target energetic electrons entering the target reach the rear (unirradiated) side where a Debye sheath forms immediately as a consequence of charge separation. The sheath reflects more electrons towards the front (irradiated side) of the target where they are reflected again from the front sheath towards the rear and so on. Thus for thinner targets the number of cycles that electrons can perform before the driving field is extinguished is greater and a larger number of electrons can perform at least one bounce.

We note that the most favourable results are obtained in the high intensity range, which makes SPW excitation a promising method to increase the maximum energy which can be transferred to particles at very high laser intensities.

Chapter 3

Magnetic field generation in presence of SPWs

The possibility of generating high magnetic fields during high power laser matter interaction with solid target has attracted considerable attention during this last decade [64, 79, 65] as it may have important consequences on the particle beams produced during the interaction. Typically in these studies a sharp-edged overdense plasma is created by ultra-short ($\tau \leqslant 100$fs) intense ($I\lambda^2 \geqslant 10^{15}$W cm$^{-2}\mu m^2$) IR laser pulses, that correspond to the interaction regime examined in the present work.

In this chapter we will investigate the role of the SPW on the creation of a steady magnetic field during laser overdense plasma interaction. To this end we develop a simple non relativistic hydrodynamic model which gives an analytic expression for the self-generated magnetic field. Within this model, valid in the low field intensity range where $v_{th} < v_{osc}$, we find that the SPW can induce (to the second order in the amplitude of the SPW field) a static magnetic field in the skin depth of the overdense plasma which has a quadratic dependence on the SPW electric field.

The magnetic field generation observed in PIC simulations will be also examined, for a large range of laser intensities ($I\lambda_0^2 = 10^{15} - 10^{20}$W cm$^{-2}\mu m^2$) and the characteristics of the field in presence of a SPW will be compared to the case of a flat target. The values of the magnetic field observed for low laser intensities and its spatial distribution will be compared to the prediction of the hydrodynamic model.

3.1 Analytical model for magnetic field generation

In section 1.6 we have studied the propagation of a surface wave at the vacuum plasma interface, by a simple, non-relativistic hydrodynamic derivation. We assume that the results of these calculations are valid in order to describe the early stages of the laser-plasma interaction, where kinetic effects are not important yet. In the model presented in the following we will carry on the calculations in the section 1.6, where we derived the surface wave field in the first order approximation, up to the second order. We will initially take into account the electron temperature and then analyze the cold plasma limit. The influence of the electron plasma density on its intensity and spatial

distribution will be also discussed. The results of this derivation can be applied to the case where a SPW is resonantly excited by a low intensity laser pulse, such that the electron quiver velocity in the field of the surface wave is less than its thermal velocity. We recall that, in the calculations, the plasma fills the half-space $x > 0$ while the vacuum occupies the half-space $x < 0$ and the wave propagates along y (see fig.1.1). We also recall that the point $x = 0$ corresponds to the point where the first order electron velocity associated with the wave vanishes, i.e. $v_1 = 0$ (notice that this condition concerns only v_1 and not the thermal speed).

We will start by considering the second order continuity equation

$$\frac{\partial n_2}{\partial t} + n_0 \nabla \cdot \mathbf{v_2} + n_1 \nabla \cdot \mathbf{v_1} + v_1 \nabla \cdot \mathbf{n_1} = 0 \tag{3.1}$$

and the second order momentum equation

$$\begin{aligned} n_0 \frac{\partial \mathbf{v_2}}{\partial t} + n_0 (\nabla \cdot \mathbf{v_1}) \mathbf{v_1} + n_1 \frac{\partial \mathbf{v_1}}{\partial t} &= -n_0 \frac{e}{m_e c} \left[c\mathbf{E_2} + \mathbf{v_1} \times \mathbf{B_1} \right] \\ &\quad -\beta^2 \nabla n_2 - \beta^2 \frac{T_1}{T_0} \nabla n_1 - n_1 \frac{e}{m_e} \mathbf{E_1} \end{aligned} \tag{3.2}$$

where the subscript 2 refers to the second order perturbation quantities. According to the adiabatic temperature-density relationship we have $T_1 = \gamma T_0 (n_1/n_0)$ which means that at this approximation order we are neglecting any thermo electric source, i.e. a term of the form $\nabla n \times \nabla T$ which gives no contribution on the fast time scales of the SPW oscillation. In fact, as the surface wave is rapidly oscillating, the electrons in the plasma do not have enough time for thermalization, and the process can be approximated as adiabatic for short timescales.
Substituting the expression of T_1 into (3.2), the second order momentum equation becomes

$$\begin{aligned} n_0 \frac{\partial \mathbf{v_2}}{\partial t} + n_0 (\nabla \cdot \mathbf{v_1}) \mathbf{v_1} + n_1 \frac{\partial \mathbf{v_1}}{\partial t} &= -n_0 \frac{e}{m_e c} \left[c\mathbf{E_2} + \mathbf{v_1} \times \mathbf{B_1} \right] \\ &\quad -\beta^2 \nabla n_2 - \beta^2 \frac{n_1}{n_0} \nabla n_1 - n_1 \frac{e}{m_e} \mathbf{E_1} \end{aligned} \tag{3.3}$$

Using the first order momentum equation (1.128) for v_1, the latter expression can be rewritten as

$$\begin{aligned} n_0 \frac{\partial \mathbf{v_2}}{\partial t} + n_0 (\nabla \cdot \mathbf{v_1}) \mathbf{v_1} &= -n_0 \frac{e}{m_e c} \left[c\mathbf{E_2} + \mathbf{v_1} \times \mathbf{B_1} \right] \\ &\quad -\beta^2 \nabla n_2 + n_1 \beta^2 \nabla n_1 - \beta^2 \frac{n_1}{n_0} \nabla n_1 \end{aligned} \tag{3.4}$$

Then we will consider the time derivative of the second order momentum equation (3.4)

$$\frac{\partial^2 \mathbf{v_2}}{\partial t^2} = -\frac{e}{m_e}\frac{\partial \mathbf{E_2}}{\partial t} - \frac{\partial}{\partial t}\left[\frac{e}{m_e c}\mathbf{v_1}\times\mathbf{B_1} + (\nabla\cdot\mathbf{v_1})\mathbf{v_1}\right] - \beta^2\nabla\frac{\partial}{\partial t}\frac{n_2}{n_0} \tag{3.5}$$

$$+\beta^2\left(1-\frac{1}{n_0}\right)\frac{\partial}{\partial t}\left(\nabla n_1\frac{n_1}{n_0}\right) \tag{3.6}$$

and the time derivative of the second order electric field from the Maxwell-Faraday equation (1.7) at the second order

$$\frac{\partial \mathbf{E_2}}{\partial t} = c\nabla\times\mathbf{B_2} + \frac{4\pi}{c}\left[en_0\mathbf{v_2} + en_1\mathbf{v_1}\right] \tag{3.7}$$

which can be combined to obtain the following relationship

$$\frac{\partial^2 \mathbf{v_2}}{\partial t^2} = -\frac{ec}{m_e}\nabla\times\mathbf{B_2} - \omega_p^2\mathbf{v_2} - \omega_p^2\frac{n_1}{n_0}\mathbf{v_1} - \frac{\partial}{\partial t}\left[\frac{e}{m_e c}\mathbf{v_1}\times\mathbf{B_1} + (\nabla\cdot\mathbf{v_1})\mathbf{v_1}\right]$$
$$-\beta^2\nabla\frac{\partial}{\partial t}\frac{n_2}{n_0} + \beta^2\left(1-\frac{1}{n_0}\right)\frac{\partial}{\partial t}\left(\nabla n_1\frac{n_1}{n_0}\right) \tag{3.8}$$

The first order magnetic field $\mathbf{B_1}$ can be obtained from the first order momentum equation (1.128) as follows

$$\frac{\partial\nabla\times\mathbf{v_1}}{\partial t} = -\frac{e}{m_e}\nabla\times\mathbf{E} = \frac{e}{m_e c}\frac{\partial\mathbf{B_1}}{\partial t} \tag{3.9}$$

$$\nabla\times\mathbf{v_1} = \frac{e}{m_e c}\mathbf{B_1} \tag{3.10}$$

which, after a simple manipulation, allows us to simplify the two terms in the squared brackets of equation (3.8)

$$\left[\frac{e}{m_e c}\mathbf{v_1}\times\mathbf{B_1} + (\nabla\cdot\mathbf{v_1})\mathbf{v_1}\right] = \left[\mathbf{v_1}\times\nabla\times\mathbf{v_1} + (\nabla\cdot\mathbf{v_1})\mathbf{v_1}\right] = \nabla v_1^2 \tag{3.11}$$

and (3.8) becomes

$$\frac{\partial^2 \mathbf{v_2}}{\partial t^2} = -\frac{ec}{m_e}\nabla\times\mathbf{B_2} - \omega_p^2\mathbf{v_2} - \omega_p^2\frac{n_1}{n_0}\mathbf{v_1} - \frac{\partial}{\partial t}\nabla v_1^2 - \beta^2\nabla\frac{\partial}{\partial t}\frac{n_2}{n_0} \tag{3.12}$$
$$+\beta^2\left(1-\frac{1}{n_0}\right)\frac{\partial}{\partial t}\left(\nabla n_1\frac{n_1}{n_0}\right)$$

Finally, by taking the curl of (3.12), we can eliminate some terms and we find the relation

$$\frac{\partial^2\nabla\times\mathbf{v_2}}{\partial t^2} = -\frac{ec}{m_e}\nabla\times\nabla\times\mathbf{B_2} - \omega_p^2\nabla\times\mathbf{v_2} - \omega_p^2\frac{1}{n_0}\nabla\times(n_1\mathbf{v_1}) \tag{3.13}$$
$$= \frac{ec}{m_e}\nabla^2\mathbf{B_2} - \omega_p^2\frac{1}{n_0}\nabla\times(n_1\mathbf{v_1}) - \omega_p^2\nabla\times\mathbf{v_2}$$

where we used the fourth of Maxwell's equations (1.1) for the divergence of the magnetic field.

Now we look for an expression connecting the second order magnetic field and the second order electron velocity. Taking the curl of the second order momentum equation (3.4) and using relation (3.11) we get

$$\frac{\nabla\partial \times \mathbf{v_2}}{\partial t} = -\frac{e}{m_e}\nabla \times \mathbf{E_2} = \frac{e}{m_e c}\frac{\partial \mathbf{B_2}}{\partial t} \tag{3.14}$$

$$\nabla \times \mathbf{v_2} = \frac{e}{m_e c}\mathbf{B_2} \tag{3.15}$$

and substituting the latter expression into (3.13) we have:

$$\frac{\partial^2 \mathbf{B_2}}{\partial t^2} - c^2\nabla^2\mathbf{B_2} + \omega_p^2\mathbf{B_2} = -\omega_p^2\frac{m_e c}{e n_0}\nabla \times (n_1\mathbf{v_1}) \tag{3.16}$$

We are looking now for the slowly varying component of the electromagnetic field, so we will assume that the term $\frac{\partial^2 \mathbf{B_2}}{\partial t^2}$ is negligible and we will take the time average of the term $\nabla \times (n_1\mathbf{v_1})$. This means suppressing the y derivatives in the curl product of equation 3.16, as we will show in the following. We develop the product $n_1\mathbf{v_1}$, rewriting the first order density and the velocity as follows $n_1 = \bar{n_1}e^{iky-i\omega t} + c.c.$, $v_1 = \bar{v_1}e^{iky-i\omega t} + c.c.$:

$$n_1\mathbf{v_1} = \bar{n_1}^*\bar{v_1} + \bar{n_1}\bar{v_1}^* + \bar{n_1}\bar{v_1}e^{2iky-i2\omega t} + \bar{n_1}^*\bar{v_1}^*e^{-2iky+i2\omega t} \tag{3.17}$$

We observe, from equations (1.163) and (1.164), that the x component of $\bar{v}_1$ has to be imaginary ($\bar{v_{1x}}^* = -\bar{v_{1x}}$) while the y component is real ($\bar{v_{1y}}^* = \bar{v_{1y}}$); from equation (1.162) we also observe that $\bar{n}_1$ is real ($\bar{n_1}^* = \bar{n_1}$). Moreover we recall that $\bar{v}_1$ and $\bar{n}_1$ have no dependence on y and time.

In order to calculate the curl product in (3.16), we first calculate the y derivative of the x component of $n_1\mathbf{v_1}$:

$$\frac{\partial(n_1 v_{1x})}{\partial y} = i2k\bar{n_1}\bar{v_{1x}}e^{2iky-i2\omega t} + i2k\bar{n_1}\bar{v_{1x}}e^{-2iky+i2\omega t} \tag{3.18}$$

and we note that the time average of this term is 0.

Now we calculate the x derivative of the y component of $n_1\mathbf{v_1}$:

$$\frac{\partial(n_1 v_{1y})}{\partial x} = \frac{\partial}{\partial x}(2\bar{n_1}\bar{v_{1y}}) + \frac{\partial}{\partial x}(2\bar{n_1}\bar{v_{1y}})\left[e^{2iky-i2\omega t} + e^{-2iky+i2\omega t}\right] \tag{3.19}$$

The time average of this term is non-zero and is given by $\frac{\partial}{\partial x}(2\bar{n_1}\bar{v_{1y}})$, so that equation (3.16) becomes

$$-c^2\frac{\partial^2\mathbf{B_2}}{\partial x^2}+\omega_p^2\mathbf{B_2}=-2\omega_p^2\frac{m_e c}{en_0}\frac{\partial(\bar{n}_1\bar{v}_{1y})}{\partial x}= \tag{3.20}$$
$$2c\frac{e}{m_e}E_{0x}^2\frac{\omega_p^2}{\omega^2}\frac{k^2-q_t^2}{q_t\omega}\left[\frac{-(q_p+q_t)q_p}{k}e^{-(q_p+q_t)x}+e^{-2q_tx}2k\right]$$

where we used relations (1.128) and (1.162). We can now solve the differential equation looking for a particular solution of (3.20) which combined with the solution of the associated homogeneous equation, will give the general solution. We will take the field B_2 of the form

$$B_{2part}=Ae^{-(q_p+q_t)x}+Be^{-2q_tx} \tag{3.21}$$

so

$$-c^2\left[A(q_p+q_t)^2e^{-(q_p+q_t)x}+B4q_t^2e^{-2q_tx}\right] \tag{3.22}$$
$$+\omega_p^2\left[Ae^{-(q_p+q_t)x}+Be^{-2q_tx}\right]=$$
$$2c\frac{e}{m_e}E_{0x}^2\frac{\omega_p^2}{\omega^2}\frac{k^2-q_t^2}{q_t\omega}\left[\frac{-(q_p+q_t)q_p}{k}e^{-(q_p+q_t)x}+e^{-2q_tx}2k\right]$$

and we find the solutions

$$A=2c\frac{e}{m_e}E_{0x}^2\frac{\omega_p^2}{\omega^2}\frac{k^2-q_t^2}{q_t\omega k}\frac{-(q_p+q_t)q_p}{\omega_p^2-c^2(q_p+q_t)^2} \tag{3.23}$$
$$B=2c\frac{e}{m_e}E_{0x}^2\frac{\omega_p^2}{\omega^2}\frac{k^2-q_t^2}{q_t\omega}\frac{2k}{\omega_p^2-4c^2q_t^2} \tag{3.24}$$

The solution of the homogeneous differential equation associated with (3.20)

$$-c^2\frac{\partial^2B_2}{\partial x^2}+\omega_p^2B_2=0 \tag{3.25}$$

is

$$B_{2om}=Ce^{-\frac{\omega_p}{c}x} \tag{3.26}$$

The general solution for the slowly varying magnetic field B_2 is

$$\mathbf{B_2}=\hat{z}(Ae^{-(q_p+q_t)x}+Be^{-2q_tx}+Ce^{-\frac{\omega_p}{c}x}) \tag{3.27}$$

On the vacuum side ($x<0$) the analog of eq. (3.20) reads $\frac{\partial^2\vec{B_{2,v}}}{\partial x^2}=0$ that gives as solution a constant field. The condition that the field is zero far away from the surface

imposes $B_{2,v} = 0$. Thus, imposing the continuity of the magnetic field we obtain the solution:

$$C = -(A + B) \tag{3.28}$$

The terms A and B can also be expressed as a function of the SPW field at the plasma-vacuum interface, $E_{sw} = |E_{1x}(x = 0)| = (1 - \frac{\omega_p^2}{\omega^2})E_{0x}$ writing[1]:

$$A = \frac{2ce}{m_e} \frac{E_{sw}^2}{(1 - \frac{\omega_p^2}{\omega^2})^2} \frac{\omega_p^2}{\omega^2} \frac{k^2 - q_t^2}{q_t \omega k} \frac{-(q_p + q_t)q_p}{\omega_p^2 - c^2(q_p + q_t)^2} \tag{3.29}$$

$$B = \frac{2ce}{m_e} \frac{E_{sw}^2}{(1 - \frac{\omega_p^2}{\omega^2})^2} \frac{\omega_p^2}{\omega^2} \frac{k^2 - q_t^2}{q_t \omega} \frac{2k}{\omega_p^2 - 4c^2 q_t^2} \tag{3.30}$$

Equations (3.27), (3.29) and (3.30) show that the surface wave gives rise to a second order magnetic field proportional to the square of the SPW field E_{sw} and confined near the interface, whose strength depends on the source field, the electron temperature and density.

Two limits are now interesting to explore, in order to clarify the dependence of B_2 on the relevant parameters. First, in the limit of $T_0 \to 0$ ($q_t \to \infty$), that is a cold plasma, we observe that B vanishes while A does not. Thus, using relations (3.27) and (3.28) we obtain the second order magnetic field for a cold plasma at $x > 0$ ($B_2 = 0$ at $x = 0$):

$$\vec{B}_{2,cold} = 2\frac{e}{m_e c\omega} \frac{E_{sw}^2}{(1 - \frac{\omega_p^2}{\omega^2})^2} \frac{\omega_p^2}{\omega^2} \frac{q_p}{k} e^{-\frac{\omega_p}{c}x} \hat{z} \tag{3.31}$$

It should be noticed that this result is difficult to obtain directly from the cold plasma equations, due to the discontinuity of the electric field E_{1x} at $x = 0$.

Then, in the limit of strongly overdense plasma $\frac{\omega_p}{\omega} >> 1$, we have $k^2 \sim \omega^2/c^2$ from the dispersion relation (1.112) and equation (3.31) can be expressed as

$$\vec{B}_{2,ovd} = sign(k) 2\frac{e}{m_e c\omega} E_{sw}^2 \frac{\omega}{\omega_p} e^{-\frac{\omega_p}{c}x} \hat{z} \tag{3.32}$$

Thus, in the case of extremely high density and low temperature, the model predicts a magnetic field having a rapidly vanishing amplitude inside the plasma, with a maximum value proportional to $\sqrt{n_c/n_e}$.

In figure 3.1 the dependence of the magnetic field given by the expression (3.27) on the electron thermal velocity (expressed by the parameter β) is shown, for $E_{sw} = 0.2 m_e \omega/e$, $\omega_{pe}^2/\omega^2 = 25$, and three values of β/c: 0.15, 0.05 and 0. The magnetic field is peaked near the plasma surface for low electron thermal temperatures while it becomes less localized when the electron thermal velocity is increased. This is consistent with the fact that if we increase the electron thermal velocity the parameter $1/q_t \sim$

[1]The field is continuous at the surface due to the presence of a finite electron temperature.

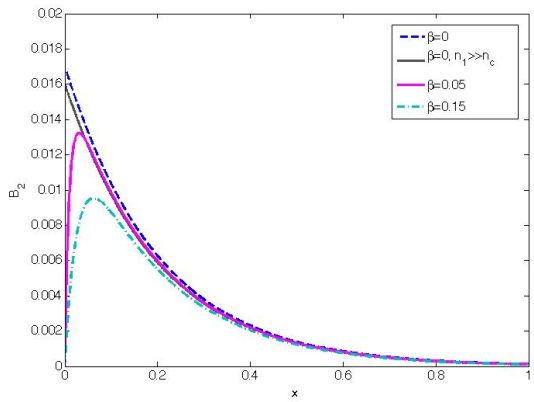

Figure 3.1: Magnetic field (absolute value $B_2 = |\vec{B}_2|$) as a function of the depth inside the plasma, given by equation (3.27), for $n_e = 25n_c$ and different values of $\beta = 0, 0.05, 0.15$ and in the limit $n_1/n_c \to \infty$ for $\beta = 0$. $E_{sw} = 0.2$. The values of the fields are given in units of $B_0 = m_e\omega/e$, the depth is in units of k^{-1}.

λ_D (where λ_D is the Debye length) increases while in the case of a cold plasma the evanescence length is simply given by the skin depth, which for our parameters, is equal to $c/\omega_{pe} = 0.2c/\omega \simeq 0.2k^{-1}$. For comparison, the curves corresponding to the limits of a cold ($T_0 \to 0$) and dense plasma ($\omega_{pe}/\omega \gg 1$) are also shown: the long dashed curve corresponds to equation (3.31) while the gray solid curve corresponds to equation (3.32). As expected a higher maximum strength of $B_{2,cold} = 0.017m_e\omega/e$ is obtained in the limit of a cold plasma, while in the limit of very high density the peak decreases to $B_{2,ovd} = 0.016m_e\omega/e$.

To complete the discussion, we have plotted in figure (3.2) the dependence of the magnetic field on the electron density for n_e =25, 50, 75 and $100n_c$ for an electron thermal velocity $\beta/c = 0.05$ (a) and in the cold plasma limit $\beta = 0$ (b). As expected from the expression (3.32) in the limit of very high density, we observe that the field amplitude decreases for increasing electron density and becomes more peaked and closer to the surface. This is consistent with the reduction of the skin depth for increasing plasma density. The same trend is observed in the cold plasma limit.

Thus, in the case of resonant excitation of the surface wave by a laser field, the model predicts the presence of a quasi-static magnetic field in the plasma skin depth, induced by the SPW, whose amplitude scales with the square of E_{sw}. The latter can be related to the laser field by the amplification factor η, as discussed in chapter 2, which means that the self-generated magnetic field would scale with the laser intensity if we consider a range where η is quasi-constant. We notice that the quasi-static magnetic field derived in this model is stronger than what was derived for the case of generation of a static magnetic field by a laser propagating in underdense, cold, homogeneous plasma, [69] where the perturbative analysis needed expansion to fourth order in order to prove the possibility of magnetic field self-generation. Nevertheless, it should be mentioned here that the validity of this approach is limited to moderate laser intensity range where $I\lambda^2 \simeq 10^{16}$W cm$^{-2}\mu m^2$ because of the hypothesis $v_{osc}/c = eE_{sw}/cm_e\omega < \beta$. Moreover,

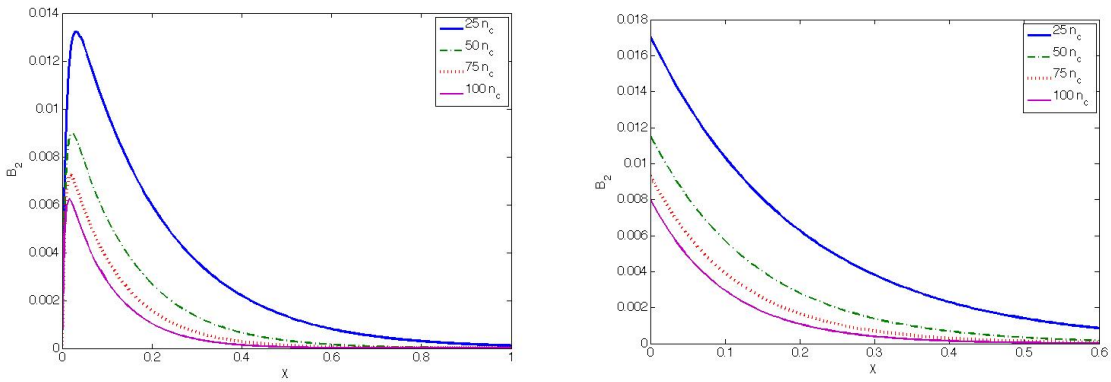

a b

Figure 3.2: Magnetic field (absolute value $B_2 = |\vec{B}_2|$) as a function of the depth inside the plasma, given by equation (3.27), for $E_{sw} = 0.2$ and different values of the n_e, for $\beta/c = 0.05$ (a) and in the limit of a cold plasma $\beta = 0$ (b).The values of the fields are given in units of $B_0 = m_e\omega/e$, the depth is in units of k^{-1}.

some limitations of the model should also be noticed such as, for example, the transfer of energy from the wave to the particle via kinetic effects (such as $J \times B$ and vacuum heating), creating hot tails in the electron distribution functions which are not described in this fluid approach. However, in the higher laser intensity range, SPW still exist, as we have seen in chapter 2 and can be an attractive way for quasi-static magnetic field generation.

In conclusion we predict, with a simple non relativistic hydrodynamic model, a new effect in a moderate intensity laser interaction regime $I\lambda^2 <\sim 10^{16}$W cm$^{-2}\mu m^2$: the significant generation of a quasi-static magnetic field by resonant excitation of a surface wave on a plasma target. The magnetic field intensity is shown to have a quadratic dependence on the SPW electric field, which can be related to the laser one, and to decrease with ω/ω_{pe} for increasing density. The model is different from previous studies on the steady magnetic field generation in laser over-dense plasma interaction, where the mechanisms proposed are of thermoelectric origin and involved the electron density gradient or the temperature anisotropy [68, 63]. The results presented in this section have been published [51].

In the next section we will examine the magnetic fields which were found in PIC simulations for both the low intensity regime, which can be compared with the model discussed in this section, and the high intensity regime, where the model cannot more be applied any more.

3.2 Quasi-static magnetic field in PIC simulations

In PIC simulations performed at different intensities we observe a strong, quasi-static magnetic field localized near the target surface within a thickness of $\sim \lambda_0$. With SPW excitation the maximum value obtained in our simulations for the magnetic field is

~ 580MG for $\lambda_0 = 1\mu$m at 7×10^{19}W cm$^{-2}\mu m^2$. The field appears at the beginning of the interaction, reaches its maximum around $500\omega_0^{-1}$, and it is found to grow with the laser intensity. (*We recall that λ_0, k_0 and ω_0 are respectively the wavelength, the wave vector and frequency of the laser pulse. In the previous section instead we have used the variables λ, k and ω which refer to the wavelength, wave vector and frequency of the SPW. When the SPW is excited, for our set of laser and target parameters, we have $\lambda \simeq \lambda_0$, $k \simeq k_0$ and $\omega = \omega_0$, so that the two sets of variables are nearly equivalent.*)

In this section we wish to analyze the characteristics of the self-generated field such as its spatial distribution, evolution in time and their dependence on the laser pulse intensity. Two regimes, low and relativistic intensity, will be analyzed. Particularly, for the low intensity regime ($I\lambda_0^2 <\sim 10^{16}$W cm$^{-2}\mu m^2$) where the calculations developed in the previous section can be valid, we will compare the field characteristics with the predictions of the analytical model.
In the following we will consider only the case of the semi-infinite target (where electrons reaching the right side of the target are cooled and reintroduced into the plasma at thermal velocity), in order to exclude effects due to electron recirculation [21] in the target, which may further complicate the understanding of the magnetic field generation.

We recall that in the simulations the box size is $6\lambda_0$ along the y direction and $46\lambda_0$ along the x direction for the semi-infinite target. The plasma starts at $x = 240k_0^{-1}$ and its extension is $8\lambda_0$. The plasma particles are initially described by a Maxwellian distribution with electron temperature $T_e = 1$keV (thermal velocity $v_{th} = 0.044c$) and ion temperature $T_i = T_e/10$ (here $m_i/m_e = 1836$, where m_i and m_e are the ion and electron mass). The charge of the ions was $Z = 1$. For the modulated target the periodicity is $a_m = 2\lambda_0$ and depth of the modulation, which will not vary in the present study (in order to have stronger coupling even for low intensities), is $d = \lambda_0$ (from the maximum to the minimum). The laser is incident at an angle $\theta = 30°$, which matches the condition for SPW excitation, reaches the target surface at $t = 240\omega_0^{-1}$ and has a duration of $240\omega_0^{-1}$ (~ 56 fs for $\lambda_0 = 1\mu$m).

3.2.1 Magnetic field when the SPW is excited

A strong quasi-static magnetic field is generated at the plasma surface when the SPW is excited. We will now analyze for $n_e = 25n_c$ this field, B_z, (which in the following is normalized to $B_0 = m_e\omega_0/e \sim 107$MG for $\lambda_0 = 1\mu$m) which was obtained by averaging over one laser cycle.

We shall start our study by considering the low intensity regime. Figure 3.3 a) shows the static magnetic field generated at the plasma surface for the pulse having $I\lambda_0^2 = 10^{16}$W cm$^{-2}\mu m^2$ at times $t_{Emax} = 460\omega_0^{-1}$ (as in fig.2.2, it corresponds to the time at which the SPW field is maximum on the modulated surface). We observe that the quasi-static magnetic field is localized at the modulation tips and on the upper part of the dips and has an extension of $\sim \lambda_0$. The latter corresponds approximately to the size of the layer of expanding plasma at the target surface, as shown in fig.3.3b. The magnetic field at the tips is positive and its maximum value is $\simeq 0.023m_e\omega/e$ (2.5MG for $\lambda_0 = 1\mu$m) while in the upper y side of the dips the field is negative and reaches $\simeq 0.034m_e\omega/e$ (3.6MG for $\lambda_0 = 1\mu$m).

Later on, the spatial distribution of the field evolves and the positive peaks tend to disappear. At a time when the pulse is over, for example at $t = 600\omega_0^{-1}$ as shown in fig.3.3c, the field has negative values at any position, and has preserved its intensity compared to the time $t_{Emax} = 460\omega_0^{-1}$.

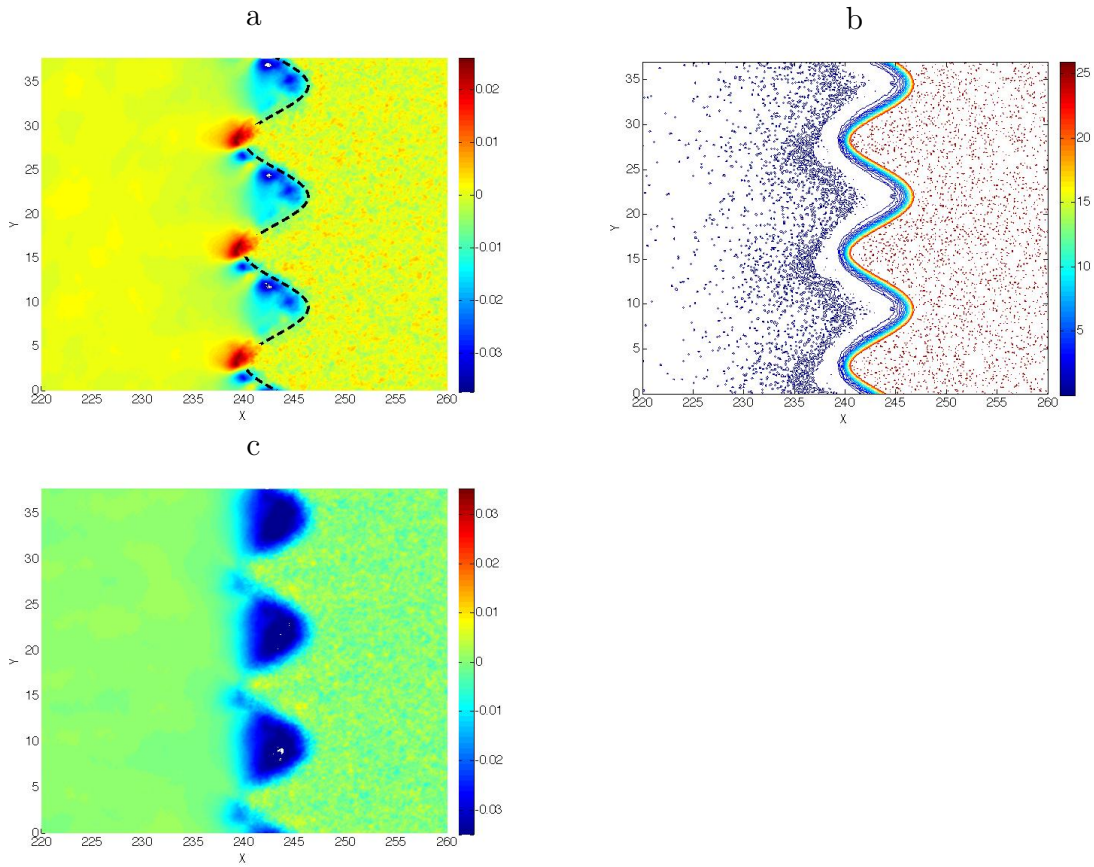

Figure 3.3: For $I\lambda_0^2 = 10^{16}$W cm$^{-2}\mu m^2$, quasi static magnetic field in the xy plane, at $t_{Emax} = 460\omega_0^{-1}$ (a) (dotted line shows the initial plasma surface), and corresponding electron density isocontours from 1 to $25n_c$ (b). Quasi static magnetic field in the xy plane at a later time $t = 600\omega_0^{-1}$ (c). The magnetic field is in units of B_0,and the lengths are in units of k_0^{-1}.

A plot of the maximum negative value of the magnetic field, generated by SPW excitation at $t = 600\omega_0^{-1}$, is shown in fig. 3.4, as a function of the maximum SPW field E_{sw}. The scaling of the magnetic field with E_{sw} is faster than linear for low intensities ($I\lambda_0^2 < 5 \times 10^{16}$W cm$^{-2}\mu m^2$) but almost linear for higher intensities.

The magnetic field in the low intensity simulations can be compared to the model presented in the previous section, using the formula (3.32) obtained in the limit of high plasma density (as here we have $n_e = 25n_c$). We notice that the sign of the field corresponds to the predictions: the wave vector of the SPW wave (which is given by $k = k_0(\sin\theta + \lambda_0/a_m) \sim k_0$), has negative sign in the $\hat{y}$ direction, as shown in fig.2.1, which would give a negative magnetic field as observed in fig.3.3c. If we apply (3.32) to the simulations performed at $I\lambda_0^2 = 10^{15-16}$W cm$^{-2}\mu m^2$, we find that the predicted

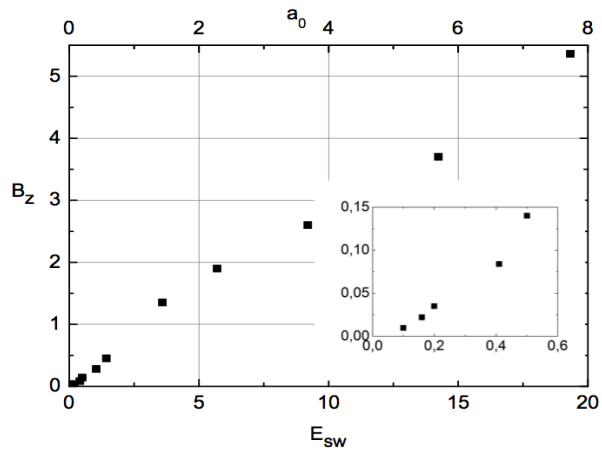

Figure 3.4: Plot of the maximum value of the magnetic field as a function of the maximum SPW field E_{sw}. The electric field is in units of $E_0 = 3 \times 10^{10} V cm^{-1}$ for $\lambda_0 = \mu$m and the magnetic field in units of B_0. *In the small frame:* zoom on the low intensity range.

field has the right order of magnitude, $\sim$ 1MG for $\lambda_0 = 1\mu$m, but it is systematically smaller than what found in the simulations. This can be related to the limit of validity of the hydrodynamic description where we recall that kinetic effects were not taken into account, and a flat and sharp plasma-vacuum interface without grating was assumed. At the same time, we notice that the extension of the field in fig.3.3c is bigger than predicted in the model (see fig.3.4) by a factor ~ 2 and the field is located in the low density region, where plasma expansion has occurred. In order to examine the effect of the density gradient scale length at the surface, simulations with fixed ions at low intensity $I\lambda_0^2 = 10^{15-16}$W cm$^{-2}\mu m^2$ have hence been performed, in order to limit the expansion of the plasma towards vacuum and the presence of electrons outside the skin depth. In fig. 3.5 we show the magnetic field for the case $I\lambda_0^2 = 10^{16}$W cm$^{-2}\mu m^2$ with immobile ions. In this case there is a weak modifications of the SPW field that takes the value $E_{sw} = 0.23$ instead of 0.2 with mobile ions (at $t_{Emax} = 460\omega_0^{-1}$). We can observe that the negative component of the magnetic field is localized in the plasma skin depth and the absolute value of the field is reduced by a factor of 2, giving better agreement with the model prediction, $B_z \sim -0.02$, from the formula above. However at $I\lambda_0^2 = 10^{15}$W cm$^{-2}\mu m^2$ the variation in the field values from the mobile to the immobile ions case is only 10%, and the predicted field is too small, so that we conclude that *even at this low intensity kinetic effects are already important.*

Analysis of the observed structure of the cycle-averaged magnetic field at late times (fig.3.4c) implies that, on the average, a positive current flows along the target parallel (y) direction on the vacuum side, while a negative return current flows in a thin surface layer. The positive current corresponds to a flow of electrons in the negative y direction, consistently with the conservation of the laser wave momentum, since $k_y < 0$. *Since most of the momentum is absorbed by the suprathermal electrons, we conclude that these electrons produce the positive current from the average of their orbits on the vacuum side, i.e. in the course of a two-dimensional "vacuum heating" process.* The return

current is localized in the skin layer and it is due to slower bulk electrons with higher density. The structure of the steady magnetic field and of the associated currents is particularly clear after the end of the laser pulse in the case of low laser intensity since the flowing of the current on the modulated surface produces peaks of the magnetic fields inside the dips of the surface modulation.

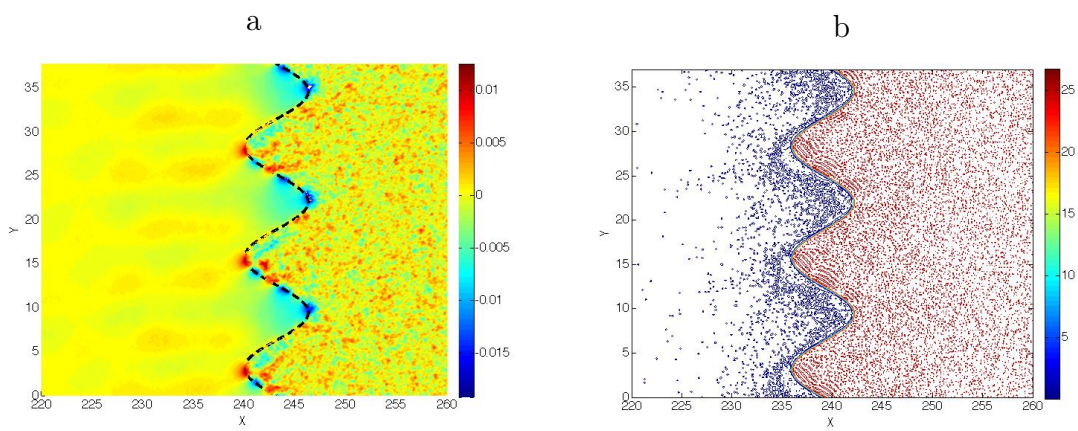

Figure 3.5: a) Quasi static magnetic field in the xy plane, at $t_{Emax} = 460\omega_0$ For $I\lambda_0^2 = 10^{16}$W cm$^{-2}\mu m^2$ and b) electron density in the case where the ions are fixed. The magnetic field is given in units of B_0, the lengths are in units of k_0^{-1}.

We will now examine the magnetic field in the *high intensity regime* ($I\lambda_0^2 > 10^{18}$ W cm$^{-2}\mu m^2$), which is *outside the validity range of the model developed in section 3.3*. The field structure initially, for $t = 500\omega_0^{-1} \sim t_{Emax}$ (fig.3.6a) has some points in common with the one observed in the low intensity case at $t \sim t_{Emax}$ (fig.3.3a), but at later times it shows a more complex structure: we observe in fig.3.6c that the negative magnetic field is less uniform than what was observed in the low intensity case (fig.3.3c) and appears stronger on the lower part of the modulation dip. This difference can be attributed to kinetic effects due to the electrons accelerated in the strong SPW field (the 'enhanced vacuum heating', mentioned in section 2.1.2, and $\vec{J} \times \vec{B}$ heating) which become very important in this regime with the *emission of bunches of particles* as shown by picture 3.6b), where the density of electrons is shown at $t = 500\omega_0^{-1} \sim t_{Emax}$, for $I\lambda_0^2 = 10^{19}$W cm$^{-2}\mu m^2$. *The stream of electrons in the vacuum strongly affects the magnetic field distribution, which is characterized by irregular negative and positive areas even at late times.*

The emission of electron bunches as well as the ion emission will not be discussed here as they will be treated in detail in chapter 4 and 5 respectively where currents and emission directions are investigated.

Finally we shall examine the dependence of the quasi-static magnetic field on plasma density, which was found to be an important parameter to determine the field strength (see eq.(3.32) in our analytical model). In tab.3.1 the magnetic field is plotted as a function of the electron density for two laser intensities $I\lambda_0^2 = 10^{16}$W cm$^{-2}\mu m^2$ and $I\lambda_0^2 = 10^{19}$W cm$^{-2}\mu m^2$ representing the low intensity and the relativistic regime respectively.

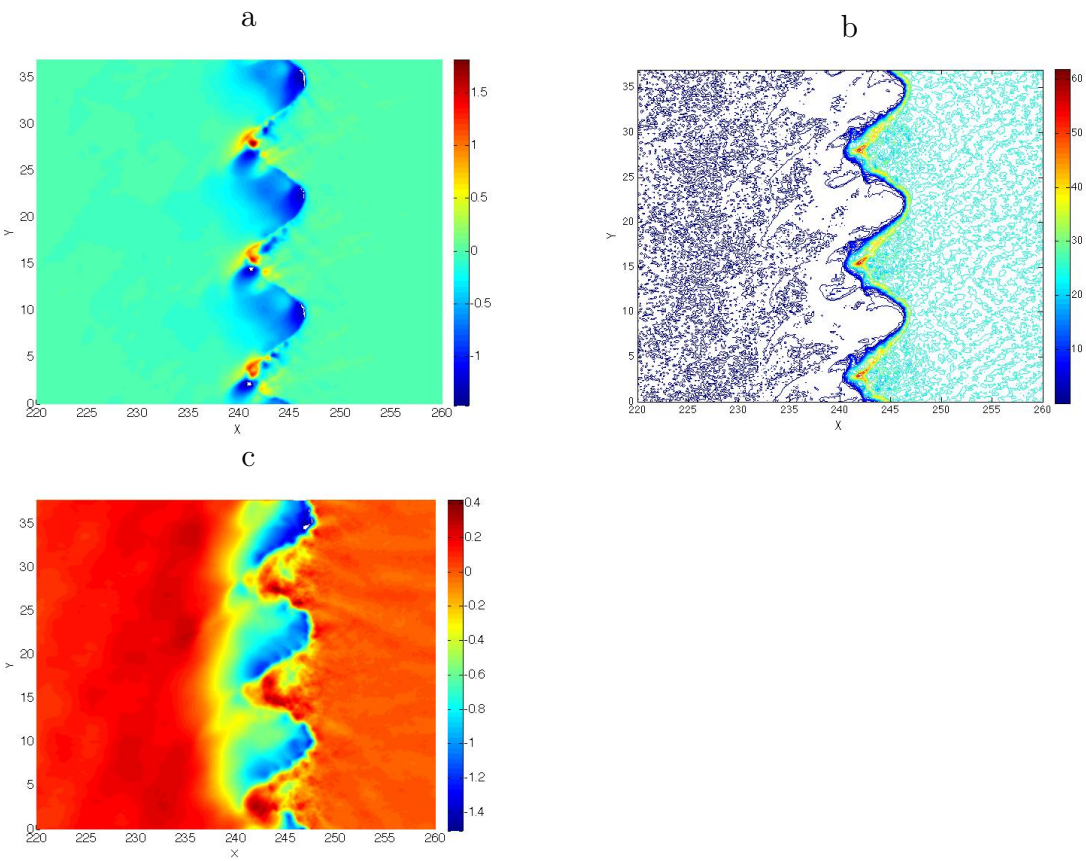

Figure 3.6: Quasi static magnetic field in the xy plane, at $t = 500\omega_0^{-1} \simeq t_{Emax}$ (a) and corresponding electron density isocontours in the xy plane (b) (given in particles per point). Quasi static magnetic field in the xy plane at $t = 600\omega_0^{-1}$ (c). The laser intensity and the target density were $I\lambda_0^2 = 10^{19}$W cm$^{-2}\mu m^2$ and $n_e = 25n_c$. The magnetic field in units of B_0, the lengths are in units of k_0^{-1} .

We notice that in both intensity regimes the field varies, weakly increasing, regularly, with the electron density while, according to the model, it was expected to strongly decrease for increasing plasma density (see fig.3.2). This result confirms further that *the magnetic field has a strong dependence on kinetic effects*. Also the expansion of the plasma has an important role as we have observed that the magnetic field spatial extension spreads in front of the target where a density gradient is present.

3.2.2 Magnetic field for the flat target

We shall now compare the characteristics of the field in the simulations where the SPW is excited with the simulations where the target is flat.

We notice that in all cases the intensity of the magnetic field is increased by SPW excitation compared to the flat target even though the scaling with E_{sw} becomes weaker at relativistic intensities. A net increase of the magnetic field is observed in the cases where the surface wave is excited: for example when $I\lambda_0^2 = \times 10^{19}$W cm$^{-2}\mu m^2$, the

Table 3.1: Quasi-static magnetic field as a function of the plasma density n_e, for the semi-infinite target with modulated surface (modulation depth $d = \lambda_0$), when the SPW is excited. The field was averaged over a laser cycle and the maximum field value (which has negative sign) is plotted. $t \simeq t_{Emax}$ and the field is normalized to B_0.

n_e/n_c	$I\lambda_0^2 = 10^{16}$W cm$^{-2}\mu m^2$	$I\lambda_0^2 = 10^{19}$W cm$^{-2}\mu m^2$
25	0.4	1.9
50	0.42	2
75	0.43	2.1
100	0.44	2.3

Table 3.2: Quasi-static magnetic field as a function of the laser intensity, for the semi-infinite target with flat surface (flat) and modulated surface (modulation depth $d = \lambda_0$), when the SPW is excited (res). The field was averaged over a laser cycle and the maximum field value (which has negative sign) is plotted. $t \simeq t_{Emax}$.

Target type	$I\lambda_0^2$ W cm$^{-2}\mu m^2$	a_0 -	B_z B_0
res	10^{16}	0.086	0.04
flat	10^{16}	0.086	0.018
res	10^{17}	0.272	0.16
flat	10^{17}	0.272	0.073
res	10^{18}	0.86	0.45
flat	10^{18}	0.86	0.28
res	10^{19}	2.72	1.9
flat	10^{19}	2.72	0.84

maximum value reaches $\sim$ 190MG (for $\lambda_0 = 1\mu$m) at $t \simeq t_{Emax}$ while it is only $\sim$ 90MG for the flat interface.

We also note that, even though an exact comparison is not possible due to the differences in some parameters, in simulations where we use a flat interface we get values of the magnetic field that are of the same order as what is found experimentally in [64] for the interaction of ultra-intense laser pulses with a solid target, and in previous

simulations [79, 62, 7]. A peculiar feature of the flat interface simulations is the appearance, inside the plasma, of filamented structures in the magnetic fields as can be seen in picture 3.7, where the typical size of the filaments is $\sim \lambda_0/6$, similar in size and in the time evolution to filaments observed and discussed by other authors [62, 79]. It is interesting to notice that a fundamental difference in the case when the SPW is excited is the absence of such filaments.

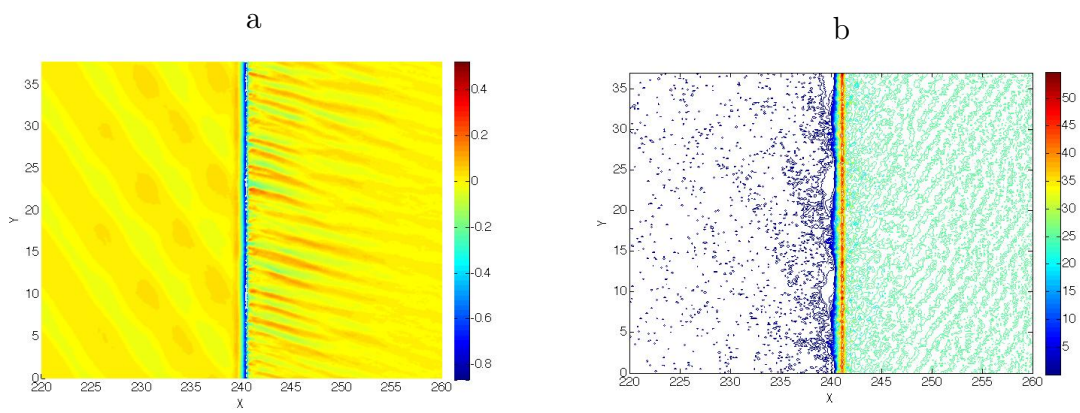

Figure 3.7: Quasi static magnetic field in the xy plane (a) and electron density (b), at $t = 500\omega_0^{-1}$ in the case of a flat surface localized at $x = 240k_0^{-1}$ (no SPW). The laser intensity and the target density were $I\lambda_0^2 = 10^{19}$W cm$^{-2}\mu m^2$ and $n_e = 25n_c$. The magnetic field in units of B_0, the lengths are in units of k_0^{-1}.

This difference can be attributed to the *capability of the strong self-generated magnetic field to partially confine the particles.* In fact we find here that the magnetic field observed when SPW is excited is much larger than what was found when no plasma wave is excited. We shall consider the Larmor radius R_L, in order to estimate the importance of this effect, which in the relativistic regime becomes $R_L = \lambda_0\gamma/(B_z 2\pi)$, where B_z is our normalized magnetic field. If we substitute the values of B_z and γ (see for example the phase space in fig.4.1) found in our PIC simulations in this expression, we find that $R_L \sim \lambda_0$ for the most energetic particles, in the relativistic regime. Since the typical size of the layer where the static magnetic field is present is of the order λ_0, this implies that the magnetic field may confine some particles near the surface, a point that may be important for potential applications.

3.3 Conclusion

In this chapter we have studied the quasi-static magnetic field analytically, with a non-relativistic hydrodynamic model, which is valid in the low intensity range ($I\lambda_0^2 \leq 10^{16}$W cm$^{-2}\mu m^2$). This model shows that the surface wave gives rise to a second order magnetic field proportional to the square of the SPW field E_{sw} and confined nearby the interface, whose strength depends on the electron temperature and density.

At the same time we have analyzed the characteristics of the magnetic field arising during laser-plasma interaction, which is observed in PIC simulation for a wide laser

intensity range ($I\lambda_0^2 = 10^{15} - 7 \times 10^{19}$W cm$^{-2}\mu m^2$), when the SPW is resonantly excited and for the case of a flat target. In simulations where we use a flat interface we observe values of the magnetic field that are of the same order as what is found experimentally in [64], $\sim$ 90MG $\lambda_0/\mu m$ for $I\lambda_0^2 = \times 10^{19}$W cm$^{-2}\mu m^2$, while when the SPW is excited we have $\sim$ 200MG $\lambda_0/\mu m$ for the same laser intensity. For $I\lambda_0^2 = 7 \times 10^{19}$W cm$^{-2}\mu m^2$ the magnetic field exceeds $\sim$ 500MG.

Comparing the model to the PIC simulations performed for a low intensity laser pulse ($I\lambda_0^2 = 10^{15-16}$W cm$^{-2}\mu m^2$), we find that the predicted field has the right order of magnitude (about $\sim$ 1MG$for \lambda_0 = \mu m$) but is systematically smaller than what was found in the simulations. We interpret this as related to kinetic effects and plasma expansion which are found to play an important role and are not taken into account by the model. Nevertheless we notice that in all cases the intensity of the magnetic field is increased by SPW excitation compared to the flat target, even at relativistic intensities. Comparison of the field structure of the flat target and resonant cases suggests that the enhanced field strength has caused partial particle confinement at the target surface when the SPW is present.

Chapter 4

Electron heating

In chapter 2 we have discussed the local amplification field and the enhancement of laser absorption which can be obtained via the resonant excitation of a surface plasma wave (SPW). We will now investigate electron acceleration in presence of a SPW.

As seen in section 1.4 the energy of the laser is transferred to the plasma via electron heating which occurs during the interaction due to different mechanisms. Especially very energetic electrons are generated [34] which are referred as *hot electrons*, i.e. electron having energy much higher than the thermal energy. For high laser intensities ($I\lambda_0^2 > 10^{18}$W cm$^{-2}\mu m^2$) they have relativistic momentum $p_{osc}/m_e c \geq 1$ and energy of the order of the laser ponderomotive energy, that is $U_p = m_e c^2(\langle\gamma\rangle - 1)$ where $\langle\gamma\rangle$ is defined in eq. (1.28).

In general these mechanisms are supposed to produce different angular distributions of the accelerated electrons: for example resonance absorption is expected to produce electrons mainly in the direction of the density gradient $\nabla \mathbf{n_e}$, while $\mathbf{J} \times \mathbf{B}$ and vacuum heating accelerate electrons in the direction perpendicular to the target. Indeed this is only a very schematic description of the electron heating, based on the model presented in section 1.4.2 and many important contributions are not taken into account [19]. For example i) electrons near the target surface will feel the radiation pressure of the laser which adds a component in the direction of pulse propagation ii) the self-generated fields, as the quasi-static magnetic field described in chapter 3 contributes to electron deflection. For these reason the trajectory of an electron may be quite complicated to predict as we will see in the following.

Furthermore the oscillation frequency at which electrons are accelerated depends on the acceleration mechanism. For example in the case of a laser pulse obliquely incident on a flat surface and having high intensity, such that $\mathbf{J} \times \mathbf{B}$ and vacuum heating are present at the same time, electrons would be accelerated by two forces having different oscillation frequencies: ω_0 for the component of the laser field perpendicular to the surface which is associated with vacuum heating and $2\omega_0$ for the $\mathbf{J} \times \mathbf{B}$ term. If instead the laser is normally incident then there will be only $\mathbf{J} \times \mathbf{B}$, which accelerates electrons at a single frequency $2\omega_0$.

In the presence of a surface wave excited at the vacuum-plasma interface, the mechanism of electron heating changes, as the component of the electric field perpendicular to the surface is amplified, as discussed in chapter 2. Moreover the characteristics of

electron acceleration are modified as shown in fig.4.1, where the case of SPW excitation is compared with the flat target case. We observe that when the SPW is excited

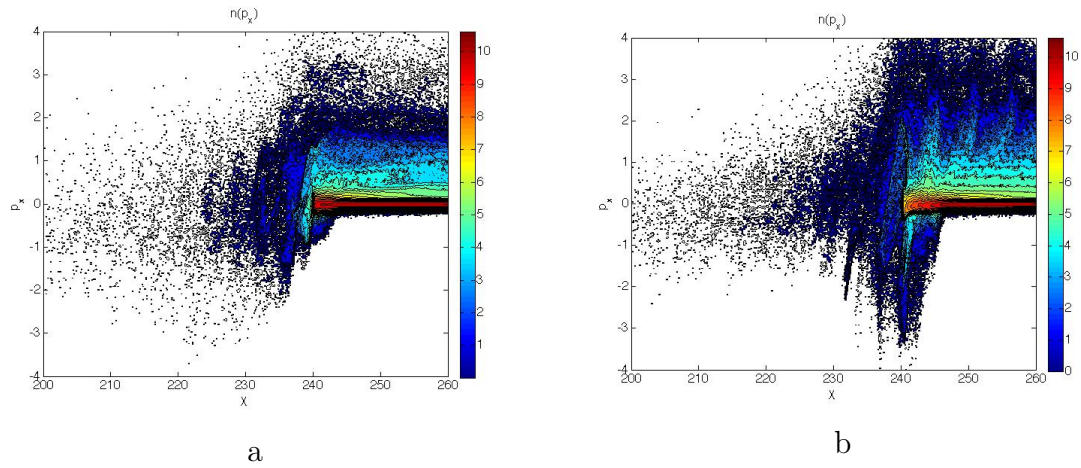

Figure 4.1: Electron (p_x, x) phase space for the flat target (a) and resonant case (where the SPW is excited) (b) at $I\lambda_0^2 = 10^{18}$W cm$^{-2}\mu m^2$. The momentum is normalized to $m_e c$, such that $p_x/m_e c = v_x\gamma(v)$ at $t = 500\omega_0^{-1}$. $n_e = 25n_c$, $d = \lambda_0$, semi-infinite target.

electron bunches are created along the x direction at the frequency of the surface wave $\omega = \omega_0$, while for the flat interface the phase space is smoother as a consequence of the mix of $J \times B$ and vacuum heating, which are characterized by two different frequencies, as mentioned above. Moreover we notice that the hot electrons energy and number rises when the SPW is excited, which can be interpreted as an effect of the field amplification and its local distribution that is observed in simulations (see chapter 2).

In this chapter we will initially study the electron heating for the case of a semi infinite target, comparing the case of the modulated target having resonant incidence with i) the plane target and ii) the case of non-resonant incident angles. Furthermore the dependence on the target modulation depth will be considered which, in section 2.4, was found to be important in order to separate the role of the target shape from the effect of the SPW. Finally, we will see the electron acceleration in the case of a laminar target, where we have electron recirculation and emission from the non-irradiated side.

We shall start by examining the electron energy obtained for different target and laser parameters, then we will analyze in detail the emission angles of the hot electrons which are generated in the laser-plasma interaction. We recall that in the simulations the box size is $6\lambda_0 \simeq 37.7k_0^{-1}$ along the y direction and the plasma starts at $x = 240k_0^{-1}$, which means that the vacuum extension in front of the target is $\simeq 38\lambda_0$. The plasma particles are initially described by a Maxwellian distribution with electron temperature $T_e = 1$keV (thermal velocity $v_{th} = 0.044c$) and ion temperature $T_i = T_e/10$ (here $m_i/m_e = 1836$, where m_i and m_e are the ion and electron mass). The charge of the ions was $Z = 1$. For the modulated target the periodicity is $a_m = 2\lambda_0$, the modulation depth is $d = \lambda_0$ and the initial density, which will be kept constant in the present chapter, is $n_e = 25n_c$. The laser reaches the target surface at $t = 240\omega_0^{-1}$ and its temporal variation is given by a Gaussian envelope, having full width at half maximum

FWHM $= 240\omega_0^{-1}$ (which corresponds to a laser pulse duration of 56 fs for $\lambda_0 = 1\mu m$) and a total length of $\sim 400\omega_0^{-1}$.

4.1 Electron energy

The determination of the number and energy of the electrons which are generated in high energy laser-matter interaction is one of the most important and controversial physics issues [32, 6, 31]. As the absorption depends on various processes (see section 1.4), it is difficult to deduce the scaling law of the hot electron temperature from laser intensity and no consistent analytical model to predict such scaling exists yet [32]. One of the most cited scalings which have been proposed is the *ponderomotive scaling* [33, 6], which was observed to be valid for laser intensities in the range $I\lambda_0^2 = 10^{19}-10^{20}$W cm$^{-2}\mu m^2$. According to this scaling the hot electron temperature is related to the ponderomotive potential defined in (1.46) for linear polarization,

$$T_{hot,pond} = U_p = m_e c^2 \left[\left(1 + \frac{a_0^2}{2} \right)^{1/2} - 1 \right] \tag{4.1}$$

An alternative scaling law which is found in literature is Beg's empirical scaling [31], which was deduced for laser intensities in the range $I\lambda_0^2 = 10^{17} - 10^{19}$W cm$^{-2}\mu m^2$:

$$T_{hot,Beg} = 0.469 m_e c^2 a_0^{2/3}. \tag{4.2}$$

where $m_e c^2 \approx 511$keV.

A model which is valid for any regime has been proposed recently [32] where the average of the electron energy used to obtain (1.46), which was averaged over the laboratory time and gives the ponderomotive scaling (4.1), is replaced by the average over the electron proper time (the phase of the electron oscillating in the wave). According to this model the electron temperature is given by the relation

$$T_{hot,phase} = \left[\frac{\pi}{2K(-a_0^2)} - 1 \right] m_e c^2 \tag{4.3}$$

where $K(-a_0^2)$ is the complete elliptical integral of the first kind. The scaling given by equation (4.3) converges to the ponderomotive scaling for $a_0 \ll 1$.

We will now analyze the electron temperature obtained in our simulations comparing the case of a flat target with the case of the resonant SPW excitation, where we expect to obtain higher temperatures than the ones predicted for the laser field alone, as a consequence of the enhanced intensity of the field at the surface (by a factor η, as discussed in 2.1.1) and of its localized spatial distribution.

In this section we will consider the case of the semi-infinite target (where electrons reaching the right side of the target are cooled and reintroduced into the plasma at the initial thermal velocity), in order to exclude effects coming from electron recirculation [21] in the target which will be treated in section 4.3. This means that the measured

temperature corresponds only to the hot electrons which have not yet reached the unirradiated plasma boundary, so that their energy is related to the actual intensity of the fields at the surface. Relativistic electrons would reach the right side in few ($\sim$ 10) laser cycles and, being cooled, they will not contribute to the hot electron energy measured at later times.

We will take $t = 500\omega_0^{-1}$ as the reference time for the electron temperature estimate. This corresponds approximately to the time for which the maximum electron energy has been reached in all the simulations. The results for the case where the SPW is excited on the modulated target (corresponding to the laser pulse angle of incidence $\theta = 30°$ with the present target parameters) and flat target are summarized in table 4.1 for different laser intensities, while the values predicted by the three models presented above are reported in tab.4.2, for the same intensity values.

We note again that the electron temperature in the case of a semi-infinite target is given by the electrons which have not reached yet the right boundary, where electrons are cooled. Thus we are considering only the electrons which are accelerated within few laser periods around $t = 500\omega_0^{-1}$ and the energy of these electrons is strictly related to the accelerating field at that time.

Table 4.1: Electron energy as a function of the laser intensity, for the semi-infinite target with $d = \lambda_0$. Two target types are considered: one having modulated surface such to resonantly excite the SPW (res) and one having flat surface (flat). $a_0 = \frac{eE_0}{m_e c\omega}$.

Target type	$I\lambda_0^2$ W cm$^{-2}\mu m^2$	a_0 -	T_{cold} keV	T_{hot} keV	E_{max} keV
res	10^{16}	0.086	1.7	40	140
flat	10^{16}	0.086	1	33	90
res	10^{17}	0.272	1.3	62	500
flat	10^{17}	0.272	1	38	320
res	10^{18}	0.86	3.71	820	2400
flat	10^{18}	0.86	5	168	1700
res	10^{19}	2.72	54	1900	13000
flat	10^{19}	2.72	38	860	6500

The temperatures, T_{cold}, T_{hot} and the energy E_{max}, in tab.4.1 are obtained from the electron spectra where two quasi-exponential slopes are observed, as reproduced in pictures 4.2. The energy of the electrons is shown for the flat and resonant target at $I\lambda_0^2 = 10^{16}$W cm$^{-2}\mu m^2$ and $I\lambda_0^2 = 10^{19}$W cm$^{-2}\mu m^2$. T_{cold} and T_{hot} are derived from the plot of $\ln(n_e)$ versus the electron energy E, assuming (as is commonly done in laser-matter interaction theory [32, 6, 31]) that the electrons have a distribution

function of the form $n_e(E) = exp(-E/k_B T_e)$. In fact, we observe two main electron populations having different exponential slopes, that we associate with a population of 'cold' electrons, which have gained less energy during the interaction (T_{cold}) and 'hot' electrons, which have been efficiently heated and have gained a considerable amount of energy (T_{hot}). In tab.4.1 we also report the cut-off energy (E_{max}), i.e. the maximum energy that a single electron can acquire, which is important in order to compare with the maximum SPW amplitude. It has to be noted that it is not intended as a temperature in the thermodynamic sense since, during the laser-plasma interaction, the situation is non-equilibrium and the mean electron flow velocity is non-zero.

We notice that the hot electron temperature for the flat target has a magnitude comparable to the scalings above (equations 4.1,4.2, 4.3 and tab.4.2), particularly to the empirical Beg's scaling, even if none of them reproduces the complete range of values found in the simulations. This is not surprising as relations 4.1, 4.2 and 4.3 were deduced for a laminar target and a laser pulse having a finite transversal profile, and these parameters may affect the electron temperature as it will be discussed in section 4.3 and 6.2 respectively.

We can observe the enhancement of the electron heating in the case where the surface wave is present compared to the flat target. The temperature increase is consistent with the amplification of the electric field reported in section 2.1.1 and it is generally more evident in the relativistic intensity range $a_0 \geq 1$. Comparing with equations 4.2 and 4.1, if we use the Beg's scaling and we consider the correction due to field amplification, the temperature should increase by a factor $\eta^{2/3}$ when the SPW is excited compared to the flat surface while for the ponderomotive scaling we would have an increase by a factor $\sim \eta^2$ in the low intensity regime and $\sim \eta$ in the relativistic regime. However we notice again that none of these scalings fits our electron temperature values: for example at $I\lambda_0^2 = 10^{19}$W cm$^{-2}\mu m^2$, taking the flat surface value of $T_{hot,flat} = 860$keV and $\eta = 4.2$, we expect $T_{hot,res} \simeq 2.17$MeV from the Beg's scaling and $T_{hot,flat} = 3.6$MeV

Table 4.2: Electron energy as a function of the laser intensity calculated from the scalings in equations 4.1 (ponderomotive scaling), 4.2 (Beg's scaling) and 4.3 (model including the electron phase). $a_0 = \frac{eE_0}{m_e c\omega}$.

$I\lambda^2$	a_0	$T_{hot,pond}$	$T_{hot,Beg}$	$T_{hot,phase}$
W cm$^{-2}\mu m^2$	-	keV	keV	keV
10^{16}	0.086	1	46	1
10^{17}	0.272	9.4	100	9.5
10^{18}	0.86	162	216	84
10^{19}	2.72	594	466	460

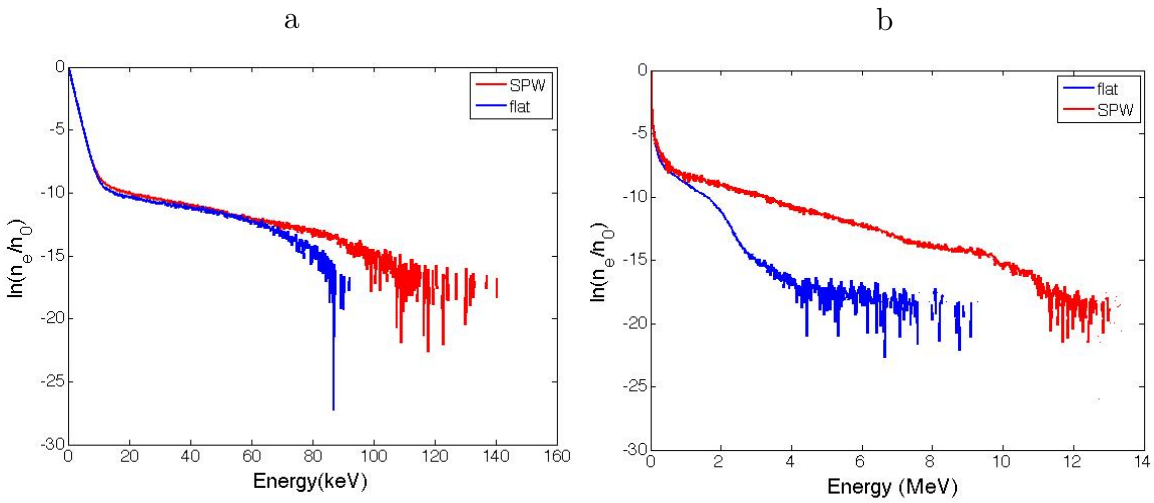

Figure 4.2: Electron spectra for the flat target (BLUE) and resonant (RED) case $I\lambda_0^2 = 10^{16}$W cm$^{-2}\mu m^2$ (a) and $I\lambda_0^2 = 10^{19}$W cm$^{-2}\mu m^2$ (b). The target is semi-infinite and $d = \lambda_0$.

from the ponderomotive scaling, when the SPW is present. It is important to consider that the spatial form of the field also gives a contribution (discussed also in chapter 2) which is difficult to include in the temperature estimate. Moreover, as we will see in the following, when the SPW is excited we have electron acceleration along the surface, which is not taken into account in these models. We note that the maximum relative enhancement, i.e. $T_{hot,res}/T_{hot,flat}$ is obtained for 10^{18}W cm$^{-2}\mu m^2$ that corresponds to the intensity for which we found the maximum damping of the wave (see section 2.1.2). This tends to confirm the assumption made in chapter 2, according to which the growth of the SPW amplitude is damped by the transfer of energy from the wave to the electrons. We also notice that the cold electron temperature is increases rapidly, growing from 1keV up to some tens of keV from $t = 240\omega_0^{-1}$ to $t = 500\omega_0^{-1}$.

4.1.1 Non-resonant angles

In order to separate the role of the target geometry from the effective contribution due to the resonant excitation of a SPW, electron heating in the case of non-resonant grating shall be studied. This will be done using the same procedure as in section 2.3, i.e. considering different angle of incidences while keeping the target parameter constant (semi-infinite, $d = \lambda_0$, $n_e = 25n_c$, $a_m = 2\lambda_0$, which match the resonance for 30°). We will analyze two different regimes, taking the simulation having the laser intensity $I\lambda_0^2 = 10^{16}$W cm$^{-2}\mu m^2$, as representative of the low intensity case, while the simulation at $I\lambda_0^2 = 10^{19}$W cm$^{-2}\mu m^2$ will represent the high intensity regime.

In fig.4.3 the electron energy distribution is shown for three angle of incidences: $\theta = 10°, 20°, 30°$, where 10° and 20° are non-resonant angles, as said before.

We found that for the *low intensity case* $T_{hot,20}$ and $T_{hot,10}$ are both higher than

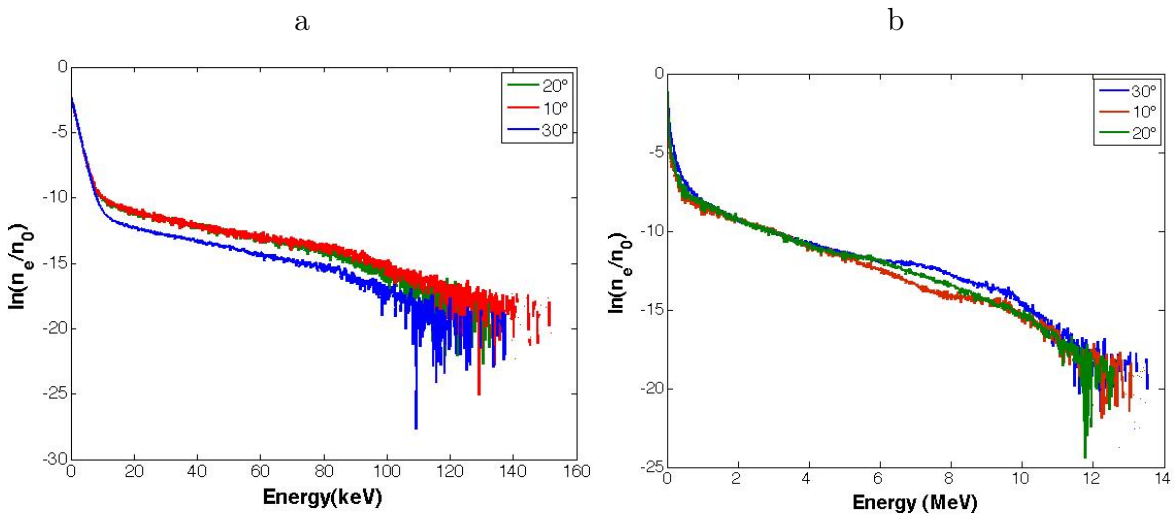

Figure 4.3: Electron spectra for different angle of incidences, $\theta = 10°, 20°, 30°$, for the semi-infinite target where $d = \lambda_0$. The resonant incidence is $\theta = 30°$ and the intensity is $I\lambda_0^2 = 10^{16}$W cm$^{-2}\mu m^2$ (a) and $I\lambda_0^2 = 10^{19}$W cm$^{-2}\mu m^2$ (b). $t = 500\omega_0^{-1}$.

$T_{hot,res}$, but the difference is only few keV: $T_{hot,20} \simeq T_{hot,10} \sim 47$keV. The maximum electron energy E_{max} is increased for the smallest angle of incidenceto $E_{max,10} \simeq 150$keV while for $\theta = 20°$ the maximum energy is approximately the same as found for the resonant case $E_{max,20} \simeq E_{max,res} \simeq 140$keV. We note that the values of T_{hot} for $I\lambda_0^2 = 10^{16}$W cm$^{-2}\mu m^2$ do not match exactly the trend of laser absorption discussed in section2.3. We recall that the absorption percents were 68%, 60% and 54% for $\theta = 30°$ (resonant incidence), 20° and 10°. Thus the higher absorption observed for the two non-resonant laser angle of incidences can be related to the fact that $T_{hot,10}$ and $T_{hot,20}$ are greater than $T_{hot,res}$ but, at the same time, the hot electron temperature for $\theta = 10°$ and $\theta = 20°$ is essentially the same while we found that the absorption for $\theta = 10°$ is higher (68%) than for $\theta = 20°$ (60%). Contrastingly we notice that the relation between the values of the maximum electron temperature, $E_{max,20} \simeq E_{max,res} < E_{max,10}$, can be related to the fact that the absorption for $\theta = 10°$ is higher than for $\theta = 20°$ but it appears in disagreement with the fact that the absorption for the resonant case ($\theta = 30°$) is lower than for the case having $\theta = 20°$. In general we may conclude that for the low intensity case the mean hot electron energy and the maximum energy are both important to determine the final absorption and in general it is difficult to establish a precise relation between the trend of the electron temperature and the laser absorption. However we notice that the electron temperature taken at a given time does not represent the total absorption process: other effects may contribute to the final result such as damping of the electron energy due to ion acceleration.

For the *high intensity case*, corresponding to the spectra in fig.4.3b), we obtain approximately the same hot electron temperature for the three angles: $T_{hot,20} \simeq T_{hot,10} \simeq T_{hot,res} \simeq 2$MeV. The maximum electron energy instead is similar for resonance incidence ($\theta = 30°$) and $\theta = 10°$, as $E_{max,10} \simeq E_{max,res} \sim 13$MeV, while for $\theta = 20°$ the

Table 4.3: Electron energy as a function of the laser intensity, for the semi-infinite target with $d = \lambda_0$. Three angle of incidences are considered $\theta = 10°, 20°, 30°$, where $10°$ and $20°$ are non-resonant angles. $a_0 = \frac{eE_0}{m_e c\omega}$.

θ	$I\lambda_0^2$	a_0	T_{cold}	T_{hot}	E_{max}
degree	W cm$^{-2}\mu m^2$	-	keV	keV	keV
10	10^{16}	0.086	1.6	47	150
20	10^{16}	0.086	1.6	47	140
30	10^{16}	0.086	1.7	40	140
10	10^{19}	2.72	47	2000	13000
20	10^{19}	2.72	38	2000	12000
30	10^{19}	2.72	54	2000	13000

maximum energy decreases to $E_{max,20} \simeq 12$MeV.

Comparing with the absorption values reported in section 2.3 we notice that, also for this intensity range, the dependence of the hot electron temperature T_{hot} on the angle of incidences does not correspond exactly to the associated laser absorption. In fact we recall that at $I\lambda_0^2 = 10^{19}$W cm$^{-2}\mu m^2$ the absorption is 60% for the angle of incidence $\theta = 20°$ and 75% for $\theta = 30°$ (i.e. the resonant angle of incidence), while here we observe a similar hot electron temperature in the two cases. Contrastingly we notice that the cut-off energy has the same trend as the absorption values: the relation between the maximum electron temperatures is $E_{max,10} \simeq E_{max,res} < E_{max,20}$ which can be associated with the fact that the absorption is approximately the same for $\theta = 10°$ (72%) and the resonant incidence (75%), while it is lower at $\theta = 20°$ (60%). We may infer that for high intensity ($I\lambda_0^2 = 10^{19}$W cm$^{-2}\mu m^2$) the most important data to consider in the comparison with laser absorption is the maximum electron energy. This suggests that the most energetic electrons play the dominant role in the absorption process for this regime: in fact, as discussed in section 2.3, these electrons may have an excursion length large enough to escape the electric field at the target surface and to be absorbed in the plasma bulk.

4.1.2 Modulation depth

In 2.4 we have examined the effect of the depth of the modulation on the absorption mechanism and the SPW excitation. The results of this study suggested that this parameter plays an important role in the absorption of the laser energy and in the damping of the wave. Especially we observed that decreasing the modulation depth to sub-λ values allows to separate the effects associated with the target geometry from those due to SPW excitation.

We will now investigate the effect of the modulation depth on the electron heating, by reducing the modulation depth from $d = \lambda_0$ to $d = \lambda_0/5$. We will again analyze two

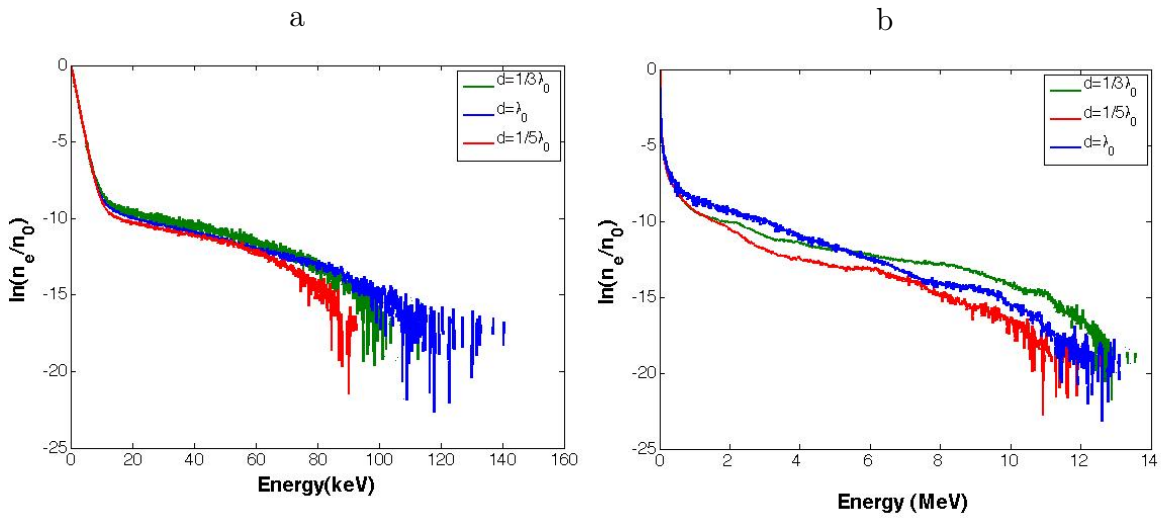

Figure 4.4: Electron spectra for different modulation depths, for the semi-infinite target at the resonant angle of incidence $\theta = 30°$. The intensity was $I\lambda_0^2 = 10^{16}$W cm$^{-2}\mu m^2$ (a) and $I\lambda_0^2 = 10^{19}$W cm$^{-2}\mu m^2$ (b). $t = 500\omega_0^{-1}$

different regimes: the simulations having laser intensity $I\lambda_0^2 = 10^{16}$W cm$^{-2}\mu m^2$, will represent the low intensity regime, those with laser intensity $I\lambda_0^2 = 10^{19}$W cm$^{-2}\mu m^2$ will represent the high intensity regime. In fig.4.4 we show the electron energy distribution for three values of the modulation depth $d = \lambda_0$, $\lambda_0/3$ and $\lambda_0/5$.

For $I\lambda_0^2 = 10^{16}$W cm$^{-2}\mu m^2$ the hot electron temperature found for varying modulation depths are $T_{hot,\lambda_0/3} \simeq 37$keV and $T_{hot,\lambda_0/5} \simeq 34$keV. These values are lower than the value obtained for $d = \lambda_0$ and larger than the flat target value, as shown in tab.4.1 and we observe that by reducing the target depth we get close to the flat target value. Similarly the maximum electron energy decreases for decreasing d and we have $E_{max,\lambda_0/3} = 100$keV and $E_{max,\lambda_0/5} = 90$keV. The reduction of the hot electron temperature and cut-off energy is consistent with the values of absorption and field amplification presented in 2.4, where we found that both absorption and amplification decreases for decreasing d: *assuming that the hot electron temperature is given by the overall process of absorption, which includes different mechanisms* (resonant absorption, vacuum heating , $J \times B$) *while the cut-off is associated with the enhanced heating via SPW*, we can interpret the lower T_{hot} as the result of the general decrease of the absorption while the lower E_{max} can be interpreted as a lowered efficiency of heating via SPW. The latter may be explained in terms of the density gradient scale length which, for $d \lesssim \lambda_0$, becomes larger than the modulation depth at $I\lambda_0^2 = 10^{16}$W cm$^{-2}\mu m^2$, as discussed in 2.4.

For $I\lambda_0^2 = 10^{19}$W cm$^{-2}\mu m^2$ the hot electron temperatures found for varying modulation depths are $T_{hot,\lambda_0/3} \simeq 2.1$MeV and $T_{hot,\lambda_0/5} \simeq 1.7$MeV. The maximum energy is approximately the same for the three values of d and we have $E_{max,\lambda_0/3} \simeq E_{max,\lambda_0/5} \simeq$ 13MeV. *Applying the argument used above, according to which the cut-off is associated with SPW excitation, we can infer that the effects of the SPW in this regime are*

dominant for the three values of d. This can be explained by considering that for $I\lambda_0^2 = 10^{19}$W cm$^{-2}\mu m^2$ the density gradient scale length is $< 0.2\lambda_0$ and weakly affects the driving SPW field.

We notice that the target with modulation depth $d = \lambda_0/3$ corresponds to the higher number of electrons accelerated in the high energy range, even more than the case at $d = \lambda_0$. This is in agreement with the interpretation of laser absorption data given in 2.4, according to which this value of d is large enough to avoid the effects of the density gradient scale length in the high intensity regime and small enough to reduce the effects of target geometry, enhancing the effects of the SPW resonance.

For this reason we will conclude this analysis by comparing the electron energies for the non-resonant angle of incidence $\theta = 10°$ with the resonant case when the modulation depth is $d = \lambda_0/3$. We observe in fig.4.5 that the electron temperature is higher for the resonant case, being $T_{hot,\lambda_0/3} \simeq 2.1$MeV, while for $\theta = 10°$ we have only $T_{hot,\lambda_0/3,10} \simeq 1.2$MeV. Also the maximum electron energy is lower for the non-resonant incidence as we have $E_{max,\lambda_0/3,10} \simeq 12$MeV for $\theta = 10°$ (instead of 13MeV for the resonant angle of incidence $\theta = 30°$). These values are consistent with those of laser absorption and field

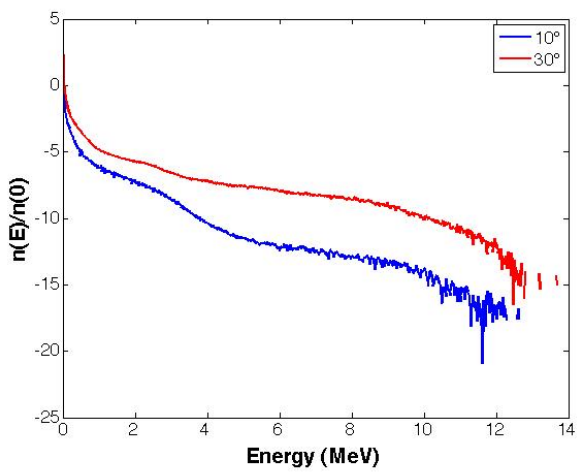

Figure 4.5: Electron spectra for the semi-infinite targets having modulation depth $d = \lambda_0/3$, taken at time $t = 500\omega_0^{-1}$ for $I\lambda_0^2 = 10^{19}$W cm$^{-2}\mu m^2$. The red/blue line correspond to the resonant/non-resonant ($\theta = 10°$) cases.

amplification reported in section 2.4, where we find that for $d = \lambda_0/3$ the absorption is increased for the resonant case compared to non-resonant incidence.

In conclusion, the analysis of the dependence of electron heating on the modulation depth has confirmed the importance of the presence of a density gradient in the process of hot electron heating via SPW. *In the low laser intensity range, where the gradient scale length becomes larger than the modulation depth at $d \simeq \lambda_0$, the electron acceleration is affected and low cut-off energies are found. In this case, the effects of the target geometry are dominant and we observe that the contribution of SPW to the electron energy is small. Contrastingly, in the high intensity range, where the laser steepens*

the density gradient, electrons are efficiently accelerated via SPW for smaller values of d. Moreover, as the reduced modulation depth reduces the contributions of the other heating mechanisms, the effects of SPW excitation are emphasized.

In order to better understand the process of electron heating via SPW excitation we will analyze in the following section the electron current and the emission angles.

4.2 Electron emission angles

In this section we will examine the electron emission angles for the case of resonant excitation and the case of a flat surface. We are particularly interested in the angular distribution of the most energetic electrons, which, in the resonant case, may be associated with the SPW excitation. Similarly to the previous section we will consider the case of a semi-infinite target (where the electrons reaching the right side of the target are cooled and reintroduced into the plasma), in order to exclude effects due to electron recirculation [21] in the target which will be treated in section 4.3.

We will define the x axis direction ($\hat{x}$) as the 'forward' direction, that corresponds to electrons moving towards the plasma, while the backward direction will be that of electrons moving towards the vacuum ($-\hat{x}$), away from the plasma. The positive angles correspond to a positive y component of electron velocity, such that 90 degree represents the motion parallel to the y axis, positive direction, as shown in the scheme of fig.4.6. *We remark that, in the present geometry, the resonant laser incidence corresponds to* $-30°$ *in the forward direction.*

In the following we will analyze two different acceleration regimes, taking the simulation having laser intensity $I\lambda_0^2 = 10^{16}$W cm$^{-2}\mu m^2$ as representative of the low intensity case, while the simulation at $I\lambda_0^2 = 10^{19}$W cm$^{-2}\mu m^2$ will represent the high intensity regime. In order to distinguish the hot electron emission angles from the cold background electrons, we will plot the electron density in the angle-energy space and consider the eventual peaks in the angular distribution. This analysis is performed using the electron momentum phase space (p_x, p_y) (integrated over the space), which allows to determine the angular direction and energy of particles.

We note that, generally, *the angular distribution of the electrons accelerated towards the vacuum is phase dependent, as it represents electrons oscillating in the field at the surface. By contrast, that of electrons moving forward, into the plasma, represents, at the same time, many phases of the acceleration, where the most energetic electrons have definitely left the field at the surface. For this reason the latter is more important to determine the emission angles which characterizes the electron heating process while the emission towards the vacuum has to be analyzed further, by examining the electron currents at different times.*

We will take the time $t = 500\omega_0^{-1}$ as the reference time for the study of the emission angles, which is the same reference time as taken for the electron energy analysis in the previous section. We also recall that $t = 500\omega_0^{-1}$ corresponds approximately to the time at which the maximum electron energy has been reached in our simulations.

We shall start by examining the emission in the low intensity regime, when $I\lambda_0^2 = 10^{16}$W cm$^{-2}\mu m^2$. For the *low intensity, at resonant incidence*, the angular distribution

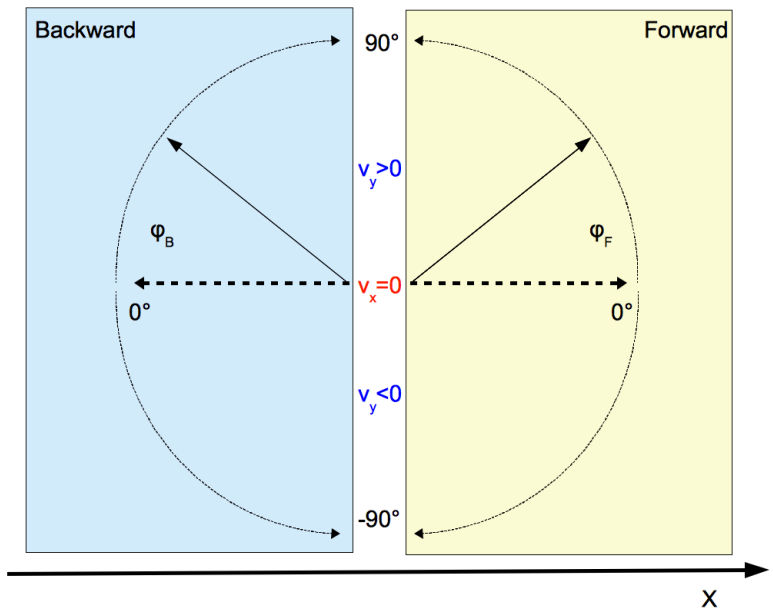

Figure 4.6: Scheme of the electron emission angles: φ_F correspond to the 'forward' emission, φ_B corresponds to the 'backward' emission. Positive/negative angles corresponds to positive/negative $\mathbf{v}_y$.

is shown in fig.4.7a,b. Observing the plot in fig.4.7a we may distinguish three main emission angles corresponding to the forward direction: an angle around 30°, one around $60°$ and one around -60°. A smaller peak is also observed around $-20°$. Fewer energetic electrons are moving in the backward direction, i.e. towards the vacuum (fig.4.7b), and their motion is quasi-parallel to the y axis (positive and negative direction), with a minor accumulation at -40°. The (p_x, p_y) phase space from which we have derived the two plots is shown in fig.4.7c.

The interpretation of the electron angular distribution described above is not obvious. Nevertheless we notice that some of the features in fig.4.7 can be related to the geometry of the target and to the SPW excitation. In fact we note that, when the target has a modulation, we may take the tangent to the modulation curve to approximate the direction parallel to the target surface, as discussed in 2.3 (see fig.2.7), that is $\theta_T = \pm 30°$, for the modulation depth $d = \lambda_0$ and the periodicity $a_m = 2\lambda_0$ (and $\pm 60°$ corresponds to the direction normal to the surface in our geometry). Thus, for the modulated target considered here, the accumulation of the electrons around $\pm 60°$ may be associated with electron emission perpendicular to the surface, while the $30°$ may be seen as emission along the target surface.

Before discussing the interpretation of electron acceleration in these directions, we will consider the *case of the flat target*, for the same pulse intensity and angle of incidence. The angular directions for the flat target are shown in fig.4.8. We observe that, as for the resonant case, the electrons moving forward (fig.4.8a) are accelerated along the normal to the surface, i.e. $\sim 0°$ for this target shape. Electrons emitted into the

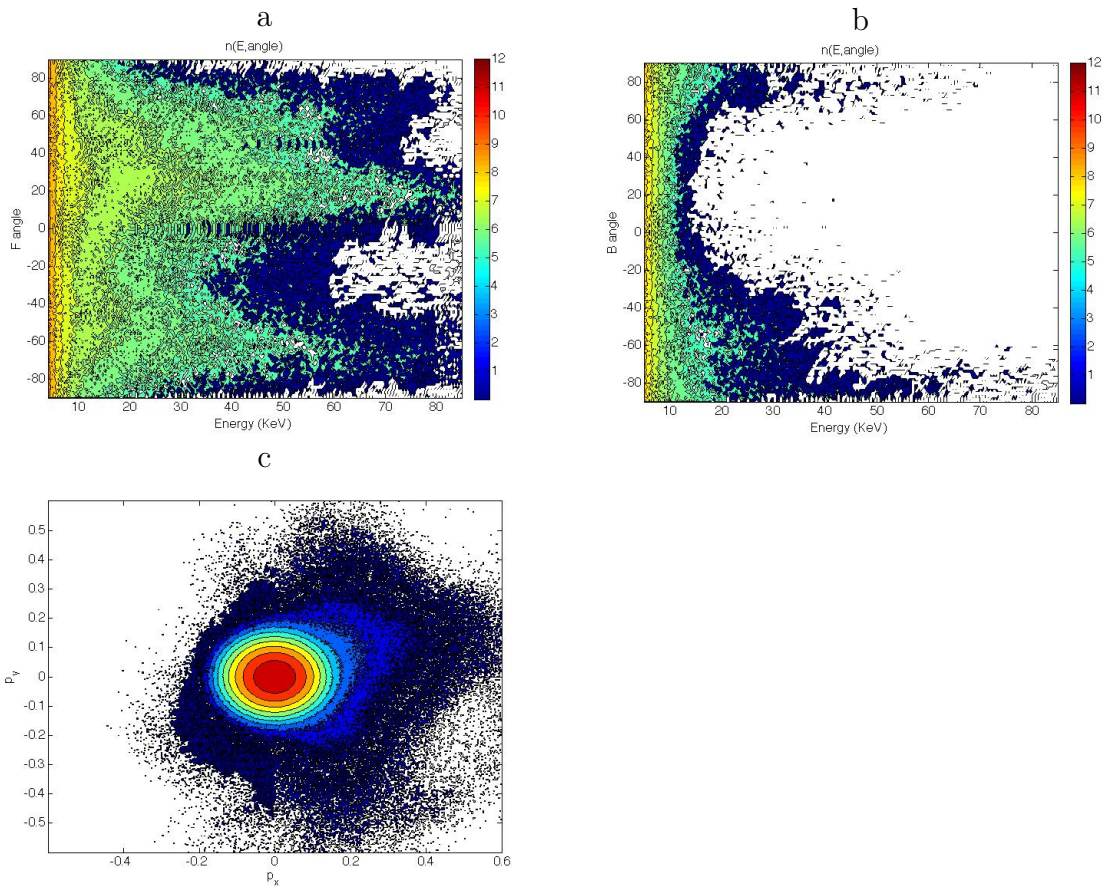

Figure 4.7: Electron emission angles as a function of energy: forward (a) and backward (b) direction and electron phase space (c) at $t = 500\omega_0^{-1}$ for $I\lambda_0^2 = 10^{16}$W cm$^{-2}\mu m^2$ ($a_0 = 0.086$), $d = \lambda_0$, for the semi-infinite target **when the SPW is excited**.

vacuum instead have angular direction $-20°$ (fig.4.8b).

Thus, taking into account the dependence on the geometry of the target, we notice that in both cases (when the SPW is excited and for a flat target) we observe forward acceleration in the direction normal to the target surface which can be attributed to resonance absorption and/or to the vacuum heating mechanisms. Contrastingly, the acceleration along the surface is present only in the case where the SPW is excited, and can be interpreted as electrons moving with the surface wave. For the electrons emitted into the vacuum instead, the interpretation is much more difficult. For the simple case of the flat target we may infer that the angular direction $-20°$ is related to the reflected pulse direction and/or to self generated fields at the target surface. For the resonant case instead, the phase of the field at the surface is very important as we will see when electron currents will be examined.

We will now analyze the emission in the high intensity regime, i.e. for $I\lambda_0^2 = 10^{19}$W cm$^{-2}\mu m^2$. For the *high intensity, when the SPW is excited* (fig.4.9), we find three main angles in the forward direction (fig.4.9a) at $t = 500\omega_0^{-1}$: a main emission angle at about -60°, a secondary angle at -30° and a positive angle around $30 - 40^o$,

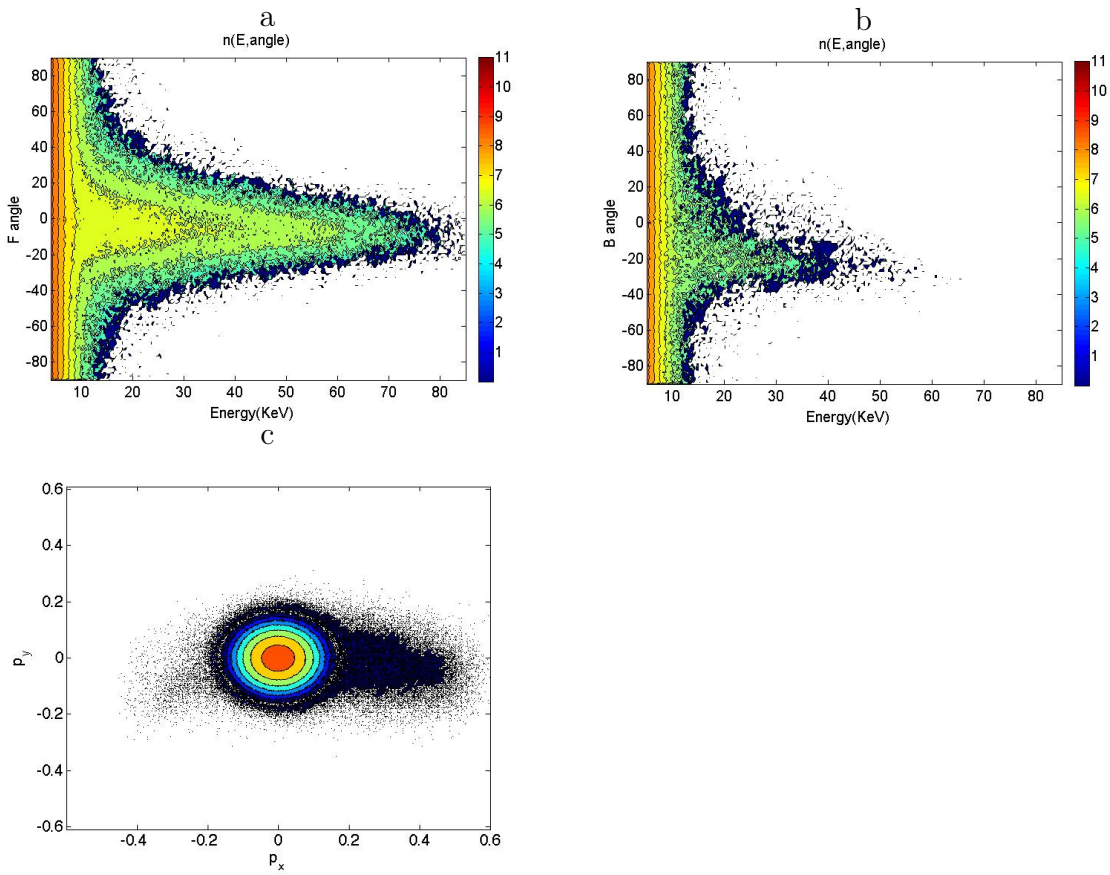

Figure 4.8: Electron emission angles as a function of energy: forward (a) and backward (b) direction and electron phase space (c) at $t = 500\omega_0^{-1}$. $I\lambda_0^2 = 10^{16}$W cm$^{-2}\mu m^2$ ($a_0 = 0.086$), $d = \lambda_0$, $n_e = 25n_c$, semi-infinite target **for the flat surface**.

eventually merging with a peak at 60°. Fewer energetic electrons are accelerated in the backward direction (fig.4.9b) with an accumulation around 60°. We also notice that a large number of hot electrons is accelerated in the direction $-\hat{y}$ (corresponding here to $-90°$), which is the direction of propagation of the surface wave.

For the *flat surface and high pulse intensity case*, the angular distribution of electrons accelerated in the forward direction (fig.4.10a), ranges from 30° to -70°. The angle at which the most energetic particles are emitted is around -20°, followed by two accumulations around -40° and -60°. In the backward direction (fig.4.10b) instead electrons are emitted in the direction parallel to the target surface ($-\hat{y}$ direction) and (very few) in the direction perpendicular to the surface (0°). Comparing the emission in the forward direction for the flat target case in the low (fig.4.8) and high (fig.4.10) intensity regimes, we notice that the emission peak has moved from 0° (at $I\lambda_0^2 = 10^{16}$W cm$^{-2}\mu m^2$) to 20° (at $I\lambda_0^2 = 10^{19}$W cm$^{-2}\mu m^2$). As at $I\lambda_0^2 = 10^{19}$W cm$^{-2}\mu m^2$ vacuum heating is dominant, this fact may appear as a contradiction with the classical vacuum heating scheme, where electrons are supposed to move in the direction perpendicular to the target for any laser intensity. Indeed the shift in the angular direction of electrons accelerated forward may be explained by considering the contribution of the laser pres-

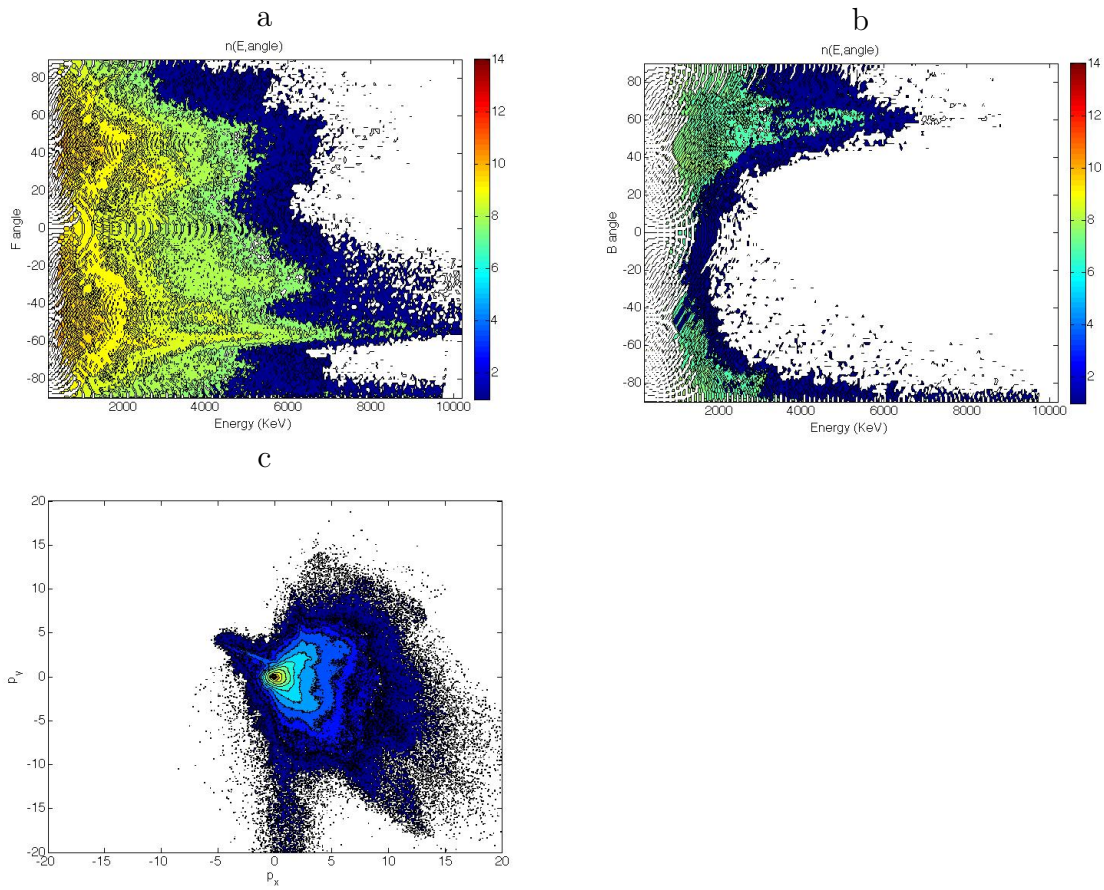

Figure 4.9: Electron emission angles as a function of energy: forward (a) and backward (b) direction and electron phase space (c) for $I\lambda_0^2 = 10^{19}$W cm$^{-2}\mu m^2$ ($a_0 = 2.72$), at $t = 500\omega_0^{-1}$, **when the SPW is excited**. $n_e = 25n_c$, semi-infinite target, $d = \lambda_0$.

sure and self-generated fields at the target surface, as discussed at the beginning of this chapter and in reference [19]. The final direction of electrons entering the plasma bulk is difficult to determine but some prediction can be done on the basis of momentum and energy conservation. According to the model in appendix .3, the direction of the particles emitted in the forward direction depends also on the intensity of the driving field such that their direction tends to be close to the target (surface) normal for low energies while it becomes closer to the laser wave vector direction for increasing laser energies. Basically we have to consider that, when the laser pulse is absorbed, its momentum is also absorbed by the plasma particles which, for high pulse energy, will be accelerated in a direction close to that of laser propagation. As the laser incidence is $-30°$ here, this model would explain qualitatively the shift observed when the laser intensity is increased and the emission angle 20°, observed for the flat target at $I\lambda_0^2 = 10^{19}$W cm$^{-2}\mu m^2$ can be associated with the laser pulse incidence.

We shall now reconsider the flat and resonant target cases in the high intensity regime taking into account the dependence on the geometry of the target, as done for the simulations in the low energy range, and considering the angular shift occurring in

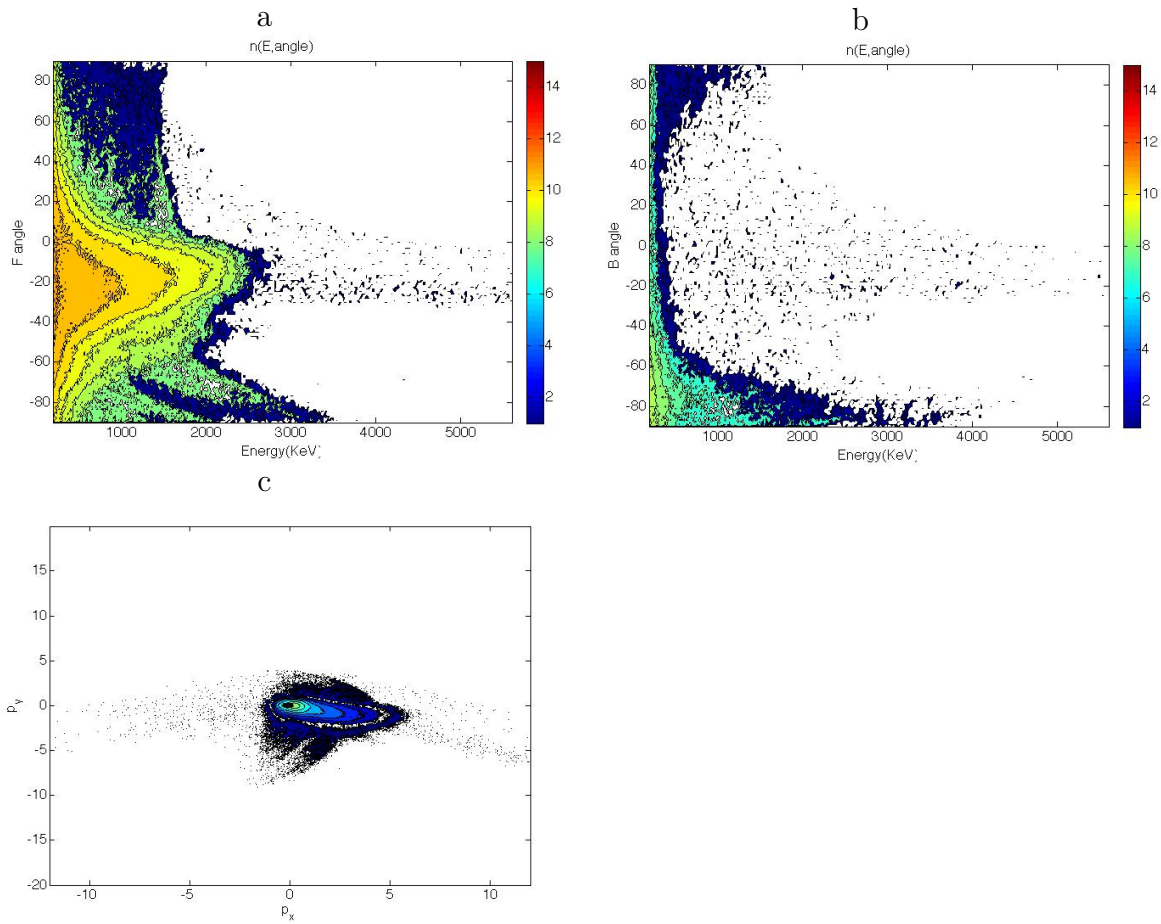

Figure 4.10: Electron emission angles as a function of energy: forward (a) and backward (b) direction and electron phase space at $t = 500\omega_0^{-1}$ for $I\lambda_0^2 = 10^{19}$W cm$^{-2}\mu m^2$ ($a_0 = 2.72$), $n_e = 25n_c$, semi-infinite target **for the flat surface**.

this regime. If we exclude angular directions which can be associated with the laser incidence or the respective target normal direction, that are present in both the flat and modulated targets, we may observe that when the SPW is excited much more energetic electrons are accelerated along the target surface ($\pm 30°$), both in the forward and backward direction, and in the direction of propagation of the wave ($-\hat{y}$). The latter effect was found also for SPW excitation at low intensity but it is more pronounced in this regime where the negative emission angles are associated with the greater electron energies.

In conclusion, the analysis of the angular distribution of the electrons accelerated when the SPW is excited and for a flat target shows that the direction of electron emission partially depends on the geometry of the target and on the laser incidence. Nevertheless, in the case where the SPW is excited, we observe very energetic electrons accelerated in the direction of propagation of the wave ($-\hat{y}$) which are not observed for the flat surface and this is particularly evident in the high intensity regime.

As announced since the beginning of this section, the study of the phase space at a given time is not sufficient to analyze electron motion, particularly the motion of electrons which oscillate at the vacuum-plasma interface. For this reason it will be necessary to compare the emission angle plots with the **electron current vector plots** of fig.4.11 ($I\lambda_0^2 = 10^{16}$W cm$^{-2}\mu m^2$) and fig.4.13 ($I\lambda_0^2 = 10^{19}$W cm$^{-2}\mu m^2$), taken for different time fractions of the laser period, in order to identify the different contributions, their localization and the dependence on the field phase.

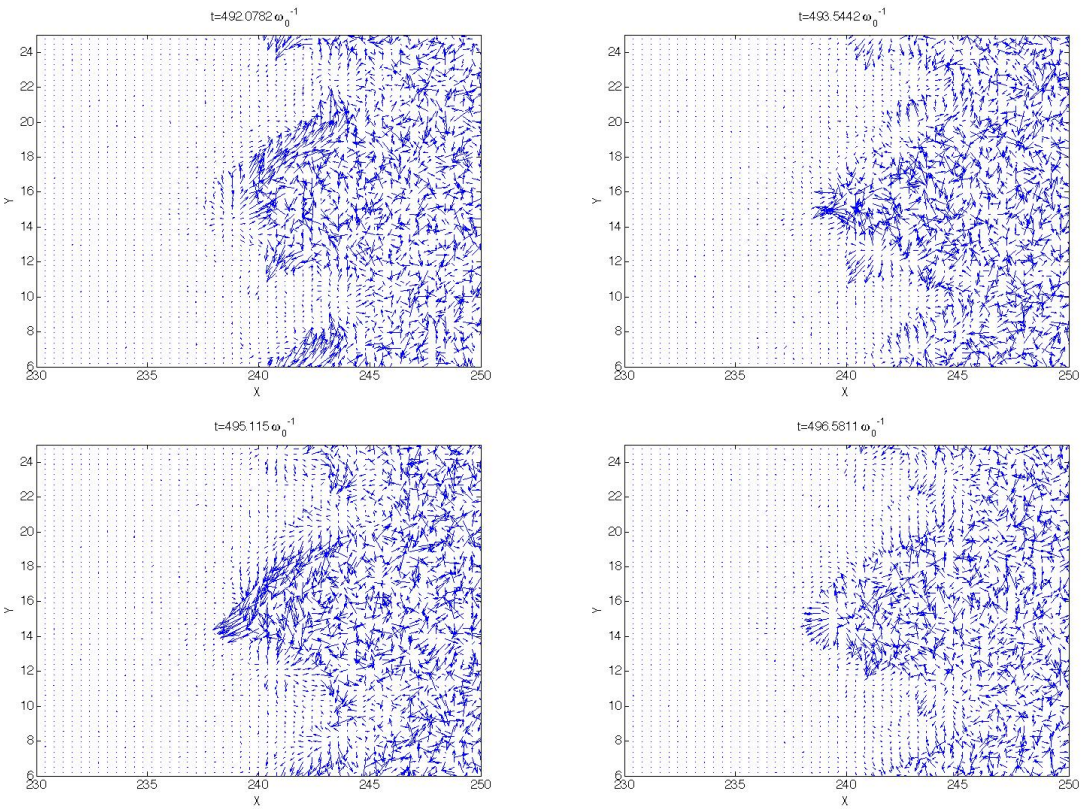

Figure 4.11: Electron current ($n_e v_e$, no charge sign) sequential vector plots taken at time intervals of $1.5\omega_0^{-1}$ ($\simeq 1/4$ laser period), starting from $t = 492\omega_0^{-1}$. $I\lambda_0^2 = 10^{16}$W cm$^{-2}\mu m^2$ ($a_0 = 0.086$), $d = \lambda_0$, $n_e = 25n_c$, semi-infinite target **when the SPW is excited**.

It has to be noticed that the current distribution is, at each point, the result of the contributions of all particles related to that space grid point and this means that a hot electron passing through the bulk thermal plasma may not be visible here. The electron current gives different informations compared to electron phase space, where each particle momentum is represented in the (p_x, p_y) space, thus we do not expect exact correspondence of the two plots. In figure 4.11 we observe a current of hot electrons which periodically exit the plasma, in a direction which is about normal to the target surface, at two main points situated on the lower part of each modulation tip, one close to the top and the other halfway between the top and the bottom (*i.e.* at a distance of $a_m/4 = \lambda_0/2$ from the top). We also observe a current of electrons inside

the plasma, moving along the target surface. In fig.4.11 we show the main steps of electron emission for $I\lambda_0^2 = 10^{16}$W cm$^{-2}\mu m^2$: the electron bunches mentioned above exit the plasma with a periodicity of one laser period, if we consider the emission from a given point, but there is a one half laser period phase lag between two emission points. Then the electrons re-enter the plasma, following the modulation surface.

In fig.4.12 we show the electric field corresponding to each phase of the emission of fig.4.11. We notice that the maximum excursion of the electrons ejected at each emission point corresponds in time to a maximum of the electric field at the surface.

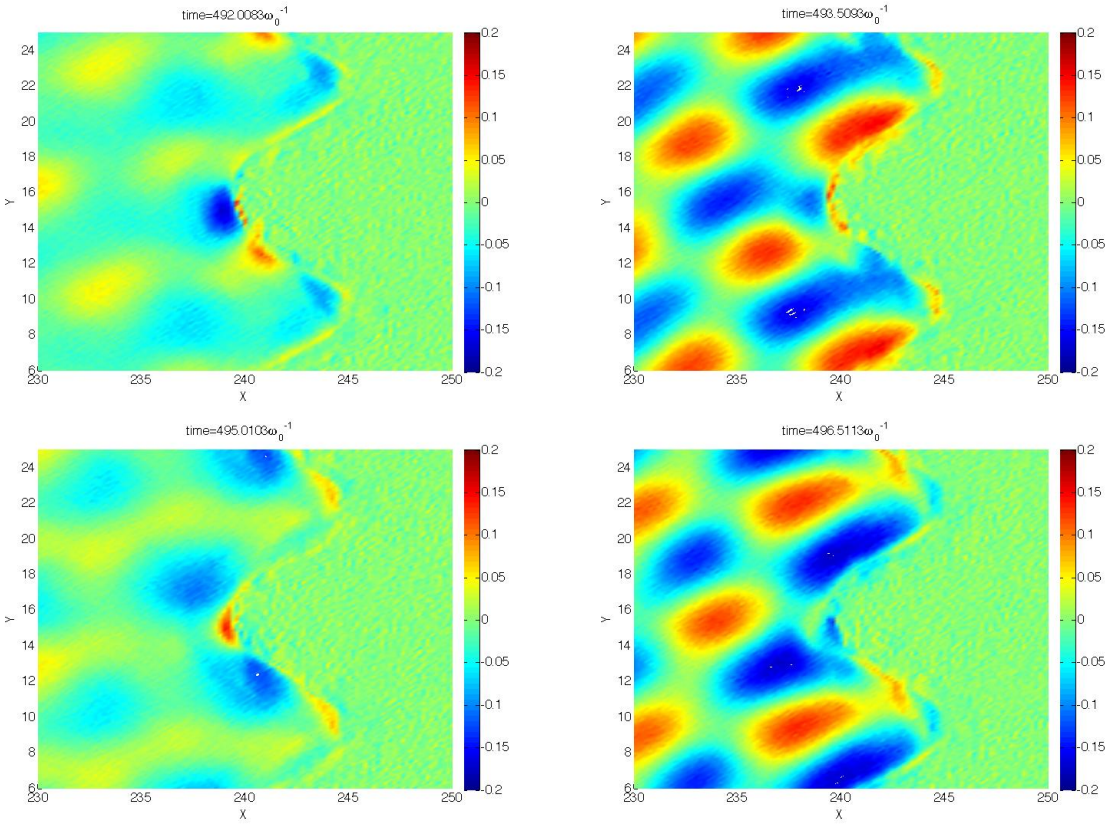

Figure 4.12: Electric field E_x, sequential plots taken at time intervals of $1.5\omega_0^{-1}$ ($\simeq 1/4$ laser period), starting from $t = 492\omega_0^{-1}$, corresponding to electron currents in fig.4.11. $I\lambda_0^2 = 10^{16}$W cm$^{-2}\mu m^2$ ($a_0 = 0.086$), $d = \lambda_0$, $n_e = 25n_c$, semi-infinite target **when the SPW is excited**.

For the high intensity regime ($I\lambda_0^2 = 10^{19}$W cm$^{-2}\mu m^2$) the current vector plot shows a result which is qualitatively similar to the one observed in the low intensity case: electrons which exit/re-enter the plasma periodically in a direction which is almost normal to the modulation surface, from two emission points, or electrons which moves along the target surface. The only difference we can notice compared to the low intensity case is the larger excursion of the electron emitted outside the plasma. In fig.4.14 we show the electric field corresponding to each phase of the emission of fig.4.13.

We will now try to give an interpretation of the electron emission features observed in both regimes. According to the results obtained in [77] for test particles entering the

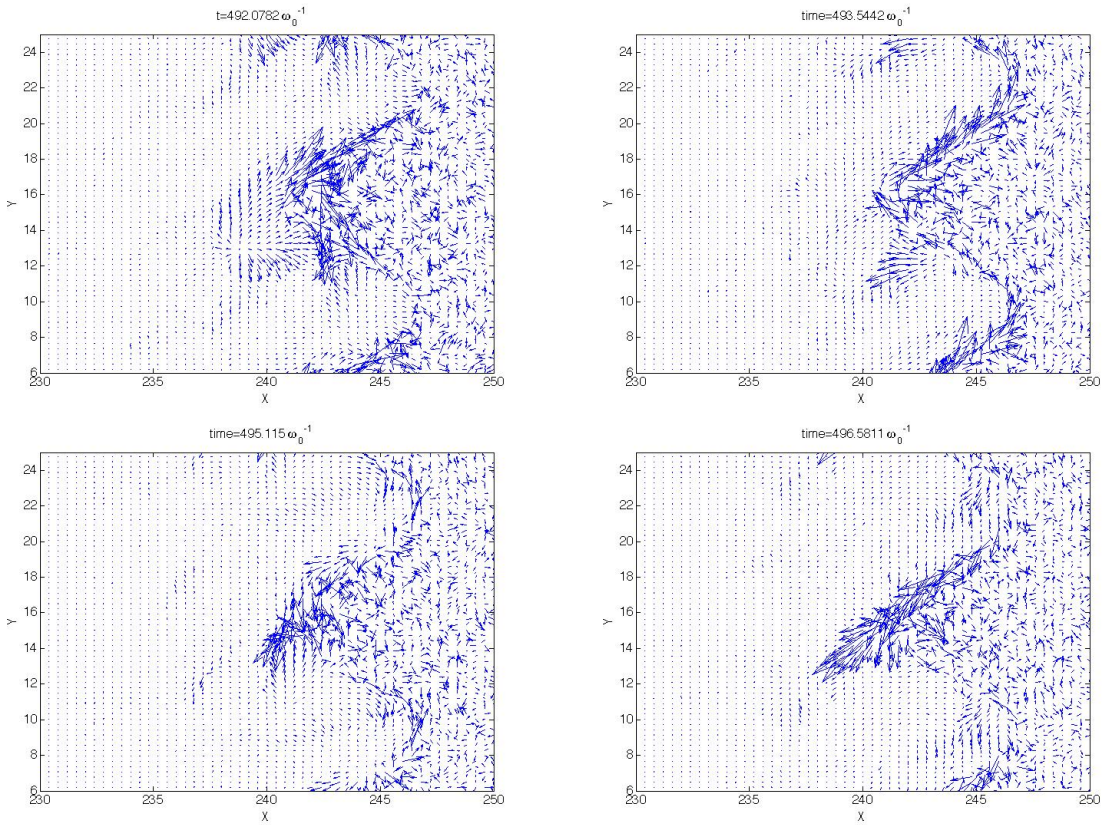

Figure 4.13: Electron current ($n_e v_e$, no charge sign) sequential vector plots taken at time intervals of $1.5\omega_0^{-1}$ ($\simeq 1/4$ laser period), starting from $t = 492\omega_0^{-1}$. $I\lambda_0^2 = 10^{19}$W cm$^{-2}\mu m^2$ ($a_0 = 2.72$), $d = \lambda_0$, $n_e = 25n_c$, semi-infinite target **when the SPW is excited**.

field of the surface wave, the most favourable phase for electron acceleration corresponds to the zeros of the SPW field, so that the electrons experience the rising part of the field amplitude (absolute value) and reach the maximum momentum at the peak of the field. Thus the emission observed at each half laser period may be related to electrons entering the wave field at the most favourable phase, which experience large oscillations: such electrons detach from the surface and exit or enter the plasma depending on whether the field is evolving towards a minimum or a maximum. Following this assumption, the emission we observe from different points would correspond to the spatial periodicity of the wave: for example if at one point we have a maximum of the field while at a second point we have a minimum, we will have emission in the vacuum from the first point while from the second one electrons are accelerated into the plasma; after half laser cycle the situation is reversed as the field has changed sign. This is confirmed by the electric field shown in 4.12 where we observe that each electron emission point corresponds to a local SPW field maximum (positive) at times $t = 492\omega_0^{-1}$ and $t = 495\omega_0^{-1}$.

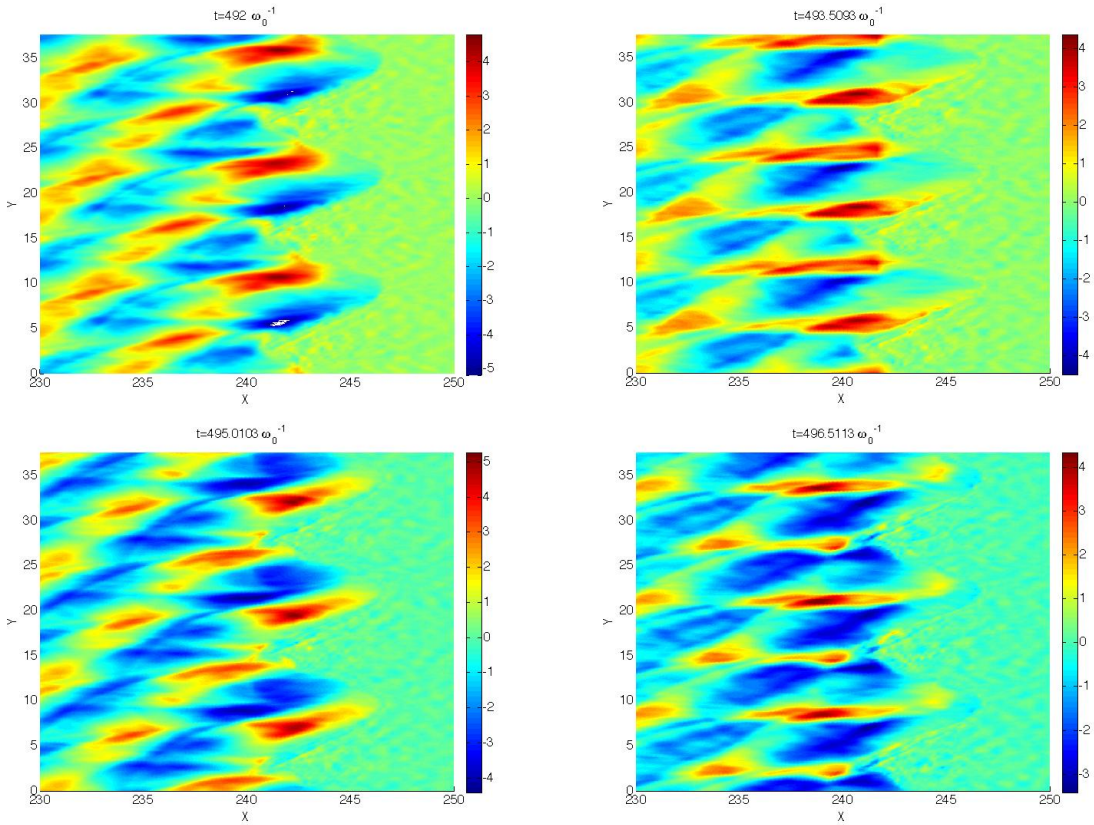

Figure 4.14: Electric field E_x, sequential plots taken at time intervals of $1.5\omega_0^{-1}$ ($\simeq 1/4$ laser period), starting from $t = 492\omega_0^{-1}$, corresponding to electron currents in fig.4.13. $I\lambda_0^2 = 10^{19}$W cm$^{-2}\mu m^2$ ($a_0 = 2.72$), $d = \lambda_0$, $n_e = 25n_c$, semi-infinite target **when the SPW is excited**.

4.2.1 Non-resonant angle of incidences

In section 4.1.1 we observed that the electron energy has a dependence on the laser pulse angle of incidenceand modulation depth. We will now analyze the dependence of the electron emission angles on the angle of incidencecomparing the angle of incidence $\theta = 30°$, which matches the parameters for SPW excitation, and the two angles out of resonance $\theta = 20°$ and $\theta = 10°$ which do not match the condition for SPW excitation.

The target parameters are kept constant: semi-infinite target, $d = \lambda_0$, $n_e = 25n_c$, $a_m = 2\lambda_0$. We will consider two laser intensities in order to compare the effect of the laser angle of incidenceon the electron emission for different interaction regimes: $I\lambda_0^2 = 10^{16}$W cm$^{-2}\mu m^2$ and $I\lambda_0^2 = 10^{19}$W cm$^{-2}\mu m^2$.

At $I\lambda_0^2 = 10^{16}$W cm$^{-2}\mu m^2$, for the angle of incidences $\theta = 20°$ (not shown here) and $\theta = 10^o$ (fig.4.15) the angular distribution of the electrons accelerated towards the plasma is similar and we observe two main angles $\pm 60°$. Electrons which are moving in the backward direction, i.e. towards the vacuum, have an angular distribution peaked around $\pm 70°$ for $\theta = 10°$ and $\pm 80°$ for $\theta = 20°$ instead. We notice that these emission angles have some similarity with those found for the resonant incidence in the

same intensity regime, where we also found the angles ±60°. Nevertheless we observe an important difference, that is the forward emission around ±30°, which could be associated with the electron motion along the surface, disappears when the surface wave is not excited. *Thus, from the comparison of the angular distribution of the electrons*

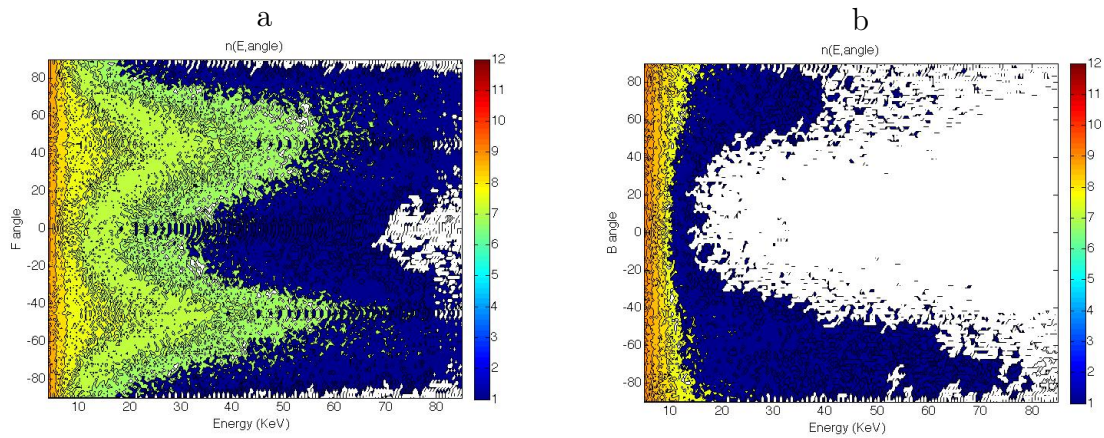

Figure 4.15: Electron emission angles as a function of energy: forward (a) and backward (b) directions at $t = 500\omega_0^{-1}$, for $I\lambda_0^2 = 10^{16}$W cm$^{-2}\mu m^2$ ($a_0 = 0.086$), $d = \lambda_0$, $n_e = 25n_c$, semi-infinite target, **for the non-resonant angle of incidence** $\theta = 10^o$ **on the modulated surface** (same target shape as for the resonant case, where the SPW was excited).

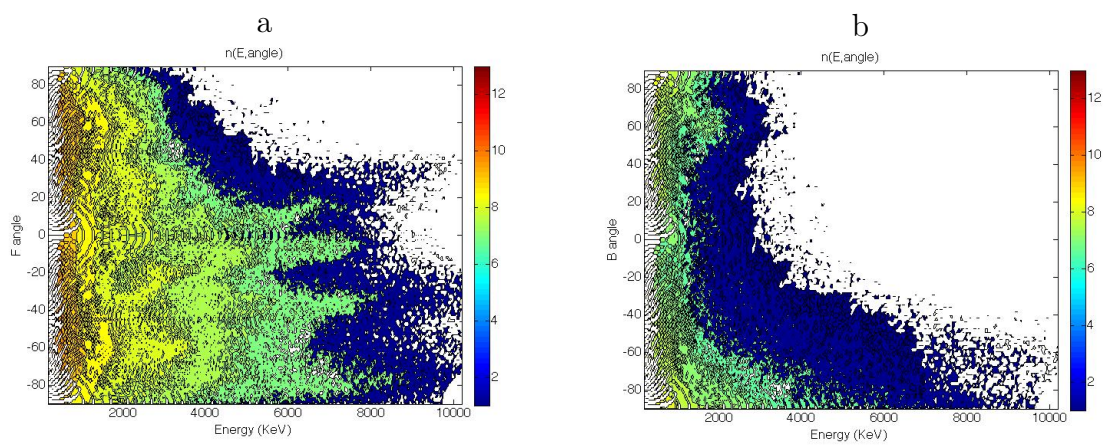

Figure 4.16: Electron emission angles as a function of energy: forward (a) and backward (b) directions at $t = 492\omega_0^{-1}$, for $I\lambda_0^2 = 10^{19}$W cm$^{-2}\mu m^2$ ($a_0 = 2.72$), $d = \lambda_0$, $n_e = 25n_c$, semi-infinite target, **for the non-resonant angle of incidence** $\theta = 10^o$ (same target shape as for the resonant case, where the SPW was excited).

emitted in the forward direction, for non-resonant angle of incidences, with the case where the SPW is excited, we may conclude definitely that angles ±60° *depend only on the shape of the target and correspond to electrons accelerated along the target normal.* We may associate the acceleration in this direction to resonance absorption mechanism,

which accelerates electrons in the direction of the density gradient, corresponding to the surface normal. In fact, as discussed in chapter 2, absorption in the density gradient plays an important role at this laser intensity and does not depend on SPW excitation.

Contrastingly, at high intensity we find a more complex result for the electron emission when the laser incidence does not match the resonance. In this interaction regime vacuum heating is dominant and, as discussed in the previous section, and the contributions of laser pressure and self-generated fields may determine the final directions of electrons which re-enter the plasma [19]. For 20° (not shown here) we find a very regular angular distribution with two emission angles at $\pm 60°$ for the emission in the forward direction while in the backward direction we find a peak at $\simeq 60°$ and a minor accumulation corresponding to the $-\hat{y}$ direction. For the case of a 10° incidence pulse instead, emission occurs mainly at negative angles, in the forward direction, as we can observe in fig.4.16.

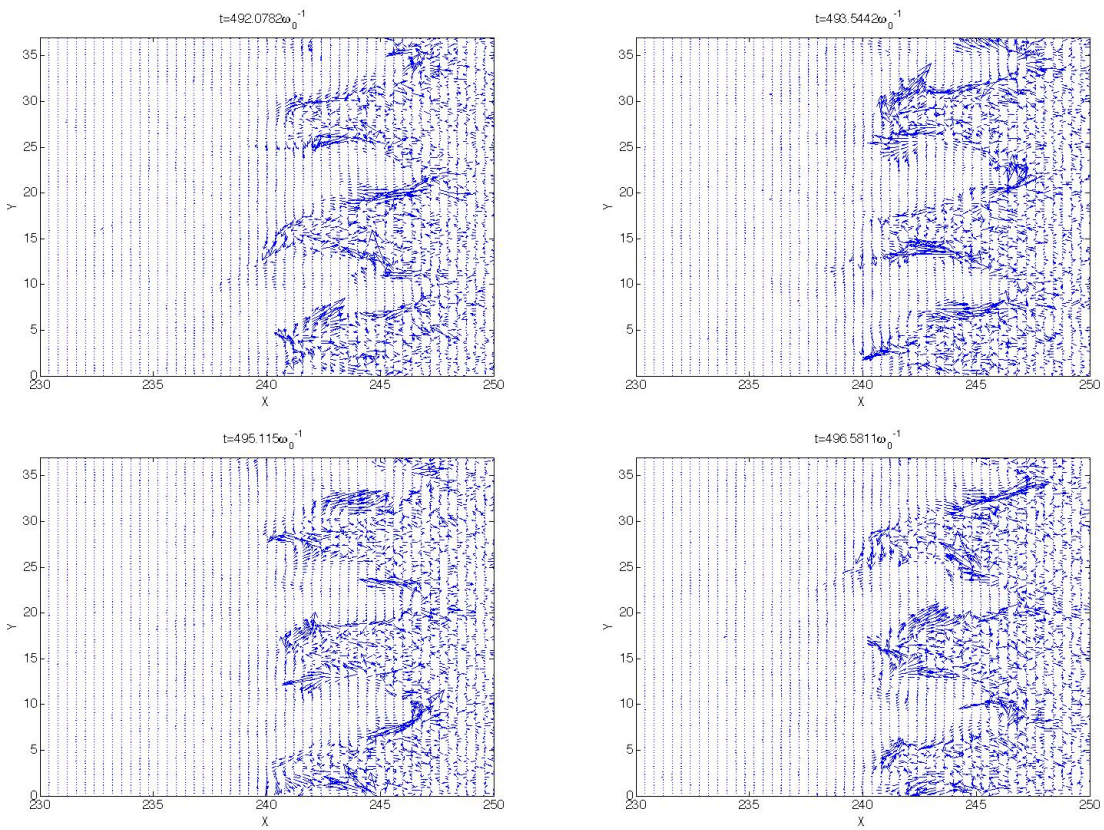

Figure 4.17: Electron current ($n_e v_e$, no charge sign) sequential vector plots taken at time intervals of $1.5\omega_0^{-1}$ ($\simeq 1/4$ laser period), starting from $t = 492\omega_0^{-1}$, for $I\lambda_0^2 = 10^{19}$W cm$^{-2}\mu m^2$ ($a_0 = 2.72$), $d = \lambda_0$, $n_e = 25n_c$, semi-infinite target, **for the non-resonant angle of incidence** $\theta = 10^o$ (same target shape as for the resonant case, where the SPW was excited).

We observe that the emission in the forward direction has four main angles around 40°, 0°, -40° and -70°. In the backward direction, emission is more dispersed compared to the resonant case but we can distinguish a distribution in the negative part

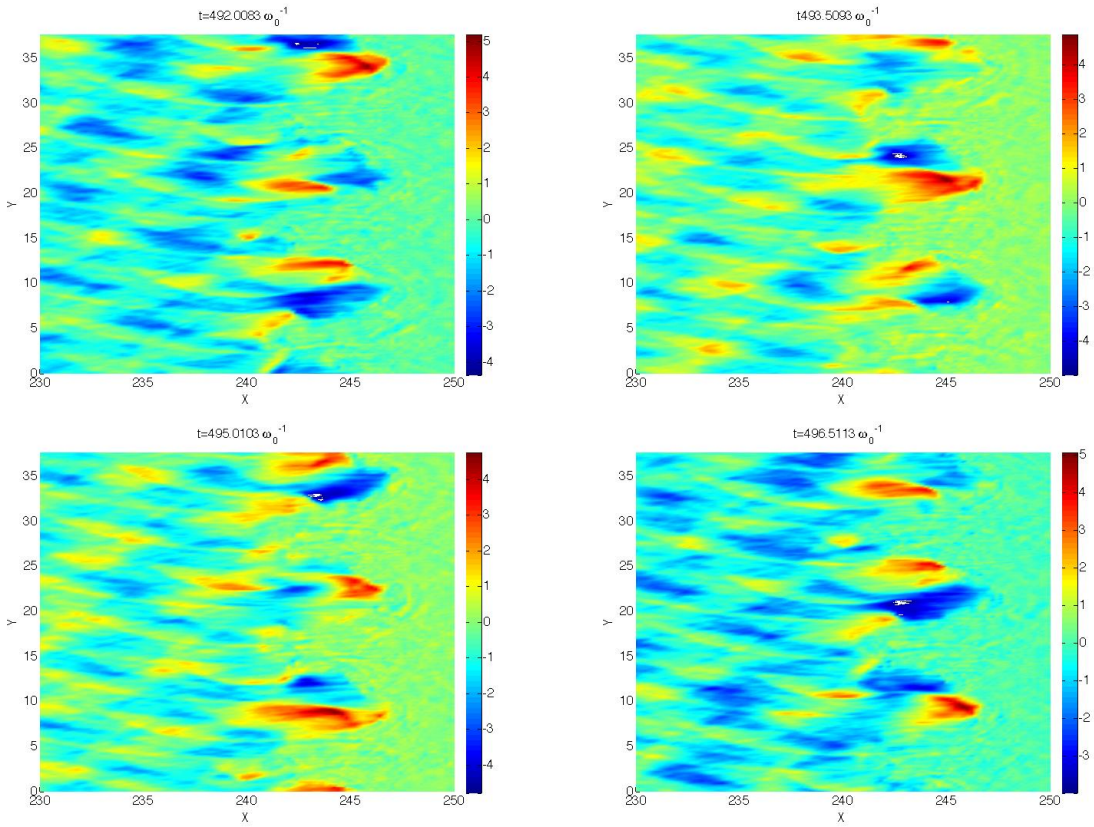

Figure 4.18: Electric field E_x, sequential plots taken at time intervals of $1.5\omega_0^{-1}$ ($\simeq 1/4$ laser period), starting from $t = 492\omega_0^{-1}$, for $I\lambda_0^2 = 10^{19}$W cm$^{-2}\mu m^2$ ($a_0 = 2.7$), $d = \lambda_0$, $n_e = 25n_c$, semi-infinite target, **for the non-resonant angle of incidence** $\theta = 10^o$ (same target shape as for the resonant case, where the SPW was excited).

of the plot, with angles ranging from -20° to -90°, peaked at -90°, and an accumulation point around $\simeq 60^o$. These angles are more difficult to interpret than for the resonant high intensity case, where the main emission angles could be associated with directions parallel or perpendicular to the surface. In order to better analyze the electron motion at the different points of the target, we compare these results with the electron current ($n_e v_e$, no charge sign) vector plots in fig.4.17. The time of the plots in fig.4.16 corresponds to the time of the top left picture of fig.4.17, allowing a comparison of the angular distribution and electron current. The first thing to be noticed is that the electron emission does not have the same periodicity of the target modulation any more, *i.e.* emission at one modulation tip is different from the emission at the next modulation tip. This can be observed in the top left frame of fig.4.17, where a bunch of electrons exit the middle tip while at the other two tips (upper and lower) there is no emission at that point. The electric field distribution near the target surface for the non-resonant angle of incidence $\theta = 10^o$ shows the same 'irregularity' of the electron emission as can be seen in fig.4.18 where the electric field component E_x is plotted. *We may infer that for non-resonant angle of incidences the electron emission is essentially determined by the interference pattern of the electric field at the target surface which*

varies according to the angle of incidence.

Thus for the high intensity regime we find that the difference between the resonant case and non-resonant angle is stronger and the 'irregularity' of the electric field pattern at the surface leads to an angular distribution which is difficult to interpret. Comparing with the low intensity case we notice that the differences in the electron distribution for non-resonant and resonant incidence are less evident there, which would confirm the assumption that at low laser intensities the main heating mechanism is resonance absorption, which accelerates electrons in the direction of the density gradient for any value of the laser angle of incidence θ.

4.2.2 Effects of the modulation depth

In section 2.4 we have examined the dependence of absorption on the modulation depth, d, and observed that it decreases for small values of d: for example, for $I\lambda_0^2 = 10^{19}$W cm$^{-2}\mu m^2$ absorption decreases from 75% to 51% when the modulation depth is reduced from λ_0 to $\lambda_0/3$. Contrastingly, in section 4.1.2 we have observed that electron heating appears quite similar for different values of the modulation depth, in the high intensity range, particularly for what concerns the maximum electron energy. This result may be explained if we associate the hot electrons population to the SPW. In this section we will study the characteristics of the electrons acceleration for reduced modulation depth in order to confirm this assumption.

In figure 4.19 we can observe hot electron emission angles for the resonant case having modulation depth $d = \lambda_0/3$. The first thing we notice in this plot is that

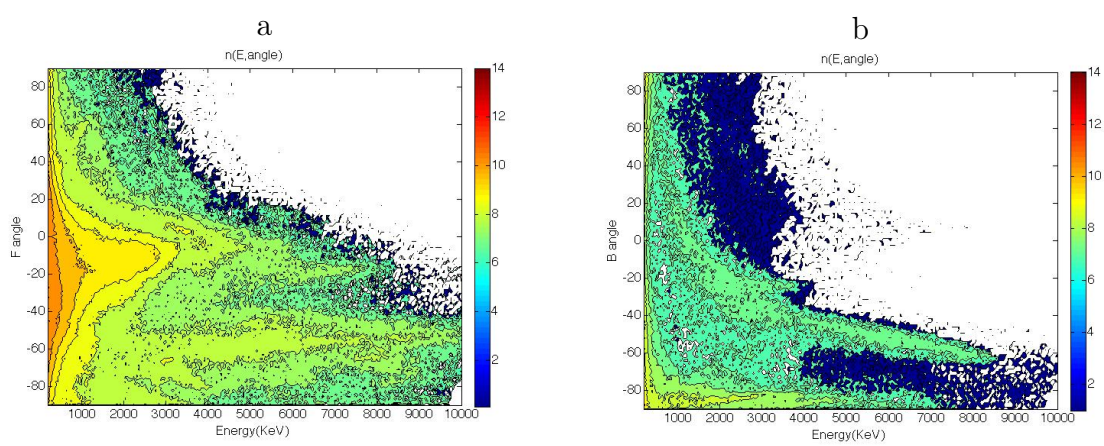

Figure 4.19: Electron emission angles as function of energy: forward (a) and backward (b) direction for $I\lambda_0^2 = 10^{19}$W cm$^{-2}\mu m^2$ ($a_0 = 2.72$) and **modulation depth** $d = \lambda_0/3$, at $t = 492\omega_0^{-1}$. Semi-infinite target, $n_e = 25n_c$ **when the SPW is excited**.

electron acceleration in the direction of the vacuum (fig.4.19b) is much more important here than in the case having a larger modulation depth, $d = \lambda_0$, as in that case the maximum energy of backward accelerated electrons was around $\simeq$ 4MeV while here we find $\simeq$ 9MeV. In the forward direction (fig.4.19a) the emission is characterized by two angles: $-15°$ and $-60°$ (approximately) while in the backward direction (fig.4.19b)

we find an emission angle around $\simeq 50°$. We also find a large number of energetic electrons accelerated along the $-\hat{y}$ direction. These angles are close to the directions perpendicular and parallel to the target surface, which for this modulation depth are $\pm 25°$ and $\pm 65°$ respectively, as shown in fig.2.7. Thus for $d = \lambda_0/3$ we can apply the same considerations done for $d = \lambda_0$, and electrons moving along the surface can be interpreted as the signature of SPW excitation. A similar result is found for the smallest modulation depth, $d = \lambda_0/5$ (not shown here) even though the emission towards the vacuum is characterized by a lower value of the maximum energy, which is $\simeq 6000$keV. In figure 4.20 we can observe in detail the electron current when the SPW is resonantly excited, for $d = \lambda_0/3$: the electron emission is qualitatively similar to the one observed in the $d = \lambda_0$ case (fig.4.13) but here we observe electrons moving further from the plasma, in agreement with the higher energy values observed for backward accelerated electrons at this modulation depth. At the same time we notice well defined bunches of electrons entering the plasma.

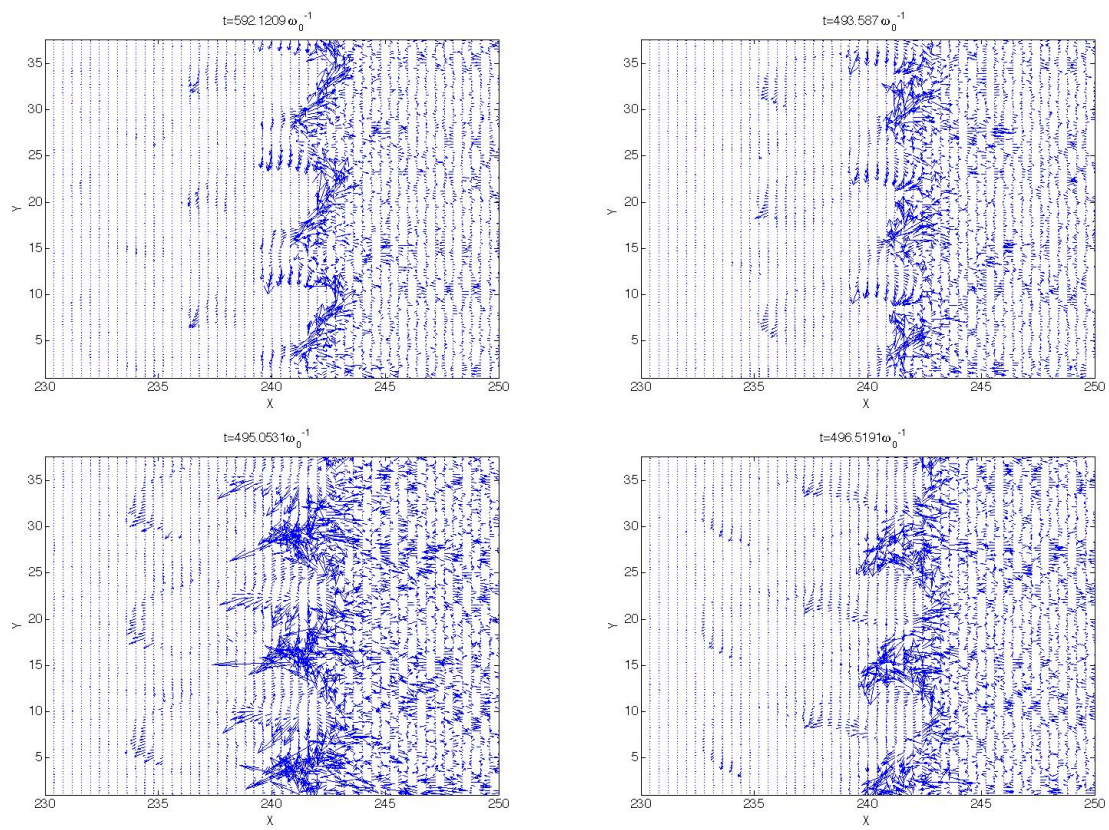

Figure 4.20: Electron current ($n_e v_e$, no charge sign) sequential vector plots for the target having modulation depth $d = \lambda_0/3$, taken at time intervals of $1.5\omega_0^{-1}$ ($\simeq 1/4$ laser period), starting from $t = 492\omega_0^{-1}$; $I\lambda_0^2 = 10^{19}$W cm$^{-2}\mu m^2$ ($a_0 = 2.72$), $n_e = 25n_c$, semi-infinite target, **when the SPW is excited**.

We remember that in section 2.4 we also found an important result for small modulation depths combined with non-resonant angle of incidences: when the modulation is reduced to $\lambda_0/3 - \lambda_0/5$ the difference between the resonant and the non-resonant

incidence is greater than what was observed for $d = \lambda_0$. For example, when $d = \lambda_0/3$, the non-resonant angle of incidence $\theta = 10°$ corresponds to only 35% absorption, which is very close to the plane target value, while for resonant incidence it is 51%. This result was further confirmed by the comparison of the electron energy for resonant and non resonant incidence at $d = \lambda_0/3$ in section 4.1.2, where we found that both the hot electron temperature and the cut-off energy of the electron are greater when the SPW is excited. We will now examine the hot electron emission angles for the non resonant angle of incidence $\theta = 10°$ when the modulation depth is $d = \lambda_0/3$. In the angular distribution of electrons accelerated forward (4.21a) we can distinguish three angles, $-30°$, $20°$ and a small peak at $-70°$. We notice that the main peaks in the forward emission, $-30°$ and $20°$, are close to the direction perpendicular to the target surface, ($\simeq 25°$) and can be interpreted as electrons accelerated by vacuum heating. In the

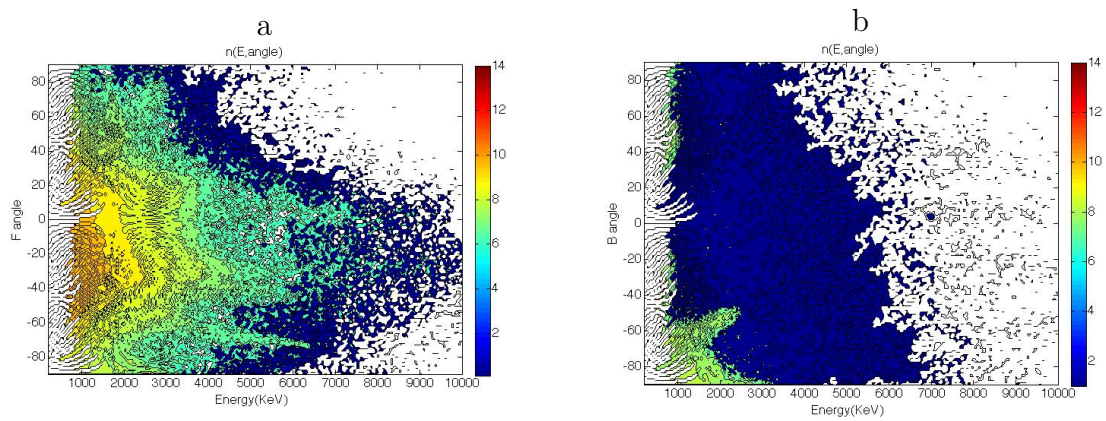

Figure 4.21: Electron emission angles as a function of energy: forward (a) and backward (b) directions for $I\lambda_0^2 = 10^{19}$W cm$^{-2}\mu m^2$ ($a_0 = 2.72$), at $t = 492\omega_0^{-1}$, and modulation depth $d = \lambda_0/3$ **for the non-resonant angle of incidence** $\theta = 10^o$ (same target shape as for the resonant case, where the SPW is excited). $n_e = 25n_c$, semi-infinite target.

backward direction (fig.4.21b) electrons are emitted over a wide angular range, with a small peak around $-60°$ and have lower energies compared to the case having $d = \lambda_0$ and the same pulse angle of incidence($\theta = 10^o$).

We shall now examine the electron currents and angular emission for angle of incidence $\theta = 10°$ when $d = \lambda_0/3$ in order to examine in detail the differences with the currents observed in the resonant case. From the current vector plot in fig.4.22 we can observe that the characteristics of electron emission are very different from the resonant case. *When the laser incidence is switched from* $30°$ *to* $10°$ *electron emission at the surface is very confused and not periodic along* $\hat{y}$*, as was also observed for the* $d = \lambda_0$ *case in fig4.17, but here electron emission outside the plasma is reduced and electrons do not perform large excursions in the vacuum, staying closer to the target surface than in the* $d = \lambda_0$ *case.* This is in agreement with the lower values of absorption and electron energy and with the angular distribution observed for this case.

To conclude, in this section we have analyzed in detail the electron acceleration for reduced modulation depth, where the geometry effects are reduced so that the effects

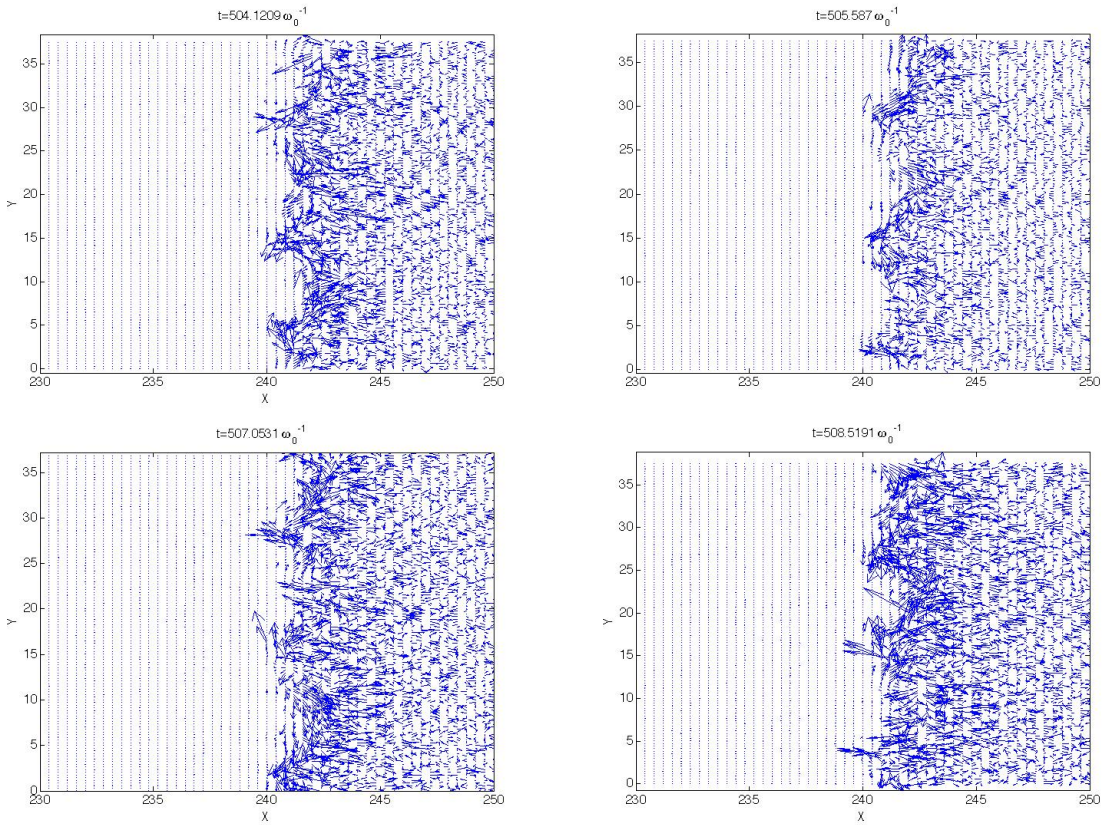

Figure 4.22: Electron current ($n_e v_e$, no charge sign) sequential vector plots for the target having modulation depth $d = \lambda_0/3$, taken at time intervals of $1.5\omega_0^{-1}$ ($\simeq 1/4$ laser period), starting from $t = 504\omega_0^{-1}$; **for the non-resonant angle of incidence** $\theta = 10^o$ (same target shape as for the resonant case, where the SPW is excited). $I\lambda_0^2 = 10^{19}$W cm$^{-2}\mu m^2$ ($a_0 = 2.72$), $n_e = 25n_c$, semi-infinite target.

of the surface wave excitation are found to be more evident. This study shows that electrons emitted at the target surface have much larger excursion length when the SPW is excited and have negative velocity in the y direction, which can be associated with the SPW wave. Electrons accelerated into the plasma have directions which can be associated with vacuum heating in the direction perpendicular to the surface or to a motion along the surface, which is more evident when the SPW is excited. *We may conclude that the high electron energies observed when the modulation depth is reduced, in the high laser intensity regime, can be attributed to SPW excitation, while other mechanisms are less efficient, as confirmed by the non-resonant cases.*

4.3 Laminar targets

In the previous sections we have examined the electron energy and emission angles for the case of a semi-infinite target where electrons reaching the right end of the plasma are cooled and re-enter the plasma at thermal velocity. We have shown that we can

define a relationship between the electron energy distribution and the SPW excitation according to which the latter is associated with a larger number of electrons accelerated in the high energy range. Electron currents for the semi-infinite case were also examined where we found that electron emission is more regular when the SPW is excited and electron bunches exit and re-enter the plasma at points corresponding to maxima of the SPW field.

We will now analyze the characteristics of particle emission in the case of a laminar target, where, as we discussed in section 2.5, electrons recirculate in the target and may interact with the accelerating field more than once. The pulse shape and duration is the same as used in the simulations of the semi-infinite target. As we aim to analyze the differences of the laminar target with the semi-infinite target, we will consider only the high intensity pulse regime ($I\lambda_0^2 = 10^{19}$W cm$^{-2}\mu m^2$) in order to produce a large number of hot electrons which will underscore the effects of recirculation. The simulation box here is $480k_0^{-1} \simeq 76\lambda_0$ along x and has the same y size ($6\lambda_0$) as the semi-infinite target. The plasma starts at $x = 240k_0^{-1}$ and we will consider two target thicknesses: $22k_0^{-1} \simeq 3.5\lambda_0$ and $50k_0^{-1} \simeq 8\lambda_0$.

4.3.1 Electron heating

As we mentioned above, the most important characteristic of electron motion which can be observed in a thin laminar target is electron recirculation [21]: energetic electrons entering the target reach the rear (unirradiated) side where a Debye sheath has formed which reflects them back, towards the front (irradiated side) of the target. There, they are reflected again from the front sheath towards the rear and so on. The hot electron density at one side then corresponds to a superposition of laser accelerated electrons and electrons that are reentering the target at intervals of the double transit time. This

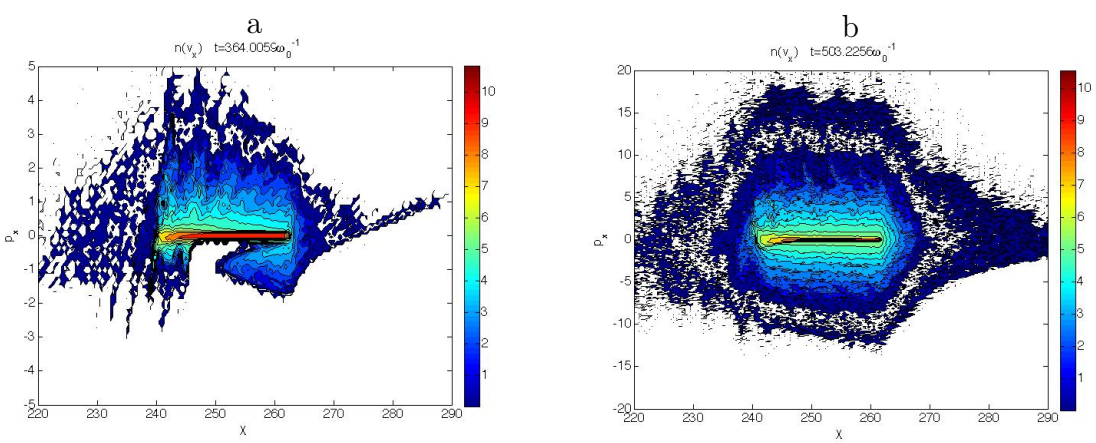

Figure 4.23: Electron phase space $(x, \gamma v_x)$ for the laminar target of thickness $22k_0^{-1} \sim 3.5\lambda_0$ taken during electron reflection at the rear (a) and after further reflection at the front (b) of the target (time $360\omega_0^{-1}$ and $503\omega_0^{-1}$). $I\lambda_0^2 = 10^{19}$W cm$^{-2}\mu m^2$ ($a_0 = 2.72$), $n_e = 25n_c$, $d = \lambda_0$, **the SPW is excited**.

process is observed in our simulations as it can be seen in fig.4.23, where the electron

phase space (x, p_x) is shown after the first electron reflection at the rear surface (a) at $x = 262k_0^{-1}$ and later, after further reflection from the front sheath (b) at $x = 240k_0^{-1}$. Electrons reach the rear surface, for the first time at $t \simeq 357\omega_0^{-1}$ and after the first reflection, are back to the front at $t \simeq 380\omega_0^{-1}$, thus their velocity is close to c (the time mentioned here *does not* correspond to fig.4.23). We may also observe that electrons are emitted in bunches with a spatial periodicity of $\simeq 6k_0^{-1}$, which is coherent, for electrons accelerated to relativistic velocities, with an accelerating field oscillating at about ω_0. This means that for a laminar target sufficiently thin to allow reflected electrons to reach the irradiated side while the driving field is still present, electrons may interact several times with the field and this results in enhanced particles acceleration and radiation absorption. Recirculation is absent in the semi-infinite target where energetic electrons entering deep in the bulk are 'lost' (absorbed) and replaced by thermal ones.

We observe in fig.4.24 that the electron energy is increased for rediced target thickness, which is consistent with the laser absorption data presented in section 2.5. We can give an estimate of the critical target thickness, h_c, for which the electrons can take advantage of recirculation, increasing their energy, using the relation $\tau_L/2c = 2h$ (where τ_L is the laser duration FWHM): for the pulse duration in our simulation $\tau_L = 240\omega_0^{-1}$ we have $h_c = 60k_0^{-1} \simeq 9.5\lambda_0$. For the two target thicknesses $h = 8\lambda_0$ and $h = 3.5\lambda_0$, the hot electron temperatures are $T_{hot,8} \simeq 2.1$MeV and $T_{hot,3.5} \simeq 2.3$MeV respectively while the maximum energies are $E_{max,8} \simeq 13.5$MeV and $E_{max,3.5} \simeq 14$MeV. The latter are both higher than the electron temperature and maximum energy of the semi-infinite case where we had $T_{hot,s-inf} \simeq 1.9$MeV and $E_{max,s-inf} \simeq 13$MeV.

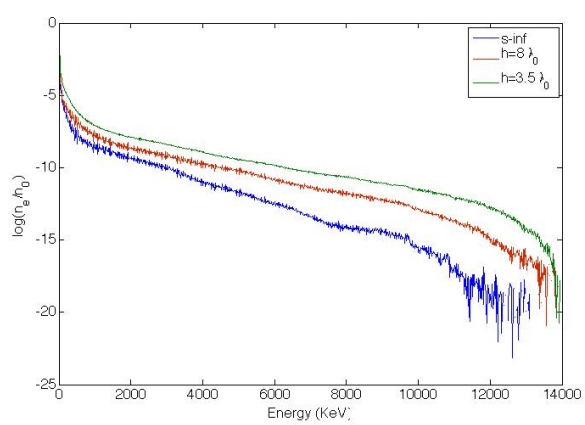

Figure 4.24: Electron spectra for the laminar targets having different thickness, $h = 3.5, 8\lambda_0$ and the semi-infinite target, taken at time $t = 500\omega_0^{-1}$ for $I\lambda_0^2 = 10^{19}$W cm$^{-2}\mu m^2$ ($a_0 = 2.72$), $n_e = 25n_c$, $d = \lambda_0$, **when the SPW is excited**.

This result can be explained as follows: in the case of the laminar target, electrons which are accelerated are not 'lost' in the absorption into the bulk plasma and an electron's energy at a given time represents the sum of the energies absorbed by the particle after multiple interactions with the driving field, if we exclude the energy that has been transferred to the ions. However ion acceleration has longer time-scales, thus the elec-

tron energy shown at $t = 500\omega_0^{-1}$ corresponds to the energy of electrons that have been accelerated, possibly more than once, by the SPW and the laser pulse. If we reduce the target thickness, a larger number of electrons will have the possibility to interact more than once with the surface field and further increase their energy. Particularly, *for the case of SPW resonant excitation at the irradiated surface, energetic electrons may interact several times with the wave having more chances to enter the wave with the correct phase (corresponding to zeros of the SPW field as discussed in 4.2) in order to get the maximum acceleration.*

We will now analyze in detail the emission angles of the electrons for the thinnest target, having thickness $22k_0^{-1} \simeq 3.5\lambda_0$, for which the differences with the semi-infinite case are more pronounced. We notice that in the laminar target the emission angle is not sufficient to separate electrons which are recirculating inside the plasma from those which are emitted towards the vacuum. Therefore, the electron phase space will be divided into 3 parts: (a) electrons emitted into the vacuum at the irradiated side ($x = [0 - 240k_0^{-1}]$), (b) electrons inside the plasma, and (c) electrons emitted into the vacuum at the rear of the target ($x = [262 - 480k_0^{-1}]$). In each section we will distinguish two directions for the electron motion: backward (i.e. moving from right to left) and forward (i.e. moving from left to right).

From figures 4.25a we see that electrons leaving the target at the left side (irradiated) are very few and have a quite homogeneous angular distribution, where we can distinguish three peaks: $-40°$ and $60°$ in the forward direction, and $-70°$ in the backward direction. The angular distribution of the electrons leaving the target at the rear side (unirradiated) is also quite smooth and we can distinguish only one peak at $-40°$, in the forward direction (figures 4.25c). The majority of hot electrons is observed inside the plasma (figures 4.25b) where the angular distribution has two main peaks, $60°$ and $-40°$ both in the forward and the backward direction. The fact that we find similar angles in the forward and backward angular distributions can be associated with the electrons recirculating inside the plasma. We may interpret these data as electron acceleration in two directions: i) approximately perpendicular to the target modulated surface (the angle at $60°$) and ii) along the laser propagation direction or along the surface (the angle at $-40°$, which is close to $\theta = -30°$), and their respective reflected angles. This is only a rough description of the dynamics, in fact electric and magnetic fields close to the surface may deflect electrons accelerated by vacuum heating, as discussed previously.

We will now analyze the corresponding electron current ($n_e v_e$, no charge sign) vector plots in fig.4.26. We recall that this current is, at each point, the result of the contributions of all the particles related to that space grid point and hot electrons passing through the bulk thermal plasma may not be visible in this plot. Nevertheless we will have the possibility to examine the different phases of electron oscillations at the surface and identify the spatial location of electron emission. Thus, as discussed for the semi-infinite target, the currents will provide information on electron motion which are complementary to angular distribution plots obtained from the electron phase space, where the momentum of each particle is represented.

In fig.4.26 we observe an emission towards the vacuum (backward), at the irradiated target side which is qualitatively similar to that observed for the semi-infinite case of

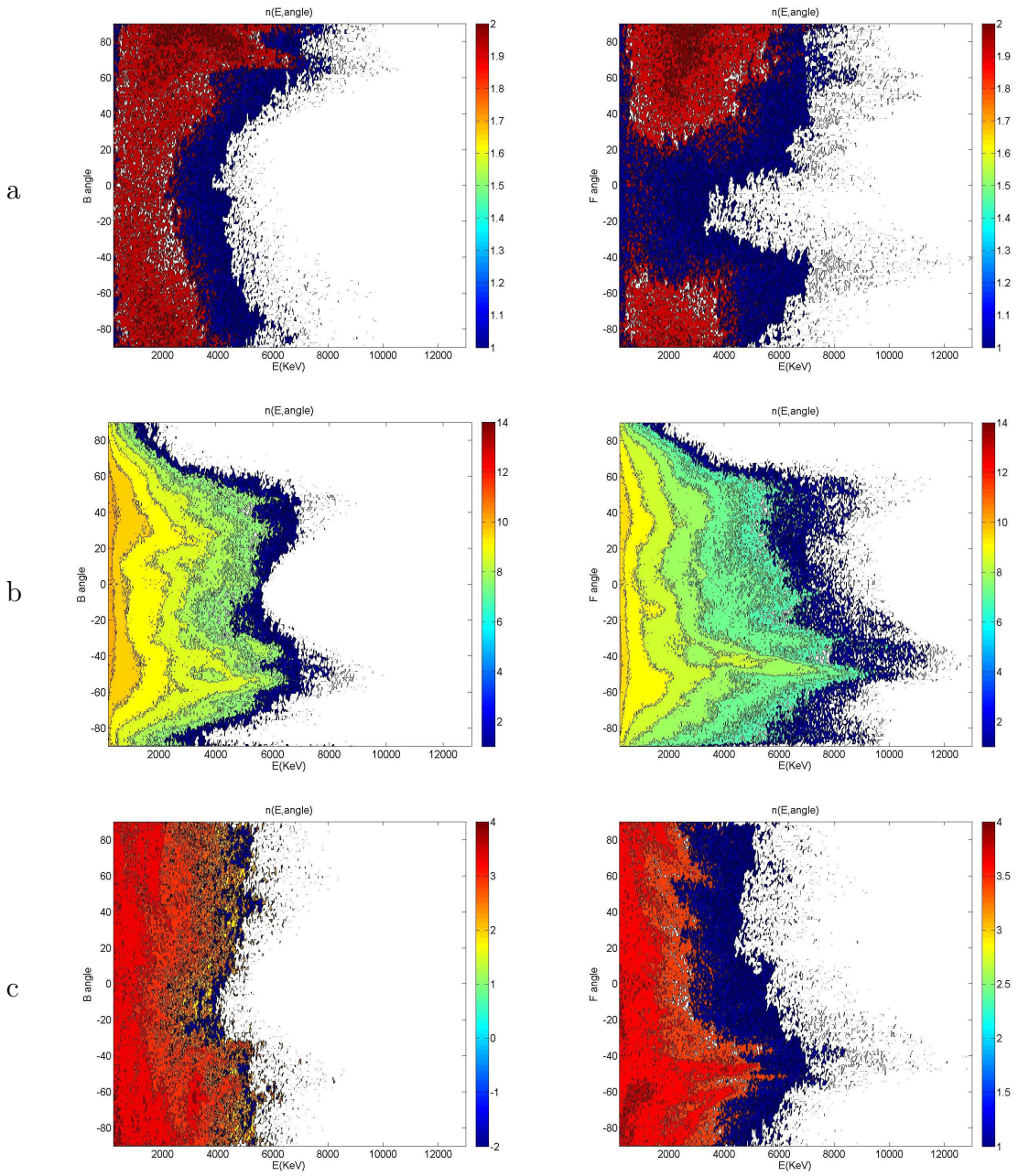

Figure 4.25: Electron emission angles backward (**B**=moving from right to left) and forward (**F**=moving from left to right), for the laminar target of thickness $22k_0^{-1} \simeq 3.5\lambda_0$, taken at $t = 500\omega_0^{-1}$; $n_e = 25n_c$, $d = \lambda_0$ and $I\lambda_0^2 = 10^{19}$W cm$^{-2}\mu m^2$ ($a_0 = 2.72$) **when the SPW is excited**.**(a)** electrons emitted into the vacuum at the irradiated side ($x = [0-240k_0^{-1}]$).**(b)** electrons inside the plasma ($x = [247-262k_0^{-1}]$).**(c)** electrons emitted into the vacuum at the rear of the target ($x = [262 - 480k_0^{-1}]$).

fig.4.13: bunches of hot electrons exit the plasma periodically, in a direction which is about normal to the target surface ($\simeq 60°$), at two main points situated on the lower part of the modulation tip: one closer to the top and the other halfway between the

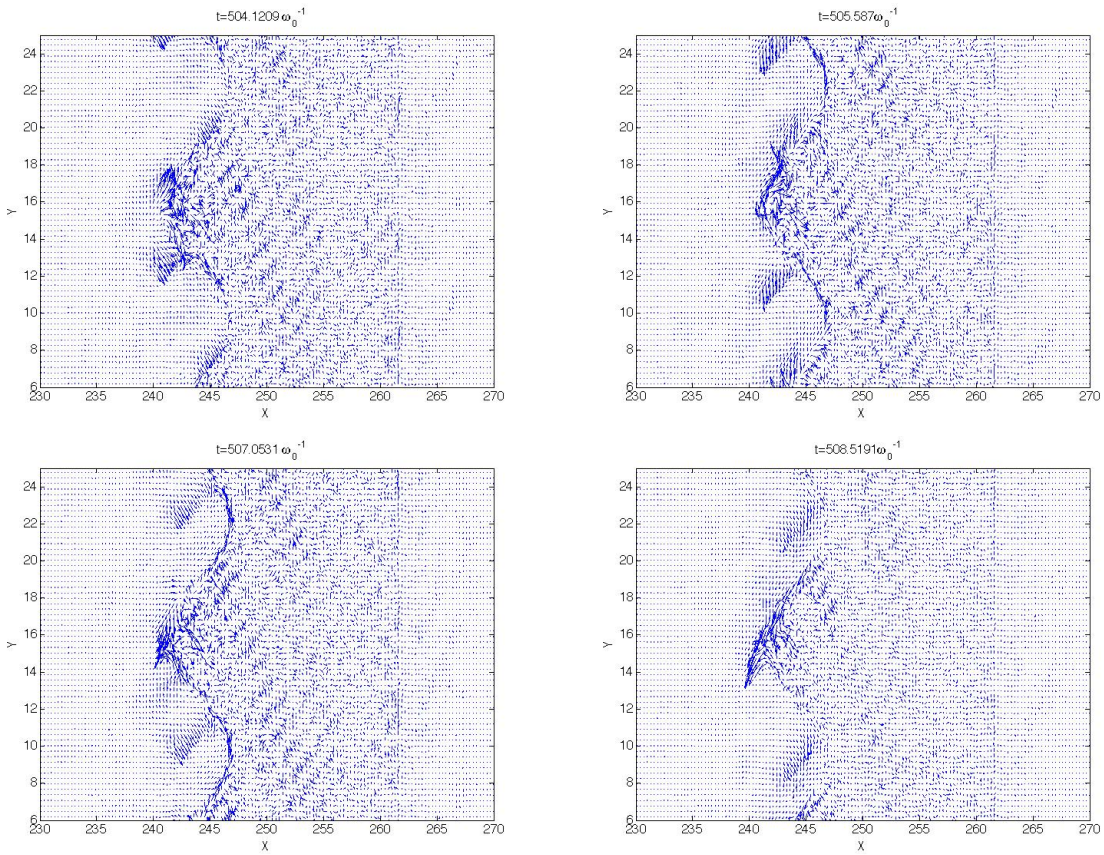

Figure 4.26: Electron current ($n_e v_e$, no charge sign) sequential vector plots for the laminar target of thickness $22k_0^{-1} \simeq 3.5\lambda_0$, taken at time intervals of $1.5\omega_0^{-1}$ ($\simeq 1/4$ laser period), starting from $t = 504\omega_0^{-1}$; $n_e = 25n_c$, $d = \lambda_0$ and $I\lambda_0^2 = 10^{19}$W cm$^{-2}\mu m^2$ ($a_0 = 2.72$) **(the SPW is excited)**.

top and the bottom of the dip. The periodicity of the emission is one laser period and there is a phase lag of half a laser period between the two emission points. Then the electrons re-enter the plasma, following the surface modulation. We may also observe bunches of electrons which are moving inside the plasma, towards the rear surface. For example, we observe electrons moving from the surface towards the rear side at the point $y \simeq 19k_0^{-1}$ in a direction which forms an angle of about 30° with the $\hat{x}$ axis. Other points from which electrons are accelerated into the plasma are found at a distance of $\simeq \lambda_0$ along y and we notice that electron motion is periodic in this direction, similarly to what was found for the semi-infinite targets where the SPW is excited.

We may conclude that in the case of the laminar target the effects of SPW excitation on electron heating are qualitatively similar to what was observed for the semi-infinite case: electron emission angles are approximately the same and show the same characteristics of spatial and temporal periodicity. *Electron recirculation enhances the efficiency of acceleration via the SPW as electrons can interact with the wave field more than once, eventually entering the field with the most favourable phase and further increasing their energy. This effect is more pronounced when the thickness of the target is*

reduced because i) the number of cycles that electrons can perform before the driving field is extinguished is greater and ii) a larger number of electrons can be reflected back to the irradiated surface at least once.

4.3.2 Non-resonant incidence and reduced modulation depth

We have seen in section 2.3 that, when the angle of incidence of the laser beam is switched from the resonant incidence to angles which do not match the conditions for resonant SPW excitation, the absorption and electron heating are modified not only because we are not exciting the SPW any more, but also as a consequence of a geometry effect. The latter may be very important for modulated targets having large modulation depths, of the order of $d \sim \lambda_0$, enough to hide the effects of SPW excitation. In section 4.2.2 we have observed that for the semi-infinite target, at non-resonant incidence the electron emission appears to be more irregular and loses the spatial periodicity found in the resonant case. Moreover, when the geometry effects are reduced, we observed that the energy of electrons is much lower when the SPW is not excited and their excursion length in the vacuum is reduced. A similar result is found for the laminar target, with the only difference that here we also observe electrons which are reflected at the rear surface, at an angle which corresponds to the angle at which the electrons were injected into the plasma. In order to avoid geometry effects and not repeat the analysis that was already done for the semi-infinite case, we will limit our investigation to the case of the non-resonant angle of incidencewith a reduced modulation depth.

Initially we study the case of a target having reduced modulation depth $d = \lambda_0/3$, in the case of a resonant angle of incidence($\theta = 30°$) and compare to the case where $d = \lambda_0$. Then the angle of incidencewill be switched to a non-resonant angle, $\theta = 10°$, in order to observe the modifications or electron heating when the SPW is not excited and the geometry effect is reduced.

Fig.4.27 shows the angular distribution of the electrons for $d = \lambda_0/3$, when the SPW is excited, at the time $t = 500\omega_0^{-1}$. In order to separate the electrons recirculating inside the target form those emitted into the vacuum, we will again divide the simulation box into three parts: electrons emitted into the vacuum at the irradiated side ($x = [0 - 240k_0^{-1}]$), electrons inside the plasma ($x = [240 - 262k_0^{-1}]$) and electrons emitted into the vacuum at the rear of the target ($x = [262 - 480k_0^{-1}]$). We observe that, comparing with electrons recirculating inside the plasma for $d = \lambda_0$ (figures 4.25b), hot electrons tend to have negative components of the velocity along y and emission angles in both directions are $\simeq -60°$ and $\simeq 0°$. As for the previous case, we may interpret this considering two groups of electrons which are bouncing back and forth at two different angles, one of which ($-60°$) can be associated with the direction parallel to the target surface for this modulation depth (as shown in fig.2.7). Hot electrons emitted outside the plasma (figures 4.25a,c) have emission angles which correspond approximately to the angles observed for the electrons inside the plasma, and may be associated with electrons which exit the plasma after some reflections.

Comparing with the semi-infinite case having the same target and laser parameters (except for the thickness), we notice that the emission angles for electrons accelerated towards the plasma, shown in fig.4.19a are the same as those found in the laminar target.

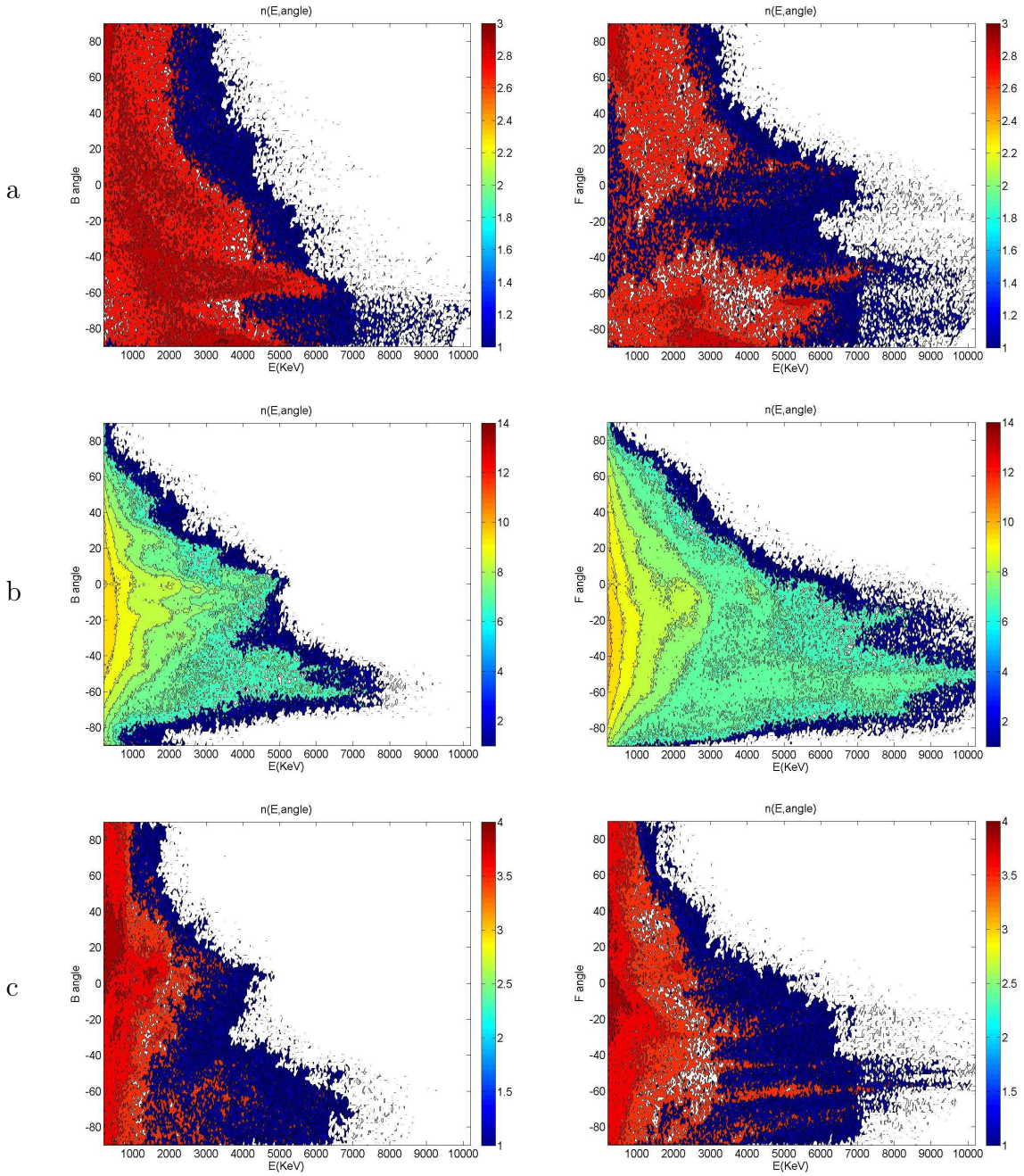

Figure 4.27: Electron emission angles backward (**B**=moving from left to right) and forward (**F**=moving from right to left), for the laminar target of thickness $22k_0^{-1} \simeq 3.5\lambda_0$ and modulation depth $d = \lambda_0/3$, at $t = 500\omega_0^{-1}$; $n_e = 25n_c$, $I\lambda_0^2 = 10^{19}$W cm$^{-2}\mu m^2$ ($a_0 = 2.72$), **when the SPW is excited.(a)** electrons emitted into the vacuum at the irradiated side ($x = [0 - 240k_0^{-1}]$).**(b)** electrons inside the plasma.**(c)** electrons emitted into the vacuum at the rear of the target ($x = [262 - 480k_0^{-1}]$).

In fact the electron currents observed for the laminar (not shown here) and semi-infinite (4.20) cases are qualitatively the same and the choice of the laminar target type only

has the effect of increasing the electron energy.

We will now examine the electron angular distribution for the same target but non-resonant laser angle of incidence $\theta = 10^o$, which is shown in fig.4.28. The main emission angles both inside the plasma (figure 4.28b) and outside (figures 4.28a,c) become $\pm 25^o$, both in the forward and backward directions. In our geometry (see fig.2.7) these directions correspond approximately to the two directions normal to the surface for the modulation having depth $d = \lambda_0/3$ and periodicity $a_m = 2\lambda_0$. If we compare the angular distribution in fig.4.28 with the corresponding resonant case (fig.4.27) we notice that in the non-resonant case the angular distribution is much more symmetric and the angular directions of electrons only correspond to the geometry of the target surface.

Thus the analysis of the reduced modulation depth for the case of the laminar target confirms the results obtained for the semi-infinite target having the same modulation depth: the differences between the resonant and non-resonant case are appears more evident and for the resonant case electrons tend to acquire a larger velocity component in the $-\hat{y}$ direction which is the direction of propagation of the SPW.

4.4 Conclusion

We have studied the electron heating for the case of the semi-infinite target, where the electrons reaching the right side of the target are cooled and re-enter the plasma at thermal velocity, and laminar targets of different thickness. For each target type we have compared the electron acceleration when the angle of incidenceis such that the SPW is resonantly excited and the case where the laser incidence does not match the resonance.

We observed that the electron acceleration depends both on the geometry of the target and on SPW excitation. Particularly in the low laser intensity regime, where the light pressure is such that the density gradient scale length at the surface is of the order of λ_0, the geometry effects are dominant, probably due to absorption mechanisms associated with the density gradient scale lenght. In this case the electron energy is not increased when the SPW is excited. Contrastingly, *in the high intensity regime, where the gradient is sharper, the target geometry dependence is partially reduced and we observe that when the SPW is excited the cut-off energy of the hot electrons is larger than in the cases where the pulse angle of incidencedoes not induce SPW excitation.*

The effects of the SPW are more pronounced when the modulation depth is small ($d < \lambda_0$), which reduces the importance of the target geometry. In this case we observe a larger difference between the resonant and non-resonant angles of incidence both in the hot electron temperature and the cut-of energy. We can also notice a difference in the angular distributions of the accelerated electrons: for non-resonant incidence they are accelerated perpendicularly to the target surface while for resonant incidence they tend to acquire a larger velocity component in the $-\hat{y}$ direction which is the direction of propagation of the SPW.

However, observing the electron currents, there is a characteristic which is found, in both the low and the high laser intensity regimes, only when the SPW is excited: a current of hot electrons which periodically exit the plasma, in a direction which is

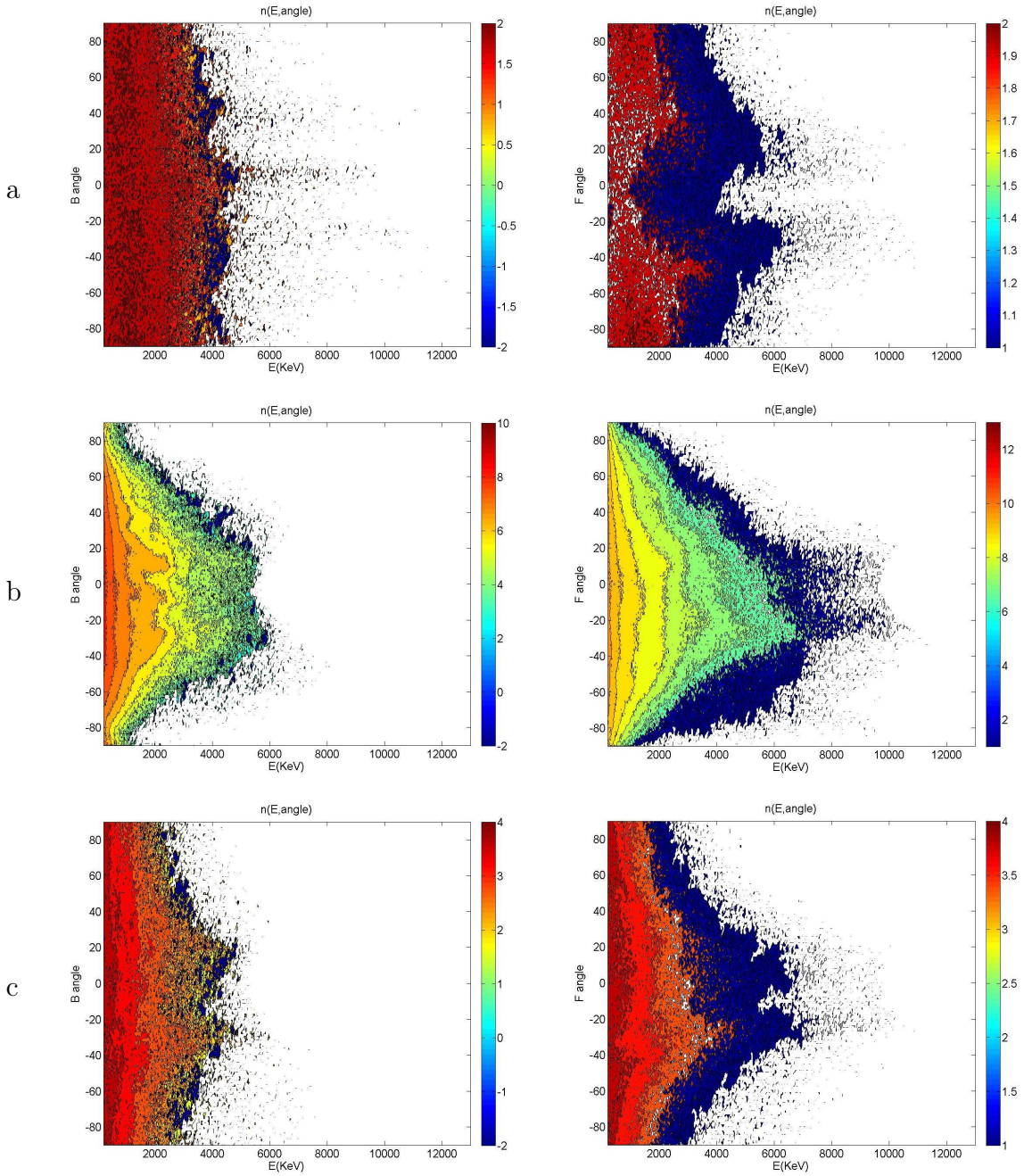

Figure 4.28: Electron emission angles backward (**B**=moving from right to left) and forward (**F**=moving from left to right), for the laminar target of thickness $22k_0^{-1} \simeq 3.5\lambda_0$ and modulation depth $d = \lambda_0/3$, taken at $t = 504\omega_0^{-1}$; $n_e = 25n_c$ and $I\lambda_0^2 = 10^{19}\mathrm{W\ cm^{-2}}\mu m^2$ ($a_0 = 2.72$) **for the non-resonant** 10° **incidence** on the modulated surface.**(a)** electrons emitted into the vacuum at the irradiated side ($x = [0 - 240k_0^{-1}]$).**(b)** electrons inside the plasma.**(c)** electrons emitted into the vacuum at the rear of the target ($x = [262 - 480k_0^{-1}]$).

about normal to the target surface, at two main points situated on the upper part of the modulation depth, one closer to the tip the other close to the bottom. The latter are ejected with a periodicity of one laser cycle, and have a dephase lag of half a laser cycle and correspond spatially to maxima of the SPW. This is coherent with the fact that the *particles are entering the field of the surface wave at the most favourable phase for electron, i.e. the zeros of the SPW field, such that the electrons experience the rising part of the field amplitude (absolute value) and reach the maximum momentum at the peak of the field. Such electrons detach from the surface and exit or enter the plasma depending whether the field is evolving towards a minimum or a maximum*, which explains the phase lag between the two emission points spatially separated by a distance of $\lambda_0/2$.

The study of the laminar target shows that in this case electrons recirculate inside the target: energetic electrons entering the target reach the rear (unirradiated) side where a Debye sheath has formed which reflects them towards the front (irradiated side) of the target. There, they are reflected again from the front sheath towards the rear and so on. The hot electron density at one side then corresponds to a superposition of laser accelerated electrons and electrons that are reentering the target at intervals of twice the transit time. Decreasing the thickness of the target increases the electron energy which is consistent with the fact that in the case of the laminar target electron energy at a given time represents the sum of the energy absorbed by particle after multiple interactions with the driving field. In fact, for thinner targets, the number of bounces that electrons can perform before the driving field is extinguished is greater and a larger number of electrons can perform at least one bounce.

Chapter 5

Ion acceleration

During the past decade, with the rapid development of the laser technology, ion acceleration has received extensive attention in the area of laser-plasma interaction. This has been motivated by the discovery of multi-MeV protons in three experiment performed independently in the year 2000 [24, 25, 26], where an ultra intense laser pulse $I\lambda_0^2 > 10^{18}\text{W cm}^{-2}\mu m^2$ was impinging on metallic targets. The protons, present as contaminants on the target surface, were emitted as a quite collimated beam in the forward direction with respect to the laser beam propagation and were detected at the rear (unirradiated) side of the target. Indeed, emission of energetic protons and heavier ions in the interaction of laser with solid targets had been observed previously at the irradiated side of the target [31], but they had a broad angular distribution and were interpreted in terms of the expansion of the hot laser-produced plasma. However the characteristics of the ion emission at the rear side of the target attracted more attention due to the high degree of collimation which was suitable for applications requiring highly localized energy deposition in dense matter, such as proton therapy [81, 82, 83] and laser fusion [84]. The emission from both the rear and the front surface can be related to the sheat field generated near the target surface due to charge separation, as described in section 1.5.1, where the Target Normal Sheat Acceleration (TNSA) was presented.

In the following we will present the results of our PIC simulations concerning ion acceleration in presence of a SPW. The TNSA mechanism, which accelerates ions towards the vacuum, was observed for the whole range of laser intensities while shock acceleration, which accelerates ions inside the plasma (see sec.1.5.2), is only observed for simulations at high laser intensities, consistently with what was observed in the literature [37, 36].

We will initially focus on the characteristics of ion emission from the irradiated surface, in order to identify the main acceleration mechanisms. The case of the resonantly excited SPW will be compared with the case of a plane target in order to contrast ion energy and emission angles for the low-intensity pulse regime ($I\lambda_0^2 = 10^{16}\text{W cm}^{-2}\mu m^2$) and the relativistic regime ($I\lambda_0^2 = 10^{19}\text{W cm}^{-2}\mu m^2$). The effects of the modulation depth and of non-resonant angle of incidences will also be studied, comparing two main values for modulation depth ($d = \lambda_0, \lambda_0/3$) and pulse angle of incidences ($\theta = 10°, 20°$). Finally we will examine the laminar target and the ions accelerated at the rear side of

the target.

5.1 Characteristics of ion emission

In this section the characteristics of the ion emission from the irradiated surface will be analyzed, in the case of a semi infinite target, for two interaction regimes corresponding to $I\lambda_0^2 = 10^{16}$W cm$^{-2}\mu m^2$ and $I\lambda_0^2 = 10^{19}$W cm$^{-2}\mu m^2$. The resonant excitation here corresponds, as for the previous chapters, to the angle of incidenceof $\theta = 30^o$ as we have a plasma density $n_e = 25n_c$ and a modulation periodicity of $2\lambda_0$. The plasma occupies the right half-space for an extension of about $8\lambda_0$ with the tips of the modulated surface located at $x = 240k_0^{-1}$ and the laser pulse peak impinges on the modulated surface at $t_{peak} = 440\omega_0^{-1}$. The modulation depth was equal to λ_0 here.

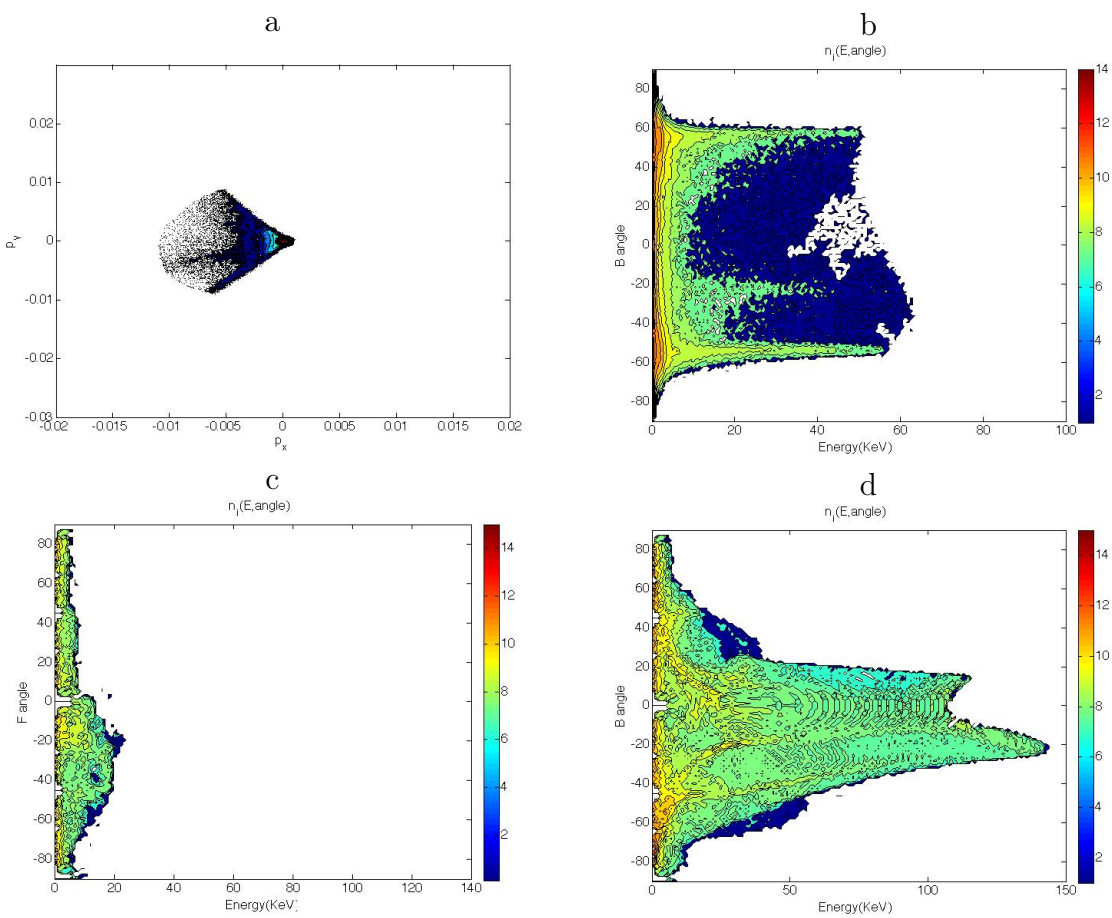

Figure 5.1: (a) Ion phase space at $t = 500\omega_0^{-1}$ where we observe no forward (F) emission. (b) Ion emission angles backward distribution (log scale) at $t = 500\omega_0^{-1}$, (c) ion emission angles forward distribution at $t = 1000\omega_0^{-1}$ (d) same as (b) at $t = 1000\omega_0^{-1}$ as a function of energy. $I\lambda_0^2 = 10^{16}$W cm$^{-2}\mu m^2$ ($a_0 = 0.086$), $d = \lambda_0$, semi-infinite target, **when the SPW is excited**. (Note: the maximum value of the abscissa varies in the different plots).

Ion emission will be observed at two different stages: i) at time $t = 500\omega_0^{-1}$, corresponding to the maximum electron heating (see chapter 4), in order to study the initial coupling with hot electrons via TNSA and ii) at time $t \simeq 1000\omega_0^{-1}$ corresponding approximately to the observed saturation of the ion acceleration mechanism, after the complete reflection of the laser pulse (occurring at $t \simeq 740\omega_0^{-1}$). In this section we will focus only on the angular emission and its evolution while the final energy of the ions will be analyzed in section 5.6.

In the *low intensity case*, *when the SPW is excited* we observe (fig. 5.1a,b) that energetic ions are emitted towards the vacuum only and have a very symmetric angular distribution peaked at two main angles, 60° and −60°, at $t = 500\omega_0^{-1}$. For the present geometry, this angular distribution can be interpreted as an expansion towards the vacuum where ions move perpendicularly to the modulated target surface (we recall that the angular direction perpendicular to the surface is approximately as 60° for the upper part of the tips and −60° for the lower one as shown in fig.2.7). This interpretation is confirmed by the corresponding ion density and current vector plot, in fig.5.2a and fig.5.2b, where we observe ions accelerated in the direction perpendicular to the target surface, towards the vacuum. We notice that the filaments of higher ion density appearing at the center of each cavity, in fig.5.2a, are due to the focusing effect of the modulation depths and are a pure geometrical effect of the target shape. A secondary angle is also identified, around (−25°, which may correspond the direction tangent to the modulation curve. The latter is not visible in the ion current plot in fig.5.2, as it is hidden by the currents associated with the plasma expansion. Figures 5.1c,d show the evolution of the angular distribution at $t = 1000\omega_0^{-1}$: the main emission angles in the forward direction have changed and we find two main angles, ±20°. We notice that the negative angle corresponds to the higher energies. Thus the most energetic ions are associated with emission angles at later times that are smaller than the emission angles found at $t = 500\omega_0^{-1}$ and their energy is significantly increased. This can be interpreted as an evolution of the initial ion velocity in the acceleration process or as the presence of two groups of ions which undergo a different acceleration.

Shock is not observed consistently with [37] and few ions are moving forwards, towards the plasma bulk (fig.5.1c).

For a *flat target and the same laser pulse intensity* $I\lambda_0^2 = 10^{16}\, W\, cm^{-2}\mu m^2$, the emission angles are distributed around the flat surface normal, corresponding here to 0°, as shown in figs.5.3b,d. This distribution does not evolve to different angular emission at later times, as it can be observed in fig.5.3c. As for the resonant case, we do not observe energetic ions (> 20keV) accelerated towards the plasma bulk, and no shock wave is produced. The ion phase space is substantially contained in the $p_x > 0$ half-space during the whole interaction, as shown in figs.5.3a,c. We notice that the final energy of the ions at $t = 1000\omega_0^{-1}$ is lower than in the resonant case.

Considering the angular direction of the ions, we may conclude that in both cases the mechanism of ion acceleration can be identified with the TNSA mechanism, which is taking place at the irradiated surface, where electrons expanding towards the vacuum are setting up a charge separation field. The latter accelerates the ions in the direction perpendicular to the target surface, as described in section 1.5.1. Moreover, according to the TNSA model, the final ion energy (which will be examined in section 5.6) depends

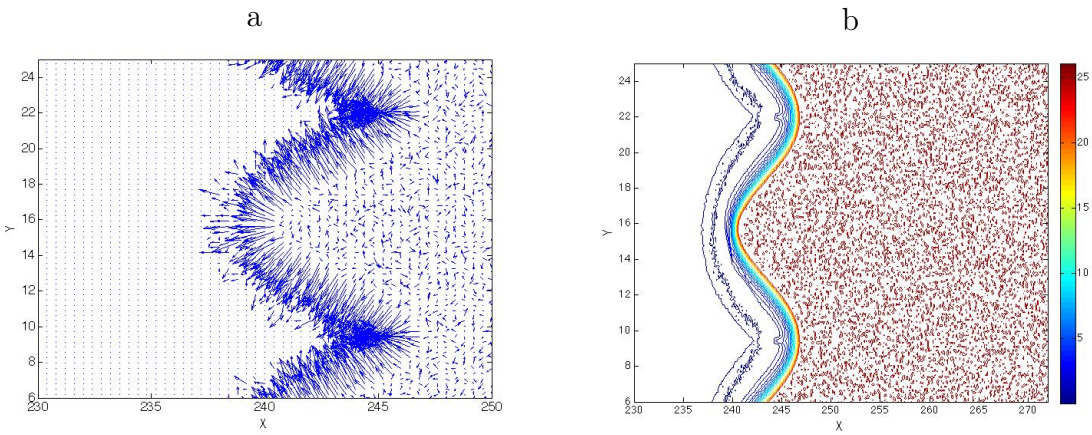

Figure 5.2: Ion current vector plot (a) and ion density (b) taken at time $500\omega_0^{-1}$. $I\lambda_0^2 = 10^{16}$W cm$^{-2}\mu m^2$ ($a_0 = 0.086$), $n_e = 25n_c$, $d = \lambda_0$, semi-infinite target, **when the SPW is excited**.

on the hot electron energy and this is coherent with the decrease of the ion energy observed for the flat target, where the electron energy is lower than for the grating target, where the SPW is excited.

In the *high intensity case, when the SPW is excited* ($I\lambda_0^2 = 10^{19}$W cm$^{-2}\mu m^2$), the ion angular distribution of the energetic ions emitted towards the vacuum is still quite symmetric at $t = 500\omega_0^{-1}$: we find a double peak on each side (positive, negative) of the angular distribution around $\pm 30°$ (fig. 5.4). However we observe that a larger number (a factor ~ 10) of ions is emitted at the negative angle -30° and the maximum ion energy is higher compared with the corresponding positive peak (30°).

Comparing the angular distribution of the ions emitted backwards at $t = 500\omega_0^{-1}$, for $I\lambda_0^2 = 10^{19}$W cm$^{-2}\mu m^2$ (fig.5.4b) with the corresponding distribution in the case having $I\lambda_0^2 = 10^{16}$W cm$^{-2}\mu m^2$ (fig.5.1b) we notice that for the high intensity case the emission angles of the ions do not correspond to the direction normal to the target surface, despite of the fact that the symmetry of the angular distribution suggests that they are related to the expanding front. Moreover, the angular direction associated with the most energetic ions evolves further at $t = 1000\omega_0^{-1}$, moving to smaller values of the emission angles, $\pm 20°$. We also notice that the distribution becomes more asymmetric and the number and energy of ions is much greater at the angle $-20°$ for $t = 1000\omega_0^{-1}$. We recall that in the low intensity case too we observed a similar evolution of the backward accelerated ions, but at $t = 500\omega_0^{-1}$ the values still corresponded to the surface normal ($\theta_T \simeq \pm 60°$). As for the low intensity case, there may be two different interpretations: i) ions are emitted perpendicularly to the surface and their angular direction changes during the acceleration ii) there are ion bunches which undergo different accelerations such that they acquire more energy and have a different a direction compared with the ions in the expanding front. Both these interpretations can be valid, as we will see in the following.

Observing the ion current and density in fig.5.5, we can identify two groups of ions: those associated with the expanding front and the *filaments emitted at different points*

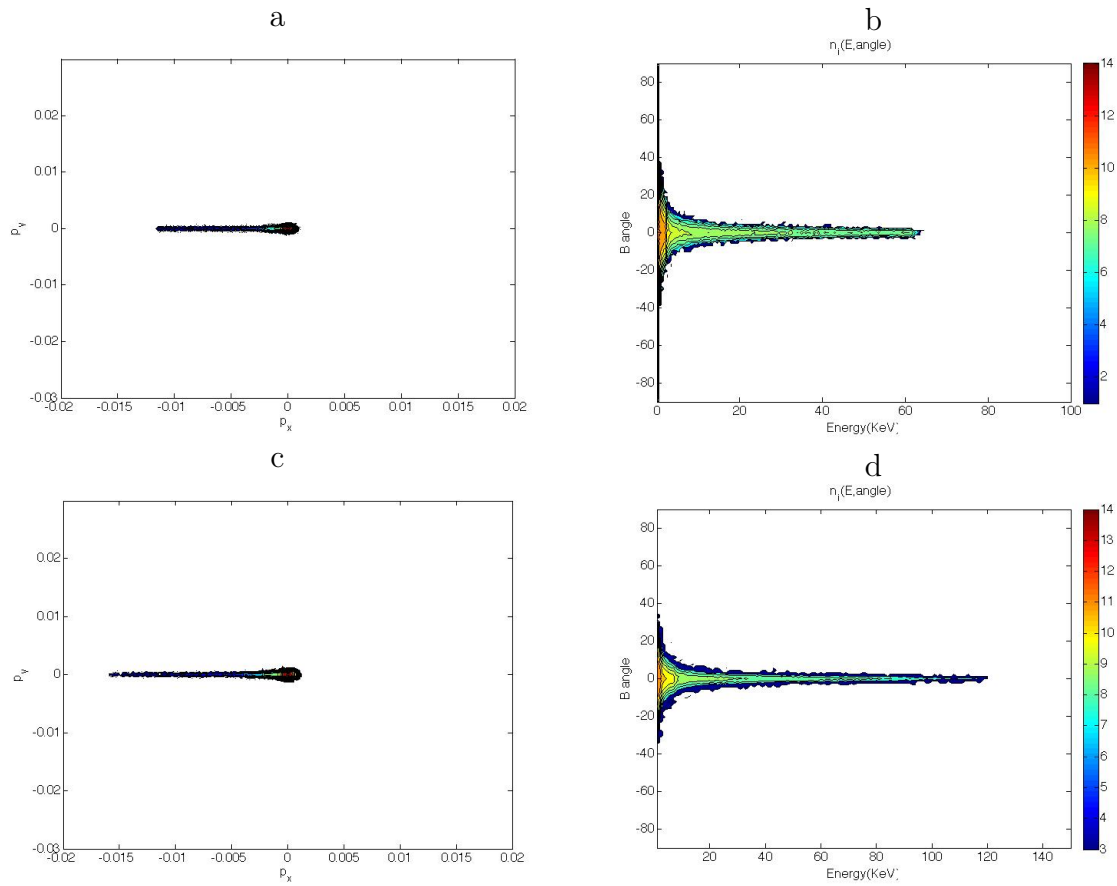

Figure 5.3: Ion phase space at $t = 500\omega_0^{-1}$ (a) and $t = 1000\omega_0^{-1}$ (c) where we observe no forward (F) emission. Ion emission angles backward (B) distribution (log scale) at $t = 500\omega_0^{-1}$ (b) and $t = 1000\omega_0^{-1}$ (d) as a function of energy and ion phase space. $I\lambda_0^2 = 10^{16}$W cm$^{-2}\mu m^2$ ($a_0 = 0.086$), $n_e = 25n_c$, semi-infinite target, **for the flat surface**.

along the lower part of each tip. The expanding front gives a similar contribution to the two peaks in fig.5.4b and fig.5.4d while the filaments can only give a contribution to the negative peak. Consequently we may infer that the filaments cause the asymmetry in the two peaks and correspond to the most energetic ions observed in the angular distribution. We also notice that *the filaments are generated at points that correspond to the emission points of the electrons bunches found in the previews chapter* (fig.4.13) which exit and re-enter the plasma periodically. Therefore we can infer that the latter may have caused a charge unbalance over many oscillation periods which has driven the ion acceleration. This mechanism would be similar to that described in reference [29], where, differently from classical TNSA, the acceleration is found to be directly driven by Brunel electrons, dragged in and out of the plasma by the laser electric field. After these considerations, if we examine again the evolution of the angular distribution in figs.5.4b,d, we notice that both the negative and positive angles evolve towards smaller values. *Thus we may conclude that the angular evolution in the backward direction is the final result of the presence of two groups of ions and of a progressive change in their*

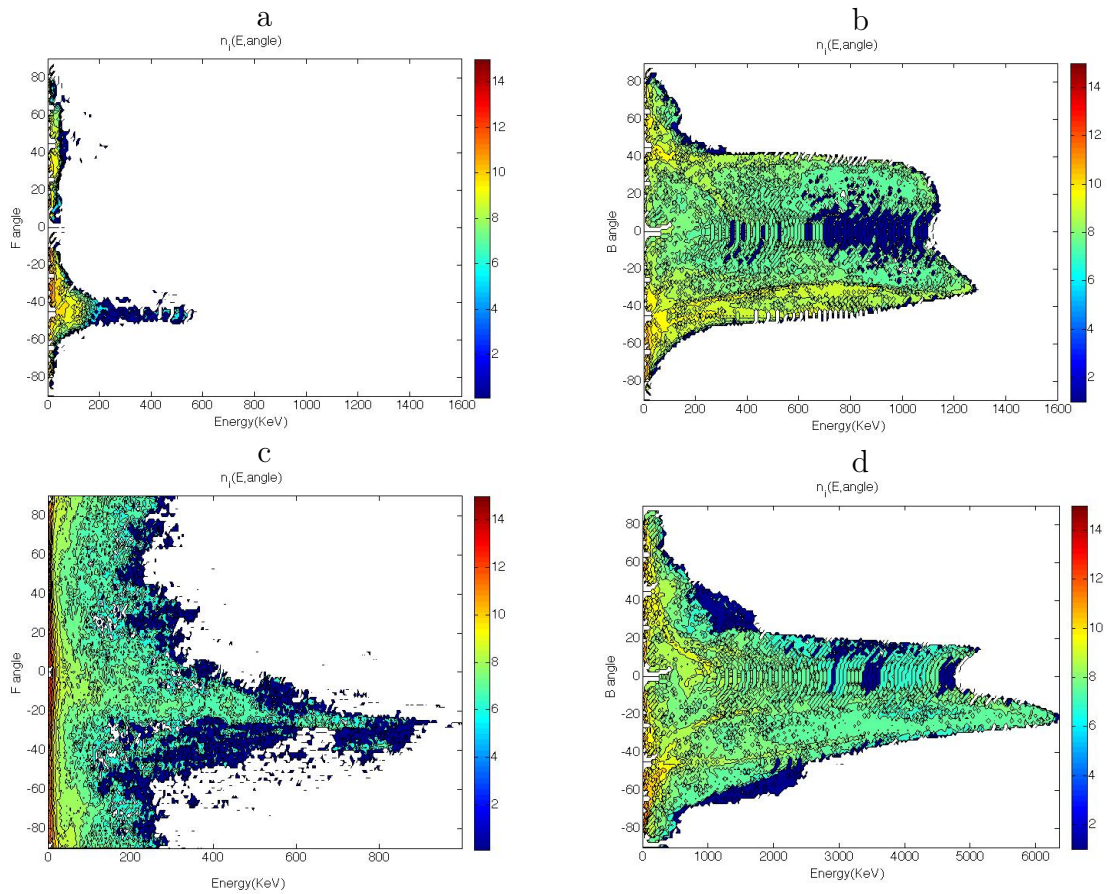

Figure 5.4: Ion emission angles forward (a) and backward (b) distributions (log scale) as a function of energy and ion phase space at $t = 500\omega_0^{-1}$; forward (c) and backward (d) distributions at $t = 1000\omega_0^{-1}$, as a function of energy. $I\lambda_0^2 = 10^{19}$W cm$^{-2}\mu m^2$ ($a_0 = 2.72$), $n_e = 25n_c$, $d = \lambda_0$, semi-infinite target, **when the SPW is excited**.

inner angular direction. We shall now consider the ion emission in the forward direction (for the high intensity case, when the SPW is excited). At $I\lambda_0^2 = 10^{19}$W cm$^{-2}\mu m^2$, in contrast with the low intensity case, ions are also accelerated towards the plasma, with an emission angle of about -40° (fig.5.4a,c). This can be interpreted as a shock front (studied in detail in section 5.2) which is propagating into the plasma, accelerating ions by the mechanism described in section 1.5.2. In fact, in the density plot of fig.5.5 we can observe a very localized high density sheath (red/yellow area), reaching $\simeq 70n_c$, that is about 3 times the surrounding plasma density. The latter can be identified with the shock front that has been ponderomotively launched and is moving from the surface towards the bulk.

Finally, *for the flat target and high intensity laser pulse* (fig.5.6) we find that the ion emission is always perpendicular to the target, both for ions emitted into the vacuum and ions accelerated by the shock front into the plasma bulk.

We notice that the ions accelerated towards the vacuum are fewer at $t = 500\omega_0^{-1}$ than the shock accelerated ions, which means that the TNSA mechanism is less efficient for the flat target. Moreover, comparing the angular plots for the forward emission in

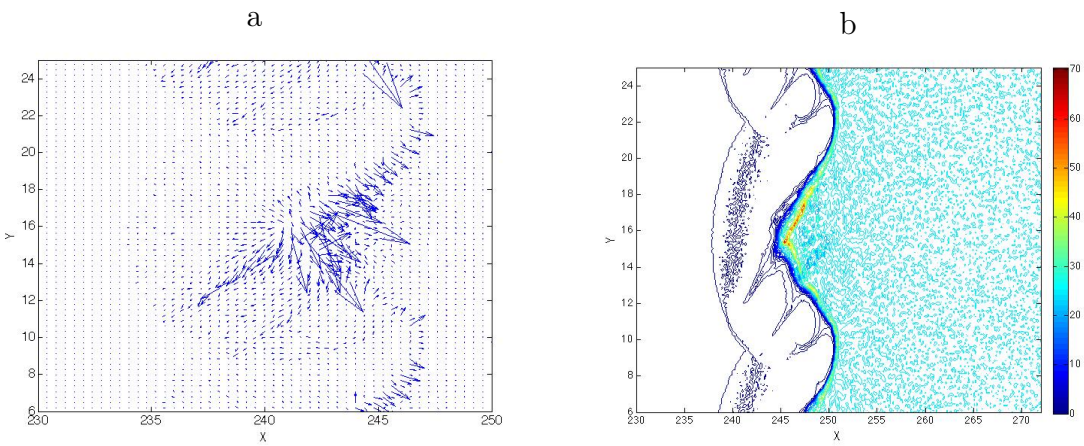

Figure 5.5: Ion current vector plot (a) and ion density (b) taken at time $t = 500\omega_0^{-1}$, for $I\lambda_0^2 = 10^{19}$W cm$^{-2}\mu m^2$ ($a_0 = 2.72$), $d = \lambda_0$, semi-infinite target,**when the SPW is excited**.

fig.5.4b and fig.5.6b, we observe that for the ions associated with the shock, the energy value when the SPW is excited and for the flat target are similar (of the order of 700keV at $t = 1000\omega_0^{-1}$), and the most important difference is found for ions accelerated by TNSA whose cut-off energy is only 1.6MeV. This is consistent with the dependence of this mechanism on hot electron energies, as the electron temperature for the flat surface is much lower than in the case of SPW excitation (see tab.4.3).

In this first overview of the ion emission, we have examined the case of resonant SPW excitation and flat surface, for two laser intensity regimes, when the target is semi-infinite. We have identified two acceleration mechanisms: the TNSA, which accelerates ions towards the vacuum and shock acceleration which pushes the ions inside the target. The first mechanism is observed in all the cases that we have examined while the second one is present only for high laser intensities ($I\lambda_0^2 > 10^{18}$W cm$^{-2}\mu m^2$). In the cases where the SPW is excited the TNSA mechanism is enhanced compared to the flat target cases. This is particularly evident in the high intensity range where we find that, when the wave is not excited, the shock acceleration is more efficient than the TNSA while in the case of SPW excitation the TNSA is dominant. The enhancement of TNSA can be traced back to the efficient electron heating due to the wave resonant field, as discussed in chapter 4. In the presence of the surface wave we also observe a general increase of the number of ions accelerated at negative angles ($v_y < 0$), in the backward direction. This effect is more pronounced in the high intensity case ($I\lambda_0^2 = 10^{19}$W cm$^{-2}\mu m^2$), where *we observe very energetic ions emitted in filaments at the lower side of each tips. We associate the ion filaments to bunches of electrons accelerated at the same points by the SPW field, as shown in chapter 4.*

In the next section we will examine shock acceleration in detail in order to determine the effect of SPW excitation on this mechanism.

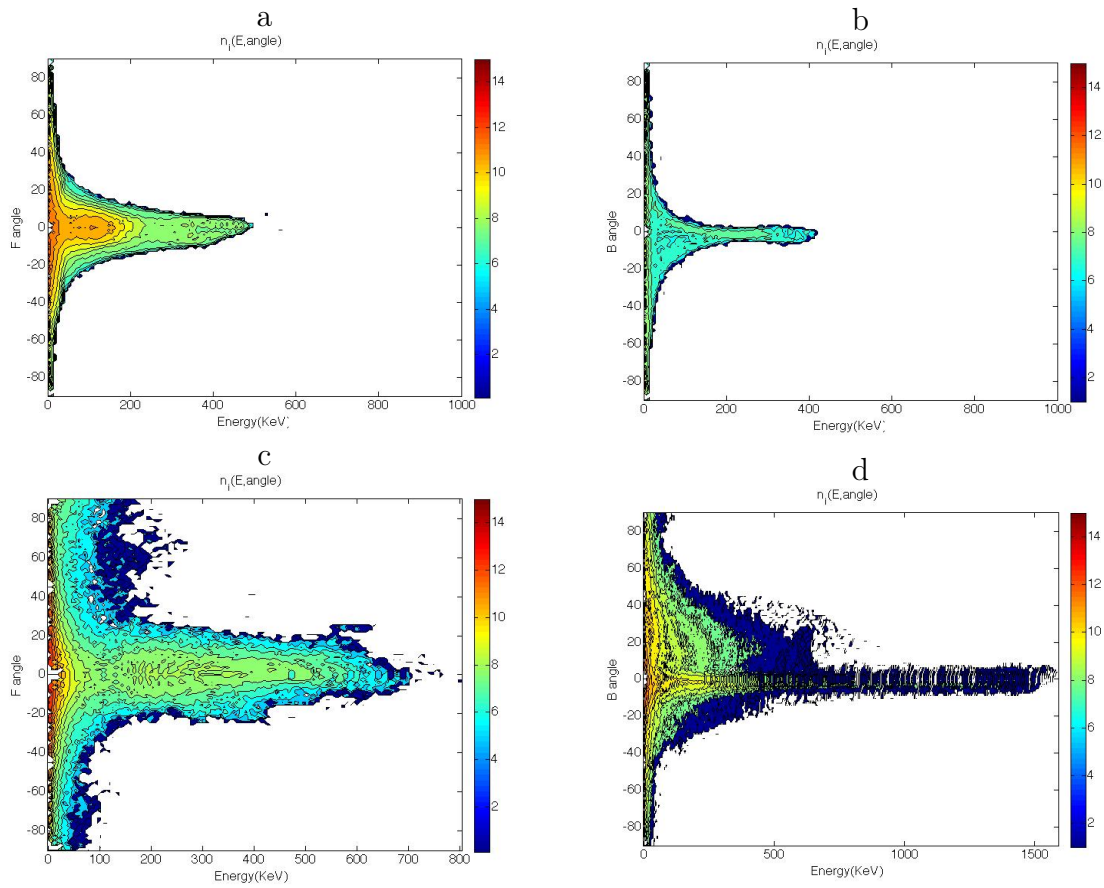

Figure 5.6: Ion emission angles forward (a) and backward (b) distribution at $t = 500\omega_0^{-1}$; emission angles forward (c) and backward (d) distributions at $t = 1000\omega_0^{-1}$, as a function of energy. $I\lambda_0^2 = 10^{19}$W cm$^{-2}\mu m^2$ ($a_0 = 2.72$), $n_e = 25n_c$, semi-infinite target, **for the flat surface**.

5.2 The shock front

In PIC simulations where the laser energy exceeds $I\lambda_0^2 \sim 10^{19}$W cm$^{-2}\mu m^2$ a shock front is observed which is formed at the irradiated target surface and propagates towards the rear side. The shock can be identified with a peak in electron/ion density which is of the order of three times the unperturbed plasma density. In order to study the possible modifications of the shock parameters when a SPW is excited at the target surface, we will compare the characteristics of the shock for the flat surface case and the case where the SPW is excited.

From the density plot of fig.5.7 we can give an estimation of the velocity of the shock. We have considered two interaction times: $t = 600\omega_0^{-1}$, that is a time at which the shock front becomes quite visible in the density plot and a later time, $t = 1000\omega_0^{-1}$, at which the surface wave is extinguished and the TNSA mechanism saturates.

If we take the point of the front situated at $y = 6k_0^{-1}$ in fig.5.7a) (corresponding to $t = 600\omega_0^{-1}$), which is initially located at $x = 246k_0^{-1}$, we find (fig.5.7b) that it has moved to $x = 250k_0^{-1}$ after $400\omega_0^{-1}$. This means that the shock velocity would be

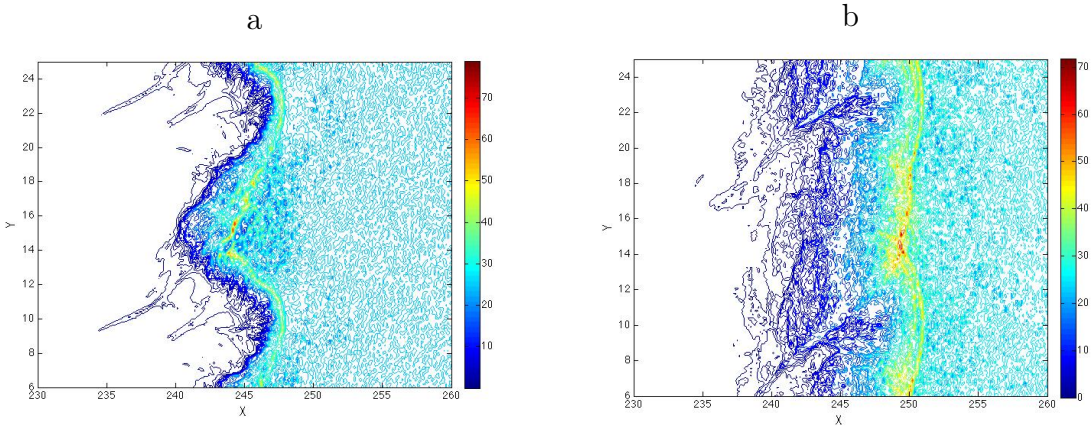

Figure 5.7: Ion density taken at time $t = 600\omega_0^{-1}$ (a), and $t = 1000\omega_0^{-1}$ (b), for $I\lambda_0^2 = 10^{19}$W cm$^{-2}\mu m^2$ ($a_0 = 2.72$), $n_e = 25_c$, $d = \lambda_0$, semi-infinite target, **when the SPW is excited**.

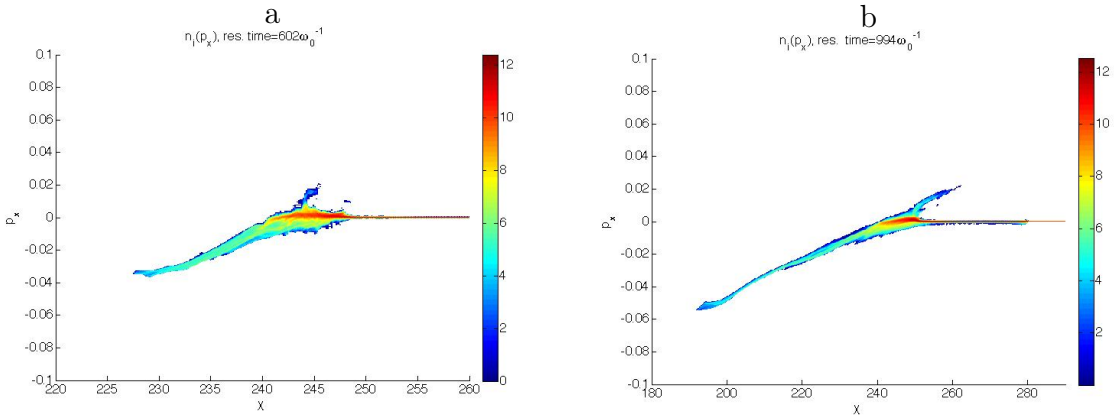

Figure 5.8: Ion phase space (p_x, x) at time $t = 600\omega_0^{-1}$ (a), and $t = 1000\omega_0^{-1}$ (b). $n_e = 25_c$, $I\lambda_0^2 = 10^{19}$W cm$^{-2}\mu m^2$ ($a_0 = 2.72$), $d = \lambda_0$, semi-infinite target, **when the SPW is excited**.

$v_{x,shock} = 0.01c$ if we neglect the fact that the shock front is also deforming. As the direction of propagation of ions moving from the surface towards the bulk was found to be at an angle of about $-40°$ with respect to the x axis, the actual shock velocity is higher than the x component and can be estimated as $\simeq v_{shock}/\cos(40°) = 0.013c$. This estimation can be verified considering the maximum ion velocity reached by the ions in the direction of propagation of the shock ($\hat{x}$). In fig.5.8 we can observe the ion (p_x, x) phase space: the shock corresponds to the positive v_x peak which is moving forwards, inside the plasma. The maximum velocity found for the x component in this direction is $v_{x,max} = 0.022c$, thus if we assume $v_{x,max} = 2v_{x,shock}$ (as predicted from the model in 1.5.2), we have $v_{x,shock} = 0.01c$, which is consistent with the previous estimation.

In order to estimate the Mach number $M = v_{shock}/c_s$, we will calculate the sound velocity $c_s = \sqrt{T_e/m_i}$ using the hot electrons energy value in tab.4.1, $T_{hot} = 1.9$MeV. We get $c_s = 0.043c$, therefore *the Mach number would be* $M = v_{shock}/c_s = 0.3$*, which*

is lower than the minimum Mach number value that is required by the model in 1.5.2 ($1 < M \geq 1.6$*) to have a shock.* We may argue that in that model the electrons are treated as isothermal while, when they are treated exactly, the limits appearing in theory do not apply [63]. For example in [36], where the electron temperature is calculated following the ponderomotive scaling of equation (4.1), Mach numbers around $M = 2-3$ are obtained while in [63], where a Maxwellian plasma is used which is impinging on a reflective wall, Mach numbers are around $M = 3-3.5$. Thus, even if the model does not apply exactly, the values found in our simulation are much lower than the values reported in literature and *the most reasonable interpretation is that the shock is driven by electrons having lower temperature.* In fact, in order to have $1 < M \geq 1.6$ with our value of the shock velocity, the electron temperature should be in the range $38-100$keV and the cold electron temperature in this case is $T_{cold} = 54$keV (see tab.4.1).

For *the flat surface* the ion density peak is found to be of the same order of the resonant case $\simeq 70-60n_c$. The shock front is located at $x = 242k_0^{-1}$ for $t = 600\omega_0^{-1}$, as we can observe in fig.5.9, and moves to $x = 247k_0^{-1}$ for $t = 1000\omega_0^{-1}$.

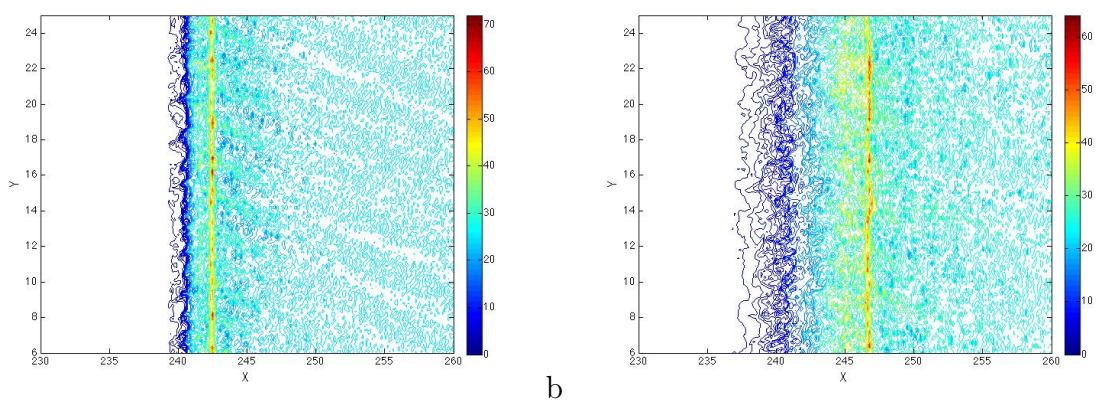

Figure 5.9: Ion density taken at time $t = 600\omega_0^{-1}$ (a), and $t = 1000\omega_0^{-1}$ (b). $I\lambda_0^2 = 10^{19}$W cm$^{-2}\mu m^2$ ($a_0 = 2.72$), $n_e = 25_c$, semi-infinite target, **for the flat surface**.

Here the shock does not deform and appears to be perpendicular to the target planar surface; we may estimate the shock velocity as $v_{flat,shock} \simeq 0.013c$, which is the same value as when the SPW is present. As previously done, we can verify this estimation from the the ion (p_x, x) phase space plot in fig.5.10 a), where we find a maximum ion velocity in the forward direction of $v_{x,max} \simeq 0.025c$, which would give a shock velocity of about $0.0125c$. In this case, if we consider the hot electron temperature, the Mach number is $M = 0.43$ (where we used the temperature $T_{hot} = 860$keV of the flat target in tab.4.1), which is once again lower than the minimum Mach number ($M = 1$) value required by the model in 1.5.2 to have a shock. By contrast, if we consider the cold electron temperature $T_cold = 38$keV the Mach number becomes $M \simeq 1.6$ and, according to the theory, this allows the generation of a shock.

Fig.5.10a) also reveals an interesting feature of the ions accelerated by TNSA at the front surface: we can distinguish two groups of ions for the flat target which were not visible in the angular distribution. One group, formed by a few ions, is more distant

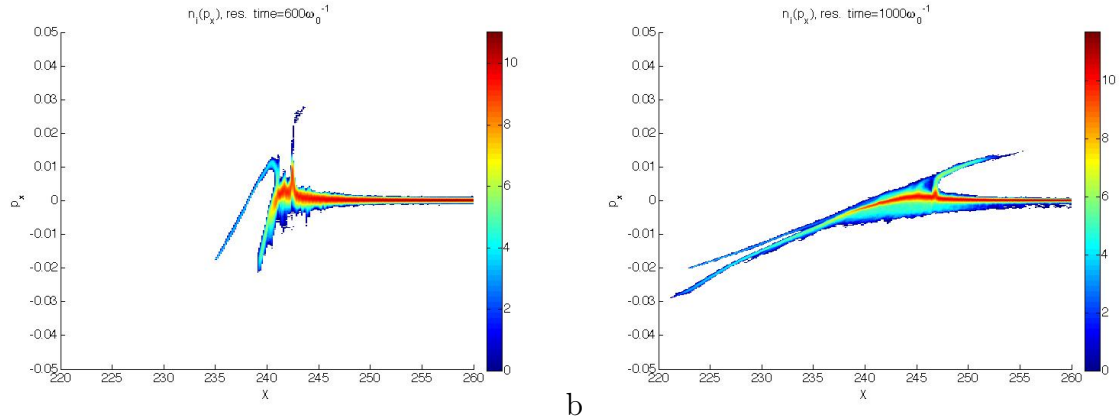

a b

Figure 5.10: Ion phase space (px, x) at time $t = 600\omega_0^{-1}$ (a), and $t = 1000\omega_0^{-1}$ (b). $I\lambda_0^2 = 10^{19}$W cm$^{-2}\mu m^2$ ($a_0 = 2.72$), $n_e = 25_c$, semi-infinite target, **for the flat surface**.

from the target surface at $t = 600\omega_0^{-1}$ (the surface is located at $x = 240k_0^{-1}$) and is moving away from the target since the beginning of the interaction while the second one, which appears later, is closer to the target surface at $t = 600\omega_0^{-1}$. These two groups seem to experience different acceleration as at time $t = 1000\omega_0^{-1}$ (fig.5.10b)) the second group has overtaken the first group and reached a velocity of $\simeq 0.3c$ while the first one has a velocity of $\simeq 0.2c$.

From the shock analysis carried out in this section we may conclude that the velocity of the shock has no dependence on the hot electrons temperature. The electrons involved in shock acceleration have a temperature of some tens keV, which corresponds to the temperature of the cold electron population, and the SPW excitation, associated with hot electron generation, does not give a crucial contribution to this acceleration mechanism.

5.3 Non-resonant angles

In section 4.2.1 we observed that electron acceleration changed drastically in the case of non-resonant angle of incidences, for which the emission along the target surface was found to be non-periodic. We expect this difference to cause some change in the ion acceleration as we observed in fig.5.5 that filaments of ions develop at the same points as where bunches of electrons are emitted in the resonant case, which suggests a strong correlation between electron and ion motion. As we found that the SPW effects on electron emission are more evident in the high laser intensity case, we will focus here on the case having pulse intensity $I\lambda_0^2 = 10^{19}$W cm$^{-2}\mu m^2$, for the study of the ion emission dependence on pulse angle of incidenceand modulation depth. This choice will allow us, at the same time, to analyze the effect of the angle of incidence on the shock, which is launched for this range of pulse intensity.

For the non resonant angle of incidence $\theta = 10°$ (fig.5.11), we find that the ions are accelerated towards the vacuum (b) at the angles $\pm 30°$ and $0°$ at $t = 500\omega_0^{-1}$. Fewer ions are accelerated forward (a), into the plasma bulk, and we can distinguish a main peak (600keV) around $\simeq 60°$ and a secondary one (400keV) around $\sim 10°$. At later

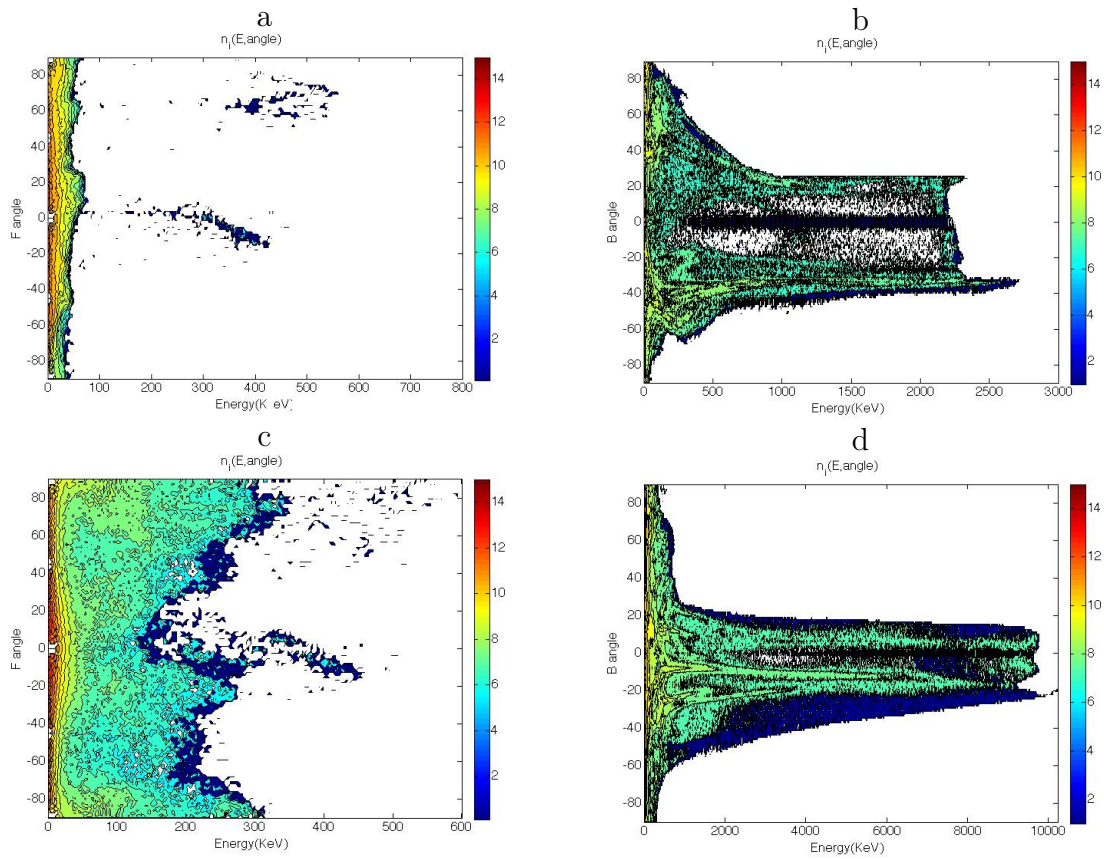

Figure 5.11: Ion emission angles forward (a) and backward (b) distributions (log scale) as a function of energy at $t = 500\omega_0^{-1}$ and emission angles forward (c) and backward (d) distributions (log scale) as a function of energy at $t = 1000\omega_0^{-1}$. $I\lambda_0^2 = 10^{19}$W cm$^{-2}\mu m^2$ ($a_0 = 2.72$), $d = \lambda_0$, semi-infinite target, **for the non-resonant angle** $\theta = 10°$.

times the angular distribution evolves and the emission angles in the backward direction (d) become $\pm 20°$ and $0°$ at $t = 1000\omega_0^{-1}$. As for the resonant incidence, we find that the angular directions of ions generally tend to converge towards smaller angles during the acceleration process. At the same time, in the forward direction (c), associated with the shock acceleration, the peaks become smooth and difficult to distinguish and are located around $0°$ and $70°$.

From the analysis of the ion density density plots in fig.5.12 taken at three different times, $t = 500\omega_0^{-1}$, $t = 600\omega_0^{-1}$, and $t = 1000\omega_0^{-1}$, we can give an interpretation of the features of the ion angular distribution and its evolution. In fig.5.12a, i.e. for $t = 500\omega_0^{-1}$, we observe an expanding ion front and some filaments at the lower part of each tip, which develop towards the vacuum. The ion front may be associated with the symmetric angles $\pm 30°$, as discussed in section 5.1, while the higher energy of the peak at $-30°$ can be associated with the filaments which have $v_y < 0$. Moreover the final angular distribution at $t = 1000\omega_0^{-1}$ can be explained by the new filaments appearing on the upper side of the tips at later times, which can be clearly seen in fig.5.12b. In fact the filaments of ions emitted in the vacuum correspond to the electron emission

points of fig.4.17, and can be interpreted as the effect, averaged over many periods, of electron oscillations at given points of the surface, which have caused charge unbalance. *As was said for the electron emission points (see section4.2.1), the generation of these filaments is not caused by the excitation of a surface wave, but is determined by the interference pattern of the laser field at the target surface.*

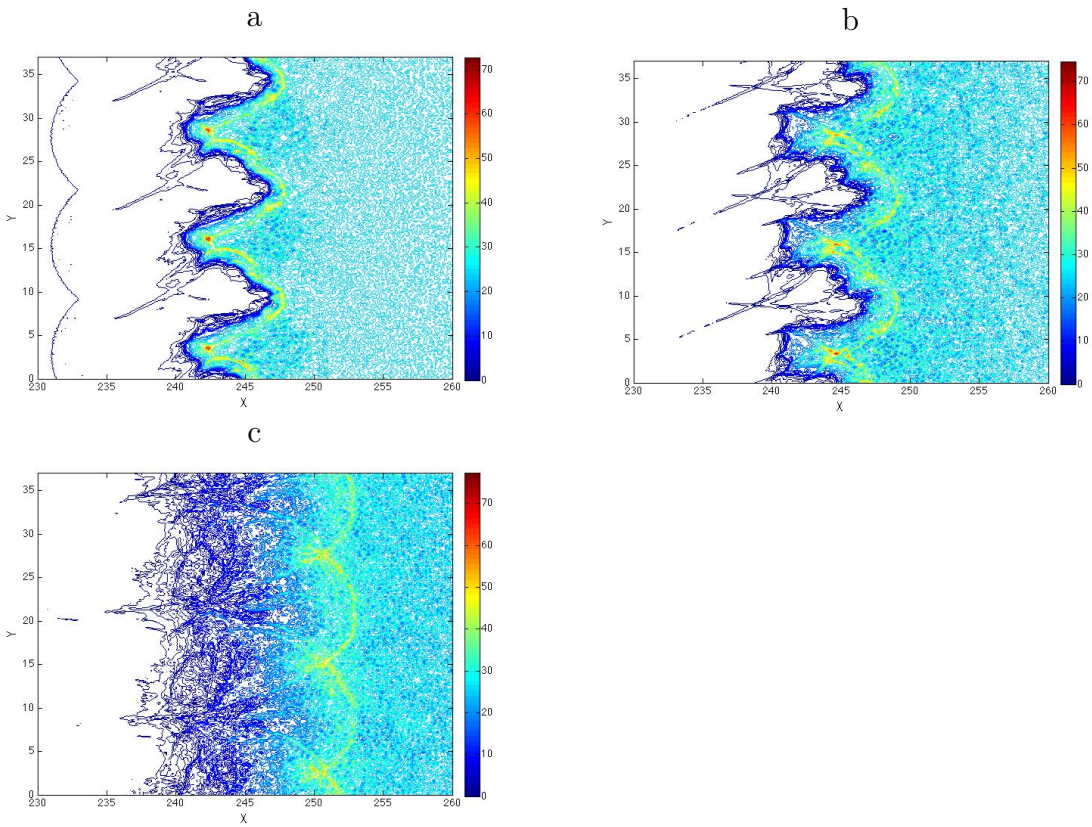

Figure 5.12: Ion density at times $t = 500\omega_0^{-1}$ (a), $t = 600\omega_0^{-1}$ (b), and $t = 1000\omega_0^{-1}$ (c) **for the non-resonant angle** $\theta = 10°$. $I\lambda_0^2 = 10^{19}$W cm$^{-2}\mu m^2$ ($a_0 = 2.72$), $d = \lambda_0$, $n_e = 25n_c$, semi-infinite target.

At $t = 500\omega_0^{-1}$, for *the non-resonant case having angle of incidence* $\theta = 20°$ (not shown here) we find essentially the same emission angles as for $\theta = 10°$. The ions accelerated backwards are emitted at three main angles, $\pm 30°$ and $0°$ while in the forward direction we find a main peak (400keV) around $\simeq 60°$ and a secondary one (100keV) at $-30°$. Also, the evolution of the angular distribution at later times ($t = 1000\omega_0^{-1}$) appears similar. In the backward direction we find the same peaks that were found for $\theta = 10°$, even though the maximum energy is lower, being only 7MeV while we had 10MeV for $\theta = 10°$. In the forward direction instead, ions have the same final energy and approximately the same angular distribution, with directions around 0° and 70°. The analysis of the angular distribution in the case non-resonant angle of incidence $\theta = 20°$ is analogous to that previously done for $\theta = 10°$: ions emitted into the vacuum have the angular direction given by the expanding front or by the filaments developing at the surface, generated by non-periodic electron oscillations and having the same

characteristics as mentioned above for $\theta = 10°$ *but different locations* (see fig.5.13c).

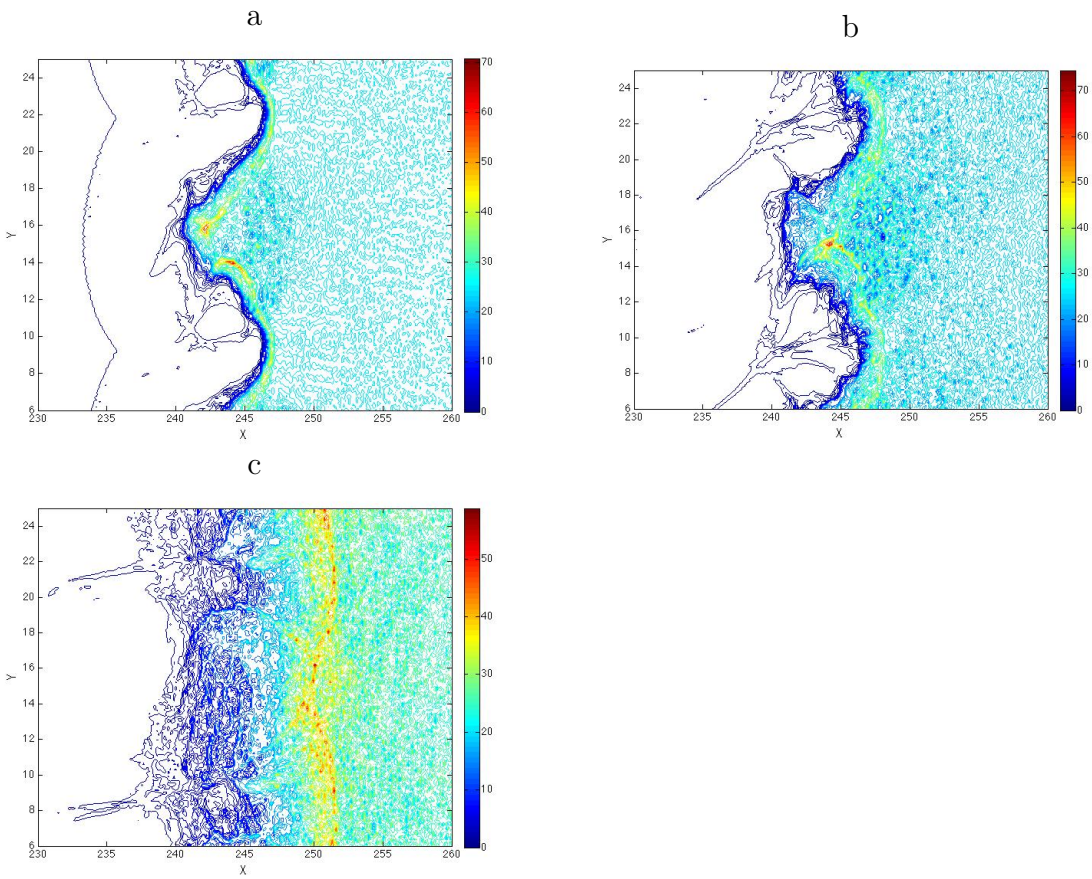

Figure 5.13: Ion density at times $t = 500\omega_0^{-1}$ (a), $t = 600\omega_0^{-1}$ (b), and $t = 1000\omega_0^{-1}$ (c) **for the non-resonant angle** $\theta = 20°$. $I\lambda_0^2 = 10^{19}$W cm$^{-2}\mu m^2$ ($a_0 = 2.72$), $d = \lambda_0$, $n_e = 25n_c$, semi-infinite target.

For the shock which accelerates the ions into the plasma, the angular directions are different for different angles of incidence. For example, comparing fig.5.12a with the forward emitted ions when the SPW is excited (fig.5.4a), we notice that for $\theta = 30°$ the angular distribution is peaked around $-40°$ while for $\theta = 10°$ very few ions are accelerated into the plasma and we have two emission angles ($\simeq 0°$ and $\simeq 60°$). The interpretation of the different angular directions is not straightforward but we note that it is consistent with the fact that the shock is driven by the laser pressure and the direction of the shock accelerated ions changes according to the laser angle of incidence. We shall estimate the shock velocity for $\theta = 10°$, from the ion density perturbation appearing in the density plot of fig.5.12: for $y = 6k_0^{-1}$ the density peak is located at $x = 248k_0^{-1}$ for $t = 600\omega_0^{-1}$ and it moves to $x = 253k_0^{-1}$ for $t = 1000\omega_0^{-1}$; therefore we can approximate the shock velocity value as $0.012c$ which is essentially the same value found for the resonant case in section 5.2, if we consider the different angular direction of the ion front.

Thus *from the analysis of the ion acceleration in the non-resonant incidence case (with modulation depth $d = \lambda_0$) we may conclude that a part of the characteristics*

observed depends only on the target geometry, which determines the angular directions associated with the ion front. The latter does not depend on the angle of incidence of the laser and gives a contribution that initially corresponds to the direction normal to the target surface, both for resonant and non-resonant angles of incidences. Contrastingly, *the emission of ion filaments is different in the two cases and we have seen that it corresponds to the different electron emission.* For what concerns the shock acceleration mechanism, even though the angular direction of the ions in the shock front changes for non-resonant laser incidence, we do not observe substantial differences in the front velocity and ion energy.

5.4 Reduced modulation depth

As we have seen in sections 2.4 and 4.2.2, the modulation depth d is an important parameter in laser-grating coupling. Particularly we have found in PIC simulations that for reduced d the sole effects of target geometry on absorption and electron heating are reduced and the importance of SPW in determining absorption and particle heating is more pronounced.

We shall examine in this section the case of the target having reduced modulation depth $d = \lambda_0/3$, for the resonant angle of incidence $\theta = 30°$ and the non resonant angle of incidence $\theta = 10°$ at $I\lambda_0^2 = 10^{19}$W cm$^{-2}\mu m^2$. We focus on these values of laser intensity, incidence, and modulation depth as i) $d = \lambda_0/3$ allows to reduce the geometry effects and preserve an efficient laser-modulation coupling at the same time (see section 2.4) while ii) the case $\theta = 10°$, for the high intensity regime, represents the maximum difference compared to the resonant case.

The ion emission for $d = \lambda_0/3$ and *resonant incidence* ($\theta = 30°$) is shown in fig.5.14. We first notice that the ions which are emitted backwards have different angles compared to the previous cases where $d = \lambda_0$: at $t = 500\omega_0^{-1}$ (fig.5.14b) we have two main angles, $\simeq 20°$ and $\simeq -30°$, which correspond approximately to the direction perpendicular to the target surface, $\theta_T = \pm 25°$. We notice that the maximum energy associated with the negative one is larger than with the positive one, as for the cases having $d = \lambda_0$, where this asymmetry was interpreted in terms of the emission of ion filaments. The angular distribution evolves at later times, as observed in all the previous simulations, and the most energetic ions are associated with smaller angles, close to 0° for $t = 1000\omega_0^{-1}$ (fig.5.14d).

Then, we also observe that the ions emitted forward (fig.5.14a), i.e., towards the plasma, present a double peak: for $t = 500\omega_0^{-1}$ the main one, corresponding to $\simeq$ 450keV energy, is at $-20°$ while a secondary peak corresponding to $\simeq$ 300keV energy, is found at $\simeq 10°$. At later times (fig.5.14c) the secondary peak tend to merge with a peak appearing around 0° and the maximum energy of ions emitted in this direction is $\simeq$ 450keV while for the main peak (around $-20°$) the maximum energy at $t = 1000\omega_0^{-1}$ is $\simeq$ 700keV.

In order to better understand the origin of the accelerated ions we will observe the ion density evolution in fig.5.15.

Ions emitted backwards at the angles 20° and $-30°$ can be traced back to the

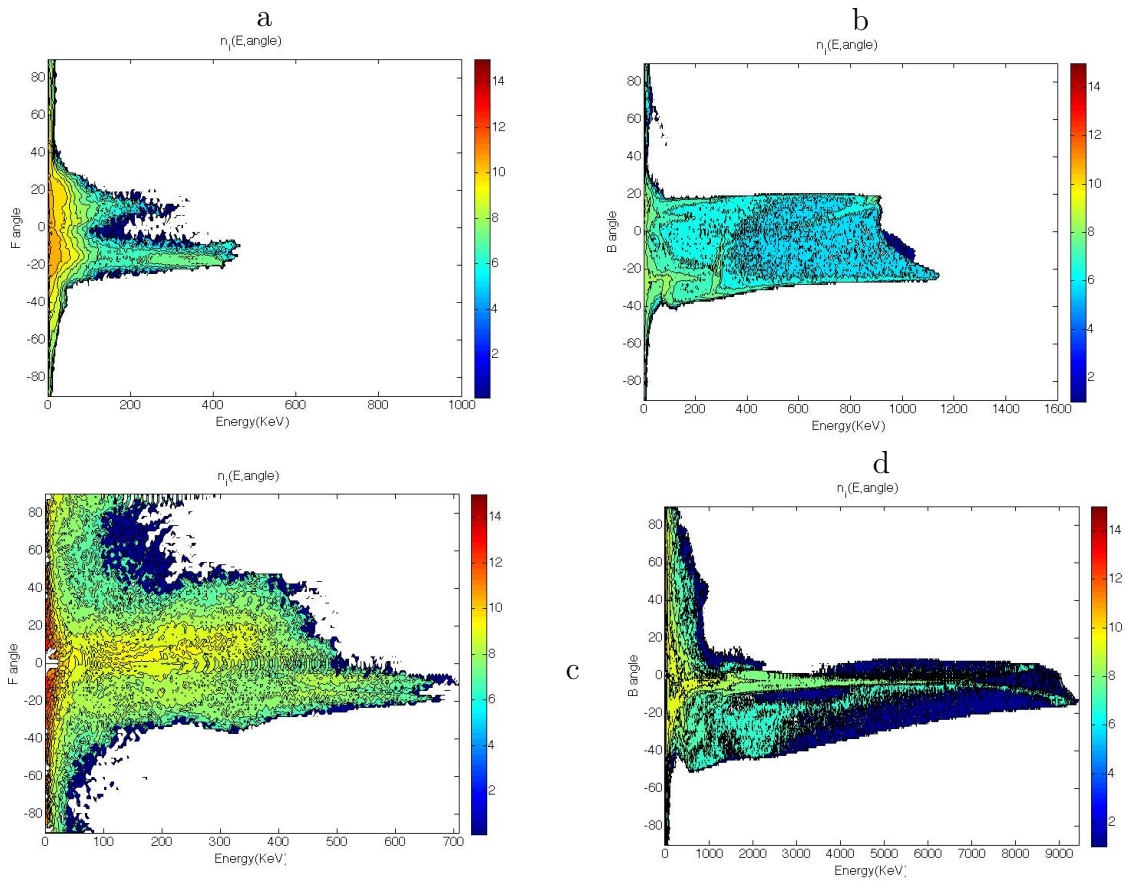

Figure 5.14: Ion emission angles forward (a) and backward (b) distributions at $t = 500\omega_0^{-1}$ and forward (c) and backward (d) distributions at $t = 1000\omega_0^{-1}$, as a function of energy. $I\lambda_0^2 = 10^{19}$W cm$^{-2}\mu m^2$ ($a_0 = 2.72$), $n_e = 25n_c$, $d = \lambda_0/3$, semi-infinite target **when the SPW is excited**.

expanding front in fig.5.15a and are initially moving in the direction perpendicular to the surface, while the filaments which are formed at the lower side of each modulation tip contribute only to the negative angle. As found in the previous cases, the latter have features which can be related to the presence of electron bunches which exit and re-enter the plasma periodically as shown in fig.4.20. The ions accelerated forward instead can be associated with the shock front which is propagating into the plasma. In fig.5.15b) we also notice that a periodic disturbance has formed in the shock, around $y = 19(\pm 2\pi)k_0^{-1}$, which can be associated with the ions moving at the positive angle $\simeq 10°$.

We shall now analyze the (p_x, x) phase space, in fig.5.16 in order to study the shock parameters in the case of modulation depth $d = \lambda_0/3$. The maximum velocity of the ions accelerated forward (into the plasma) is estimated from the positive momentum peak that is observed in the plot, where $v_{x,max} \sim 0.035c$. Thus, as discussed in section 5.2, we can estimate the shock velocity value in this direction as $v_{x,shock} \sim 0.017c$. However, as we have observed two different angles for the velocity of the ions in the shock, we cannot estimate v_{shock} from the x component. This value of $v_{x,shock}$ can be

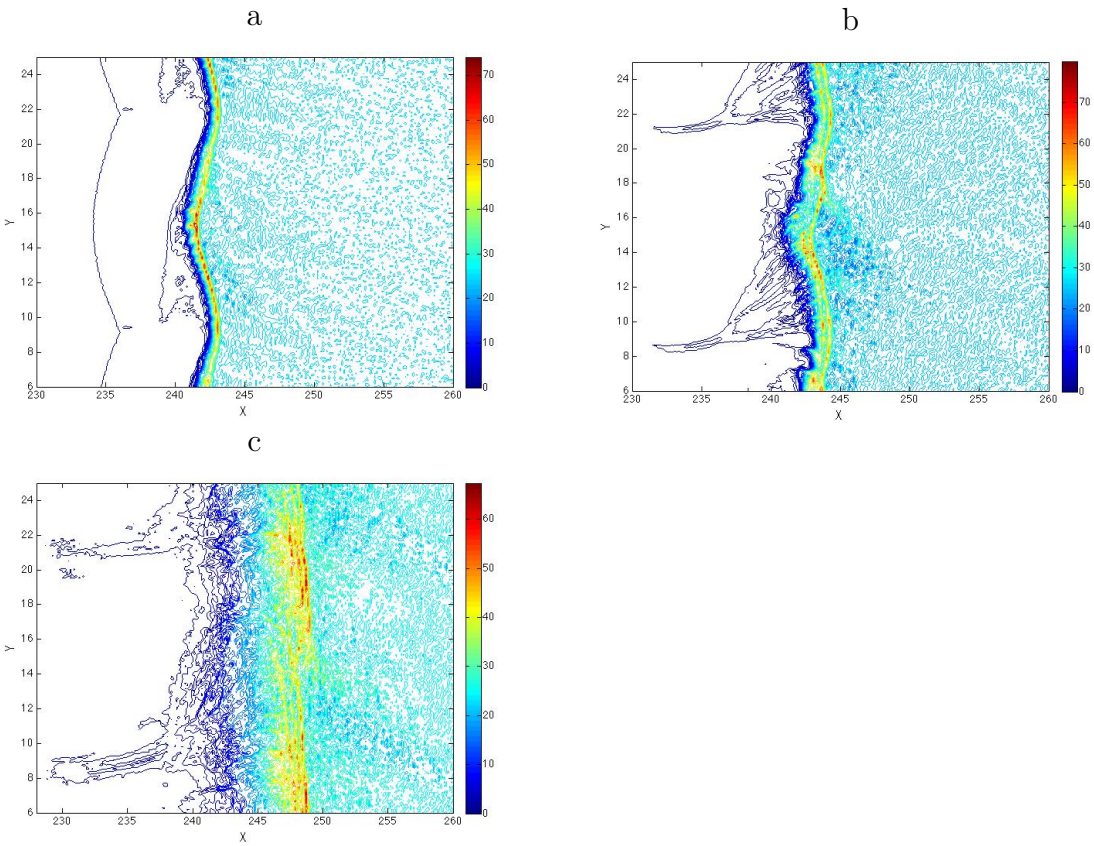

Figure 5.15: Ion density at times $t = 500\omega_0^{-1}$(a), $t = 600\omega_0^{-1}$(b), and $t = 1000\omega_0^{-1}$(c). $I\lambda_0^2 = 10^{19}$W cm$^{-2}\mu m^2$ ($a_0 = 2.72$), $n_e = 25n_c$, $d = \lambda_0/3$, semi-infinite target **when the SPW is excited**.

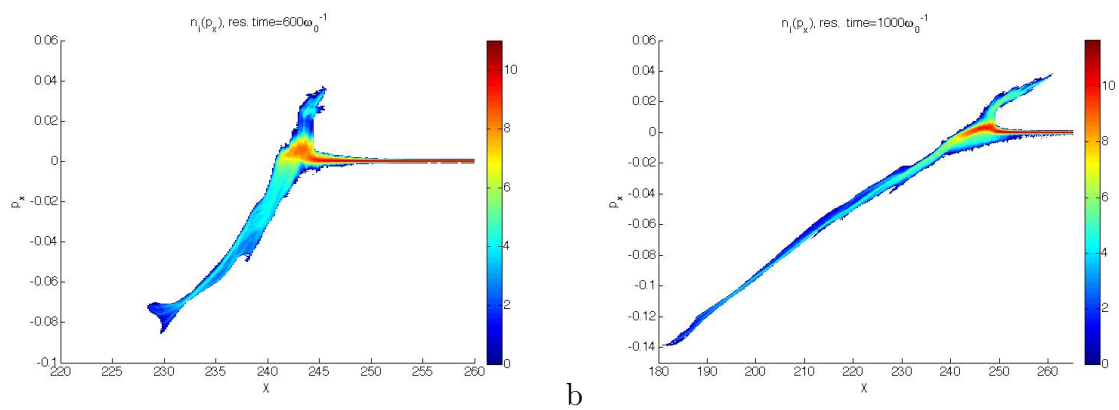

Figure 5.16: Ion phase space (x, p_x) at times $t = 600\omega_0^{-1}$ (a), and $t = 1000\omega_0^{-1}$ (b) .$I\lambda_0^2 = 10^{19}$W cm$^{-2}\mu m^2$ ($a_0 = 2.72$), $n_e = 25n_c$, $d = \lambda_0/3$, semi-infinite target **when the SPW is excited**.

verified by comparing the density plots of figs.5.15a) and b), where we observe the density perturbation front that moves from $x = 244k_0^{-1}$ to $x = 249k_0^{-1}$ in the time $\Delta t = 400\omega_0^{-1}$, from which we obtain the shock velocity $v_{x,shock} \simeq 0.012c$. The latter

value is lower than the previous estimation but this can be explained by considering the deformation of the shock front during the propagation, which does not allow a precise measurement. Note that the shock velocity obtained for $d = \lambda_0/3$ is slightly higher than the one observed for the case $d = \lambda_0$ ($v_{x,shock} \simeq 0.01c$); this may depend on the different angular direction of the ions in the shock, which was $-40°$ for $d = \lambda$.

Finally, we complete the analysis by comparing the case having modulation depth $d = \lambda_0/3$ and resonantly incident laser pulse, with the case having the same modulation depth but an angle of incidence, $\theta = 10°$, which does not match the conditions for SPW excitation.

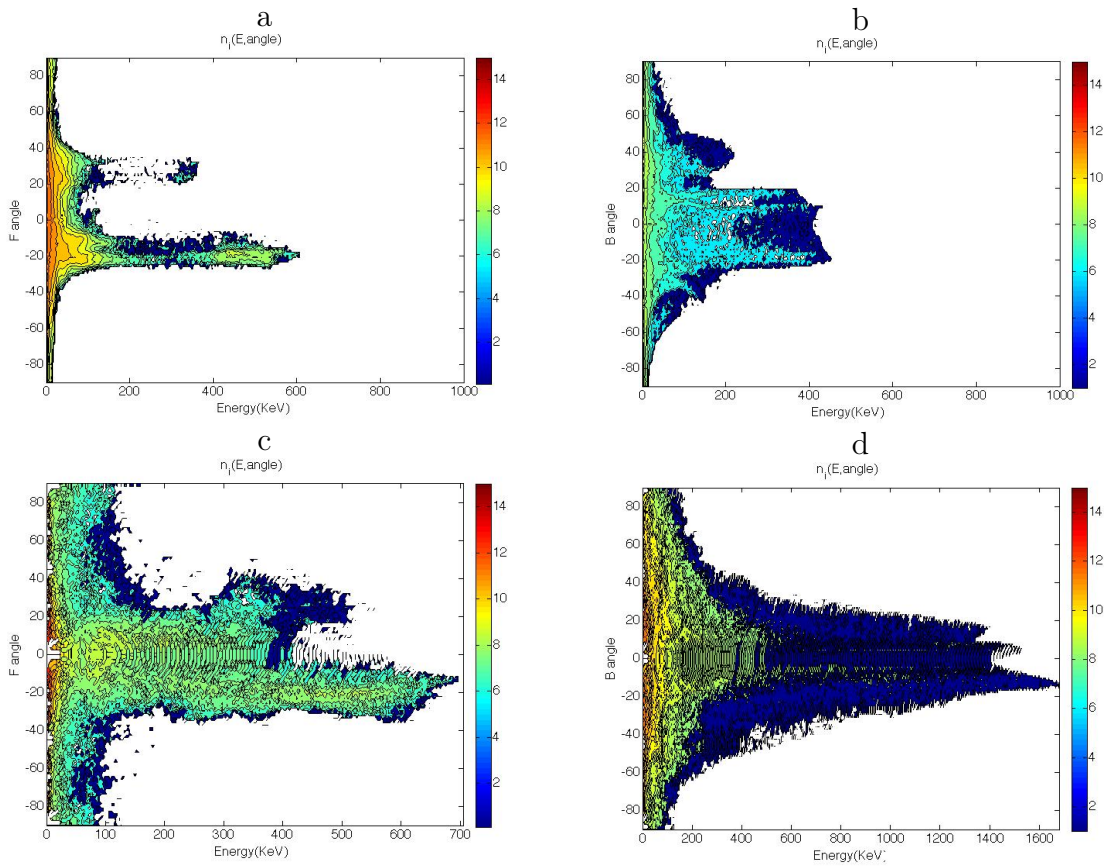

Figure 5.17: Ion emission angles forward (a) and backward (b) distributions at $t = 500\omega_0^{-1}$and forward (c) and backward (d) distributions at $t = 1000\omega_0^{-1}$ as a function of energy. $I\lambda_0^2 = 10^{19}$W cm$^{-2}\mu m^2$ ($a_0 = 2.72$), $n_e = 25n_c$, $d = \lambda_0/3$, semi-infinite target, **for the non-resonant angle of incidence** $\theta = 10°$.

In figs.5.17b,d we observe that very few ions are emitted backwards, towards the vacuum, and their final energy is only $\simeq 1.6$MeV at $t = 1000\omega_0^{-1}$. We can distinguish three peaks in the angular distribution corresponding to $\pm 20°$ and $10°$ whose position do not evolve between $t = 500\omega_0^{-1}$ to $t = 1000\omega_0^{-1}$. These angles can be associated, as done in the previous cases, with the expanding ion front observed in the ion density plot 5.18a), which gives angular directions perpendicular to the target surface ($\theta_T = \pm 25°$ here). In contrast with the case having the same angle of incidence($\theta = 10°$, non-resonant), but

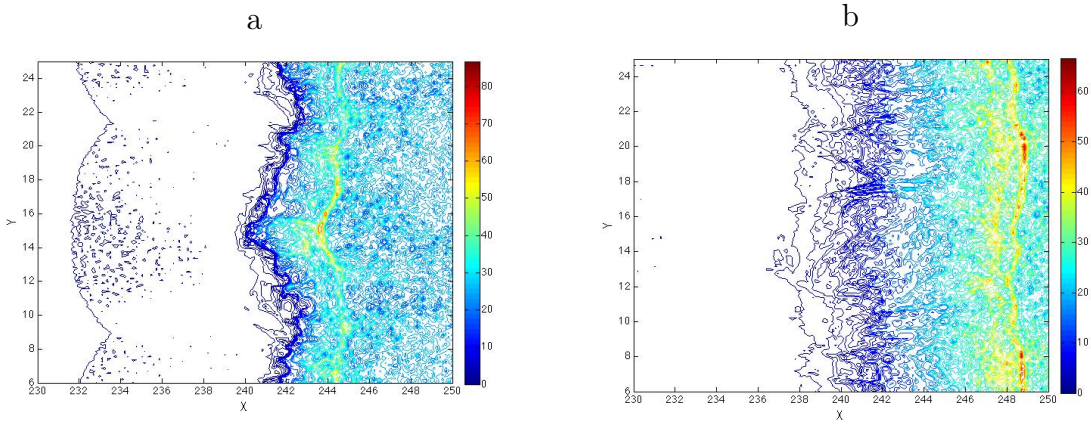

Figure 5.18: Ion density at times $t = 600\omega_0^{-1}$ (a) and $t = 1000\omega_0^{-1}$ (b). $I\lambda_0^2 = 10^{19}$W cm$^{-2}\mu m^2$ ($a_0 = 2.72$), $n_e = 25n_c$, $d = \lambda_0/3$, semi-infinite target, **for the non-resonant angle of incidence** $\theta = 10°$.

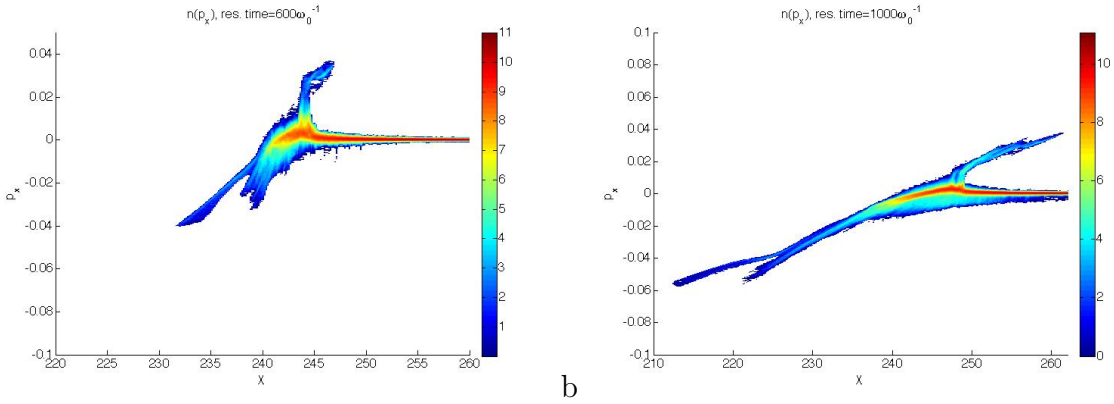

Figure 5.19: Ion phase space (x, p_x) at times $t = 600\omega_0^{-1}$ (a), and $t = 1000\omega_0^{-1}$ (b). $I\lambda_0^2 = 10^{19}$W cm$^{-2}\mu m^2$ ($a_0 = 2.72$), $n_e = 25n_c$, $d = \lambda_0/3$, semi-infinite target, **for the non-resonant angle of incidence** $\theta = 10°$.

deeper modulation ($d = \lambda_0$), *we do not find the ion filaments expanding towards the vacuum that were observed in fig.5.12. This is can be related to the characteristics of the corresponding electron currents that were shown in fig.4.22, where we noticed that, in this case, electrons have reduced excursions towards the vacuum.*

For the ions accelerated into the plasma (fig.5.17a,c) at angle of incidence $\theta = 10°$, we notice a double emission angle, as for the resonant case: a negative angle $-20°$, that was found also for the resonant case, and a positive angle $\simeq 30°$, which is greater than the positive angle of the resonant case ($\simeq 10°$). The ion energy associated with the negative and positive angles is 600keV and 400keV respectively at $t = 500\omega_0^{-1}$. From the (x, p_x) phase space (fig.5.19) we observe that for the non-resonant case with $d = \lambda_0/3$ the maximum velocity of the ions in the shock is $v_{x,max} \simeq 0.035c$ as for the resonant case having the same d. This means that *both resonant and non-resonant case have the same shock velocity despite the great difference in the hot electron temperatures (see fig.4.4). This fact further confirms that the hot electrons are not involved in the shock*

mechanism.

The analysis of the effects of modulation depth on ion acceleration has shown that, when the surface wave is excited, the ion emission has similar characteristics for different values of the modulation depth. For example, similar ion filaments are generated at the irradiated surface, at points which correspond spatially to the bunches of electrons which we have observed in the previous chapter, oscillating in the SPW field. Nevertheless the angular distribution changes for different values of d and we observe that the emission angles depend on the shape of the target surface, in agreement with the TNSA mechanism. We also notice that, when the modulation depth is reduced, the effects of target geometry are reduced and the difference between the characteristics of ion acceleration in the case of resonant and non-resonant laser incidence are more pronounced.

5.5 The laminar target

In the previous sections we have examined the electron energy and emission angles for the case of a semi-infinite target where electrons reaching the right end of the plasma are cooled and re-enter the plasma at thermal velocity. We have found that the angular direction of the ions emitted towards the vacuum at the irradiated surface is partly determined by the shape of the surface and partly by the electron oscillations at the surface. These characteristics are coherent with TNSA model. An other acceleration mechanism was also identified, shock acceleration, which pushes ions forward, towards the plasma bulk.

In the case of the laminar target we also observe *ion emission from the rear side.* As mentioned in the introduction (sec.1.5.1) the only [1] relevant mechanism for ion acceleration from the non-irradiated side is related to the generation of strong space-charge fields generated as a consequence of the hot electron production since the beginning of the laser-plasma interaction. Hot electrons are generated at the irradiated side of the target and reach the rear where they set-up a sheath field which accelerates the ions. The driving field depends on the hot electron density and temperature, as derived in section 1.5.1. Thus it may be enhanced by electron recirculation [21] because several bunches of electrons, which have been reflected at the front and rear sides of the target, give a contribution to the hot electron density. Moreover we have shown in section 4.3.1, where we examined the electron temperature as a function of target thickness, that electrons having interacted more than once with the electric field at the irradiated surface can reach higher temperatures.

The latter effect of recirculation on electron temperature is relevant also for the emission of ions at the irradiated side, towards the vacuum, which occurs with the same mechanism occurring at the rear side.

We will consider the laminar target having the smaller thickness, $h = 3.5\lambda_0$, in order to better stress the differences with the semi-infinite target in the study of the emission at the irradiated side and of the shock acceleration. The laser intensity will be $I\lambda_0^2 = 10^{19}\text{W cm}^{-2}\mu m^2$ and the modulation parameters are $d = \lambda_0$ for the modulation

[1] for target thickness $h > \lambda_0$

depth and $a_m = 2\lambda_0$ (resonant for $\theta = 30°$ for $n_e = 25n_c$). The modulation tips are located at $x = 240k_0^{-1}$, while the rear surface is at $x = 262k_0^{-1}$ and the vacuum at the rear of the target extends for $218k_0^{-1}$, up to $x = 480k_0^{-1}$, where the simulation box ends.

The plots in fig.5.20 and fig.5.21 show the angular distribution of the ions corresponding to three different parts of the simulation box: (a) the vacuum in front of the plasma ($x = 0 - 240k_0^{-1}$), (b) the bulk plasma ($x = 247 - 262k_0^{-1}$) and (c) the vacuum at the rear of the target ($x = 247 - 262k_0^{-1}$). In fig.5.20 the angular distribution is taken at $t = 500\omega_0^{-1}$, that is approximately the time at which we found the maximum electron temperature in the simulations while fig.5.21 corresponds to time $t = 1000\omega_0^{-1}$, that is the time at which we estimate that the ion acceleration begins to saturate (as will be explained in section 5.6).

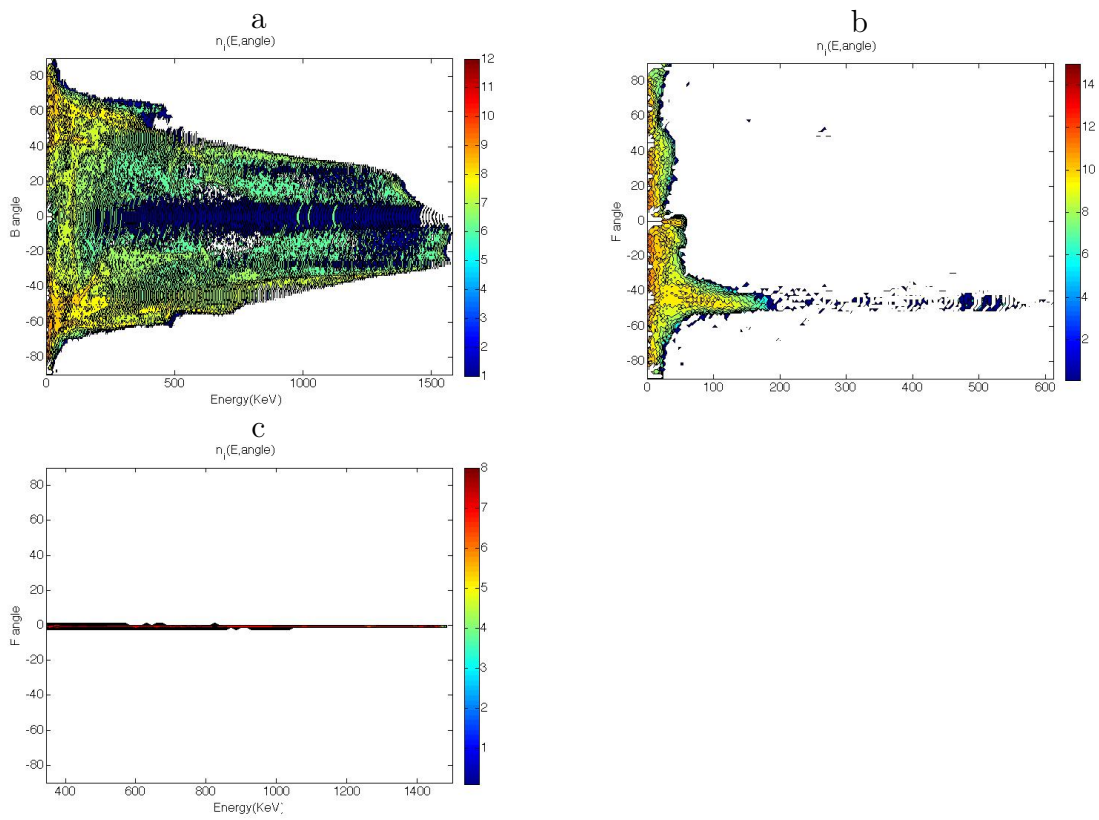

Figure 5.20: (a) Ion emission towards the laser source at the irradiated side, ions accelerated into the plasma (b), and (c) forward emission at the unirradiated side, as a function of energy for the laminar target **when SPW is excited**; $I\lambda_0^2 = 10^{19}$W cm$^{-2}\mu m^2$ ($a_0 = 2.72$), $n_e = 25n_c$, $t = 500\omega_0^{-1}$, $d = \lambda_0$, $h = 3.5\lambda_0$.

As done previously, we examine the ion acceleration at times $t = 500\omega_0^{-1}$ and $t = 1000\omega_0^{-1}$ in order to follow the evolution of the angular distribution of the ions that have been accelerated by 'hot' electrons. As for the semi-infinite case the angular distribution of the ions accelerated backwards into the vacuum at the irradiated surface is broader for earlier times: at $t = 500\omega_0^{-1}$ (5.20a) we find two main peaks located at $\pm 40°$ and two minor peaks around $\pm 60°$. The ions accelerated inwards (5.20b) , associated with

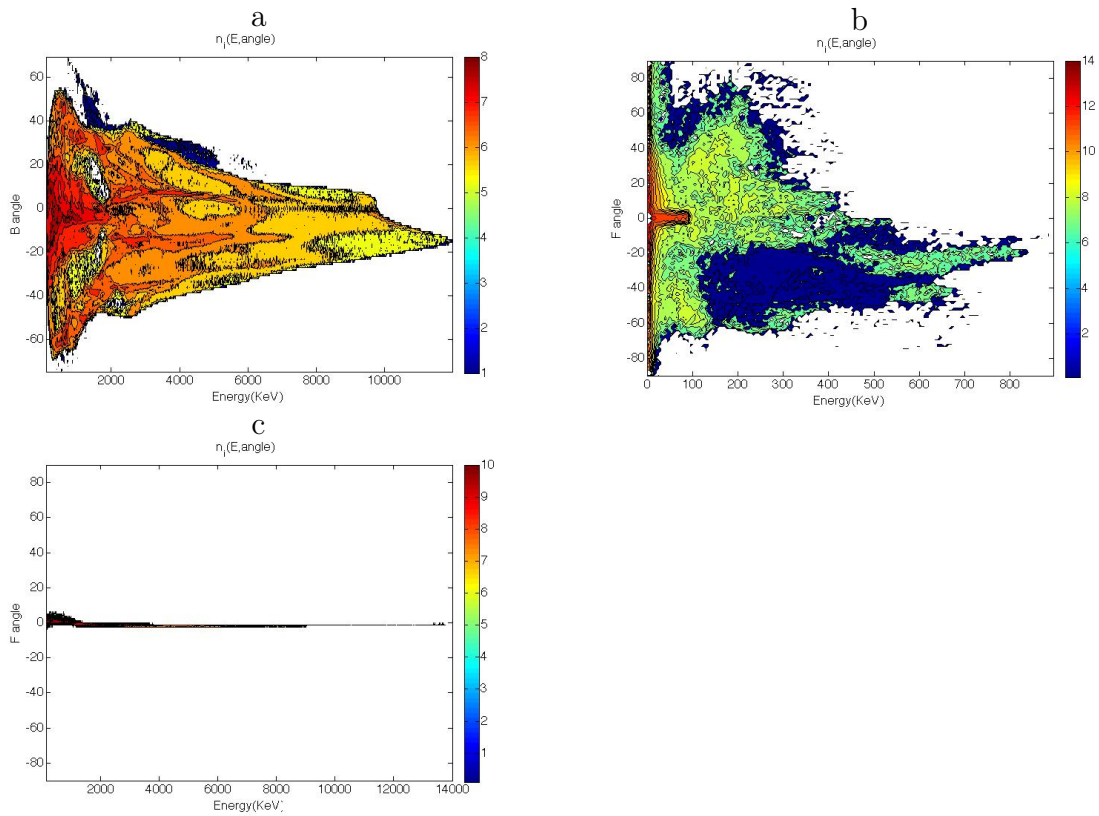

Figure 5.21: (a) Ion emission towards the laser source at the irradiated side, ions accelerated into the plasma (b), and (c) forward emission at the unirradiated side as a function of energy for the laminar target **when the SPW is excited**; $I\lambda_0^2 = 10^{19}$W cm$^{-2}\mu m^2$ ($a_0 = 2.72$), $n_e = 25n_c$, $t = 1000\omega_0^{-1}$, $d = \lambda_0$, $h = 3.5\lambda_0$.

the shock wave, have an angular distribution peaked at an angle of about 45°, similarly to the semi-infinite case having the same parameters (thickness excluded). Finally, at the rear of the target (5.20c), ions are emitted towards the vacuum in the direction normal to the surface with a very small angular spread $\simeq 2°$.

At $t = 1000\omega_0^{-1}$, we observe that ions accelerated into the vacuum in front of the plasma (fig.5.21a) have two main emission angles, $-20°$ and $10°$. These angles are smaller than the ones found at $t = 500\omega_0^{-1}$ and we notice again that in general smaller angles correspond to higher ion energy. We also notice, inside the main angular distribution, some denser regions, eventually corresponding to substructures as filaments. The energy of the ions emitted in this direction grows from 1.52MeV at $t = 500\omega_0^{-1}$ to 11.8MeV at $t = 1000\omega_0^{-1}$. Ions accelerated into the vacuum at the rear of the target (fig.5.21c) are much more energetic than those accelerated at the front, with a maximum energy of 14MeV at $t = 1000\omega_0^{-1}$. Notice that the final energy of the ions corresponds approximately to the electron maximum energy found for this target parameters in section 4.3.1.

The angular distribution can be better understood by analyzing the ion density in fig.5.22: at the irradiated side of the target it is possible to observe the ion front

expanding towards the vacuum, which initially propagates perpendicular to the modulated surface, and some filaments, that appear inside the expanding front. As mentioned above, the latter can be associated with the secondary features in the angular distribution noticed in fig.5.21a. Just as for the semi-infinite case, the ion filaments develop at the points where we had observed electron bunches which exit and re-enter the plasma periodically.

We will now examine the shock propagating inside the plasma for the case of the laminar, resonant, target. From the ion density in fig.5.22, we can estimate the shock

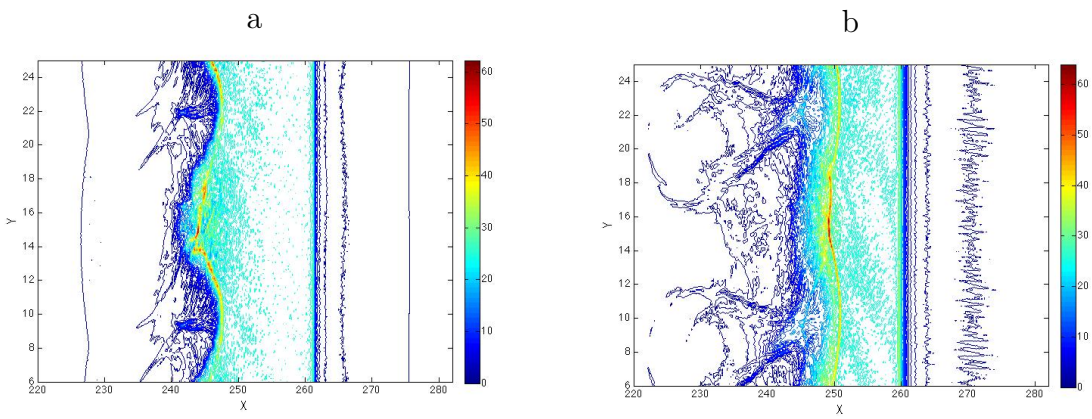

Figure 5.22: Ion density taken at times $t = 600\omega_0^{-1}$ (a) and $t = 1000\omega_0^{-1}$ (b), $I\lambda_0^2 = 10^{19}$W cm$^{-2}\mu m^2$ ($a_0 = 2.72$), $n_e = 25n_c$, with modulation depth $d = \lambda_0$ **for the laminar target of thickness** $h = 3.5\lambda_0$**, when the SPW is excited.**

velocity component in the x direction as $v_{x,shock} = 0.01c$, as we observe that the perturbation front covers $4k_0^{-1}$ in $400\omega_0^{-1}$. This is the same value that we found for the semi-infinite case, at the resonant incidence, even though we notice that the ion peak density associated with the shock, $n_e = 61n_c$, is lower than the value $n_e = 75n_c$ found for the semi-infinite case.

Similarly to what done for the semi-infinite target, we shall consider the ion emission for *the case of a laminar target having flat surface*, in order to compare the angular distribution with the modulated target. The target thickness, the density and the laser parameters will not change compared to the resonant case described above. There is not much evolution, except for the energy, of the emission angles in the flat surface case, between $t = 500\omega_0^{-1}$ and $t = 1000\omega_0^{-1}$, hence only the later time plots are shown here. The angular distribution in fig.5.23, has a single angular direction for ions emitted both outwards and inwards (shock accelerated ions), that is normal to the target (0°). Eventually, a secondary peak can be distinguished for ions emitted towards the vacuum, at the irradiated surface, around 10°.

We notice that in the flat surface case the ions emitted outwards have the same energy, 8.5MeV, in both emission directions, i.e. towards the vacuum, in front of the irradiated surface and at the rear side. This energy is much lower than the energy of the resonant case that was about 14MeV at the rear side and 11.8MeV at the front of the target. Contrastingly, we notice that this energy is much higher than that found

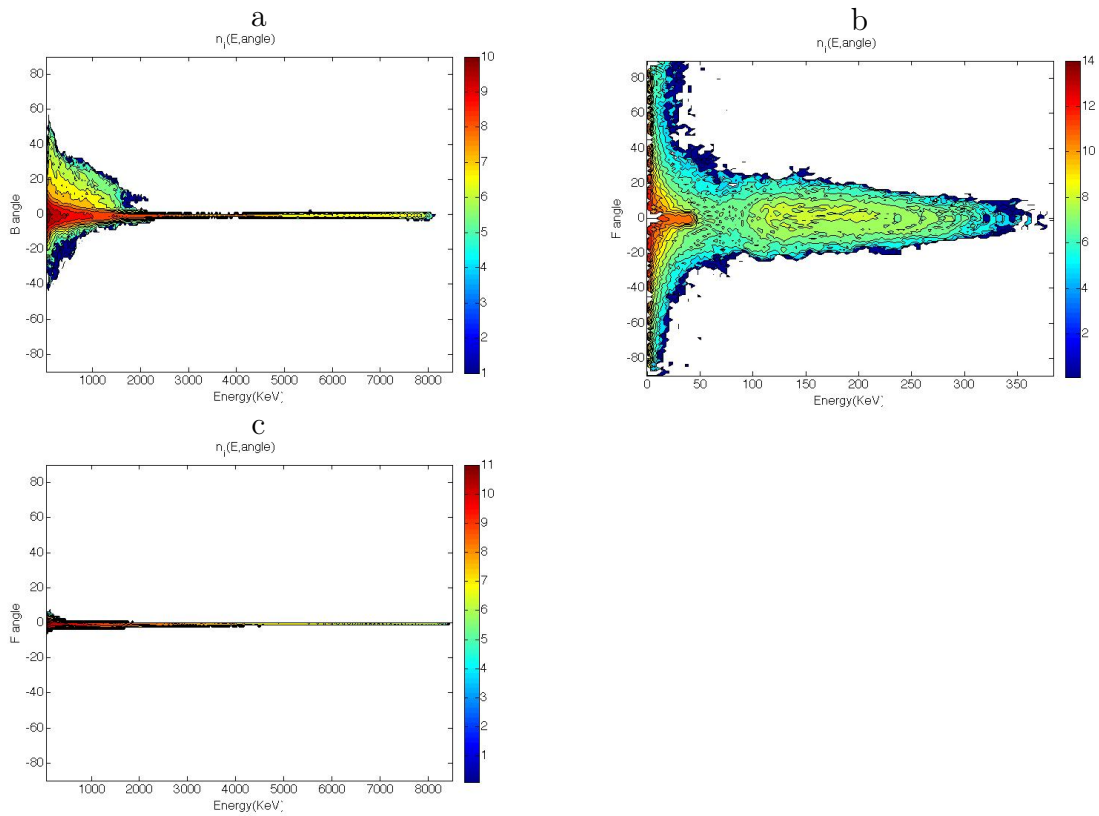

Figure 5.23: (a) Ion emission towards the laser source at the irradiated side, ions accelerated into the plasma (b), and (c) forward emission at the unirradiated side, as a function of energy **for a flat target of thickness** $h = 3.5\lambda_0$; $I\lambda_0^2 = 10^{19}$W cm$^{-2}\mu m^2$ ($a_0 = 2.72$), $t = 1000\omega_0^{-1}$, $n_e = 25n_c$.

for the emission at the irradiated side in the semi-infinite case with a flat surface where we had only 1.6MeV at $t = 1000\omega_0^{-1}$.

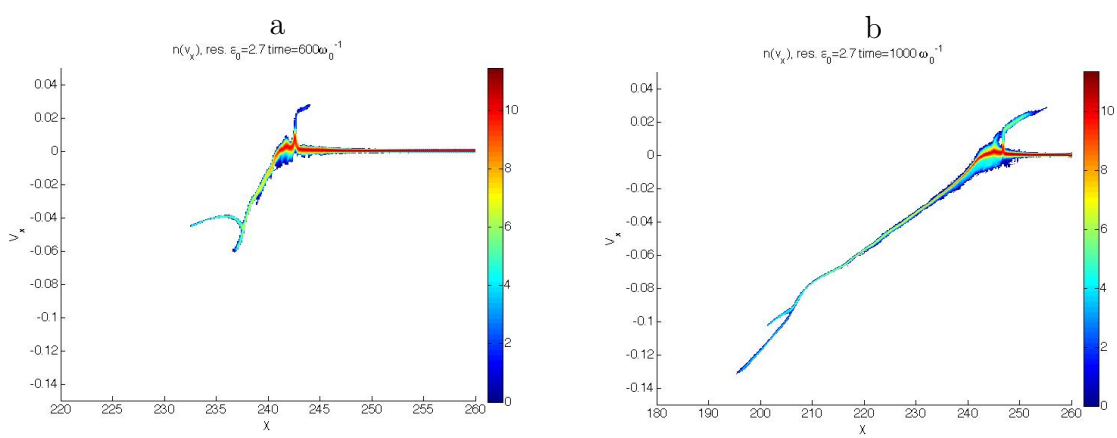

Figure 5.24: Ion phase space (x, p_x) at times $t = 600\omega_0^{-1}$ (a), and $t = 1000\omega_0^{-1}$ (b).$I\lambda_0^2 = 10^{19}$W cm$^{-2}\mu m^2$ ($a_0 = 2.72$), $n_e = 25n_c$, **for the flat target** of thickness $h = 3.5\lambda_0$.

We may conclude that, *qualitatively, the ion acceleration for the laminar and the semi-infinite targets are similar, despite the fact that some values, such as the shock peak density or the ion energy, may vary.* The data presented in this section show that *the energy of the ions emitted towards the vacuum is increased thanks to electron recirculation which make the TNSA mechanism more efficient*, bringing a larger number of hot electrons at the target surface. This mechanism causes a further enhancement of SPW effects when a thin laminar target is considered. Indeed, comparing fig.5.22 and fig.5.7 we also notice that *the ion filaments developing at the irradiated surface last longer*; this is probably also due to recirculation, which renews the electron bunches at the irradiated surface which are involved in the acceleration of ion filaments.

5.5.1 Non-resonant angles and reduced modulation depth

As we discussed in the previous section, the case of the modulated target with reduced modulation depth $d = \lambda_0/3$ is particularly interesting in order to stress the effect of the SPW excitation on particle acceleration and laser absorption compared to the non-resonant case. In the following we will examine the case of the laminar target having $d = \lambda_0/3$ (and thickness $h = 3.5\lambda_0$, as in the previous section) with resonant incidence and then compare with the case where the SPW is not excited, for the non-resonant angle of incidence $\theta = 10°$.

Comparing the ion emission at the irradiated side (figures 5.25a and 5.26a) for $d = \lambda_0/3$ with the corresponding emission for the laminar target having $d = \lambda_0$ (figures 5.20a and 5.21a) we notice that *for $d = \lambda_0/3$ we have emission angles in the backward direction, which are smaller than for $d = \lambda_0$.* The change in the angular distribution for reduced modulation depth is consistent with the change in the shape of the target, as the normal to the modulated surface approach 0° when the depth of the modulation is reduced. This implies that the ions in the expanding front, which are emitted in the direction perpendicular to the surface, have smaller emission angles. The main emission angles in the backward direction at $t = 500\omega_0^{-1}$ (fig.5.25a), are $-10°$ and 10° while at $t = 1000\omega_0^{-1}$ (5.26a) they are $-10°$, 0° and 10°.

As found in all the previous cases, we notice that the emission angles evolve during ion acceleration and the most energetic ions tend to have smaller angles, approaching the target normal direction (0°). *The angular distribution is similar to that of the semi-infinite target having the same modulation parameters, and also the density distribution, shown in fig.5.27, is characterized by the same filaments as those observed in fig.5.15 at the irradiated surface.* For what concerns the shock, the velocity is approximately the same as for the semi-infinite case: the value can be estimated from the perturbation in the ion density, which is propagating inside the plasma, as $v_{x,shock} = 0.012c$.

The most important result is found for the ion emission at the unirradiated side: as we can observe in fig.5.26c, *the cut-off energy of the ions for $d = \lambda_0/3$ is the same that was found for the $d = \lambda_0$ case (fig.5.21), that is $14MeV$ at $t = 1000\omega_0^{-1}$.* The angular direction is always perpendicular to the rear surface, with small angular spread ($\sim 2°$), which is consistent with the TNSA acceleration mechanism. As for the $d = \lambda_0$ laminar case, we notice that the maximum ion energy corresponds approximately to the maximum electron energy which was reported in section 4.3.1.

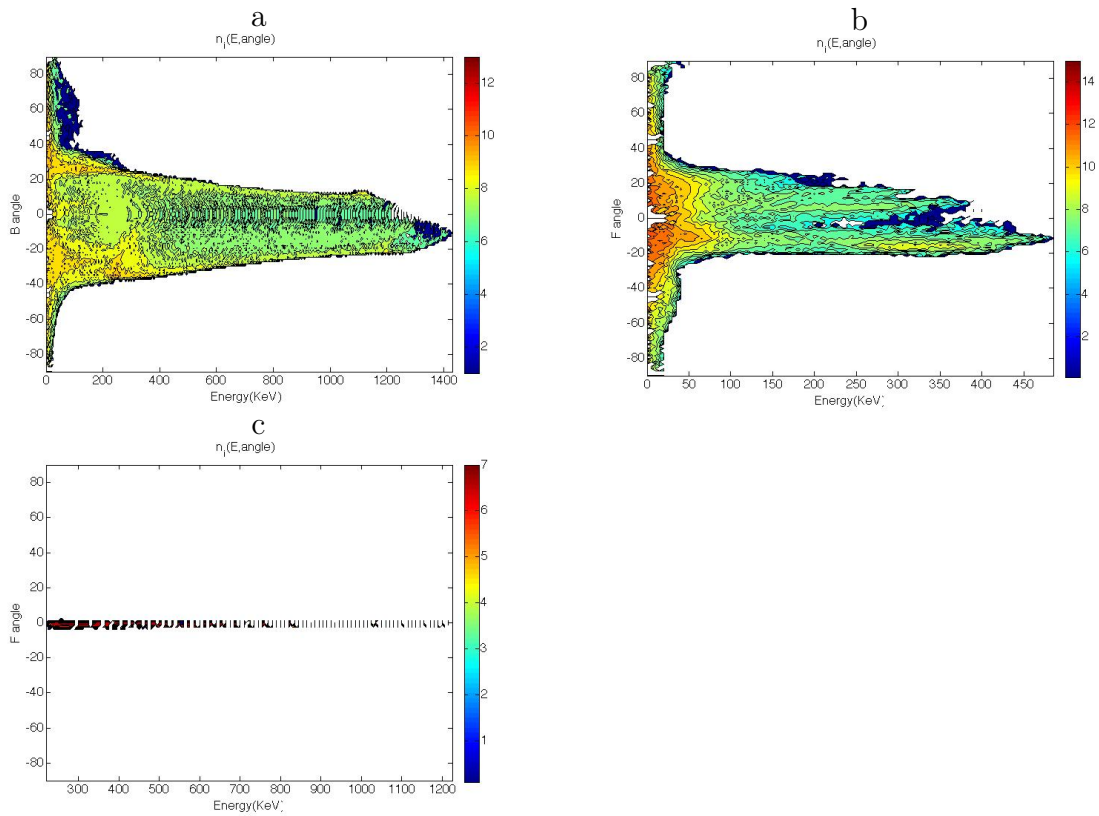

Figure 5.25: (a) Ion emission towards the laser source at the irradiated side, ions accelerated into the plasma (b), and (c) forward emission at the unirradiated side at $t = 500\omega_0^{-1}$, as a function of energy, for the laminar target of thickness $h = 3.5\lambda_0$, **when the SPW is excited**; $I\lambda_0^2 = 10^{19}$W cm$^{-2}\mu m^2$ ($a_0 = 2.72$), $n_e = 25n_c$, $d = \lambda_0/3$.

We shall now compare these results with those for a *laminar target having modulation depth* $d = \lambda_0/3$, interacting with a laser pulse having the same intensity ($I\lambda_0^2 = 10^{19}$W cm$^{-2}\mu m^2$) *but angle of incidence* $\theta = 10°$, which does not match the conditions for resonant SPW excitation. The density and thickness will be the same as those used for the resonant case described above, $n_e = 25n_c$ and $h = 3.5\lambda_0$. The angular distribution, shown in fig.5.28 at $t = 500\omega_0^{-1}$ and fig.5.29 at $t = 1000\omega_0^{-1}$, has many similarities with the one observed for the resonant target (fig.5.25 and fig.5.26). At the irradiated side ions are emitted backwards at angles $\pm 20°$ for $t = 500\omega_0^{-1}$ and tend to merge to a single angle, $\simeq 0°$, at $t = 1000\omega_0^{-1}$ while at the rear they are accelerated perpendicularly to the surface, corresponding to 0°. However the energy at $t = 1000\omega_0^{-1}$ is different for the angle of incidence $\theta = 10°$ and the resonant cases: at the rear surface, in the non-resonant case the maximum energy is 12MeV energy, 2MeV less than for the corresponding resonant case. Also the ions emitted at the irradiated surface (5.29a) have a lower cut-off as the maximum energy reached is 10MeV, while for the resonant case we had 12.5MeV. Contrastingly the final energy of the ions accelerated towards the plasma (5.29b) does not change compared to the resonant case, suggesting once more that electrons involved in the shock formation are not 'hot electrons' and

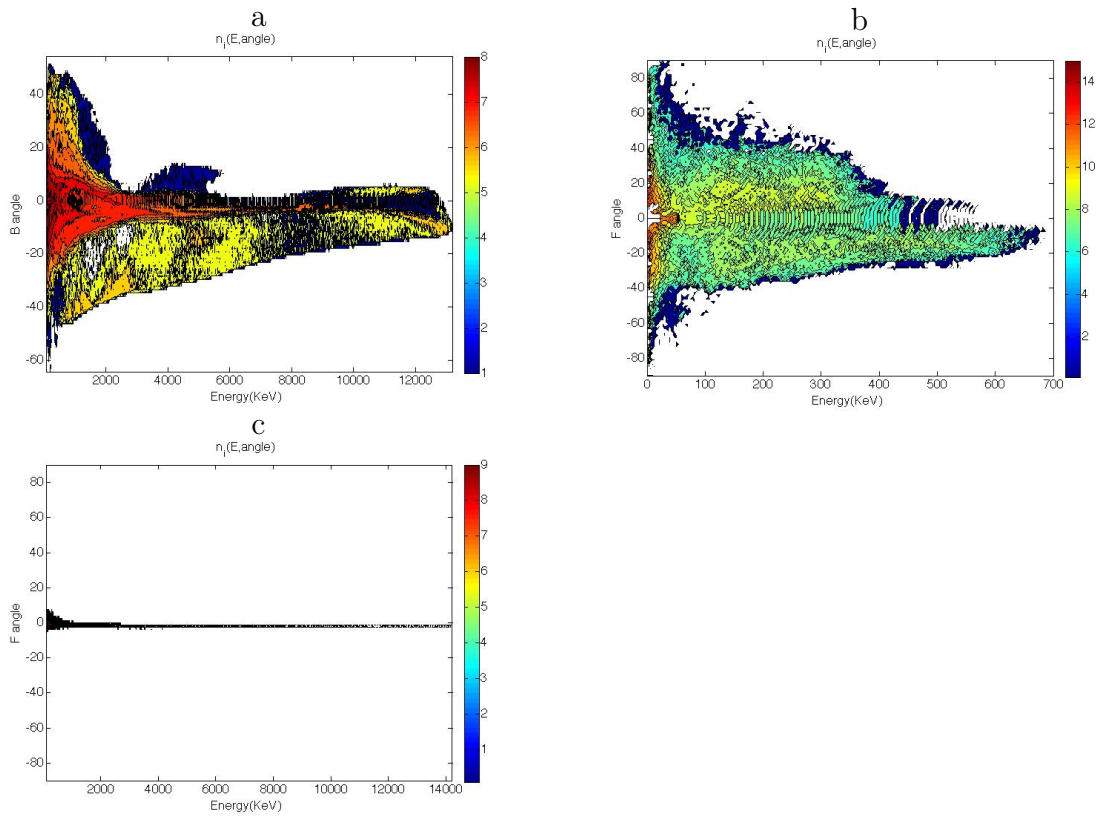

Figure 5.26: (a) Ion emission towards the laser source at the irradiated side, ions accelerated into the plasma (b), and (c) forward emission at the unirradiated side at $t = 1000\omega_0^{-1}$, as a function of energy, **when the SPW is excited**, for the laminar target of thickness $h = 3.5\lambda_0$; $I\lambda_0^2 = 10^{19}$W cm$^{-2}\mu m^2$ ($a_0 = 2.72$), $n_e = 25n_c$, $d = \lambda_0/3$.

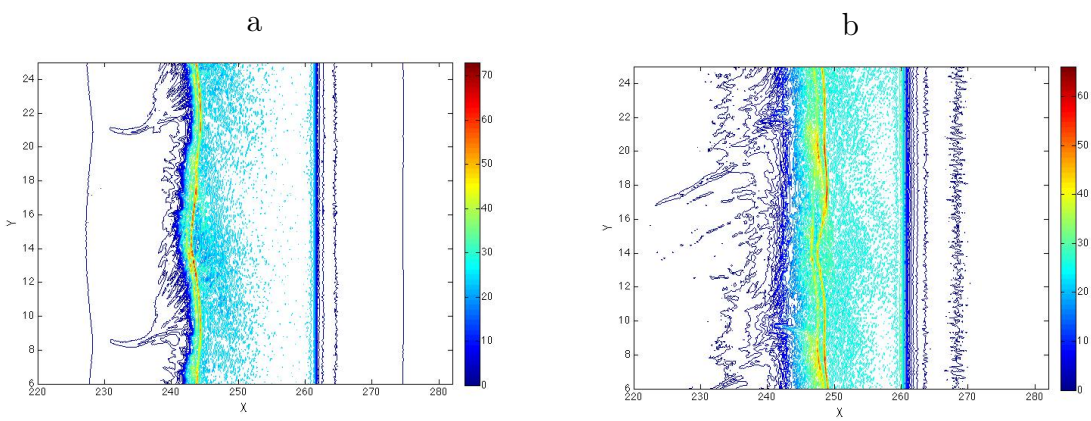

Figure 5.27: Ion density taken at time $t = 600\omega_0^{-1}$ (a) and $t = 1000\omega_0^{-1}$ (b), for $I\lambda_0^2 = 10^{19}$W cm$^{-2}\mu m^2$ ($a_0 = 2.72$), $n_e = 25n_c$, $d = \lambda_0/3$, for the laminar target of thickness $h = 3.5\lambda_0$ **when the SPW is excited.**

the shock formation is not substantially influenced by SPW excitation.

From the ion density plot of fig.5.30, we may infer that the velocity of the shock

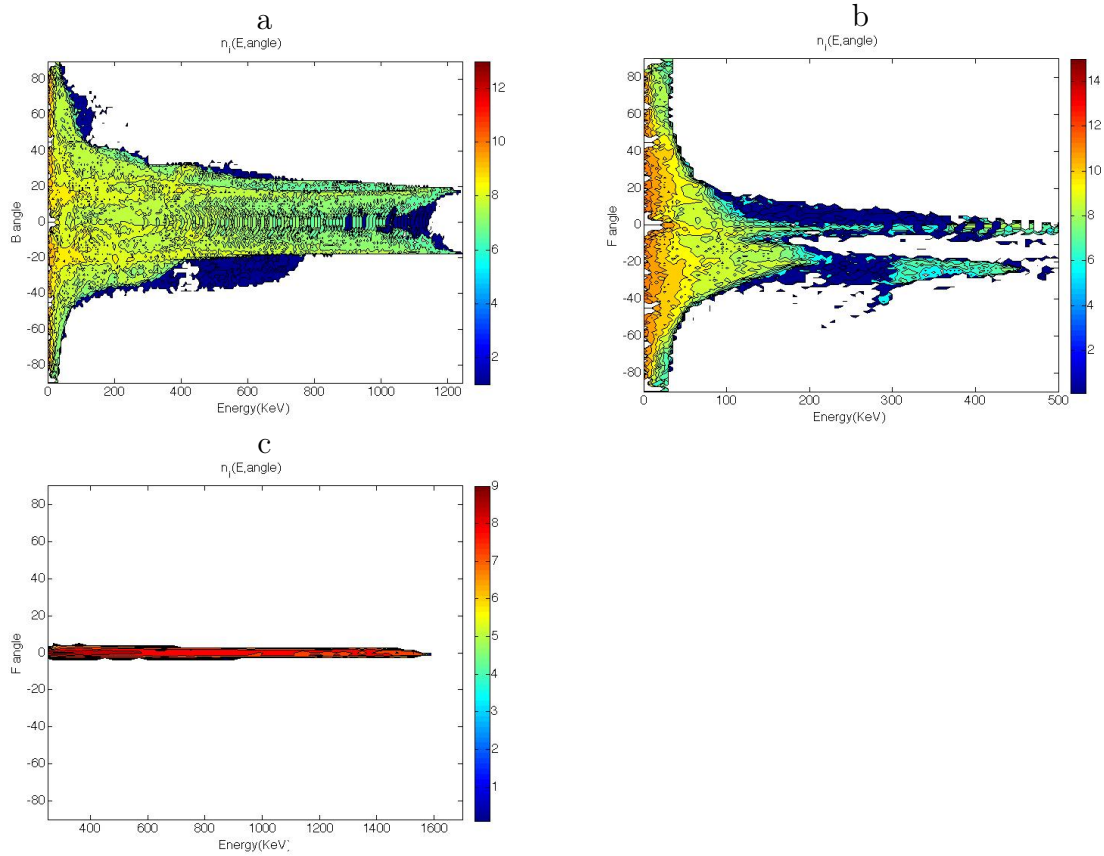

Figure 5.28: (a) Ion emission towards the laser source at the irradiated side, ions accelerated into the plasma (b), and (c) forward emission at the unirradiated side, as a function of energy, for the laminar target of thickness $h = 3.5\lambda_0$, **for the non-resonant angle of incidence** $\theta = 10°$ at $t = 500\omega_0^{-1}$; $I\lambda_0^2 = 10^{19}$W cm$^{-2}\mu m^2$ ($a_0 = 2.72$), $n_e = 25n_c$, $d = \lambda_0/3$.

which is propagating inside the plasma is $v_{x,shock} = 0.012$, i.e. the same as the resonant case, which would confirm that the shock parameters are not changed.

The results reported in this section show that *the reduced modulation depth makes the effects of SPW excitation more evident, not only in the quality of particles emission, as the emission angles, but also in the values of their energy.* Contrastingly when the modulation depth is equal to the laser wavelength, the contribution from the target geometry may hide the contribution coming from SPW excitation. This effect, discussed in section 2.3, is a consequence of the scalar product of the incident field with the surface normal which determines electron heating. *As the driving field which accelerates the ions via TNSA depends on hot electrons, the ion energy also has a dependence on the geometry factor.*

Thus, as found for absorption and electron heating, we may conclude that the maximum advantage from SPW excitation corresponds to the case where the modulation depth is reduced to $\lambda_0/3$ which minimizes the geometry effects.

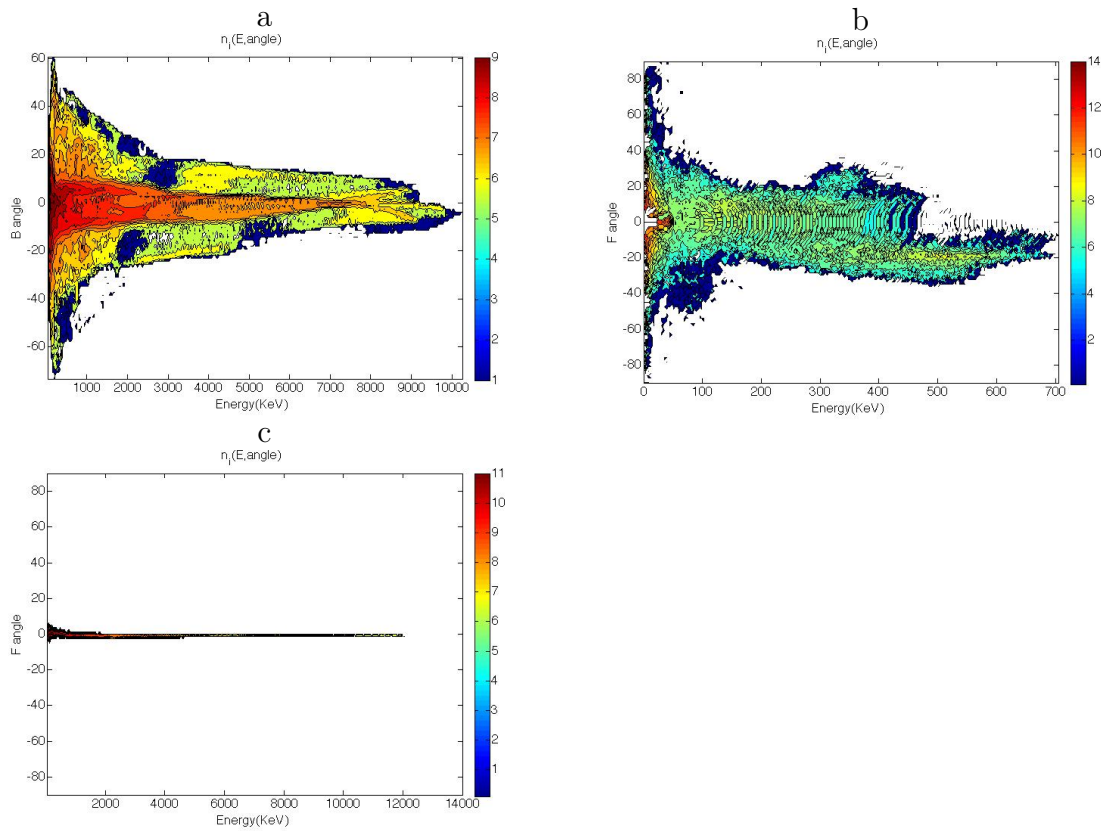

Figure 5.29: (a) Ion emission towards the laser source at the irradiated side, ions accelerated into the plasma (b), and (c) forward emission at the unirradiated side, as a function of energy, for the laminar target of thickness $h = 3.5\lambda_0$, **for the non-resonant angle of incidence** $\theta = 10°$ at $t = 1000\omega_0^{-1}$; $I\lambda_0^2 = 10^{19}$W cm$^{-2}\mu m^2$ ($a_0 = 2.72$), $n_e = 25n_c$, $d = \lambda_0/3$.

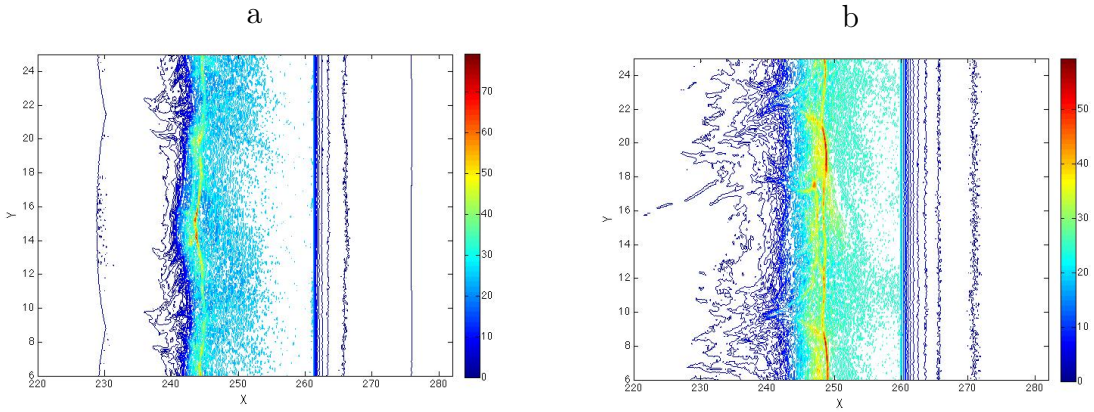

Figure 5.30: Ion density taken at time $t = 600\omega_0^{-1}$ (a) and $t = 1000\omega_0^{-1}$ (b), for $I\lambda_0^2 = 10^{19}$W cm$^{-2}\mu m^2$ ($a_0 = 2.72$), $n_e = 25_c$, with modulation depth $d = \lambda_0/3$ **for the non-resonant angle of incidence** $\theta = 10°$.

5.6 Ion energy at the end of the interaction

Finally we will examine the ion energies *at the end of the interaction*, for different simulations, in order to compare with the electron energies found in chapter 4 and verify the TNSA scaling for the ions emitted into the vacuum.

The time at which the ion acceleration is found to saturate in the semi-infinite target is around $t = 1000\omega_0^{-1}$. This time can be also considered approximately as the time of saturation for the laminar target, of thickness $h = 3.5\lambda_0$. In fact following the model in [41], which is partly reported in section 1.5.1, the relevant time for the saturation of the process of ion acceleration by TNSA is $t_f = h/2c_s$. The value of t_f can be calculated by taking the ion sound speed $c_s = 0.013c$, estimated from the velocity of the shock v_{shock} for the laminar target of thickness $h = 3.5\lambda$ and assuming $M = v_{shock}/c_s = 1$ (the minimum required by the theory in 1.5.2 in order to have a shock). We obtain $t_f \simeq 270\omega_0^{-1}$. This time is a rough estimate as it was assumed that c_s is constant and corresponds to the velocity of plasma expansion into the vacuum. Remembering that the total duration of the pulse is $400\omega_0^{-1}$, we may conclude that the relevant time for ion acceleration is the pulse duration, which is longer than t_f. As the complete reflection of the laser pulse occurs at $t \simeq 740\omega_0^{-1}$, *we can consider* $t = 1000\omega_0^{-1}$ *as the final stage of ion acceleration.*

Comparing the ion energies in tab. 5.1 with the electron temperatures in tab. 4.1, we observe that, in general, for the *semi-infinite target*, the ion energy $\mathcal{E}_{front}$ is of the order of magnitude of the electron energy E_{max}. Only one value appears lower than the corresponding electron energy, as we observe that for $I\lambda_0^2 = 10^{19}$W cm$^{-2}\mu m^2$, when the SPW is excited, we find $\mathcal{E}_{front} \simeq 0.5E_{max}$. As for the laminar target this discrepancy is not observed, we may infer that in this case a large amount of electrons has been accelerated from the surface into the plasma bulk and, in the case of a semi-infinite target, they cannot contribute to ion acceleration any more. In fact, *for the laminar target, where electrons can be reflected at the rear surface and recirculate, the ions emitted at both the irradiated and rear target ($\mathcal{E}_{rear}$ in tab. 5.1) always have energies close to the corresponding E_{max}.* The maximum energy of the ions emitted towards the vacuum is always higher when a laminar target is considered compared to a semi-infinite target. *Thus we may conclude that, for the semi-infinite case, as the most energetic electrons are rapidly lost into the bulk plasma, ion acceleration by TNSA is less efficient, as fewer electrons contribute to the process.*

Contrastingly, if we examine the energy $\mathcal{E}_{plasma}$ of the shock accelerated ions at $I\lambda_0^2 = 10^{19}$W cm$^{-2}\mu m^2$, we notice that $\mathcal{E}_{plasma}$ is higher for the semi-infinite case than for the laminar targets. This may indicate that ion emission towards the vacuum and plasma expansion at the rear of the target have a negative effect on the final energy of the ions accelerated by the shock and the maximum energy is not reached. We also observe, comparing the cases of flat and modulated targets, that there is a variation of the energy of the shock accelerated ions even if the shock velocity values that we have calculated have little difference. This may be the result of the fact that we cannot properly estimate the velocity of the different elements of a deforming front when the target is modulated and the y component of the shock velocity is not taken into account properly. However the energy of the shock accelerated ions do not vary when the target

shape is not varied (see $\mathcal{E}_{plasma}$ for resonant incidence in tab. 5.1), even if we change the angle of incidence. Therefore we may still conclude that the SPW excitation does not play a fundamental role in this mechanism.

5.7 Conclusion

In this chapter we have studied the ion acceleration and its dependence on SPW excitation for different laser and target parameters. We have considered both the low and high intensity regimes, corresponding respectively to $I\lambda_0^2 = 10^{16}$W cm$^{-2}\mu m^2$ and $I\lambda_0^2 = 10^{19}$W cm$^{-2}\mu m^2$, resonant and non-resonant laser incidence, different modulation depths and target thicknesses. Two mechanisms of ion acceleration can be identified in the simulations, one, the Target Normal Sheath Acceleration (TNSA) accelerates the ions towards the vacuum, the other, the shock acceleration, pushes them from the surface into the plasma. Both mechanisms have a dependence on the electron temperature, thus the enhanced electron heating via SPW is expected to play an important role. The first mechanism causes acceleration normal to the target surface, driven by the space charge field associated with an electron plasma sheath, set up by the hot electrons accelerated by the laser pulse at the front surface. Hot electrons also propagate through the target so that, for a laminar target, TNSA is observed both at the front and at the rear of the target. In the low intensity regime the ions are found to be emitted in the direction perpendicular to the target surface, consistently with the TNSA mechanism while shock acceleration is not observed. In the high intensity regime, instead, we find both ions emitted into the vacuum and shock accelerated ions. *We have studied the characteristics of the shock which is ponderomotively driven for laser intensities greater than $I\lambda_0^2 = 10^{18}\,W\ cm^{-2}\mu m^2$ and the analysis of the velocity and peak density of the shock suggests that it does not depend on SPW excitation and can be associated with the cold electron population.* Contrastingly, *acceleration by the TNSA mechanism, which is driven by the hot electrons, is strongly enhanced when the SPW is present.*

As for electron emission, we have examined the dependence on the geometry of the target and observed that for non-resonant incidence, the ion angular distribution at the irradiated surface can be traced back to plasma expansion, corresponding to emission in the direction perpendicular to the modulated surface. The same angles are found also for the resonant incidence but in this case we have more ions which have negative $\hat{y}$ component of the velocity. These ions are the ones having the greatest energy, which represents the cut-off observed in the spectra.

Comparing the ion currents and density we have found that ion filaments develop at the same points where we had previously observed the electron bunches which exit and re-enter the plasma, when the SPW is present. Thus *the SPW can be associated with the production of high energy ions at the irradiated target surface whose acceleration is driven by hot electrons associated with the surface wave field, via the TNSA mechanism.* As observed for electron heating, the effects of SPW excitation are dominant over geometry effects due to plasma expansion when the modulation depth is reduced.

For laminar targets, we also considered the *ion emission at the rear side of the target*, which is unirradiated. In this case the angular direction of the ions is always

perpendicular to the surface, which is flat at the rear side. Nevertheless, *SPW excitation has an effect on these ions too as the energy of the hot electrons which drive the ion acceleration via TNSA is increased.* Higher ion energies are observed compared to the the cases where the wave is not present: for example at $I\lambda_0^2 = 10^{19}\text{W cm}^{-2}\mu m^2$ the maximum ion energy is 14MeV when the SPW is excited while for a flat target it is only 8.3MeV. *Thus the excitation of a SPW is found to be an efficient mechanism in order to increase the energy of the ions emitted in laser-plasma interaction.*

Table 5.1: Ion energy at $t = 1000\omega_0^{-1}$, as a function of the laser intensity, and target parameters. flat=flat target, res= resonant case (modulated surface and $\theta = 30$), n-r= non resonant angle of incidence (modulated surface).

Target (type)	$I\lambda^2$ W cm$^{-2}\mu m^2$	h λ_0	d λ_0	$\mathcal{E}_{front}$ keV	$\mathcal{E}_{plasma}$ keV	$\mathcal{E}_{rear}$ keV
res	10^{16}	inf	1	150	20	–
flat	10^{16}	inf	0	120	15	–
res	10^{17}	inf	1	500	30	–
flat	10^{17}	inf	0	160	25	–
res	10^{18}	inf	1	1800	40	–
flat	10^{18}	inf	0	60	40	–
res	10^{19}	inf	1	6500	1000	–
flat	10^{19}	inf	0	1600	400	–
res	10^{19}	3.5	1	11800	800	14000
res	10^{19}	8	1	10000	850	11000
res	10^{19}	inf	1/3	9200	700	–
n-r	10^{19}	inf	1/3	1650	700	–
res	10^{19}	3.5	1/3	12500	700	14000
n-r 10°	10^{19}	3.5	1/3	10000	700	12000
flat	10^{19}	3.5	0	8100	380	8300
flat	10^{19}	8	0	5800	380	6000

Chapter 6

The case of a Gaussian laser pulse

In the previous chapters we have used a laser pulse shape which had a plane spatial profile in the y direction, i.e. perpendicular to the propagation direction. This do not reproduce the real envelope of a laser pulse, which has a given transversal size (the 'waist'). This choice was motivated by the need to investigate the mechanisms which are relevant in the processes of light absorption and particle acceleration, when a surface wave is excited by laser-gating interaction, reducing the number of effects which have to be taken into account at the same time.

Moreover, the choice of a laser profile having uniform intensity along y, allows us to reduce the computational requirements and to perform a larger number of simulations, testing different parameters.

In this chapter we will examine the effect of the finite transversal size of the pulse envelope, by approximating its y profile with a Gaussian function. The pulse will be focused on the center of the target surface, with a focal spot (intended as the FWHM of the Gaussian) of $10\lambda_0$, and will have the same temporal dependence as in the previous chapters. This focal spot size corresponds to the typical transverse size of the pulse in the experiments where the interaction of a laser with a laminar target is studied [26, 27, 28]. In the simulation, we will use a laminar target of thickness $3.5\lambda_0$ and density $n_e = 25n_c$, with a modulation at the surface of periodicity $a_m = 2\lambda_0$ and depth $d = \lambda_0$. The pulse will be incident at the resonance angle $\theta = 30°$. As the pulse is no more periodic in the y direction, we will take a simulation box size of $110\lambda_0 \simeq 691k_0^{-1}$ along y, in order to avoid unwanted effects from the boundaries (which have periodic conditions along y), while the total box size will be $480k_0^{-1}$ along x.

In order to underscore the computational requirement associated with this simulation, we have to consider that, in this case, we have 18440 plasma points along y and 590 along x, i.e. a total of 10^7 plasma points. Thus the total number of particles is now $\sim 10^9$. The code was parallelized (see appendix .1) and 461 processors were necessary in order to treat such a large number of particles and grid points (we recall that when the pulse is uniform along y we need just 32 processors). The total CPU time necessary to complete a simulation, which has a typical duration of $1000\omega_0^{-1}$, is $\sim 4000H$. The outputs of this simulation occupy more than 1TB, $\sim$ 15 times bigger than the space occupied by the data of the previous simulations.

In order to give an overview of the simulation set-up, in fig.6.1 we show the x component

of the electric field, for the Gaussian pulse.

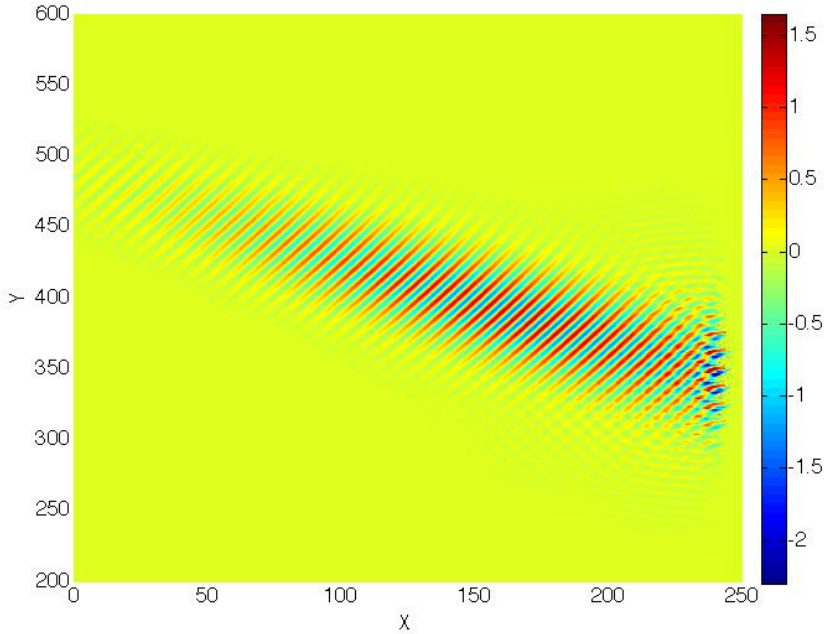

Figure 6.1: Electric field E_x at $t = 390\omega_0^{-1}$ for the Gaussian pulse, $I\lambda_0^2 = 10^{19}$W cm$^{-2}\mu m^2$ ($a_0 = 2.72$), $d = \lambda_0$, $n_e = 25n_c$, semi-infinite target **when the SPW is excited by a Gaussian laser pulse**. The plasma starts at $x = 240k_0^{-1}$, the pulse focus is at $y \simeq 345.5k_0^{-1}$ and the focal spot size is $10\lambda_0 \simeq 63k_0^{-1}$.

We will compare the case of the Gaussian profile pulse with the simulation having the same target parameters (and the same laser intensity) but plane laser transverse envelope. The aim of this study is to understand qualitatively the modifications that we can expect when comparing our previous parametric study to a more realistic set-up.

6.1 SPW excitation

We will first consider the absorption values for the Gaussian pulse, and compare with the absorption for the pulse having a plane transversal profile, impinging on the same target type, for $I\lambda_0^2 = 10^{19}$W cm$^{-2}\mu m^2$. We observe that the absorption for the Gaussian pulse is 74%, a value lower than the plane pulse value which was 85%. This result is not surprising as, in general, we have observed that absorption in the high intensity regime always increases with intensity and for the Gaussian profile the intensity spatially decreases away from the center of the pulse. This means that, in contrast with the case where the laser intensity is uniform along y, the local absorption will gradually decrease when the distance from the laser focus increases and the total value will be lower than the one found when the intensity is uniform. However the difference is not dramatic and 74% is still a high value.

Then we will examine the electric field E_x, which is associated with the SPW excitation, in order to verify i) the periodicity of its spatial distribution, which should be $\lambda \sim \lambda_0$ and ii) its frequency, which is expected to be the same as the laser pulse, i.e. $\omega = \omega_0$. In fig.6.2 the electric field E_x is shown at time intervals of $1.5\omega_0^{-1}$ ($\sim 1/4$ laser period), starting from $t = 492\omega_0^{-1}$, for a portion of surface of $6\lambda_0$ around the laser focus ($y \simeq 345.5k_0^{-1}$). The field distribution at the center is very similar to that

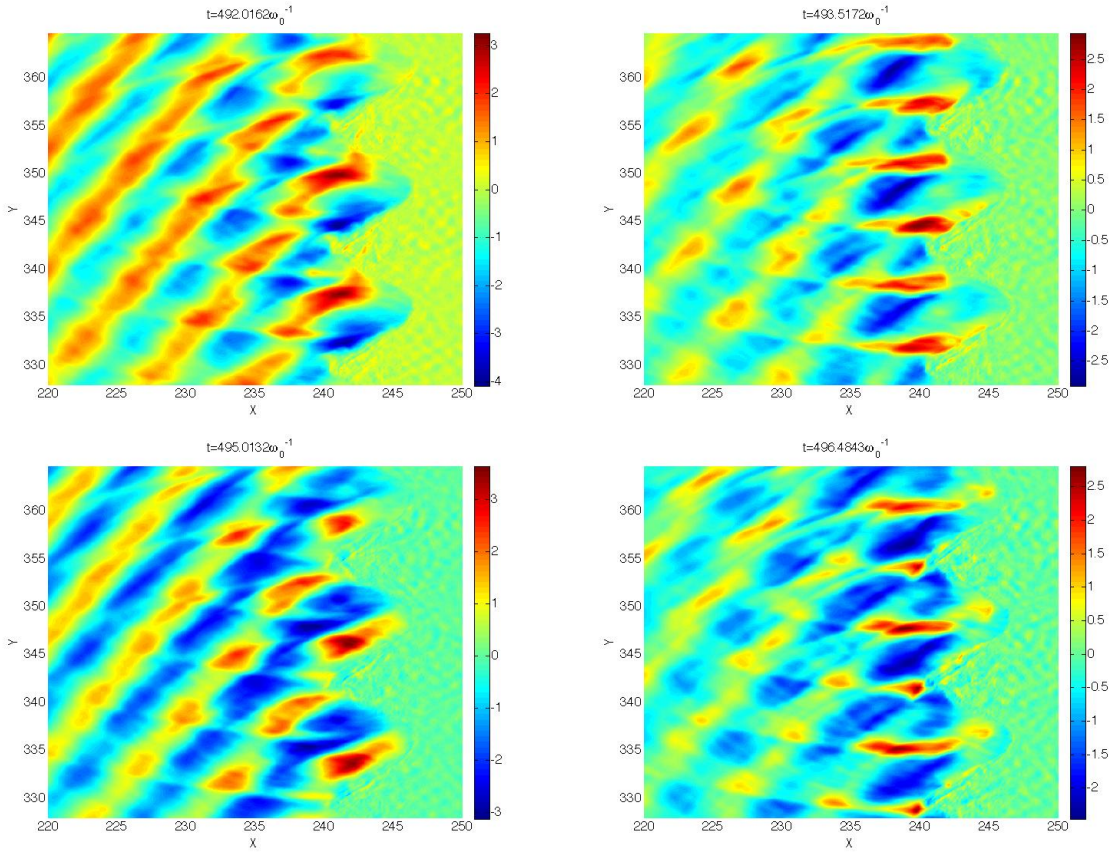

Figure 6.2: Electric field E_x, sequential plots taken at time intervals of $1.5\omega_0^{-1}$ ($\sim 1/4$ laser period), starting from $t = 492\omega_0^{-1}$. $I\lambda_0^2 = 10^{19}$W cm$^{-2}\mu m^2$ ($a_0 = 2.72$), $d = \lambda_0$, $n_e = 25n_c$, for a laminar target of thickness $h = 3.5\lambda_0$ **when the SPW is excited by a Gaussian laser pulse**.

observed for the pulse having a plane transverse profile: we observe a localized field at the surface which has 6 periods along y that correspond to a periodicity of $\simeq \lambda_0$. Away from the center the intensity of the field is progressively lower, but, as shown in fig.6.2, the intensity can be considered quasi-constant over a small portion of surface. The oscillation frequency that we observe confirms the resonant excitation of the SPW , as we find $\omega \sim \omega_0$. This can be also verified by comparing E_x in fig.6.2 for $t = 492\omega_0^{-1}$ and about a half period later, at $t = 495\omega_0^{-1}$, as we notice that the field at the surface at a given position has opposite signs in the two pictures.

The maximum local amplification, of the field at the focal spot, is $\eta = 3.4$ that is essentially the same value as obtained in the simulation where we used the same target

parameters and laser intensity but a uniform y profile for the pulse envelope (where we had $\eta = 3.5$).

Thus we may conclude that for a pulse having a Gaussian shape we can still excite the surface wave: its maximum amplitude will be almost the same as that predicted for the pulse having uniform transversal profile and will correspond, in space, to the laser focal spot area. The absorption fraction, instead will decrease slightly, and this can be interpreted as a consequence of the lower intensity values far from the center of the pulse, which are generally associated with lower absorption values.

6.2 Electron heating

We have seen that SPW excitation by a Gaussian pulse, if we observe a small portion of the target surface, has characteristics which are very similar to those presented in the previous chapters, where the laser pulse was uniform on the target surface.

However as far as the electron acceleration is concerned, we expect some important differences as we have to take into account the non-homogeneity of the field along y, which will give a different contribution to electrons involved in the vacuum heating process.

We will now analyze in detail the emission angles of the electrons for the Gaussian laser pulse impinging on a laminar target of thickness $22k_0^{-1} \sim 3.5\lambda_0$. We recall that in the laminar target the emission direction (forward/backward) is not sufficient to separate electrons which are recirculating inside the plasma from those which are emitted into the vacuum. Thus the phase space of electrons will again be divided into 3 parts: (a) electrons emitted into the vacuum at the irradiated side ($x = [0 - 240k_0^{-1}]$), (b) electrons inside the plasma, and (c) electrons emitted into the vacuum at the rear of the target ($x = [262 - 480k_0^{-1}]$). In each section, we will distinguish two directions for the electron motion: backward (i.e. moving from left to right) and forward (i.e. moving from right to left).

We observe that, in general, the electron motion in the three sections (plasma and vacuum at the front and rear side) has two main angles, $\pm 60°$, which correspond to the direction perpendicular to the grating surface. The only exception is the emission at the irradiated side, shown in fig.6.3a, where we notice a peak around $-80°$, both in the backward (towards the vacuum) and forward (towards the plasma) directions.

In fig.6.4, where the electron currents are shown, we observe an electron emission towards the vacuum (backward), at the irradiated side of the target, which is qualitatively similar to that observed (in fig.4.26) for the same simulation parameters but uniform laser intensity along y. In fact we notice similar bunches of hot electrons that exit the plasma periodically, in a direction which is nearly normal to the target surface ($\simeq 60°$), at two main points situated on the lower part of the modulation tip: one closer to the top and the other halfway between the top and the bottom of the dip. The periodicity of the emission is one laser period and there is a phase lag of half a laser period between two emission points. Then the electrons re-enter the plasma, following the surface modulation. We may also observe bunches of electrons which are moving inside the plasma, towards the rear surface, where they are reflected. Comparing with

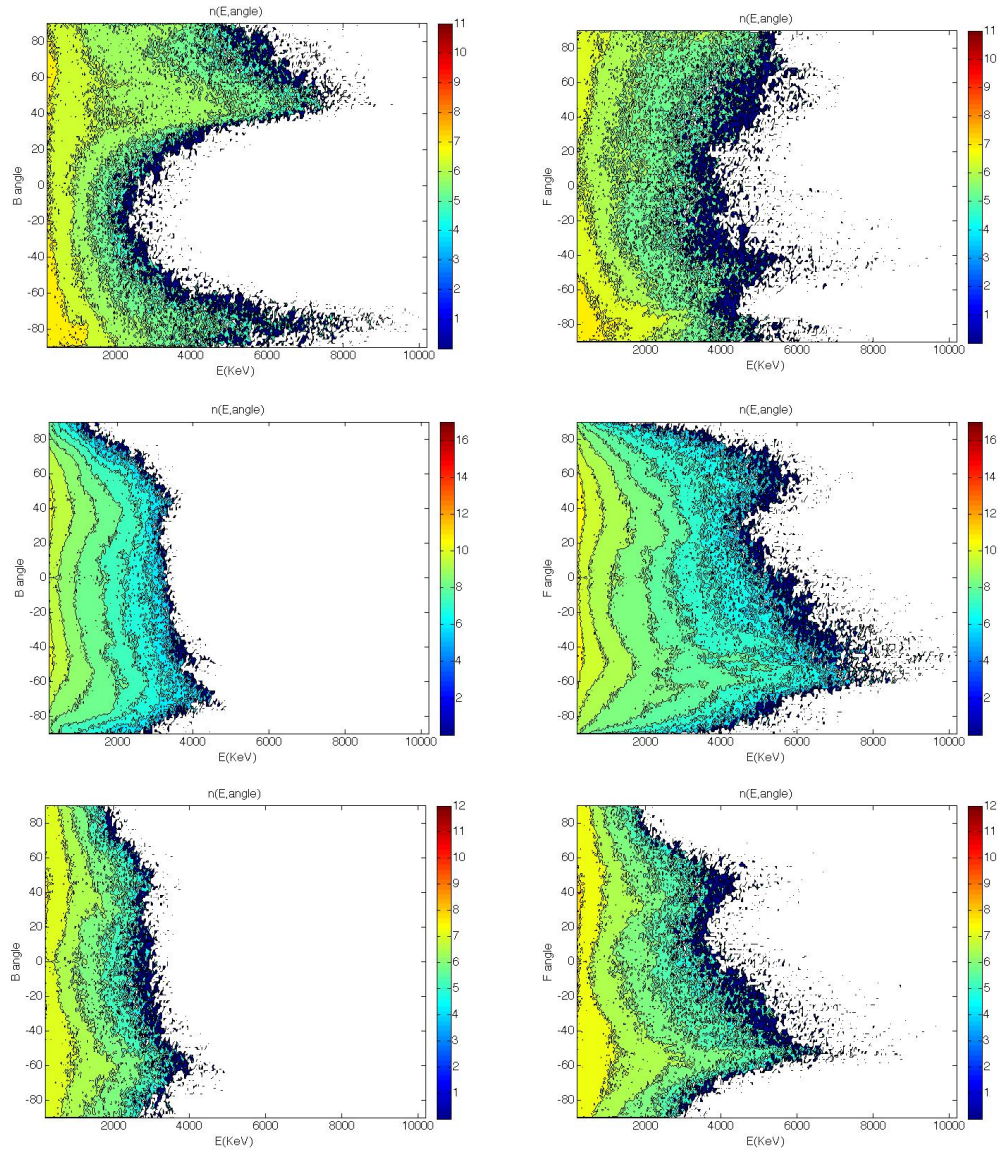

Figure 6.3: Electron emission angles backwards (**B**=moving from left to right) and forwards (**F**=moving from right to left), for the laminar target of thickness $22k_0^{-1} \sim 3.5\lambda_0$, taken at $t = 492\omega_0^{-1}$; $I\lambda_0^2 = 10^{19}$W cm$^{-2}\mu m^2$ ($a_0 = 2.72$), $n_e = 25n_c$. **The SPW is excited by a Gaussian laser pulse.(a)** electrons emitted into the vacuum at the irradiated side ($x = [0 - 240k_0^{-1}]$).**(b)** electrons inside the plasma ($x = [247 - 262k_0^{-1}]$).**(c)** electrons emitted into the vacuum at the rear of the target ($x = [262 - 480k_0^{-1}]$).

the corresponding electric field distribution in fig.6.2, where E_x is plotted for the same times, we notice that the points at which electrons are emitted correspond to local (positive) maxima of the SPW field. This result is the same as what was found in all the cases where the surface wave was excited (see chapter 4) and can be interpreted as follows: electrons which experience large oscillations at the surface have entered the

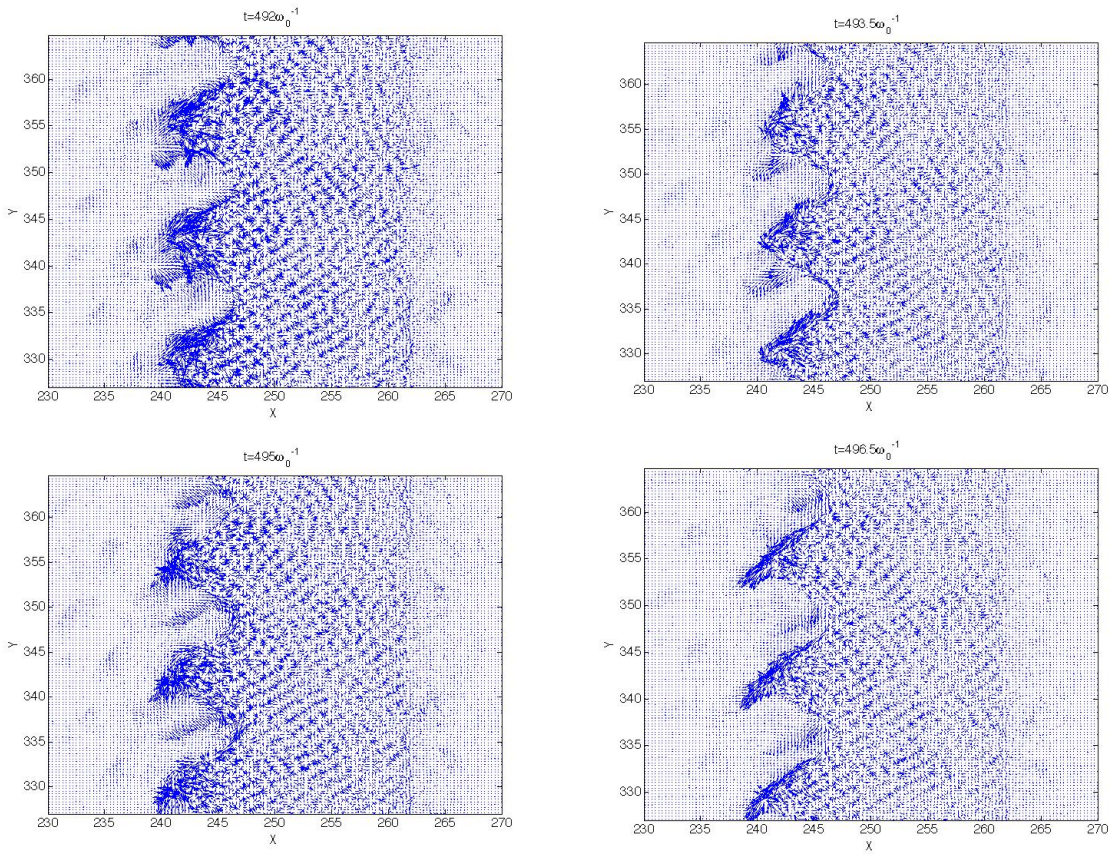

Figure 6.4: Electron current ($n_e v_e$, no charge sign) sequential vector plots taken at time intervals of $1.5\omega_0^{-1}$ ($\simeq$ 1/4 laser period), starting from $t = 492\omega_0^{-1}$. $I\lambda_0^2 = 10^{19}$W cm$^{-2}\mu m^2$ ($a_0 = 2.72$), $d = \lambda_0$, $n_e = 25n_c$, laminar target of thickness $h = 3.5\lambda_0$. **The SPW is excited by a Gaussian laser pulse**.

wave field at the most favourable phase, i.e. at a zero, as discussed in [77], and reached the maximum excursion when the amplitude of the field was maximum. Such electrons can detach from the surface and exit or enter the plasma depending whether the field is evolving towards a minimum or a maximum.

However the temperature of the hot electrons is generally reduced compared to the simulation where a pulse having a uniform y profile was used, in fact here we have only $T_{hot,Gaussian} = 1.4$MeV while in the previous case (where the laser profile is uniform along y) we had $T_{hot,uniform} = 2.3$MeV. Furthermore the maximum electron energy is lower: $E_{max,Gaussian} = 11$MeV while in the case of the laser with uniform transversal profile $E_{max,uniform} = 14$MeV. This may be interpreted as consequence of the fact that, as the intensity of the field is not homogeneous on the target surface, only electrons at the focal spot can be efficiently accelerated, resulting in a lower percent of hot electrons. This effect is evident from the observation of the lower electron emission at only $3\lambda_0$ from the center of the target, as shown in fig.6.5. We notice that the bunches of electrons which were observed to exit the plasma at $t = 496.5\omega_0^{-1}$ rapidly decrease their excursion into the vacuum when we observe the zones away from the laser spot. Also

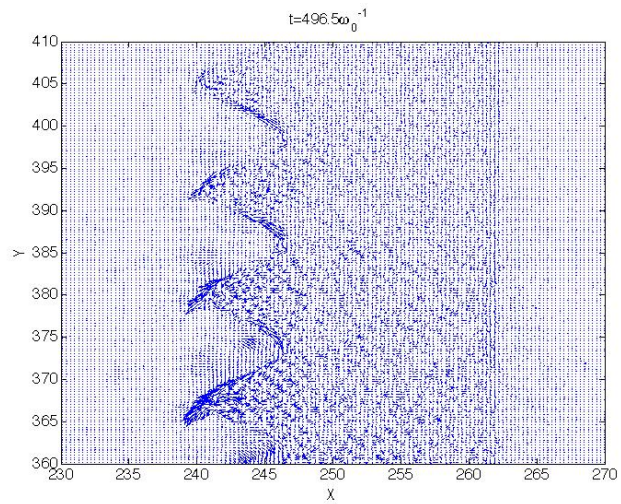

Figure 6.5: Electron current ($n_e v_e$, no charge sign) vector plot at time $t = 496.5\omega_0^{-1}$, starting at $y = 360k_0^{-1}$ (the laser spot is centered at $y \simeq 345.5k_0^{-1}$). $I\lambda_0^2 = 10^{19}$W cm$^{-2}\mu m^2$ ($a_0 = 2.72$),$d = \lambda_0$, $n_e = n_c$, laminar target of thickness $h = 3.5\lambda_0$. **The SPW is excited by a Gaussian laser pulse**.

the recirculation mechanism may be less efficient as electrons that are emitted with a given angle, after being reflected at the rear surface, will return to the irradiated surface at a point which is different from the emission one and where the accelerating field has a different value. Schematically, an electron accelerated at the laser focus, $y = 345.5k_0^{-1}$, and having angular direction $\simeq 60°$, would return to the irradiated surface at the point $y = 345.5 + 2h\sin\theta \simeq 383.6k_0^{-1}$ (i.e. at the edge of the focal spot), after the first reflection, where the field is much lower. This effect may be reduced by reducing the target thickness h or the electron emission angles. We notice that the latter condition is difficult to achieve as, for example, reducing the modulation depth we reduce the emission angles associated with the direction perpendicular to the modulation but the angles associated the direction tangent to the modulation increase. One solution may also consist in varying the angle of incidence of the laser pulse (adapting the target parameters for the resonance), in order to extend the irradiated area.

We may conclude that the process of electron heating, when the pulse envelope has a Gaussian shape, is qualitatively similar to what observed, for the same target parameters, but with uniform laser intensity along the transverse direction. In the zone corresponding to the maximum laser intensity on the target, we observe the same electrons bunches which are associated with the surface wave excitation. Nevertheless the electron temperature value is lower than the one found for the uniform pulse and this can be traced back to the non-uniformity of the laser intensity at the target surface which reduces the effects of recirculation.

6.3 Ion acceleration

In chapter 5 we have analyzed the process of ion acceleration both in the case of semi-infinite and laminar targets, when the transverse profile of the pulse is uniform. We recall that two acceleration mechanisms were identified, one, shock acceleration, pushes the ions from the irradiated surface towards the plasma bulk, while the other one, the TNSA mechanism, accelerates ions towards the vacuum, both at the irradiated and at the rear sides of the target. We observed that shock mechanism is weakly dependent on the SPW excitation while the TNSA was strongly enhanced by SPW excitation. In fact, in the TNSA, ion acceleration is driven by the space charge field associated with the hot electrons and, as their temperature and number grows when the surface wave is excited, the mechanism becomes more efficient.

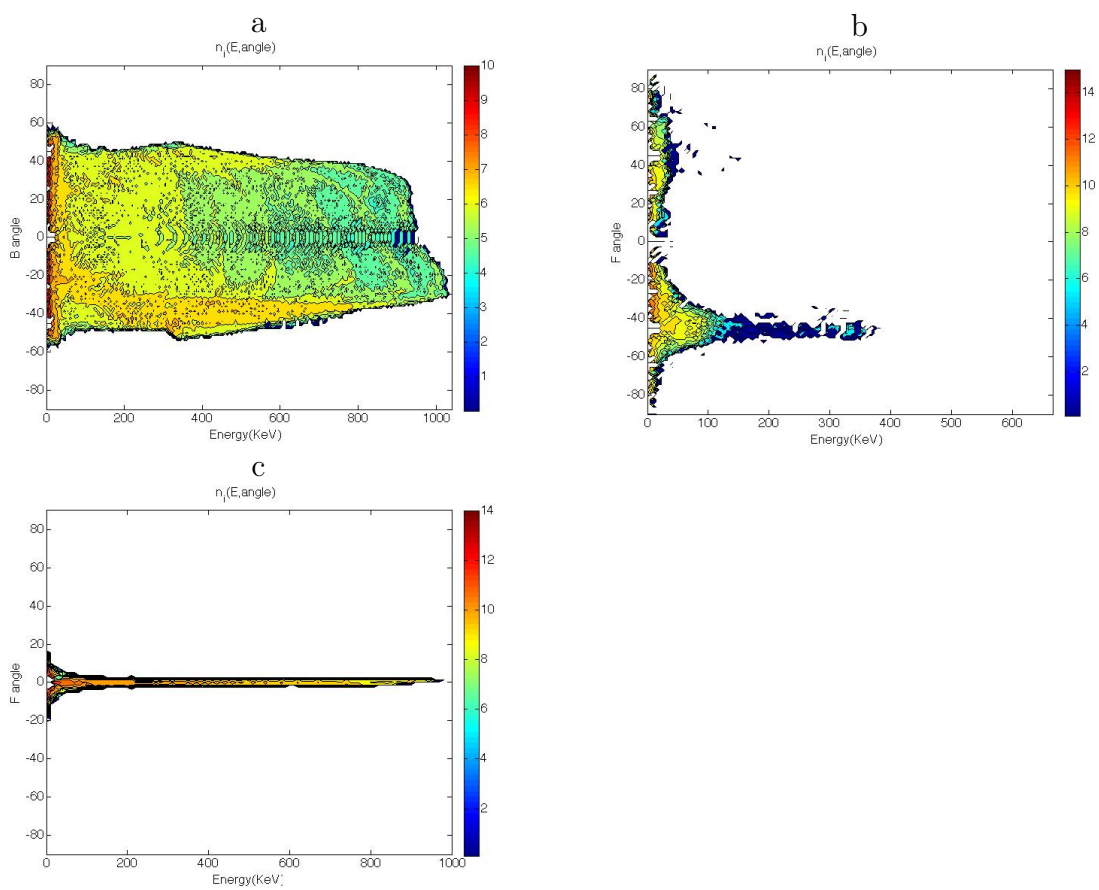

Figure 6.6: (a) Ion emission towards the laser source at the irradiated side, ions accelerated into the plasma (b), and (c) forward emission at the unirradiated side, as a function of the emission angle and energy for the laminar target **when the SPW is excited by a Gaussian pulse**; $I\lambda_0^2 = 10^{19}$W cm$^{-2}\mu m^2$ ($a_0 = 2.72$), $n_e = 25n_c$, $t = 500\omega_0^{-1}$, $d = \lambda_0$, laminar target of thickness $h = 3.5\lambda_0$.

In this section we will examine the ion emission when the laser y profile is Gaussian and the intensity of the pulse is not uniform over the target surface. As we are interested

in the processes where SPW excitation plays a relevant role, we will focus on the TNSA mechanism.

We will start by considering the angular distribution at two different times. As in chapter 5 we will consider $t = 500\omega_0^{-1}$, which is approximately the time at which electrons reach their maximum energy and $t = 1000\omega_0^{-1}$, which is the time at which ion acceleration starts saturating and ions reach the maximum energy.

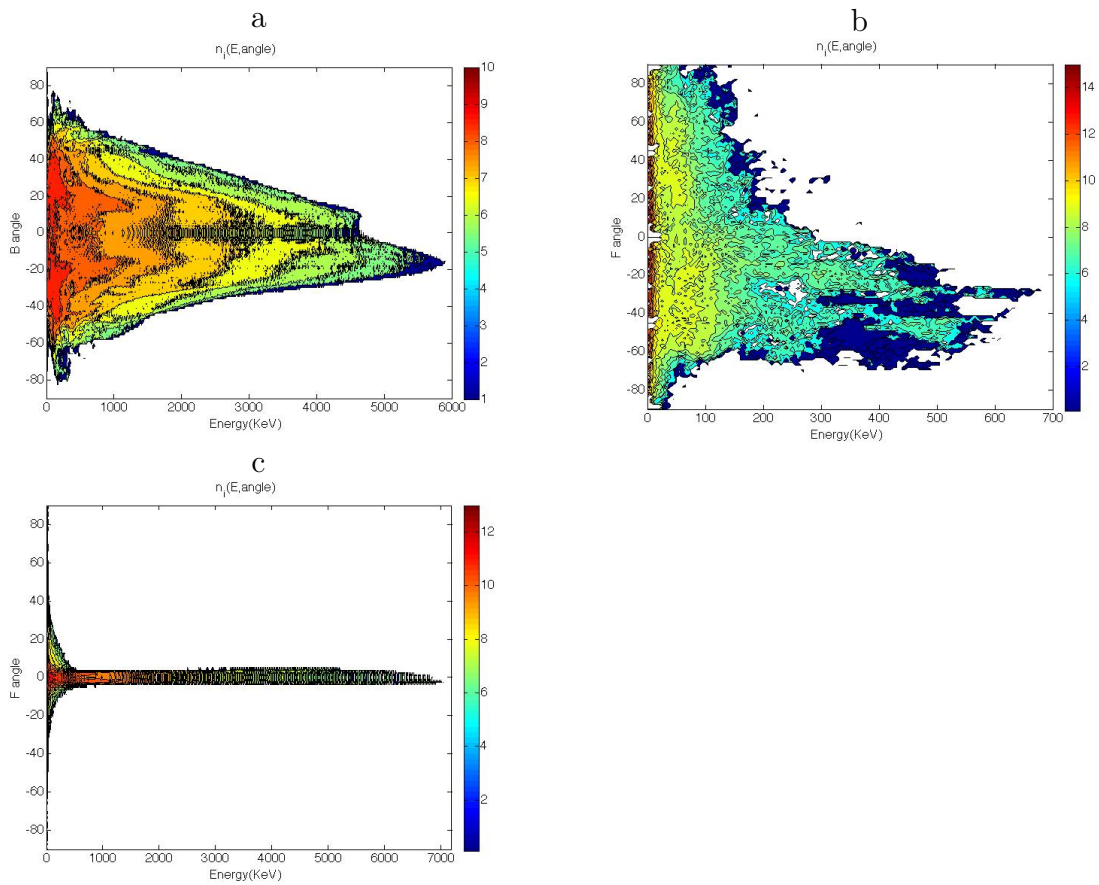

Figure 6.7: (a) Ion emission towards the laser source at the irradiated side, ions accelerated into the plasma (b), and (c) forward emission at the unirradiated side, as a function of the emission angle and energy, for the laminar target **when the SPW is excited by a Gaussian laser pulse**; $I\lambda_0^2 = 10^{19}$W cm$^{-2}\mu m^2$ ($a_0 = 2.72$), $n_e = 25n_c$, $t = 1000\omega_0^{-1}$, $d = \lambda_0$, laminar target of thickness $h = 3.5\lambda_0$.

In fig.6.6 we show the angular distribution of ions at $t = 500\omega_0^{-1}$. We observe that the emission angles have not changed substantially compared to the case where a pulse with a uniform transverse profile was used. Ions emitted in the backward direction (fig.6.6 a), at the irradiated side have a quite symmetric distribution, with two peaks around $\pm 40°$, which can be associated with the expanding ion front, as discussed in chapter 5. The most energetic ions correspond to the negative angle, as found in all the cases where the SPW was excited, and can be associated with the development of ion filaments. The latter are generated at the points where electron bunches are observed which oscillate at the target surface. The ions emitted at the rear (fig.6.6 c)

are accelerated in the direction perpendicular to the flat surface, i.e. 0° as for the the simulation where the pulse profile was uniform along y, but here they have a larger angular spread, $\simeq 7°$ instead of $\simeq 2°$. The increased angular spread may be traced back to the inhomogeneity of the space charge field at the surface, due to the inhomogeneous distribution of the hot electrons reaching the rear side of the target, which may induce a defocusing effect on the ions. We also see that the direction of shock accelerated ions, moving inside the plasma, does not change for the Gaussian pulse shape, being around 40°.

At later times, for $t = 1000\omega_0^{-1}$, we observe that the angular distribution of the ions moving backwards (fig.6.7a) has evolved and the most energetic ions corresponds to angles $\pm 20°$. This evolution was also found in the other simulations where the surface had a modulated profile and may be associated both to an evolution of the particles trajectories in the external field and to the presence of groups of ions that are emitted at different times (see chapter 5). The final energy of the ions moving backwards, from the irradiated target surface is 6MeV for the Gaussian pulse case, much lower than in the case where the pulse was uniform along y, where we found 12.5MeV. Also the ions emitted at the rear side of the target (non-irradiated) have lower final energies: as shown in fig.6.7c, the maximum energy in this case is only 7.1MeV, while, for the simulation where pulse intensity was uniform on the target surface, the maximum energy was 14MeV. We notice that, by contrast, the final energy of ions accelerated into the plasma bulk (fig.6.7b) has changed only slightly, from 800keV when the pulse is uniform on the target surface to 700keV for the Gaussian one. Moreover we notice, observing

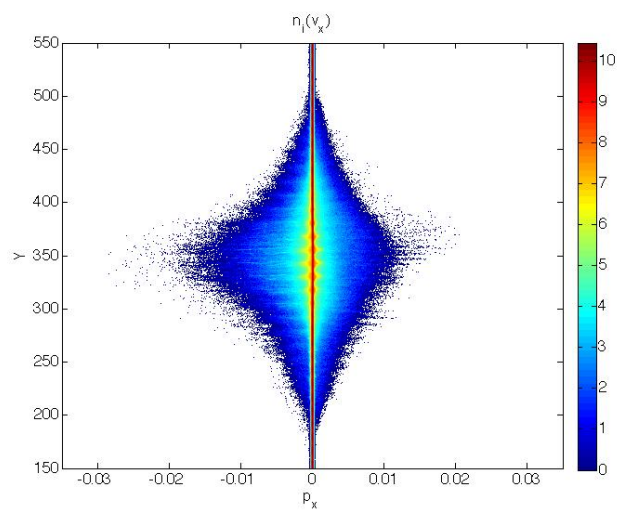

Figure 6.8: Ion phase space (y, p_x) for the laminar target **when SPW is excited by a Gaussian laser pulse**; $I\lambda_0^2 = 10^{19}$W cm$^{-2}\mu m^2$ ($a_0 = 2.72$), $n_e = 25n_c$, $t = 500\omega_0^{-1}$, $d = \lambda_0$, laminar target of thickness $h = 3.5\lambda_0$.

the ion momentum p_x as a function of y (fig.6.8), that the emission is concentrated, along y, at the point where the laser intensity is maximum and that far from that point the emission gradually decreases.

We may conclude that, qualitatively, the ion emission in the case where the laser pulse has a Gaussian envelope in the transverse direction is similar to the case where the pulse has uniform intensity in the transverse direction, if we look only at the zone of the laser spot (that is the center of the target, at $y = 345.6k_0^{-1}$). Nevertheless, the angular spread of the electrons crossing the target, combined with the fact that the field intensity is not uniform along the surface, led to a decreased efficiency of recirculation and the energy of the ions is reduced down to the values of the semi-infinite target. The same ion energy reduction is observed also for a plane laminar target when the laser pulse has a Gaussian envelope: if we consider a simulation having the same laser and target parameters as the one described above, but flat target surface, the energy of the ions emitted at the unirradiated side is 4MeV. This means that, when the SPW is excited, the ion energy is increased of the same factor $\simeq 1.8$ (compared to a plane target) that is found in the case where the laser has uniform intensity in the transverse direction (see tab.5.1).

6.4 The magnetic field

The inhomogeneity of the electron emission along the target surface, shown in fig.6.5 and of the plasma expansion (fig.6.8), which are observed for the Gaussian laser pulse, have important consequences on the characteristics of the quasi-static magnetic field.

In fig.6.9 we can observe the magnetic field distribution for the case of the Gaussian laser pulse. We notice that the sign of the magnetic field changes around $y = 345.5k_0^{-1}$,

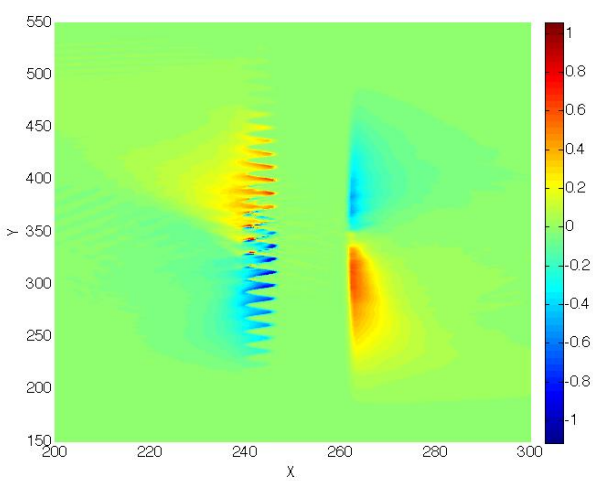

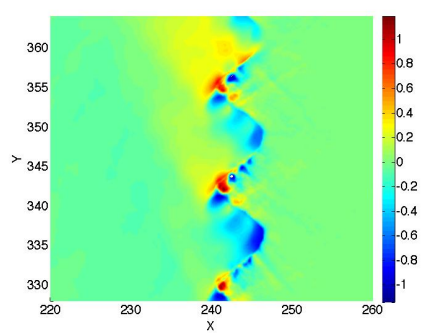

Detail of B_z inside the focal spot (which is centered at $y = 345.5k_0^{-1}$)

Figure 6.9: Magnetic field B_z (Normalized to $B_0 \simeq 107$MG for $\lambda_0 = 1\mu$m) averaged over the laser cycle for the laminar target **when the SPW is excited by a Gaussian laser pulse**; $I\lambda_0^2 = 10^{19}$W cm$^{-2}\mu m^2$ ($a_0 = 2.72$), $n_e = 25n_c$, $t = 500\omega_0^{-1}$, $d = \lambda_0$, laminar target of thickness $h = 3.5\lambda_0$. The laser transverse size (FWHM) is $10\lambda_0 \simeq 63k_0^{-1}$.

that is the 'focus' of the laser pulse: at the irradiated target side the magnetic field is positive for $y > 345.5k_0^{-1}$ and negative for $y < 345.6k_0^{-1}$ while at the rear of the target the sign of the field is negative for $y > 345.5k_0^{-1}$ and positive for $y < 345.5k_0^{-1}$. This

fact can be explained by considering the mentioned inhomogeneity of plasma expansion: the electron current is maximum at the point where the laser is more intense and this applies both to electrons accelerated towards the vacuum, at the irradiated surface, and to electrons which have reached the rear surface. The spatial distribution of the field suggests that the hot electrons leaving front and back surfaces are pulled back by the space charge. As they are emitted with an angular spread, they will return to the target along curved trajectories and this corresponds qualitatively to the scheme called 'fountain effect' which is described in references [86, 87]. This process, combined with the local ion and electron current unbalance, leads to the final spatial distribution observed in fig.6.9. The maximum magnetic field observed in the simulation is about ~ 120MG for $\lambda_0 = 1\mu$m

Nevertheless if we observe in detail the magnetic field distribution inside the focal spot, we notice that it is very similar to the distribution observed when the laser pulse was uniform along y (see fig.3.6). This means that in this area the electron acceleration associated with the surface wave dominates over the other effects and determines the characteristics of the quasi static magnetic field.

This results further confirms that the self-generated magnetic field found in our simulations essentially depends on kinetic effects: the inhomogeneity of particles emission, due to the Gaussian pulse profile, produces a bipolar magnetic field, far from the laser spot, while inside the focal spot the field distribution depends on the electrons accelerated in the SPW field.

6.5 Conclusion

We have examined the case where a laser pulse having a Gaussian profile, with $10\lambda_0$ FWHM, excites a surface wave on a laminar target of thickness $h = 3.5\lambda_0$. The aim of this study was to compare this case, which is computationally demanding but closer to typical experimental parameters [27], to the cases where pulse was uniform along y, which required less computational resources and allowed the parametric study of laser-grating interaction.

We observe that the surface wave is excited and that the electric field perpendicular to the surface, if we limit our observations to the laser spot, is similar to what we found when the pulse transverse profile was uniform. Similarly, the quasi static magnetic field generated on the target surface, inside the focal spot area, has the same distribution as observed when the pulse intensity was uniform along y. We also observe the same bunches of electrons, oscillating at the surface, which were found in all the cases where the wave was excited. However their excursion decreases far from the center of the target (which is the focus of the pulse), as the intensity of the laser field decreases.

Moreover we observe that when the pulse has a Gaussian shape, the electron temperature is lower compared to the value found when the pulse intensity is uniform along y. This can be related to the fact that the energy of the electrons accelerated at different points of the surface is different and only the electrons at the center of the target may reach the maximum energy. Furthermore the effects of recirculation are reduced as electrons, which are accelerated at an angle and reflected at the rear surface, will

find a reduced field intensity in the zones far from the laser spot.

The different electron heating entails important changes for ions accelerated by TNSA, both at the front and at the rear of the target. The maximum ion energy decreases from 14MeV to 7.1MeV when the pulse transverse profile changes from uniform to Gaussian, a value close to the one found when the target is semi-infinite. The maximum ion energy does not correspond to the maximum electron energy (11MeV), as was the case when the pulse had a plane transverse profile and this may indicate that recirculation is less efficient, providing fewer hot electrons at a given point. *Nevertheless the ion energy is higher than the value found experimentally for similar laser and target parameters, where the SPW is not excited. For example in [80], where the laser pulse intensity and duration were respectively* $I\lambda_0^2 = 3 \times 10^{19}\, W\, cm^{-2}\mu m^2$ *and* $80fs$*, and the target thickness was* $\sim 5\lambda_0$*, the maximum ion energy was* $2.4MeV$*.*

We may conclude that, in general, when a Gaussian pulse is used, the absorption, and electron/ion energy are lower (74%) than the values found in the simulations where the laser intensity was uniform on the target surface (85%). From the analysis done in this chapter, we may infer that this effect is a mere consequence of the pulse shape and does not depend on SPW excitation. This means that we expect a quantitative difference between the values found in all the simulations in the previous chapters and experimental values on laser-grating interaction. *The simulation examined in this chapter, by contrast, shows a qualitative agreement with the study presented in the previous chapters, where we used a pulse profile which was uniform along* y*. Thus we have demonstrated that the simplified simulations where the effect of transverse pulse size is not considered, can efficiently predict the qualitative dependence of SPW excitation, electron heating and ion acceleration on laser and target parameters.*

Conclusions

The problem of the excitation of a plasma surface wave by the interaction of a laser pulse on a structured target has been investigated in this work, both analytically and numerically. We have seen that describing the surface wave with a simple fluid model, we can find the surface wave dispersion relation which, combined with the phase matching conditions, allows us to determine the periodicity of the modulation at which the wave is resonantly excited, as a function of the pulse angle of incidence. The dynamics of the plasma and the distribution of the fields associated with SPW excitation are reproduced using two-dimensional particle-in-cell (PIC) simulations, where the plasma surface is initially pre-formed so that the SPW excitation conditions are fulfilled. The surface wave excitation has been examined for a large range of laser intensities ($I\lambda_0^2 = 10^{15} - 10^{20}$W cm$^{-2}\mu m^2$) in order to study the transition from the non-relativistic to the relativistic regime. The simulations in which the wave is resonantly excited are compared to cases in which the resonant conditions are not provided and the different coupling of the laser with the target is analyzed. We have considered the following aspects of the laser-plasma interaction, for different laser and target parameters: i) the laser absorption and the field intensity at the surface ii) the generation of a quasi-static magnetic field iii) the electron heating and iv) the ion acceleration.

We have found that in the cases where the surface wave is excited the electric field component normal to the target near the surface is amplified compared to the laser field. The amplification factor ranges from $\eta = 7.2$ to $\eta = 3.2$, depending on the laser intensity and its variation can be associated with the absorption process, whose efficiency varies with laser intensity. At low intensities a density gradient is found at the target surface which has a scale larger length than the one found in the high intensity regime so that the absorption mechanisms associated with the density gradient scale lenght are more important. By contrast, when the laser pulse has higher intensities ($I\lambda_0^2 > 10^{18}$W cm$^{-2}\mu m^2$), the laser pressure steepens the density gradient and the main absorption mechanism becomes vacuum heating which is associated with particles oscillating in the field perpendicular to the target, having an excursion large enough to escape the field and enter the bulk plasma. The latter mechanism is enhanced by the SPW excitation because of its greater field intensity and more localized distribution. In fact the laser absorption is enhanced in the presence of a surface wave, for example it rises from 27% when the SPW is not excited up to 73% at $I\lambda_0^2 = 10^{19}$W cm$^{-2}\mu m^2$. At the same time the wave is damped by electrons which are absorbing its energy so that its maximum amplitude may be reduced and this explains the variation of the amplification factor with the laser intensity. The dependence of the laser absorption

and field amplification on different target parameters has also been studied. We have considered different plasma densities (from 25 to 100 times the critical density) and found that the absorption is slightly reduced, even if it remains always higher than the case of a flat target, where the SPW was not excited. This is consistent with the weak dependence on electron density of the fraction of laser energy absorbed via vaccuum heating, discussed in reference [10]. Then we have studied the dependence of absorption and field amplification on the target geometry, considering a pulse impinging on a modulated target at different angle of incidences, which did not match the resonant condition. It has been observed that there is an important effect associated with the angle between the laser field and the normal to the modulation curve which may induce large absorption even for non-resonant incidence. Reducing the modulation depth to values smaller than the wave length reduces this effect and we notice a great difference in the absorption when the SPW is excited compared to the non-resonant incidence, where laser absorption approaches the value obtained for a flat target. However the modulation depth cannot be reduced too much as the coupling may be affected for values smaller than the gradient scale length at the target surface. Finally, we have examined the dependence of absorption and field amplification on the target thickness, considering a semi-infinite target and two different laminar targets: we find that the absorption increases for reduced target thickness, while the amplitude of the SPW field decreases. This can be attributed to the electrons which are recirculating inside the target and interact several times with the wave field, absorbing more energy. For thinner targets the number of cycles that electrons can perform before the driving field is extinguished is greater and a larger number of electrons can perform at least one bounce.

One of the aspects of laser-overdense plasma interaction that we have examined is the generation of a quasi-static magnetic field. We have studied the quasi-static magnetic field analytically, with a non-relativistic hydrodynamic model, which is valid in the low intensity range, in order to investigate the role of the surface wave in the magnetic field generation. This model shows that the surface wave gives rise to a second order magnetic field proportional to the square of the SPW field and confined near the interface, whose strength has a dependence on the electron temperature and density.

At the same time we have analyzed the characteristics of the magnetic field arising during laser-plasma interaction which is observed in PIC simulations for a wide laser intensity range, when the SPW is resonantly excited and for the case of a flat target. Comparing the model to the simulations performed for low intensity laser pulse, we find that the predicted field has the right order of magnitude (of the order of a MegaGauss) but it is systematically smaller than the values found in the simulations. We interpret this as related to kinetic effects and plasma expansion which are found to play an important role and are not taken into account by the model. Nevertheless we notice that *in all cases the intensity of the magnetic field is increased by the SPW excitation compared to the flat target case, even at relativistic intensities*. The values found in PIC simulations for laser intensity $I\lambda^2 = 10^{19}$W cm$^{-2}\mu m^2$ are of the same order, $\sim$ 90MG, of those found in experiments [64] when the surface wave is not excited, while they increase of more than a factor 2 when the SPW is present. Comparing the field structure of the

flat target and resonant cases suggests that the enhanced field strength, which exceeds 500MG at $I\lambda^2 = 7 \times 10^{19}$W cm$^{-2}\mu m^2$, has caused partial confinement of particles at the target surface when the SPW is present.

The electron heating corresponding to different target and laser parameters has been studied analyzing their energy and angular distribution. We observed that the *electron energy* dependence on SPW excitation is different, depending on the laser intensity regime considered. In the low intensity regime, the geometry effects are dominant, due to absorption mechanisms associated with the density gradient scale length, as mentioned above. In this case, if we consider different laser angle of incidences (resonant and non-resonant) on the same target, we find that electron energy is not increased when the SPW is excited. By contrast, in the high intensity regime, where the density gradient is sharper, the target geometry dependence is reduced and we observe that when the SPW is excited the cut-off energy of the hot electrons is larger than in the cases where the pulse angle of incidence does not match the resonance conditions. However the effects of the SPW are more pronounced when the modulation depth is small, which reduces the importance of the target geometry. In this case we observe a larger difference between the resonant and non-resonant incidence both in the hot electron temperature and the cut-off energy.

The *angular distribution* of accelerated electrons, by contrast, changes when the SPW is excited, both in the low and high intensity regimes: for non-resonant incidence the electrons are accelerated perpendicularly to the target surface, so that their angular distribution depends only on the target shape, while for resonant incidence they also acquire a large velocity component in the direction of propagation of the SPW.

Moreover, observing the electron currents, there is a characteristic which is found, in both laser intensity regimes, only when the SPW is excited: bunches of hot electrons are ejected with a periodicity of one laser cycle, whose position on the surface is related to the SPW field distribution. Their spatial location and periodicity suggest that the particles are entering the field of the surface wave at the most favourable phase for electron acceleration, i.e. the zeros of the SPW field, so that they experience the rising part of the field amplitude and reach the maximum momentum at the peak of the field.

In the case of laminar targets we have also observed that *electrons recirculate inside the target*, being reflected several times at the rear and irradiated surfaces. This mechanism further enhances the effects of the SPW as, for sufficiently thin targets, the electrons may interact more than once with the accelerating field.

Then we have studied the ion acceleration and its dependence on SPW excitation. In the simulations, we have identified two different mechanisms: one, the Target Normal Sheath Acceleration (TNSA), accelerates the ions towards the vacuum, the other one, the shock acceleration, pushes them from the surface into the plasma. The TNSA mechanism causes acceleration normal to the target surface, driven by the space charge field associated with an electron plasma sheath. The latter is set by the hot electrons accelerated by the laser pulse or the SPW field at the front surface. Hot electrons also propagate through the target so that, for a laminar target, the TNSA is found

both at the front and at the rear of the target. Shock acceleration is observed for laser intensities greater than $I\lambda_0^2 = 10^{18}\text{W cm}^{-2}\mu m^2$ and the analysis of the velocity and peak density of the shock suggests that it does not depend on the SPW excitation and can be associated with the cold electron population. Contrastingly, an ion emission consistent with TNSA is found in both the low ($I\lambda_0^2 < 10^{18}\text{W cm}^{-2}\mu m^2$) and high intensity regime and we observe that *when the SPW is excited the energy of the ions increases by a factor of* 4 *for the ions emitted at the irradiated side and by a factor* 2 *for the ions emitted at the rear.*

As for electron emission, we have examined the *angular distribution* of the ions accelerated for different laser angle of incidences and target geometries. We observed that for non-resonant laser incidence the ion angular distribution *at the irradiated surface* can be traced back to plasma expansion, corresponding to emission in the direction perpendicular to the target surface. A similar expansion is also found for the resonant incidence but in this case we also observe *filaments of ions having very high energies, which develop at the same points where we had observed the electron bunches which exit and re-enter the plasma, when the SPW is present.* This suggests that *the acceleration of the ions in the filaments is driven by the hot electrons oscillating in the surface wave field, via the TNSA mechanism.*

For laminar targets we have also examined the angular distribution of the ions accelerated at the rear side of the target, which is not irradiated. In this case, the ion emission is always perpendicular to the surface, which is flat at the rear side. *Nevertheless SPW excitation has an effect also on these ions as the energy of the hot electrons which drive the ions acceleration via TNSA is increased. For example, in the case of a laminar target of thickness* $h = 3.5\lambda_0$*, at* $I\lambda_0^2 = 10^{19}\,W\,cm^{-2}\mu m^2$*, the maximum ion energy was* $14MeV$*.*

Finally, we have examined the effects of the finite transverse size of the laser pulse envelope, introducing a laser pulse with a Gaussian profile. *The processes of SPW excitation and particle acceleration, when the laser pulse has a Gaussian profile, show a qualitative agreement with the previous simulations where the laser intensity was uniform on the target surface.* The maximum amplitude of the surface wave was the same as for the pulse having a uniform transverse profile and corresponds to the laser focal spot area. Comparing with the previous simulations, where a laminar target was used, we observe that the electron recirculation is less efficient for the case of a Gaussian pulse. For example the absorption decreases from 85% to 74% for a laminar target of the same thickness, at $I\lambda_0^2 = 10^{19}\text{W cm}^{-2}\mu m^2$. However this value of absorption is still much higher than the values reported in literature ($\sim 40\%$) for plane targets, where no SPW was excited [22, 31, 33].

Thus, the finite transversal size of the laser pulse is not expected to affect the enhancement of laser absorption and particle acceleration due to the surface wave field.

In conclusion we have demonstrated the possibility to excite a surface plasma wave on a structured target so as to match the resonance conditions for a large range of laser intensity. We have defined the optimal conditions for efficient coupling which increase

laser absorption. In such conditions the surface wave is found to enhance the production of hot electrons which, in turn, increases the energy of the ions accelerated at both the irradiated and unirradiated target surfaces.

These results have motivated an experimental campaign (see appendix .4), which started at the CEA (Saclay, France) in June 2012. The objective of the experiment is the measurement of laser absorption, electron temperature and ion energy when a laser pulse interacts with a grating when the conditions for SPW excitation are fulfilled. The preliminary results, that will not be included in this work, appear to be in agreement with our study.

Thus, surface plasma wave excitation via intense laser-grating interaction is a promising tool to increase the energy of the accelerated particles. This is of particular interest in applications such as ion acceleration for adron-therapy [81, 82, 80, 83] or the production of high energy electrons required in inertial confinement fusion, where the fast ignitor scheme is used [84].

PIC simulations with a Gaussian laser pulse profile will be further developed in order to better reproduce the experimental conditions, particularly for the case of very thin laminar targets ($\sim \lambda_0$). Future work will also include the investigation of new target geometries, such as the study of the possibility to excite a SPW on the wall of conical target, enhancing the electron focusing described in ref.[85]. Also the analysis of different types of plasmas, having higher ion mass and charge (Z) will be considered, in order to determine the role of these parameters.

Appendices

.1 Particle In Cell codes

Particle-in-cell codes (PIC) are commonly used in order to study numerically the dynamics of particles involved in laser-plasma interaction. In the particle in cell scheme the individual (macro-) particles in a Lagrangian frame are tracked in continuous phase space, whereas moments of the distribution such as densities and currents are computed simultaneously on Eulerian (stationary) mesh points.

We will give here a general description of this class of codes with references to the code that we have used to perform the simulations in this work.

.1.1 The principle of PIC technique

We will see in the following how the relevant plasma equations are transformed in a discrete set to be solved numerically.

In the simulations of plasma dynamics, the aim is to solve the Boltzmann equation for the distribution function $f_\alpha(\mathbf{x}, \mathbf{p}_\alpha, t)$ of each specie considered, $\alpha = e, i$ (electrons and ions)

$$\left[\partial_t + \mathbf{v}_\alpha \partial_{\mathbf{x}} - q_\alpha \left(\mathbf{E} + \frac{\mathbf{v}_\alpha}{c} \times \mathbf{B}\right) \partial_{\mathbf{p}_\alpha}\right] f_\alpha = (\partial_t f_\alpha)_{(coll)} \tag{1}$$

where the particle velocity is $\mathbf{v}_\alpha = \frac{\mathbf{p}_\alpha}{m_\alpha}\left(1 + \frac{\mathbf{p}_\alpha^2}{m_\alpha^2 c^2}\right)^{-\frac{1}{2}}$, coupled with Maxwell's equations for the electromagnetic fields. The collisional term $(\partial_t f_\alpha)_{(coll)}$ will take into account all the effects as Coulomb collisions or ionization processes that cannot be included in the Hamiltonian function and, when it can be neglected, equation (1) reduces to the relation known as Vlasov equation. In our work, ionization is not taken into account and collisions do not play an important role, due to the high plasma temperature; nevertheless the code includes the possibility to compute coulomb collisions with a method similar to the one described by Nambu in [89].

The Boltzmann equation is coupled with Maxwell's equations via the charge density ρ and the current $\mathbf{j}$, which are derived from the distribution function as follows

$$\begin{aligned} \rho &= \sum_\alpha q_\alpha \int d\mathbf{v}_\alpha f_\alpha(\mathbf{x}, \mathbf{p}_\alpha, t), \\ \mathbf{j} &= \sum_\alpha q_\alpha \int \mathbf{v}_\alpha d\mathbf{v}_\alpha f_\alpha(\mathbf{x}, \mathbf{p}_\alpha, t). \end{aligned} \tag{2}$$

where q_α is the charge of the specie α. This system of equations can be solved numerically as a boundary value problem.

The *Particle-In-Cell* (PIC) method for the simulation of the collective dynamics of the plasma consists in the numerical solution of the Boltzman equation with a Lagrangian approach. The phase space is divided into small domains which moves in time along the trajectories of the particles, which are determined by the self-consistent fields. The latter are calculated in space at the points of a mesh. Thus we have a discrete description of the plasma as a collection of macro-particles, having a defined extension and associated with an individual equation of motion.

This is equivalent to assuming a discrete representation of the distribution function $f(q,p,t)$, where q and p are generic vectors in the phase space (for example the position and momentum):

$$f(q,p,t) = f_0 \sum_{n=0}^{N_p-1} g\left[q - q_n(t)\right] \delta\left[p - p_n(t)\right] \tag{3}$$

where g is a generic analytical function that will be discussed later, δ is the Dirac function and f_0 is a normalization constant.

We will now derive the equation of motion for the discretized distribution function. First we rewrite the Vlasov (for simplicity we neglect the treatment of collisions) equation in the phase space

$$\left(\partial_t + \dot{q}\partial_q + \dot{p}\partial_p\right) f(q,p,t) = 0 \tag{4}$$

$$\dot{q} = \frac{p}{m} \quad , \quad \dot{p} = F(q,p,t) \tag{5}$$

then we insert (3) in (4) and obtain the relation

$$\begin{aligned} &\sum_{n=0}^{N_p-1} -\dot{q_n} g'\left[q - q_n(t)\right] \delta\left[p - p_n(t)\right] - \dot{p_n} g\left[q - q_n(t)\right] \delta'\left[p - p_n(t)\right] \\ &+ \frac{p_n}{m} g'\left[q - q_n(t)\right] \delta\left[p - p_n(t)\right] + F(q, p_n(t), t) g\left[q - q_n(t)\right] \delta'\left[p - p_n(t)\right] = 0 \end{aligned} \tag{6}$$

Then integrating the latter relation for dp we get

$$\sum_{n=0}^{N_p-1} \left(-\dot{q_n}(t) + \frac{p_n(t)}{m}\right) g'\left[q - q_n(t)\right] = 0 \tag{7}$$

which, for any form of the function g', gives the relation

$$\dot{q_n}(t) = \frac{p_n(t)}{m} \tag{8}$$

In the calculation we have used the properties of the Dirac functions δ and δ'

$$\int \delta(q - \bar{q}) dq = 1 \tag{9}$$

$$\int \delta'(q - \bar{q}) dq = 0 \tag{10}$$

If we assume that the properties above apply also for the function g, then integrating (6) for dq we get

$$\sum_{n=0}^{N_p-1} \left[-\dot{p_n}(t) + \bar{F_n}\right] \delta'\left[p - p_n(t)\right], \tag{11}$$

$$\bar{F_n}(q_n(t), p_n(t), t) = \int g\left[q - q_n(t)\right] F(q, p_n, t) dq \tag{12}$$

and the relation for the momentum variables becomes

$$\dot{p_n}(t) = \bar{F}_n(q_n(t), p_n(t), t). \tag{13}$$

Thus the problem of computing the distribution function f is reduced to $2N_p$ equations, (8) and (13), that describe the motion of N_p computational particles. To each particle is associated a value $p_n(t)$ of the momentum and a spatial extension with a shape given by the function $g\,[q - q_n(t)]$, so that the macro-particle is associated with the average position q_n. The term $\bar{F}_n$ is the force averaged in the space $F(q, p_n, t)$, which in the present case will be the Lorentz force:

$$\mathbf{F} = q_\alpha \left(\mathbf{E} + \frac{\mathbf{v}_\alpha}{c} \times \mathbf{B} \right) \tag{14}$$

where q_α and $\mathbf{v}_\alpha$ are the charge and velocity of the particle $\alpha = e, i$ (electrons or ions), as in equation (1).

Thus the equations for charge and current density (2) can be rewritten in the discrete form:

$$\rho(x,t) = f_0 \sum_{\alpha,n} q_\alpha g(x - x_n(t)), \tag{15}$$

$$\mathbf{j}(x,t) = f_0 \sum_{\alpha,n} \mathbf{v}_n q_\alpha g(x - x_n(t))$$

where we used x to indicate the spatial coordinate (instead of q), in order to distinguish it from the charge q_α. Once the sources (charge and current) are known, they can be used to find a numerical solution of Maxwell equations and find the electro-magnetic fields. In order to calculate the solutions, fields and currents are defined at the points of a spatial grid, which divides the simulation box into cells, and are calculated from the particles distribution. At each time-step Δt the Lorentz force corresponding to the position of the macro-particles is calculated by performing a spatial interpolation over the grid points involved and the momenta and the positions of the particles are updated. Then the currents and the density are calculated for the new particles positions and used in the Maxwell's equations to obtain the new fields and so on.

.1.2 Technical aspects

We have derived the principles of the PIC computational technique from the basic equations used for the kinetic description of a plasma. We shall now consider some more technical aspects of these codes: the particle mover, the field solver, the accuracy and stability conditions.

The schemes used for the *particle mover* can be classified in two categories, implicit and explicit solvers. While implicit solvers calculate the particle velocity from the already updated fields, explicit solvers use only the old force from the previous time step. The latter are simpler and faster, but require a smaller time step. In the code used for our simulations we used the *leapfrog method* [90], which has the following form

in plasma applications (for the non-relativistic case)

$$\frac{x_{n+1} - x_n}{\Delta t} = v_{n+1/2}$$
$$\frac{v_{n+1/2} - v_{n-1/2}}{\Delta t} = \frac{q}{m}\left(E_n + \frac{v_{n+1/2} - v_{n-1/2}}{2} \times B_n\right) \tag{16}$$

where the subscript n refers to the quantities from the previous time step, $j+1$ to updated quantities from the next time step (i.e. $t_{n+1} = t_n + \Delta t$), and velocities are calculated in-between the usual time steps. For the relativistic generalization of equation (16) we use $\mathbf{u} = \gamma \mathbf{v}$ rather than $\mathbf{v}$ so that the relativistic form of the *leapfrog method* is

$$\frac{x_{n+1} - x_n}{\Delta t} = \frac{u_{n+1/2}}{\gamma_{n+1/2}}$$
$$\frac{u_{n+1/2} - u_{n-1/2}}{\Delta t} = \frac{q}{m}\left(E_n + \frac{u_{n+1/2} - u_{n-1/2}}{2\gamma_n} \times B_n\right) \tag{17}$$

The most commonly used methods for solving Maxwell's equations (or more generally, partial differential equations (PDE)) belong to one of the following three categories: i) finite difference methods (FDM) ii) finite element methods (FEM) iii) spectral methods.
With the FDM, the continuous domain is replaced with a discrete grid of points, on which the electric and magnetic fields are calculated. Derivatives are then approximated with differences between neighboring grid-point values and thus PDEs are transformed into algebraic equations.
Using FEM, the continuous domain is divided into a discrete mesh of elements. The PDEs are treated as an eigenvalue problem and initially a trial solution is calculated using basis functions that are localized in each element. The final solution is then obtained by optimization until the required accuracy is reached.
Also spectral methods, such as the fast Fourier transform (FFT), transform the PDEs into an eigenvalue problem, but this time the basis functions are high order and defined globally over the whole domain. The domain itself is not discretized in this case, it remains continuous. Again, a trial solution is found by inserting the basis functions into the eigenvalue equation and then optimized to determine the best values of the initial trial parameters.
The method used in the code EMI2D to solve the partial differential equation is the first one, the finite difference method with the relativistic formulation in equation (17).

In the previous section, where we introduced the principles of PIC simulations, we have seen that the charge and current density are assigned to simulation particles, the so called *macro-particles*. The latter can be situated at any point of the continuous domain, as their position is defined by x_n but their contribution to a mesh point, where currents and fields are calculated, depends on its shape $g(x - x_n)$. The shape of the macro-particle, or weighting, has to satisfy the following conditions: space isotropy, charge conservation, and increasing accuracy (convergence) for higher-order interpolation terms. Moreover the order of the field interpolation has to be the same as the one of charge and current in order avoid self-forces.

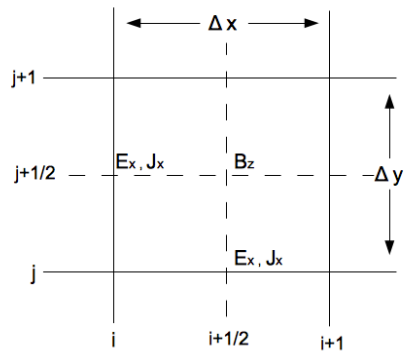

Figure 10: Spatial lay-out of the field grid for the 2D, TM (transverse magnetic) fields and currents. i, j are the indices associated with a grid point, for the x and y coordinates respectively.

The code used in this work is 2D and all spatial variations are in the (x, y) plane. The relative spatial variation is chosen so as to provide centered spatial differencing as shown in fig.10.

In this scheme, the (2D, TM) finite differenced Maxwell's equations becomes:

$$\frac{B^{n+1/2}_{z,i+1/2,j+1/2} - B^{n-1/2}_{z,i+1/2,j+1/2}}{\Delta t} = -c\frac{E^n_{y,i+1,j+1/2} - E^n_{y,i,j+1/2}}{\Delta x} + c\,\frac{E^n_{x,i+1/2,j+1} - E^n_{x,i+1/2,j}}{\Delta y} \tag{18}$$

$$\frac{E^{n+1}_{x,i+1/2,j} - E^n_{x,i+1/2,j}}{\Delta t} = c\frac{B^{n+1/2}_{z,i+1/2,j+1/2} - B^{n+1/2}_{z,i+1/2,j-1/2}}{\Delta y} - J^{n+1/2}_{x,i+1/2,j} \tag{19}$$

$$\frac{E^{n+1}_{y,i,j+1/2} - E^n_{y,i,j+1/2}}{\Delta t} = -c\frac{B^{n+1/2}_{z,i-1/2,j+1/2} - B^{n+1/2}_{z,i+1/2,j+1/2}}{\Delta x} - J^{n+1/2}_{x,i,j+1/2} \tag{20}$$

where n is the index of the of the (old) time step in the *leapfrog* scheme. The accuracy of this method is second order in space and time. The code alternates, first advancing the electric field (time-step n) and then the magnetic field $(n + 1/2)$. At each step the new value of a field over-writes the old value in memory such that it is not necessary to keep values for any field more then once. We observe that the magnetic field is given only for the half integer times, i.e. $n \pm 1/2$ while in the leapfrog equation of momentum (16) the time has to be integer for both magnetic and electric fields. In order to get the B^n value, the integration of $\mathbf{B}$ is decomposed into two steps, advancing the magnetic field only half way:

$$B^n_{z,i+1/2,j+1/2} = B^{n-1/2}_{z,i+1/2,j+1/2} - c\frac{\Delta t}{2}\frac{E^n_{y,i+1,j+1/2} - E^n_{y,i,j+1/2}}{\Delta x} + c\frac{\Delta t}{2}\frac{E^n_{x,i+1/2,j+1} - E^n_{x,i+1/2,j}}{\Delta y} \tag{21}$$

A similar method is used for currents, where the particle position at half integer times is mediated between the integer time positions. Notice that one (macro-)particle contributes to the 4 nearest grid points and the 'weight' $W_{i,j}$ of the particles at each point i, j, is given by:

$$W_{i,j} = \left(1 - \frac{x - X_i}{\Delta x}\right)\left(1 - \frac{y - Y_j}{\Delta y}\right) \tag{22}$$

$$W_{i+1,j} = \left(\frac{x - X_i}{\Delta x}\right)\left(1 - \frac{y - Y_j}{\Delta y}\right) \tag{23}$$

$$W_{i,j+1} = \left(1 - \frac{x - X_i}{\Delta x}\right)\left(\frac{y - Y_j}{\Delta y}\right) \tag{24}$$

$$W_{i+1,j+1} = \left(\frac{x - X_i}{\Delta x}\right)\left(\frac{y - Y_j}{\Delta y}\right) \tag{25}$$

where $X_i = i * \Delta x$, $Y_i = j * \Delta y$ and (x, y) is the position of the particle in the 2D space.

The *Courant condition* gives the minimum requirement for the stability of the code, relating the cell size and the time step: $c\Delta t \leq \Delta x$. The requirements on the cell size instead depend on the physical process that has to be investigated. Following [90] a rough rule to avoid the non-physical instabilities caused by the grid finite size (aliasing instability) is $\Delta x \leq \pi\lambda_D$ where λ_D is the Debye length. *This means that the cell size will depend on the density and temperature of the plasma, which are evolving and the instability may be negligible in some cases even for larger values of* Δx.

From this requirements, we may have an idea of the typical size of a simulation of the type (2D) presented in this work. For example for the cases having density $n_e = 25n_c$, with $T_e = 1$keV, we have $\lambda_D = 0.083k_0^{-1}$, therefore the grid size would be about $\Delta x = 0.025k_0^{-1}$. This means that a plasma target, such as the one typically used in our simulations, of size $6\lambda_0 \times 8\lambda_0$, corresponds to $1507 \times 2010 \sim 3 \times 10^6$ grid points, at which the fields (3 variables) and the currents (2 variables) are defined. Besides if we consider that for each cell we have used 100 particles, each having 2 variables of position and 3 variables of momentum, we may understand the computational requirement of such simulations. For this reason *parallelization* of the code is required: the simulation box is divided into slices along the y direction, each of which is treated by a different processor (communicating with the next slice at the boundary). In the simulation where the box size was $6\lambda_0$ along the y direction we used 32 processors.

.2 Modifications, diagnostics and tests

The original code EMI2D [88], developed by A. Héron and J.C. Adam, was modified in order to study the particular case of SPW excitation by laser-grating interaction.

target geometry The modifications included the possibility to choice a modulated target interface, selecting the periodicy and the amplitude of the modulation. Also the possibility to choose a wedge profile, was introduced, which allows the 2D study of a conical target having modulated walls. The interest in the conical target is motivated

by the possibility to focus strong electron currents at the cone tip, as discussed in ref.[85]. However this latter geometry has not been examined in this work and will be the subject of a future study.

diagnostics The study of particle acceleration in presence of a surface wave required the extension of the code diagnostics. Especially the ion (p_x, p_y) phase space was added to the simulation outputs, in order to determine the emission angles. Moreover the possibility to generate multiple phase spaces was included, both for ions and electrons, corresponding to different zones of the simulation box. This has permitted the separate analysis of the angular direction of ions and electrons accelerated at the front or rear surface of the target and inside the plasma. We also included the possibility to write separate electron and ion current outputs, which provide a complementary diagnostic to the particle phase space.

tests The code has been validated for the peculiar grid size and particle number used in the simulation. The grid size used in the simulation presented in this work, $\Delta x = 5\lambda_D$ and $\Delta y = 4\lambda_D$, has been tested in order to exclude self heating. We compared two simulations, having laser intensity $I\lambda_0^2 = 10^{15}$W cm$^{-2}\mu m^2$, one with the spatial grid mentioned above and the other having $\Delta x = \Delta y = 3\lambda_D$, i.e. respecting the theoretical limit defined in appendix .1.2 to avoid self-heating. We observed no substantial differences in the electron velocity and field intensity, which proves that, even for very low laser intensities, the time scales of the heating processes under investigation allow the use of a spatial grid slightly larger than $3\lambda_D$. We also tested the number of particle per cell $N = 100$ used in the simulations. A simulation where $N = 100$ was compared to a simulation where $N = 400$, for low laser intensity ($I\lambda_0^2 = 10^{16}$W cm$^{-2}\mu m^2$) and high electron density ($n_e = 100n_c$), corresponding to a range of parameters for which the density gradient is expected to play an important role. We found that the differences in the two simulations were limited to a few percent: the absorption increased of 2% for $N = 400$, while the electric field had essentially the same value. These results validate the set of parameters used to describe the plasma dynamics in the regime investigated in this work.

.3 Angle-energy relation for laser-accelerated electrons[1]

In the process of vacuum heating, where electrons at the target surface are pulled into the vacuum by the laser field, many effects may contribute to the trajectories of the particles, such as laser pressure and self-generated fields. For this reason it is difficult to determine the final direction of electrons which re-enter the target. Nevertheless some predictions may be done considering the following simple scheme.

In this model it is assumed that electrons are accelerated at a laser-plasma interface in planar geometry, and that acceleration occurs via the absorption by each electron of a well-defined number N of "laser" photons of frequency ω. The laser pulse (actually

[1] A. Macchi, private communication.

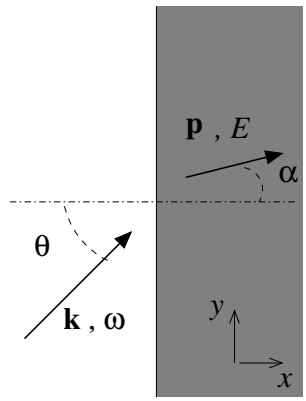

a plane wave) impinges at the angle of incidence θ. The conservation of energy and of the momentum component in the transverse (y) direction yield for the electron energy E and transverse momentum p_y

$$E = N\hbar\omega, \tag{26}$$

$$p_y = (N\hbar\omega/c)\sin\theta = (E/c)\sin\theta \tag{27}$$

For the electron we have

$$E = \sqrt{\mathbf{p}^2c^2 + m_e^2c^4} - m_ec^2 \tag{28}$$

Let α be the emission angle, i.e. $\tan\alpha = p_y/p_x$. Then

$$\sin\alpha = \frac{E\sin\theta}{[(E + m_ec^2)^2 - m_e^2c^4]^{1/2}} \tag{29}$$

The two limiting cases to be considered are:

$$\sin\alpha \simeq \left(\frac{E}{2m_ec^2}\right)^{1/2}\sin\theta, \qquad E \ll m_ec^2 \tag{30}$$

$$\sin\alpha \simeq \sin\theta, \qquad E \gg m_ec^2 \tag{31}$$

Thus, the non-relativistic and strongly relativistic electrons would be accelerated along the target normal and the incidence direction, respectively.

We note that this result is simply a consequence of the assumptions (26) and (27). There is not a rigorous proof that such relations should hold. Near the surface, electrons oscillate in the overlapping fields of the laser pulse and of the plasma oscillations; we may speculate that if the latter are excited due to linear coupling with the laser field, they have the same frequency and transverse wavevector, so that the four-momentum of each 'quantum' which may be absorbed by the electrons is the same. This picture seems to be consistent with the qualitative description of electron acceleration due to the vacuum heating mechanism [18, 19].

.4 Laserlab project (June 2012)

LASERLAB EUROPE: Application for experimental time

Description of the project (to be provided in pdf format)
Please note that for CLF, LULI and PALS specific forms should be used for this part!

PART 2: Detailed scientific description of the project

List the main objectives of the proposed research *(half a page maximum)*:

The objective of the experiment is to investigate enhancement of absorption and acceleration of electrons and ions in the interaction of high-intensity, ultrashort laser pulses with structured targets. These latter include both grating targets, such that resonant excitation of surface waves is allowed, and other nanostructured targets for which a strong increase of the absorption coefficient has been found in numerical simulations, e.g. targets whose surface is covered with nanometric demi-spheres. Early structure damage by the laser prepulse will be prevented by the use of a double plasma mirror device to obtain extremely "clean", high-contrast pulse and allowing to extend this class of interactions to higher intensities. Measurements will be taken as a function of the incidence angle and polarization of the laser pulse to seek for highest absorption conditions and to discriminate resonant vs. non-resonant absorption mechanisms. The energy spectrum of electrons as well as their spatial emission will be investigated and compared to the result of multi-dimensional particle-in-cell simulations to test the prediction of preferential emission at certain angles and to clarify how the highest energy electrons are accelerated. The spectra of protons emitted from the rear side of the targets will be also measured to evaluate the enhancement of ion acceleration via the target normal sheath acceleration mechanism.

Give a brief description of the scientific background and rationale of your project *(half a page maximum)*:

The interaction of femtosecond, multi-terawatt laser pulses with solid targets is the key to the development of bright laser-driven sources of radiation (electrons, ions, X- and gamma-rays) for possible applications in spectroscopy, nuclear physics and medicine. It also provides a test bed for laser-interaction physics of relevance for inertial confinement fusion. Key to most applications is to obtain the highest efficiency and/or the highest energy per particle in the radiation produced, while using table-top laser systems with modest values of the pulse energy. To this aim, a possible strategy is to use a target with a structured surface that may either allow a more efficient "geometrical" coupling with the laser pulse or lead to the enhancement of fields at the surface via the excitation of both propagating and localized electromagnetic modes. A well known example is the resonant excitation of surface plasma waves (SPW) which is possible for a grating target, i.e. with a periodical surface modulation, for a given angle of incidence of the laser pulse so that phase matching conditions are fulfilled. Several other suggestive examples of mode excitation and local field enhancement may be provided by the study of plasmonics, making it attractive to extend such investigations in the high-intensity regime. However, the development of what may be called "high field plasmonics" has been limited so far by the well known problem of "prepulses" which are typical of multi-terawatt laser system and often lead to early target damage and plasma formation before the actual interaction with the "main" ultrashort, high-intensity pulse occurs; this issue has so far limited the study of structured targets to moderate intensity regimes. Recently, the development of "pulse cleaning" techniques such as the "plasma mirror" has allowed investigations with ultrahigh pulse contrast so that the short pulse interaction really occurs with the solid density target and surface structuring may be preserved. It then becomes of interest both to study SPW-excitation at the highest possible intensity and to test suitable target structuring for enhancement of absorption and more efficient production of, e.g. , energetic electrons and ions. In the present project both grating targets and other types of nanostructures will be investigated following indications from previous theoretical and simulation work. As an example of the latter we include below a sketch of the direction of fast electron jets observed in two-dimensional simulations of surface wave excitation in a grating target (of density 3.9 X 10^{22} cm-3) by a 0.8 μm, 10^{18} W/cm^2 *P*-polarized laser pulse at 31° incidence; in these simulations, a fractional absorption of 72% was found with respect to the 18% value in the absence of SPW excitation. The use of very high-contrast and ultrashort pulses and, more in general, a context of well-controlled and characterized interaction conditions will enable to obtain accurate data allowing to clarify in detail how laser energy absorption and transfer to electron and ions occur and to assess the potential of target nanostructuring for applications' development.

1

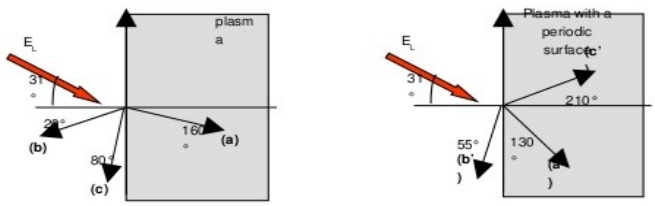

Figure showing a sketch of electron jets direction observed in PIC simulations for a plane target surface (left) and for a periodic surface in conditions of resonant surface wave excitation (right).

Present the proposed experimental method working plan *(half a page maximum)*:

The interaction will be studied as a function of the incidence angle and of the polarisation, since both parameters are critical for the laser coupling with a structured surface. For instance, resonant SPW excitation occurs only for *P*-polarized light and for a given relation (weakly dependent on the electron density) between the grating period *a*, the wavelength λ and the incidence angle. The resonant coupling condition does not depend on the surface modulation *d* will be typically a fraction of λ. However, if targets with different values of *d* will be available, it will be of interest to evaluate any dependence on *d* which is commonly neglected in the simplest "zero-order" picture of SPW excitation which assumes the SPW dispersion relation to be independent on *d*. This would be also a test that, thanks to the ultra-high contrast, the laser pulse effectively interacts with the structured surface. It will be important indeed to infer from first experimental data that the pulse contrast is high enough to prevent target damage and early plasma formation by laser prepulses, which is a necessary condition for the experiment. Although it would be of great interest to test absorption enhancement and related effects at the highest intensity possible, in the case of non-negligible prepulse effect the laser pulse will be defocused (or the pulse energy will be decreased) below the preplasma formation threshold. This would not prevent the possibility to demonstrate absorption enhancement in structured targets.

Structured targets may be prepared directly by team members (e.g. at CTU Prague). By uniform spreading of a solution of Formvar in 1,2-dichlorethane on the surface of water, ultrathin foils with very flat surface can be prepared The impact side of the target can be subsequently covered by monolayers of closely packed polystyrene microspheres of variable size (to be purchased from Microparticles GmbH, Germany); such monolayers can be prepared by their self-assembly at the interface of water/air. To prepare thin targets with periodical topography in the sub-micrometric range nanocasting of surface reliefs created by interference lithography and thermal imprinting may be used. Solutions of appropriate polymers may be spread onto lithographically structured surfaces by spin-coating and final thin replica foils can be peeled out and mounted on target holder. Alternatively, suitable grating targets may be purchased in laboratories to which CEA has connections, e.g. LabHC at University of Saint-Etienne.

To demonstrate the effect of surface structures on laser-target coupling, the absorption fraction should be evaluated accurately. Details of the measurement technique are described in the next section. In addition, ion and electron spectra should be measured possibly with angular resolution to search for preferential directions of emission as predicted by simulations. From the latter we also expect the effects on ion and electron spectra to be strong enough that the sensitivity and accuracy of routinely available diagnostics will be sufficient to give an experimental evidence.

Give a brief description of the experimental arrangement including main optics and diagnostics required *(half a page maximum)*:

The arrangement must allow the possibility to change the polarization and incidence angle of the laser pulse since the coupling with the structured targets will be strongly dependent on these parameters. As an example, for resonant SPW excitation in Si targets, for λ=0.8μm the expected resonance angle is 30° for a grating period *a*=1.6μm. It must also be possible to vary the size of the laser spot in order to reduce the prepulse intensity if necessary. For SPW excitation, varying the spot size would also allow modify the number of grating periods involved in the interaction, which could play a significant role in the SPW excitation.

For an accurate measurement of absorption an Integrating Ulbricht Sphere (IUS) may be used if available.

Since the use of the IUS may be constrained by the geometry of the interaction and prevent the simultaneous use of particle diagnostics, a more flexible and suitable estimate of absorption may be provided by optical imaging of the reflected light, which could be calibrated to provide quantitative information.

Electron spectrometers will be used to record the spectrum of electrons escaping from the target and, as possible, to detect preferential emission in certain direction as suggested by numerical simulations. Proton emission from the rear side of the target will be diagnosed by a Thomson parabola or by a Radio-Chromic Film (RCF) stack which should already provide fairly accurate information on the proton spectrum.

Additional diagnostics will be provided by X-ray spectroscopy, which will bring complementary information on the energy of fast electrons. It will be also of interest to evaluate any X-ray yield enhancement in structured targets. X-ray measurements will be mostly based on a X-ray, cooled CCD that may either be coupled with a diffraction crystal or provide low-resolution spectra in single-photon-per-pixel mode.

Please provide a sketch of the experimental set-up.

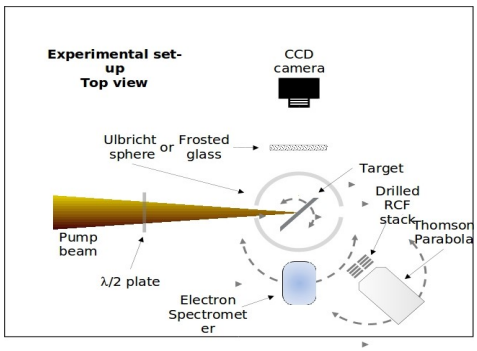

Indicate the proposed time schedule including expected duration of access time *(half a page maximum)*:

We estimate at least one week to be required for the set-up of the experiment. The time required for the measurements should be sufficient to collect a significant amount of data for both types of target ("grating" and "microsphere") with the necessary re-positioning of target and diagnostics. Thus we propose three weeks of laser time for the experiment in addition to the first week for the set-up.

Please estimate the difficulty of the experiment (high, medium, moderate).

Moderate

Host infrastructure

Indicate your preferred LASERLAB-EUROPE host infrastructure: **SLIC UHI 100 TW laser facility**

Explain briefly why your project will be best carried out at this specific host infrastructure:

The key condition for the success of the experiment will be the availability of extremely "clean", high-contrast laser pulses of ultrashort (few tens of fs) duration in order to prevent early target damage by prepulses and to preserve the surface nanostructuring during the interaction. The host group at SLIC UHI 100 TW laser facility has developed a double plasma mirror system whose efficiency has been demonstrated by experiments on ion acceleration in interactions with ultrathin targets. The host infrastructure therefore provides ideal conditions for the experiment and an extremely valuable expertise on diagnostics for the phenomena under investigation.

Please indicate the name of the local correspondent, if known: Dr **Tiberio Ceccotti**

If possible, list other LASERLAB-EUROPE facility(ies) where your experiment could alternatively be

carried out:

Additional information

Have you already submitted an Access Proposal to any of the participating facilities under this or previous EU Programs? **NO**

If yes, please indicate the name of the institution, submission date and reference number for each such proposal:

Is this a resubmission of a previous proposal (see guideline#1)? **NO**

If yes, please give the exact reference number and submission date. Please describe briefly the changes made in comparison to the rejected version.

Is this a continuation of an earlier project funded under the EU Access Program at the same facility (see guideline#2)? **NO**

If yes, please give the exact reference number and submission date. Please indicate also what has been achieved in the previous experiment and the reasons why the objectives have not been fully obtained.

Guidelines

1. Select "yes" if this application is a revised version of a proposal submitted to LASERLAB before and rejected by the selection panel.

Select "yes" if this project would be the continuation of a project with identical objectives already carried out at the same infrastructure.

PART 3: Technical information

When possible, please specify your requests regarding the laser characteristics (wavelengths, pulse energy, power, line width, pulse length, repetition rate, focusing optics, etc.), auxiliary equipment and diagnostics to be provided or any other specific requirements (including specific support such as target lab, scientific computing, etc.):

Apart from the key requirement of pulses with ultrahigh contrast up to 10^{12} (to be obtained using the double plasma mirror) the standard laser parameters (25 fs duration, up to 100 TW power) at the host infrastructure are fully adequate to search for absorption enhancement by target structuring, with a wide margin in the power range to demonstrate the effect at possibly the highest intensities investigated so far. A not too tight focusing optics (e.g. 300 mm focal length parabola) may be preferable for surface wave excitation in order to preserve a reasonable “close-to-plane wave” geometry with a laser spot extending over several grating periods. Most of diagnostics (Thomson parabolas for electrons and ions, RCF stack for protons, simple optical imaging system for reflected light) should either be of routine use at the host laboratory or, at least, may be borrowed by collaborating groups (e.g. Ulbricht sphere). The external users should provide either most of or all the structured targets as well as theoretical and simulation support.

List all samples and chemicals to be brought to the LASERLAB Facility:

Structured targets prepared by part of the collaborating team or borrowed in external laboratories as discussed in Part 2.

Information on any safety issues concerning the experiment. Please tick the appropriate boxes and give detailed information for each potential risk present during the experiment (except of laser risk).

- ☐ Chemical risk:
- ☐ Biological risk:
- ☐ Radiological risk:
- ☐ Other risk(s):

PART 4: Additional information about the applicant’s (and group’s) expertise

Expertise of the group in the domain of the application (including theoretical support):

The applicant, A.Macchi, has a long time-experience in the field of laser-matter interactions at high intensity and will coordinate the experiment. Researchers from the same group (CNR/INO research unit in Pisa, Italy)

including A.Giulietti, L.A.Gizzi and L.Labate will participate to the experimental campaign. Their expertise is based on established experience on laser-matter interaction experiments (e.g. on acceleration of electrons and ions and on X-Ray generation) performed in laboratories in Pisa or in facilities abroad.
The proposed experimental measurement have been elaborated on the basis of theoretical work both by a collaborating team including the applicant and researchers at French laboratories (C.Riconda, LULI, Ecòle Polytechnique; A.Bigongiari and M.Raynaud, CEA\DSM\IRAMIS\LSI; A.Héron, CPhT, Ecòle Polytechnique) and by researchers at CTU Prague (O.Klimo, J.Psikal, J.Limpouch). who studied absorption on microsphere-covered surfaces. These two groups have high-level theoretical experience on topics such as surface-wave enhanced interactions and laser-driven ion acceleration, respectively, and will provide theoretical support also via advanced PIC simulations and access to supercomputing facilities; group leaders will also work closely with the main applicant in the coordination of the experiment. A team also at CPU Prague (lead by J. Proska) working in nanoscience and lithography will contribute to target preparation and characterization.
Additional support to the experimental may come from experienced researchers affiliated to French laboratories such as LULI (J.Fuchs, B.Albertazzi) and CELIA, Bordeaux (G.Geoffroy).

Short CV of the applicant:

Andrea Macchi (Ph.D in Physics, Scuola Normale Superiore, Pisa, Italy, 1999) is a staff research scientist at CNR/INO (the National Institute of Optics of the National Research Council) and a Lecturer of Plasma Physics at the University of Pisa. His present interests focus on the theory and simulation of laser-plasma interactions and particularly on mechanisms of collective absorption and ion acceleration. He participated directly to experiments in the early stage of his career and later he has been frequently involved in the proposal, design and interpretation of experiments in collaboration with experimental groups. He has published about fifty papers on peer reviewed journals, achieving a present h-index of 16, and presented several invited talks in international conferences and academic or research institutions. Further details can be found at the web page www.andreamacchi.eu .

A list of 5 recent, relevant publications of the participating scientists in the field of the project:

K. Quinn, P. A. Wilson, C. A. Cecchetti, B. Ramakrishna, L. Romagnani, G. Sarri, L. Lancia, J. Fuchs, A. Pipahl, T. Toncian, O. Willi, R. J. Clarke, D. Neely, M. Notley, P. Gallegos, D. C. Carroll, M. N. Quinn, X. H. Yuan, P. McKenna, T. V. Liseykina, A. Macchi, M. Borghesi, "Laser-driven Ultrafast field propagation on solid surfaces", *Phys.Rev.Lett.* **102** (2009) 194801.

L. Romagnani, A. Bigongiari, S. Kar, S. V. Bulanov, C. A. Cecchetti, T. Zh. Esirkepov, M. Galimberti, R. Jung, T. V. Liseykina, A. Macchi, J. Osterholz, F. Pegoraro, O. Willi, M. Borghesi, "Observation of magnetized soliton remnants in the wake of intense laser pulse propagation through plasmas", *Phys.Rev.Lett.* **105** (2010) 175002.

F. Zamponi, A. Lübcke, T. Kämpfer, I. Uschmann, E. Förster, A. P. L. Robinson, A. Giulietti, P. Köster, L. Labate. T. Levato, and L.A. Gizzi, Directional Bremsstrahlung from a Ti Laser-Produced X-Ray Source at Relativistic Intensities in the 3–12 keV Range", *Phys.Rev.Lett*, **105** (2010) 085001

O. Klimo, J. Psikal, J. Limpouch, V.T. Tikhonchuk, "Monoenergetic ion beams from ultrathin foils irradiated by ultrahigh-contrast circularly polarized laser pulses", *Phys. Rev. Spec. Top.-Acc. Beams* **11** (2008) 031301.

M. Raynaud, J. Kupersztych, C. Riconda, J-C Adam and A. Héron, "Strongly enhanced laser absorption and electron acceleration via resonant excitation of surface plasma waves", *Phys. Plasmas* **14** (2007) 92702

Bibliography

[1] Mourou G. A., Tajima T. and Bulanov S. V., Rev. Mod. Phys. **78**, 309 (2006).

[2] C. Thaury, F. Qur, J.-P. Geindre, A. Levy, T. Ceccotti, P. Monot, M. Bougeard, F. Rau, P. dOliveira, P. Audebert, *et al.*, Nature Physics **3**, 424-429 (2007).

[3] *Handbook of Mathematical Functions* (Abramowitz, M. and I. A. Stegun,eds.) Nationa Bureau of Standards, *Applied Mathematics Series* **55**, 1964.

[4] T. M. Antonsen Jr, and P. Mora, Phys. Rev. Lett. **69**, 2204-2207 (1992).

[5] S. C. Wilks and W. L. Kruer, IEEE J. Quantum Electron. **33**, 1954 (1997).

[6] S. C. Wilks *et al.*, Phys. Plasmas **8**, 542 (2001).

[7] S.C. Wilks, W.L. Kruer, M. Tabak and A.B. Langdon, Phys. Rev. Lett. **69**, 1383, (1992).

[8] W. L. Kruer,*The Physics of Laser-Plasma Interaction*, Addison-Wesley, New York (1988).

[9] F. Chen, *Introduction to Plasma Physics and Controlled Fusion: Plasma physics*, Spriger, 1984.

[10] S. Kato *et al.*, Phys. Fluids **5**, 564 (1993)

[11] C. Kittel, *Introduction to Solid State Physics*, New York: Wiley (1996).

[12] H. Reather, *Surface Plasmons on Smooth and Rough Surfaces and on Gratings*, Springer-Verlag Berlin Heidelberg (1988).

[13] G. Diaz, N. Garcia and H. Reather, Surface Sci. **146**, 1 (1984).

[14] N.G. Denisov, Sov. Phys. **4**,544 (1957).

[15] D. Bauer, P. Mulser, and W.H. Steeb, Phys. Rev. Lett. **75** 4622 (1995).

[16] P. J. Catto and M. R. More, Phys. of Fluids **20**, 704 (1997).

[17] W. L. Kruer and K. Estabrook, Phys. of Fluids **28**, 430 (1985).

[18] F. Brunel, Phys. Rev. Lett. **59**, 52 (1987); ibid, Phys. of Fluids **31**, 2714 (1988).

[19] P. Gibbon and A. R. Bell, Phys. Rev. Lett. **68**, 1535 (1992).

[20] Hong-bo Cai, *et al.*, Phys. Plasmas **13**, 094504 (2006).

[21] Y. Sentoku *et al.*, Phys. Plasmas **10**, 2009 (2003).

[22] C. Ren *et al.*, Phys. Plasmas **13**, 056308 (2006).

[23] M. I. K. Santala *et al.*, Phys. Rev. Lett. **84**, 1459 (2000).

[24] A. Maksimchuk *et al.*, Phys. Rev. Lett. **84**, 4108 (2000).

[25] E. L. Clark *et al.*, Phys. Rev. Lett. **84**, 670 (2000).

[26] R.A. Snavely *et al.*, Phys. Rev. Lett. **85**, 2945 (2000).

[27] M. Borghesi, J. Fuchs, S. V. Bulanov, A. J. Mackinnon, P. K. Patel, and M. Roth, Fusion Science and Technology **49**, 412 (2006).

[28] M. Borghesi *et al.*, Phys. Rev. Lett. **92**, 055003 (2004).

[29] M. Veltcheva *et al.*, Phys. Rev. Lett. **108**, 075004 (2012).

[30] G. Guethlein, M. E. Foord, and D. Price Phys. Rev. Lett. **77**, 1055 (1996).

[31] C. Beg *et al.*, Phys. Plasmas **4**, 447 (1997).

[32] T. Kluge *et al.*, Phys. Rev. Lett. **107**, 205003 (2011).

[33] K. Wharton *et al.*, presented at *High Temperature Plasma Diagnostic Conference*, Monterey, CA, 12-14 May, 1996.

[34] K. Wharton *et al.*, Phys. Rev. Lett. **81**, 822 (1998).

[35] Guang-yue Hu *et al.*, Phys. Plasmas **17**, 033109 (2010).

[36] L.O. Silva *et al.*, Phys. Rev. Lett. **92**, 015002 (2004).

[37] Min Chen *et al.*, Phys. Plasmas **14**, 053102 (2007).

[38] F.F. Chen, *Introduction to Plasma Physics and Controlled Fusion*, Plenum Press, New York and London (1984).

[39] E. G. Gamaliy and R. Dragila, Phys. Rev. A **42**, 929 (1990).

[40] J. E. Crow, P.L. Auer, and J.E. Allen, J. Plasma Phys. **14**, 65, (1975).

[41] P. Mora, Phys. Rev. Lett. **90**, 185002 (2003). P. Mora, Phys. Rev. E **72**, 056401 (2005).

[42] C. Ren, M. Tzoufras, J. Tonge, W.B. Mori, F.S. Tsung, M. Fiore, R.A. Fonseca, L.O. Silva, J.C. Adam and A. Heron, Phys. of Plasmas **13**, 056308 (2006).

[43] J.A. Cobble *et al*, Phys. Rev. A **39**, 454 (1989).

[44] J.-C. Gauthier, *et al.*, Phys. Plasmas **4**, 1811 (1997).

[45] R.N. Sudan, Phys. Rev. Lett. **70**, 3075 (1993).

[46] R.J. Mason and M. Tabak, Phys. Rev. Lett. **80**, 524 (1998).

[47] J. C. Gauthier, S. Bastiani, P. Audebert, J.P. Geindre, K. Neuman, T.D. Donnelly, R. W. Falcone, R.L. Shepherd, D.F. Price and W.E. White, Proc. SPIE **2523**, 242-253 (1995).

[48] J. Kupersztych, M. Raynaud and C. Riconda, Phys. of Plasmas **11**, 1669-1673 (2004).

[49] M. Raynaud, J. Kupersztych, C. Riconda, J. C. Adam and A. Héron, Phys. of Plasmas **14**, 092702 (2007).

[50] A. Bigongiari, M. Raynaud, C. Riconda, A. Héron, A. Macchi, Phys. of Plasmas **18**, 102701 (2011).

[51] A. Bigongiari, M. Raynaud and C. Riconda and A. Hŕon, Phys. Rev. E **4**, 015402 (2011).

[52] P. Gibbon and A. Bell, Phys. Rev. Lett. **68**, 1535 (1992).

[53] J.P. Geindre, R.S. Marjoribanks and P. Audebert, Phys. Rev. Lett. **104**, 135001, (2010).

[54] P. Mulser and D. Bauer, *High Power Laser-Matter Interaction*, (Springer, 2010)

[55] Subhendu Kahaly *et all.*, Phys. Rev. Lett. **101**, 145001 (2008).

[56] X. Lavocat-Dubuis and J.-P. Matte, Phys. of Plasmas **17**, 093105 (2010).

[57] W.-M. Wang, Z.-M. Sheng and J. Zhang, Phys. of Plasmas **15**, 030702 (2008)

[58] O. Klimo, J.P. Psikal, J. Limpouch, J. Proska, F. Novotny, T. Ceccotti, V. Floquet and S. Kawata, New J. Phys. **13**, 053028 (2011).

[59] P. K. Kaw and J. B.McBride, Phys. of Fluids **13**, 1784-1790 (1970).

[60] J. A. Stamper, K. Papadopoulos, R.N. Sudan, S. O. Dean, E.A. McLean and J.M. Dawson, Phys. Rev. Lett. **26**, 1012 (1971).

[61] A. Pukhov and J. Meyer-ter-Vehn, Phys. Rev. Lett. **76**, 3975 (1996).

[62] Y. Sentoku, K. Mima, S. Kojima and H. Ruhl, Phys. Plasmas **7**, 689 (2000)

[63] D. W. Forslund and J. U. Brackbill, Phys. Rev. Lett. **48**, 1614, (1982).

[64] A. Gopal, M. Tatarakis, F.N. Beg, E.L. Clark, A.E. Dangor, R.G. Evans, P. A. Norreys, M. S. Wei, M. Zepf and K. Krushelnick,Phys. of Plasmas **15**,122701, (2008)

[65] A.S. Sandhu, A.K.Dharmadhikari, P.P. Rajeev, G.R. Kumar, S. Sengupta, A. Das, and P.K. Kaw , Phys. Rev. Lett., **89**, 225002, (2002).

[66] H. Cai, S. Zhu, M. Chen, S. Wu, X.T. He and K. Mima, Phys. Rev. E **83**, 036408 (2011).

[67] V.S. Belyaev, V.P. Krainov, V.S. Lisitsa and A. P. Matafonov, Physics Uspekhi **51**, 793, (2008); and references herein.

[68] R.J. Mason, E. S. Dodd, and B.J. Albright, Phys. Rev. E **72**, 015401 (R) (2005).

[69] L. Gorbunov, P. Mora and T. M. Antonsen, Jr. , Phys. Rev. Lett. **76**, 2495, (1996). L. Gorbunov, P. Mora and T. M. Antonsen, Jr. , Phys. of Plasmas **4**, 4358, (1997).

[70] A. Macchi, A. Bigongiari, F. Ceccherini, T. V. Liseikina, S. Borghesi, S. Kar, and L. Romagnani, Plasma Phys. Contr. Fusion **49**, B71-B78, (2007).

[71] L.M. Gorbunov and R.R. Ramazashvili, Journal of Experimental and Theoretical Phys. **87**, 461-467, (1998).

[72] J. M. Pitarke, V. M. Silkin, E. V. Chulkov and P.M. Echenique,*Theory of surface plasmons and surface-plasmon polaritons*, Rep. Prog. Phys.**70**,1-87, (2007).

[73] P. K. Kaw and J. B.McBride, Phys. of fluids **13**,1784-1790, (1970).

[74] A. Macchi, F. Cornolti and F.Pegoraro, Phys. of Plasmas **9**, 1704, (2002).

[75] A. Macchi, F. Cornolti, F.Pegoraro, T. V. Liseikina, H. Ruhl, and V. A. Vshivkov, Phys. Rev. Lett. **87**, 205004, (2001).

[76] J. Kupersztych, M. Raynaud and C. Riconda,Phys. of Plasmas **11**, 1669, (2004).

[77] M. Raynaud, J. Kupersztych, C. Riconda, J. C. Adam and A. Heron, Phys. of Plasmas **14**, 092702, (2007).

[78] T. Katsouleas and W. B. Mori, Phys. Rev. Lett. **61**, 90, (1988).

[79] J. C. Adam, A. Heron and G. Laval,Phys. Rev. Lett. **97**, 205006, (2006).

[80] H. Schwoerer *et al.*, *Nature* **439**, 445 (2006).

[81] L. Robson *et al.*, *Nature* **3**, 798 (2007).

[82] T. Bartal *et al.*, *Nature*, advance online publication, doi:10.1038/nphys2153 (2011).

[83] V. Malka *et al.*, Med. Phys. **31**, 1587 (2004).

[84] S. Atzeni Physics of Plasmas **6**, 3316-3326 (1999).

[85] R. Kodama *et al.*, *Nature* **412**, 798 (2001). Y. Sentoku *et al.*, Phys. of Plasmas, **11**, 3083, (2004). T. Nakamura *et al.*, Phys. Rev. Lett. **93**, 265002, (2004).

[86] P. Kolodner and E. Yablonovitch, Phys. Rev. Lett. **43**, 1402, (1979).

[87] A. Macchi, arXiv:1202.0389v1, (2012).

[88] Developed at CPhT, Ecole Polytechnique by J. C. Adam and A. Heron.

[89] K. Nanbu, Phys. Rev. E **55**, 4642 (1997).

[90] Birdsall, Charles K. A. Bruce Langdon, *Plasma Physics via Computer Simulation.* McGraw-Hill (1985).

[91] Boris, J.P. (November 1970). *Relativistic plasma simulation-optimization of a hybrid code.* Proceedings of the 4th Conference on Numerical Simulation of Plasmas. Naval Res. Lab., Washington, D.C.. pp. 3-67.

Les ondes de surface ont été observées pour la première fois par Wood en 1902 qui note des anomalies dans le spectre de diffraction d'une lumière continue sur un réseau métallique. Pour certaines longueurs d'onde, le spectre diffracté présente des lignes noires que Fano interprète quelques années plus tard (1941) comme dues à l'excitation d'ondes de surface. De façon analogue, on peut exciter par laser de facĪ§on résonante une onde plasma de surface à la surface d'un plasma sur-dense créé par interaction laser-solide, si les conditions d'excitation de l'onde sont satisfaites. L'onde de surface se propage le long de l'interface plasma-vide et se caractérise par un champ électrique résonant haute-fréquence localisé. Dans ce travail, la dynamique du plasma et les champs associés à l'excitation par laser de l'onde de surface sont décrits numériquement avec des simulations bidimensionnelles Particule-In-Cell dans lesquelles la surface du plasma est initialement pré-structurée de sorte à satisfaire les conditions d'excitation de l'onde de surface. L'intensité laser a été varié entre $I\lambda_0^2 = 10^{15}$W cm$^{-2}\mu m^2$ et $I\lambda_0^2 = 10^{20}$W cm$^{-2}\mu m^2$ afin d'étudier la transition entre un régime d'excitation non-relativiste et relativiste. Les simulations dans lesquelles l'onde de surface est excitée sont comparées à celles où elle ne l'est pas et le couplage du laser avec la cible est analysé. Pour différents paramètres du laser et de la cible, nous avons considéré les quatre aspects suivants de l'interaction laser plasma : i) l'absorption laser et le champ électrique à la surface du plasma, ii) le champ magnétique quasi-statique généré, iii) le chauffage électronique et iiii) l'accélération des ions. Nous avons démontré la possibilité d'exciter une onde plasma de surface pour une large gamme d'intensité laser. Lorsque l'onde de surface est excitée, la composante perpendiculaire à la surface du plasma du champ électrique est amplifiée par rapport au champ laser sur la surface plasma-vide d'un facteur allant de 3.2 à 7.2 selon les cas. L'absorption augmente également fortement de 27% lorsque l'onde de surface n'est pas excitée à 73% lorsqu'elle l'est pour $I\lambda_0^2 = 10^{19}$W cm$^{-2}\mu m^2$ par exemple. Cette étude nous a permis de définir les conditions optimales pour lesquelles le couplage entre le laser et l'onde de surface est le plus efficace. Elles correspondent au régime d'intensité laser relativiste dans lequel le mécanisme d'absorption principale est le vacuum heating: les particules gagnent de l'énergie en oscillant dans le champ électrique perpendiculaire à la cible. En présence de l'onde de surface, cette oscillation est fortement augmentée par la présence du champ localisé de l'onde de surface plus intense que le celui du laser. La possibilité de créer des champs magnétiques quasi-statiques auto-générés en présence d'une onde de surface a de plus été étudiée analytiquement et les résultats ont été comparés à ceux des simulations. Les structures de champ obtenues suggèrent que l'intensité du champ magnétique généré induit un confinement partiel des particules sur la surface de la cible lorsque l'onde de surface est excitée. Enfin, nous avons observé un effet induit par l'excitation de l'onde de surface encore plus fort dans des cibles minces dans lesquelles les électrons peuvent circuler d'un bord à l'autre de la cible et interagir plusieurs fois avec le champ de l'onde. Le champ de charge d'espace ainsi créé au cours de l'interaction induit une augmentation importante de l'énergie des ions émis sur les deux faces de la cible mince. L'ensemble de ce travail nous a permis de montrer que l'excitation d'une onde de surface par interaction laser-plasma structuré est un mécanisme physique prometteur pour augmenter l'énergie des particules émises. C'est un point particulièrement intéressant pour les applications liées à la production de protons énergétiques telles que la thérapie hadronique ou à celle d'électrons de hautes énergies indispensables dans le processus de fusion inertiel dans lequel le schéma de l'allumeur rapide est utilisée.